WARSAW UNIVERSITY OF TECHNOLOGY

Ph.D. Thesis

Discipline of Science:
Physical Sciences

Field of Science:
Natural Sciences

Agata Marta Zdanowicz, M.Sc. Eng.

Collective properties of superfluid fermionic mixture in neutron star crust

Supervisor
PhD, D.Sc. Eng. **Gabriel Wlazłowski**, University Professor

Warsaw 2025

Acknowledgements

I want to express my huge gratitude to my supervisor, prof. Gabriel Wlazłowski. I am full of admiration for his endeavour, commitment and patience that I could experience from him during my studies. These four years of common work made me believe in myself both as a scientist and a person, for which I am truly grateful. I also give thanks to prof. Piotr Magierski for the scientific guidance and support. The wonderful atmosphere of Nuclear Theory Group has made my studies a true pleasure. I am convinced that the time spent there would be undoubtedly one of my best memories.

This work could have not come to an end without the admirable support of the members of Nuclear Theory Group at Faculty of Physics. I would like to give the special thanks to Daniel Pęcak and Nicolas Chamel – anytime I needed help, you have always been there with your advice and experience, which I truly appreciate.

Most importantly, I am grateful for my mom for being with me during my scientific journey. Indeed, there are no words with which I can express my admiration and gratitude for your support and love. Thanks to many years during which I could observe your attitude towards various issues, now I believe that there are no difficulties – both scientific and everyday – which cannot be overcome.

Unfortunately, I cannot give thanks to two special people – my dad and grandfather. Nevertheless, I am convinced that the wisdom and support that I have received from them through all the years spent together have brought me to the place where I am today.

We acknowledge PRACE for awarding us access to resource Piz Daint based in Switzerland at Swiss National Supercomputing Centre (CSCS), decision No. 2021240031. We acknowledge Polish high-performance computing infrastructure PLGrid for awarding this project access to the LUMI supercomputer, owned by the EuroHPC Joint Undertaking, hosted by CSC (Finland) and the LUMI consortium through PLL/2024/07/017-603, PLL/2023/04/016476, PLL/2022/03/016433.

Abstract

This thesis presents a detailed description of the collective properties of nuclear matter in the neutron star crust, investigated by means of methods of computational physics and based on Density Functional Theory.

Chapter 1: Nuclear Matter in Neutron Stars provides the essential theoretical information from the field of neutron stars. At first, the internal structure of neutron stars is described. Then, I discuss the phenomenon of superfluidity and the dynamic properties of the inner crust.

In Chapter 2: Theoretical Background – Methodology I have presented the theoretical background of the numerical tool applied in this research. At first, the basics of Mean Field Approximation methods are introduced. Then, I provide the general information about Density Functional Theory and its modification for superfluid systems. The concept of energy functionals, with a dedicated section on Brussels-Montreal Skyrme functionals, is introduced. The details of the numerical software, W-BSk Toolkit, are also discussed.

Chapter 3: Linear Movement of Impurity in Neutron Matter starts with the description of the state of the art in the field of effective mass estimation. Then, the discussion of the new method, based on dynamic calculations within the framework of Density Functional Theory, is provided. I present the results obtained within this method and analyze the mechanisms of dissipation in the nuclear matter of the neutron star crust.

In Chapter 4: Oscillations of Impurity in Neutron Matter, another method of estimation of mass parameters, based on oscillations of collective variables, is discussed. Initially, the procedure for extracting the effective mass within the framework of this new approach, along with an examination of dissipative processes, is presented. The method is also applied to obtain another mass parameter, which is connected to the spatial deformation of the impurity.

Chapter 5: Vortex-Nucleus Interaction is focused on the analysis of vortex-nucleus interaction. The standard methods for examining the inner crust dynamics are briefly discussed. Then, I discuss the crucial quantities obtained within the DFT-based method, including the interaction force, system energy, vortex length, pinning energy, and tension force. Finally, deformation of impurity arising from the vortex-nucleus interaction is discussed.

Chapter 6: Summary summarizes the achievements of this thesis and outlines some possibilities for further research.

Keywords: *Neutron Stars, Density Functional Theory, Effective Mass, Collective Modes, Deformation, Vortex-Nucleus Interaction*

This thesis is based on the following publications:

- D. Pęcak, A. Zdanowicz, N. Chamel, P. Magierski and G. Wlazłowski, *Time-Dependent Nuclear Energy-Density Functional Theory Toolkit for Neutron Star Crust: Dynamics of a Nucleus in a Neutron Superfluid*, Phys. Rev. X 14, 041054 (2024).
- A. Zdanowicz, D. Pęcak, P. Magierski, G. Wlazłowski, *Dynamical scheme for computing the mass parameter of a system in a medium*, Phys. Rev. C 112, 045804 (2025).

Streszczenie

W niniejszej rozprawie omówiono właściwości kolektywne materii jądrowej w skorupie gwiazdy neutronowej. Badania zostały wykonane z zastosowaniem pakietu numerycznego opartego na Teori Funkcjonału Gęstości.

Rozdział 1: Materia jądrowa w gwiazdach neutronowych przedstawia najważniejsze informacje z dziedziny gwiazd neutronowych. Omówiona została struktura gwiazdy neutronowej wraz z ideą modeli efektywnych, zjawisko nadciekłości i dynamiczne właściwości skorupy gwiazdy neutronowej.

W Rozdziale 2: Wstęp teoretyczny – Metodologia znajdują się podstawy teoretyczne niezbędne w przeprowadzonych badaniach. W pierwszej kolejności zostały przedyskutowane podstawowe metody przybliżenia pola średnia, przedstawiono również informacje dotyczące Teorii Funkcjonału Gęstości i jej rozszerzenia na przypadek układów nadciekłych. Omówiono również ideę funkcjonałów gęstości ze szczególnym uwzględnieniem klasy funkcjonałów Brussels-Montreal Skyrme. Ostatnia część rozdziału jest poświęcona szczegółom pakietu numerycznego W-BSk.

W początkowej części Rozdziału 3: Linearny ruch domieszki w materii neutronowej zamieszczono opis aktualnego stanu wiedzy w dziedzinie wyznaczania masy efektywnej. Następnie przedyskutowano nową metodę opartą na obliczeniach dynamicznych z zastosowaniem Teorii Funkcjonału Gęstości. Przedstawiono również wyniki uzyskane za pomocą tej metody, a także analiza procesów dyssypacyjnych w materii jądrowej skorupy gwiazdy neutronowej.

W Rozdziale 4: Oscylacje domieszki w materii neutronowej przedstawiono alternatywną metodę wyznaczania parametrów masowych na podstawie oscylacji zmiennej kolektywnej. W pierwszej części tego rozdziału znajduje się opis procedury wyznaczania masy efektywnej domieszki za pomocą tej metody, a także analiza mechanizmów dyssypacji. Następnie wyznaczono również inny parameter masowy, związany ze zmianami kształtu domieszki.

Rozdział 5: Oddziaływanie wir-domieszka przedstawia analizę oddziaływania między wirem kwantowym a domieszką. W początkowej części rozdziału znajduje się krótka dyskusja dotycząca obecnie stosowanych metod opisu tego oddziaływania. Następnie przedyskutowano kluczowe parametry związane z tym oddziaływaniem, które wyznaczono za pomocą metody opierającej się na Teorii Funkcjonału Gęstości. Wśród tych parametrów znajdują się między innymi siła oddziaływania, energia układu, długość wiru, a także wielkości znane jako *pinning energy* oraz *tension force*. W końcowej części rozdziału przeanalizowano również deformację domieszki spowodowaną jej oddziaływaniem z wirem.

Rozdział 6: Podsumowanie podsumowuje najważniejsze osiągnięcia tej pracy. Przedstawione są również możliwe przyszłe kierunki rozwoju dalszych badań.

Słowa kluczowe: *gwiazdy neutronowe, Teoria Funkcjonału Gęstości, masa efektywna, mody kolektywne, deformacja, oddziaływanie wir-domieszka*

Niniejsza rozprawa powstała na podstawie następujących publikacji:

- D. Pęcak, A. Zdanowicz, N. Chamel, P. Magierski and G. Wlazłowski, *Time-Dependent Nuclear Energy-Density Functional Theory Toolkit for Neutron Star Crust: Dynamics of a Nucleus in a Neutron Superfluid*, Phys. Rev. X 14, 041054 (2024).
- A. Zdanowicz, D. Pęcak, P. Magierski, G. Wlazłowski, *Dynamical scheme for computing the mass parameter of a system in a medium*, Phys. Rev. C 112, 045804 (2025).

Contents

Chapter 1

Introduction

Since their discovery at the beginning of the previous century, neutron stars have become one of the major fields of interest in modern astrophysics. Being the examples of extremely dense matter, they seem to be perfect "laboratories" [1] for the examination of various phenomena taking place in such conditions. As reported in the literature, within a neutron star, one can find states such as quark-gluon plasma or hyperonic matter [2]. The internal matter of a neutron star is also a perfect environment for studies of various phase transitions [2, 3].

The term "neutron star" was first used by Baade and Zwicky in [4], where it was stated that the supernova explosion leads to the creation of objects consisting of very closely packed neutrons [2]. The first experimental evidence of the existence of neutron stars was linked to the phenomenon of glitches, which were initially considered a signal from an extraterrestrial civilization [5]. Years after this discovery, the connection of this effect with the occurrence of the superfluid phase in the neutron star matter has been raised (e.g., by Migdal in [6]) and established (e.g., in [7]). However, the examination of superfluidity in the neutron star matter still remains the major problem, as there is no possibility to study such objects in straightforward experiments [3]. Therefore, there was a need to develop another method for their investigation.

It soon turned out that in many-body quantum systems, the approach known as Density Functional Theory can provide a reliable description at a low computational cost [3]. As reported in the literature [8, 9], this approach can be successfully applied to examine nuclear matter in an astrophysical context. At this point, one should give special interest to numerical simulations conducted within the framework of this method. Within such calculations, one can obtain the parameters of the effective models of neutron stars, which provide the complex view of the internal structure of the crust and

the various processes taking place inside of it [10].

This thesis is focused on the investigation of the inner crust of a neutron star, which is expected to show superfluid properties. Taking a closer look at the structure of the crust, one can see that in the shallower layers it consists of single nuclei immersed in the neutron matter. Deeper in the crust, these nuclei become "modified" into the more exotic phases (such as pasta phase). Among the parameters describing the structure of the crust included in effective models, one can point out the mass parameters. In general, they refer to the mass of impurities, which turns out to be sensitive to various processes taking place in the crust.

During this research, various mass parameters have been extracted. As examples, the effective mass of impurity and the mass parameter connected with deformation have been considered. Furthermore, the phenomenon of superfluidity is also associated with dissipative processes, which have been analyzed. To proceed with this research, a new numerical software dedicated to the study of nuclear matter, the W-BSk Toolkit [3], has been developed. The construction of such a tool and its application to the extraction of mass parameters for effective models of neutron star crust have been the main goals of this research.

Chapter 2

Nuclear Matter in Neutron Stars

2.1 Internal Structure of Neutron Star

Neutron stars are formed due to the supernova explosion, which takes place as the nuclear synthesis reactions in a massive star come to an end [11]. The properties of neutron stars, such as mass and radius, are usually described with regard to the solar parameters. Despite the fact that the mass of neutron stars is typically about 1.4 times the solar mass [12], their radii are significantly smaller; they are supposed to be about 10 km, which is about 10^5 less than the solar radius and therefore makes neutron stars examples of extremely dense matter [12].

Apart from mass and radius, one should also mention the parameter called compactness. It describes the relation between gravitational energy (defined as GM/R with G being the gravitational constant, M meaning the mass of the star, and R – its radius) and mass energy (Mc^2, where c denotes the speed of light) [5]. It turns out that the compactness of neutron stars is usually about 0.4 [5]; in contrast, for Earth, it is approximately 10^{-9}, and for the Sun, it is 10^{-6} [5]. Therefore, it can be seen that neutron stars are considered among the most compact astrophysical objects.

Another important quantity describing neutron stars is surface gravity. As the compactness parameter introduced the so-called gravitational redshift [5] (which is connected with strong gravitational field of the star and leads to the shift e.g. in velocity of photons emitted from it's surface), the gravity of neutron star turns out to be about $2.4 \cdot 10^{12}\ \mathrm{m/s^2}$ [5], which is about 10^{11} times larger than the surface gravity of Earth [5].

The details of the internal structure of neutron stars, as well as many of the properties, still remain either uncertain or unknown. One of the ways of their examination

is the analysis of electromagnetic radiation emitted by some of them (for example, by pulsars) [2, 12]. This radiation can be detected in the form of regular pulses (with a period from milliseconds to a few seconds), which is connected with the rotation of such stars [2, 12]. Considering the change in the period of rotation over time, it turns out that these changes are very slow [12]; for example, the pulsar Crab slows down by about 13 μs per year [2]. Therefore, neutron stars are supposed to be one of the most precise clocks in the universe [2, 13].

However, over many years of observations, sudden jumps in the frequency of rotation (called glitches) have been detected [12]. It turns out that from time to time the star tends to suddenly spin up; later on, after (approximately) a few weeks of relaxation period [14], it comes back to the original frequency of rotation. As an example, in the case of the Vela pulsar, a few glitches over nearly 30 years of observation could have been detected [14]. Despite many attempts at explanation, nowadays the phenomena connected with superfluidity in neutron star crust seem to be the most convincing ones [2, 14]. The phenomenon of glitches is described in detail in Sec. 2.5.3.

The schematic view of the internal structure of a neutron star is shown in Fig. 2.1. In general, a neutron star consists of several main layers, among which one can distinguish:

- atmosphere – the most external one;
- outer crust – consists of ions and electrons [14]. The highest density reached in this layer is assumed to be about $4 \cdot 10^{11}$ g/cm^3 [15]. Electrons in the outer crust form a gas, which becomes degenerate deeper in this layer and can be considered as an interacting Coulomb system [12]. In general, the Fermi energy of electrons increases with density; as a result, the nuclei in the deeper layers of the outer crust become neutron-rich due to beta captures caused by this energy [12]. Then the neutrons drip out of nuclei and start to form the neutron matter [12, 2];
- inner crust – the thickness of this layer can be about one kilometer [12]. It consists of electrons and nuclei immersed in the sea of neutrons [15, 12]. Therefore, the structure of the inner crust (shown schematically in panel B of Fig. 2.1) is often described as a mixture of protons in the form of clusters (which are, in fact, single nuclei) and neutrons showing superfluid properties (in addition, in neutron matter quantum vortices can occur) [14]. At the top of this layer the density can

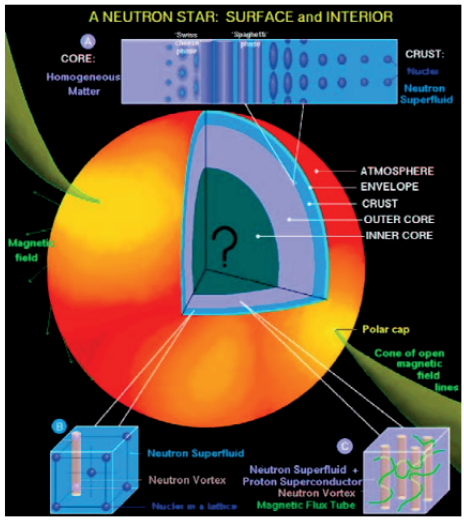

FIGURE 2.1: The schematic structure of a neutron star [14].

be close to $4 \cdot 10^{11}$ g/cm^3 [12], while in the bottom layers (close to the core) it can reach about 0.5 ρ_0 (where ρ_0 is the nuclear matter saturation density $2.8 \cdot 10^{14}$ g/cm^3) [12]. The density of neutrons in the inner crust depends on the depth (deeper in the crust, the number of neutrons increases). Consequently, as pressure also increases with density, the nuclei become more neutron-rich and start to form various exotic structures [16] (as it is shown in panel A of Fig. 2.1), beginning with single proton impurities at lower densities, through *spaghetti* and *cheese* phases [16] to *pasta* phase for densities close to the core [16, 2, 15];

- outer core – it can extend up to a few kilometers with densities from 0.5 ρ_0 to 2 ρ_0 [12]. Outer core consists mainly of homogenous neutron matter with a small percentage of protons, electrons, and muons μ, which form the so-called *npe* μ mixture [12]. Strongly interacting neutrons form a superfluid Fermi liquid, protons may exhibit superconductivity [14], while electrons and muons can be treated as an ideal Fermi gas [2]. As a result of the superconductivity, in the outer core, magnetic flux is supposed to occur [5]. This leads to the creation of fluxons, being the analogous structures to quantum vortices in superfluids [5];

- inner core – the densities in this layer can be extremely high (even to 10 – 15 ρ_0)

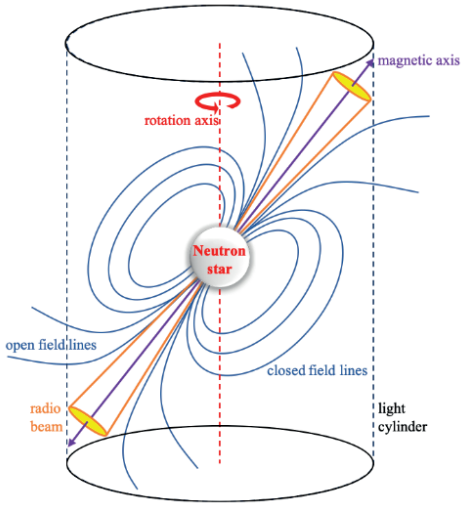

FIGURE 2.2: The schematic of the electromagnetic field structure of a neutron star [17].

[12]. The structure of the inner core remains unknown; among various hypotheses describing the processes inside the core, one can point, for example, to the creation of quark-gluon plasma, the emergence of hyperons, and Bose-Einstein condensation [12].

2.1.1 Measurements of Parameters of Neutron Stars

As it is marked in Fig. 2.1, rotating neutron stars (called pulsars) emit electromagnetic radiation [2, 17]. However, as it is mentioned in [17], the mechanism of this emission is still not fully understood. Among various attempts (such as the lighthouse model [18]), the magnetic dipole model gives some convincing explanation of this phenomenon [17].

Fig. 2.2 schematically shows the idea of the magnetic dipole model. As can be seen, the magnetic axis of the pulsar is inclined at a certain angle to the rotation axis. As the pulsar rotates, charged particles are emitted from the crust along the magnetic axis in the form of a beam, creating a magnetosphere that rotates together with the entire star [17]. The magnetosphere is, however, limited by the so-called *light cylinder* with a

certain radius; once it is exceeded, the field lines are no longer closed [5]. As the particles in the magnetosphere are accelerated, they start to emit photons, reacting with the magnetic field [17]. As a result, electron-positron pairs are formed and can be observed as electromagnetic radiation [17].

Based on the analysis of the spectrum of emission, one can obtain, e.g., the mass and radius of a star with regard to the Stefan-Boltzmann law. In addition, the temperature of a star based on the blackbody emission model [2] can also be estimated. Referring to the period of rotations and its derivative, the age of the pulsar is estimated [5]. However, establishing a connection between experimentally accessible observables and the internal structure of a neutron star remains a significant challenge. This connection can be explored through the application of effective models of neutron star matter.

2.1.2 Effective Models

The examination of the internal matter of neutron stars reveals itself as an extremely demanding and complicated problem. For example, one can investigate the structure of the inner crust, which is the primary focus of this thesis. As mentioned before, the inner crust is supposed to consist of superfluid neutrons and clusters of protons (called impurities), which can be considered remnants of nuclei. Such a composition of internal matter of the crust can occur due to the extremely high pressure in the crust. As a result, the neutrons are expected to drip out of nuclei and form neutron matter, while the protons from these nuclei are left in the form of clusters [15, 2]. Due to the presence of these proton structures, such a system is not homogeneous and therefore cannot be studied with many-body calculations designed for the treatment of uniform systems; moreover, strong interactions between nucleons make this examination even more difficult. On the other hand, such a system cannot be studied experimentally, which leads to the idea that phenomenological effective models [10] are of crucial importance in the investigation of the complex systems of neutron stars.

In the neutron star crust, phenomena taking place at different length scales can be described with regard to various models. As this scale is altered, the system can be examined with regard to different degrees of freedom and, consequently, also within another set of parameters. What is particularly important is that the parameters obtained within a model describing the system at a certain length scale are used as an

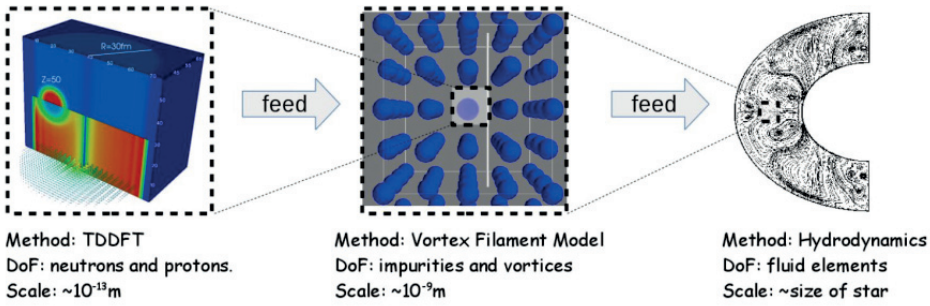

FIGURE 2.3: The hierarchy of effective models used in neutron star studies [19].

input for the more general ones (describing the system at larger scales) [19, 20]. In this way, one can construct a hierarchy of models used to describe neutron stars.

The idea of hierarchy of models is schematically shown in Fig. 2.3 [19]. Starting from the lowest resolution, one of the fundamental ones used in the description of neutron stars at the largest length scales is the hydrodynamic model, which belongs to the class of so-called macroscopic models [15]. In general, models operating at the largest scales enable the description of phenomena that can be directly observed in experiments. For example, regarding the hydrodynamic approach, which in this case refers directly to the two-fluid model, one can explain the phenomenon of glitches [14, 2]. Therefore, the length scale at which macroscopic models are used can be considered as of the order of the whole neutron star. The parameters that are used in this type of model are therefore connected with the properties of (super)fluids at the most general level; among them, one can distinguish, e.g., their viscosities or mutual friction parameters [20].

Lower in the hierarchy, at smaller length scales, one can distinguish mesoscopic models providing an input for macroscopic ones; one of these models is, e.g., the Vortex Filament Model (VFM) [21]. Examining the inner crust in more detail reveals the structure of the fluids. One of them is the superfluid neutron matter with quantum vortices, filled with proton impurities [2], which can be considered as the second fluid component. Therefore, the degrees of freedom that can be distinguished with regard to mesoscopic models are, e.g., impurities and vortices (and, as a consequence, the length

scales characteristic for this class of models are of the order of the size of these structures). Moreover, it can be seen that the parameters obtained within mesoscopic models provide the necessary input for the macroscopic ones. For example, consider the drag force acting between vortices and impurities, which leads to the force associated with mutual friction [10, 20].

Later on, at the length scale of femtometers, microscopic models are used, where the degrees of freedom are protons and neutrons. At this level, their behaviour can be analyzed within a quantum mechanical description. The fundamental theoretical method commonly used at this scale is Density Functional Theory, which is also a crucial tool in this case. Coming back to the example of mutual friction, one can consider, e.g., the effective interaction between neutrons forming vortices and protons creating impurities, which is the origin of the drag force present in the mesoscopic model [10, 20].

2.2 Structure of Inner Crust in the Frame of Effective Models

As it was mentioned in Sec. 2.1.2, one can distinguish various models of neutron star crust. One of them is the liquid drop model, which can be considered as a mesoscopic one and provides useful insight into the structure of the crust. In contrast to the liquid model, the microscopic model, which analyzes the fundamental elements (such as protons, neutrons, and electrons) and their mutual interactions, is based on quantum mechanics. In the following section, an insight into these models is provided.

2.2.1 Liquid Drop Model

One of the useful and simplest models is called the liquid drop model. The fundamental theorem that stands behind it is called the Wigner-Seitz approximation [15, 12]. At first, it was used to describe the behaviour of electrons in metals forming a symmetrical lattice. However, it can also be applied to nuclear systems, assuming that free neutrons in the crust behave in a similar way to electrons in solids [15]. One of the fundamental concepts arising from the lattice's symmetry is the idea of cells, into which the system can be divided; each cell is expected to contain only one site of the lattice. However, the choice of such a cell is not arbitrary and therefore turns out to be a nontrivial problem [15]. One of the common approaches has been suggested by Wigner and Seitz's

theorem. According to this idea, the Wigner–Seitz cell is restricted by a set of points closer to the chosen lattice point than any others. In the inner crust of a neutron star, the Wigner-Seitz cells take the form of spheres with proton impurity being the center of a single sphere (and a single site of the lattice as well) [15]. Then, such a sphere with a cluster inside can be considered as a kind of exotic nucleus. As a consequence, the proper decomposition of the inner crust into these spheres allows us to define its structure.

In the liquid drop model, proton clusters are treated as incompressible liquid drops [12]. As the density of these drops is assumed to be close to the nuclear saturation density, the contributions to the total energy of a cell connected with volume and surface of impurity are proportional to A and $A^{2/3}$ (where A is the atomic number of the single nuclei) [15]. Therefore, one can parametrize these contributions to energy by A and Z (being the mass number of nuclei); however, it turns out to be difficult due to the varying relation between A and Z over the crust. In addition, due to the influence of neutron matter surrounding impurities, the surface term is expected to decrease with density; another effect arising from this impact is the compression of nuclear matter [12]. Therefore, apart from the contributions to energy mentioned before, one should also consider, e.g., the size of the impurity, as well as the densities of protons and neutrons inside it (as the cluster turns out to be penetrable for neutrons [15].

In the energy associated with a single cell, one can distinguish the volume, surface, and Coulomb terms. Volume and surface terms are the nuclear contribution to the whole energy of a particular cell [12]. One should also consider the contribution to kinetic energy coming from electrons forming a uniform Fermi gas [12]. Based on that, the total energy E (expressed in terms of A and Z) of a single sphere can be written as [12]:

$$E = E_V + E_S + E_C + E_e, \tag{2.1}$$

where E_V is the term corresponding to volume energy, E_S – surface energy, E_C – Coulomb energy and E_e – contribution from electron gas.

The volume term (which is, in other words, the bulk energy of nucleons in the Wigner-Seitz cell) can be expressed as [12]:

$$E_V = V_c \left[w\varepsilon_i + (1-w)\varepsilon_o \right]. \tag{2.2}$$

Here, ε_i is the energy density in the impurity, and ε_o means the energy density of neutron matter surrounding the impurity. In addition, V_c is the volume of the Wigner-Seitz cell, and w means the volume fraction occupied by protons. In this case, it is equal to $(r/r_c)^3$, where r is the radius of the impurity (with the assumption that the cluster is spherical) and r_c is the radius of the Wigner-Seitz cell [12].

Next, one can consider the surface component connected with the influence of neutron matter on impurity [12]. This contribution can be defined with regard to the two most significant parameters connected with effects taking place on the surface of the impurity [15]:

- chemical potential μ, defined with regard to a fixed number of N neutrons adsorbed at the surface of the cluster and forming the so-called neutron skin:

$$\mu = \frac{\partial E_S}{\partial A},\ N = \text{const}, \tag{2.3}$$

- surface thermodynamic potential σ per fixed area $\mathcal{A}$ of the nuclear surface:

$$\sigma = \frac{\partial E_S}{\partial N},\ A = \text{const}\,. \tag{2.4}$$

  Here, the area can be approximated as $4\pi r^2$, where r denotes the radius of spherical nuclei. In addition, once the curvature corrections (proportional to A/r) are neglected [12], one can approximate the surface potential by the surface tension [12] and the number of adsorbed neutrons as νA, where ν means the surface density of these neutrons [12].

Therefore, the surface term is defined as [15]:

$$E_S = \sigma\mathcal{A} + N\mu. \tag{2.5}$$

Last of the contributions, which is the Coulomb term, can be written with regard to the Wigner-Seitz approximation [12]:

$$E_C = \frac{16\pi^2}{15}(\rho_{p,i})^2\, r^2\, f_3(w). \tag{2.6}$$

The variable $\rho_{p,i}$ means the density of protons in the center of the impurity. In addition, the function $f_3(w)$ is defined as $1-(3/2)w^{1/3}+(1/2)w$.

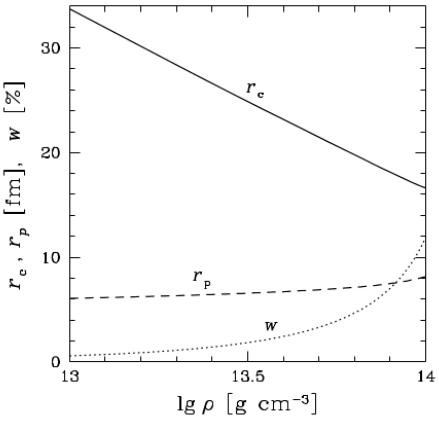

(A) Radius of a Wigner-Seitz cell (r_c), radius of impurity (r_p) and volume fraction of proton (w) as a function of average nuclear density ρ [22].

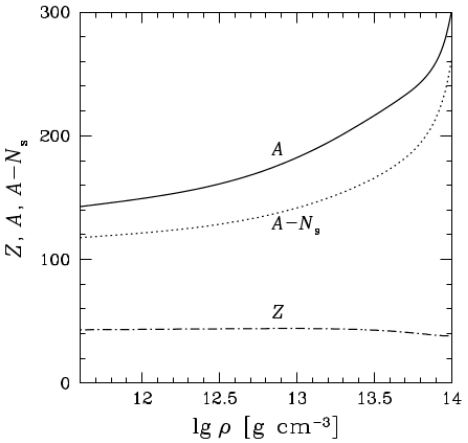

(B) Number of protons Z, number of nucleons A and mass number without skin neutrons N_s as a function of average nuclear density ρ [22].

The liquid drop model allowed to calculate the structure of the inner crust. For example, consider the results from [22], as shown in Figs. 2.4a and 2.4b. The first of them presents geometrical parameters: radius of a single cell r_c, radius of impurity r_p, and the volume fraction of protons w as a function of nuclear density ρ [12]. Fig. 2.4b shows the mass number A and proton number Z, also in terms of density. In addition, in panel b), one can see a line corresponding to A without neutrons forming a skin layer N_s [12]. According to Fig. 2.4a, as the density increases, the distance between nuclei (corresponding to the radius of a cell) becomes smaller. However, the radius of impurities remains approximately constant. As it can be seen in Fig. 2.4b, the number of protons (approximately equal to 40) in nuclei remains approximately constant through the whole range of densities in the inner crust (according to [11], these densities vary, approximately, from $4 \cdot 10^{11}$ g/cm^3 to 10^{14} g/cm^3). On the contrary, one can observe an increasing total number of nucleons. What is also interesting is that the number of skin neutrons starts to increase rapidly for densities higher than approximately one third of normal nuclear density [12]. This happens as a result of the fact that for this range the density of neutrons inside of the impurity and the density of neutron matter surrounding it become comparable [12].

2.2.2 Quantum Approach

The next important method is based on a quantum approach, which is a crucial concept, for example, in nuclear band theory [15]. Again, in this approach, the idea of Wigner-Seitz spheres is used. The properties of the system within the Wigner-Seitz cell are described by the following equation (where index q denotes either protons (p) or neutrons (n), therefore $q = n, p$) [23]:

$$-\nabla\frac{\hbar^2}{2m_q^*(\boldsymbol{r})}\nabla\varphi_\alpha^{(q)}(\boldsymbol{r}) + U_q(\boldsymbol{r})\varphi_\alpha^{(q)}(\boldsymbol{r}) + \frac{W_q(\boldsymbol{r})}{\boldsymbol{r}}\boldsymbol{l}\cdot\boldsymbol{\sigma}\varphi_\alpha^{(q)}(\boldsymbol{r}) = \epsilon_\alpha^{(q)}\varphi_\alpha^{(q)}(\boldsymbol{r}). \tag{2.7}$$

In Eq. 2.7, $\varphi_\alpha^{(q)}(\boldsymbol{r})$ is a single-particle wave function with a set of quantum numbers α and $\epsilon_\alpha^{(q)}$ – energy corresponding to the state described with such a function. The variable $\boldsymbol{l}$ means the orbital angular momentum operator, and $\boldsymbol{\sigma}$ – a vector consisting of Pauli spin matrices. In addition, in Eq. 2.7 one can also find several fields: $\hbar^2/(2m_q^*(\boldsymbol{r}))$ (in short $B_q(\boldsymbol{r})$), mean field potential $U_q(\boldsymbol{r})$ and spin-orbit potential $\boldsymbol{W}_q(\boldsymbol{r})$, which originate from nuclear forces [23]. Single-particle wave functions $\varphi_\alpha^{(q)}(\boldsymbol{r})$ (which are the solutions of Eq. 2.7 for a specific cell) can be defined according to the Floquet-Bloch approach [15, 23]:

$$\varphi_\alpha^{(q)}(\boldsymbol{r}+\boldsymbol{T}) = e^{i\alpha\cdot\boldsymbol{T}}\varphi_\alpha^{(q)}(\boldsymbol{r}) \tag{2.8}$$

with $\boldsymbol{T}$ being translation vector of the lattice. Then, it can be seen that these wave functions have the meaning of Bloch waves that also exhibit periodicity with regard to the lattice [15]:

$$\varphi_\alpha^{(q)}(\boldsymbol{r}) = e^{i\alpha\cdot\boldsymbol{r}}u_\alpha^{(q)}(\boldsymbol{r}). \tag{2.9}$$

Obtaining the wave function for one cell allows us to calculate these functions for all the cells in the lattice, which can be done through Eq. 2.8. Therefore, the energy spectrum takes the form of bands, each of which is also a function of α [15]. Once the single-particle wave functions are computed from Eq. 2.7, one can analyze various properties, such as particle number density distribution [15]:

$$\rho_q(\boldsymbol{r}) = \sum_\alpha |\varphi_\alpha^{(q)}(\boldsymbol{r})|^2. \tag{2.10}$$

The first attempt to calculate the structure of inner crust within a quantum approach has been done by Negele & Vauterin [24] through minimization of the total energy per nucleon in a single Wigner-Seitz cell for a fixed number of nucleons. As a result of these

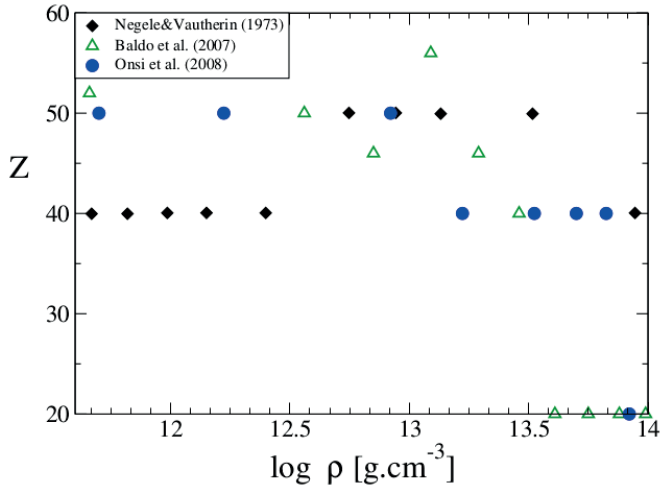

FIGURE 2.5: Number of protons in Wigner-Seitz cell as a function of nuclear matter density of inner crust obtained within different methods of quantum calculations [15].

calculations, one could obtain the structure of the inner crust, which is shown in Fig. 2.5 [15]. Apart from results by Negele & Vauterin, structures by Baldo et al. (from [25, 26]) and Onsi et al. (described in [27]) are also provided. Despite the fact that the structure by Negele & Vauterin is in good agreement with the prediction of the liquid drop model (Figs. 2.4a - 2.4b), it differs a lot from the other results of quantum calculations presented in Fig. 2.5. Firstly, this discrepancy is connected with the fact that in the approach of Negele & Vauterin, the pairing correlations between nucleons have not been taken into consideration [15]. Later on, as it has been shown in the research of Baldo et al. [25, 26], the attractive interaction between nucleons (responsible, e.g., for superfluid effects) can affect the obtained structure [15]. In addition, the calculations by Onsi et al., proceeded with regard to effective interaction between nucleons [27], also differ from predictions of Negele & Vauterin. However, the obtained structure also depends on the choice of Wigner-Seitz cell, which can lead to differences in predictions from various calculations [25, 26].

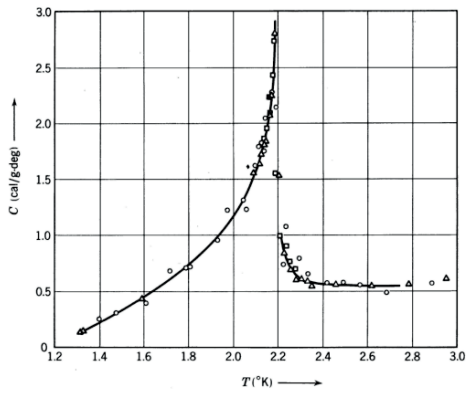

FIGURE 2.6: Specific heat as a function of temperature of liquid ^{4}He, taken from [31].

2.3 The Fundamentals of Superfluidity

Historically, the phenomenon of superfluidity was discovered accidentally during investigations of superconductivity in metals [28, 29]. According to [28, 29], it has been observed that liquid Helium (in particular, the ^{4}He isotope) stopped boiling at a temperature equal approximately 1.8 K. Later on, with regard to the research by Keesom [30], below a temperature equal to 2.7 K, the discontinuity in specific heat of Helium was observed. This characteristic temperature has been called the lambda point, as the plot of specific heat as a function of temperature (shown in Fig. 2.6) looks similar to the Greek letter λ [29]. Helium above this characteristic temperature has been named Helium I and below it – Helium II [31]. Then, in a famous work by Kapitza [32], Helium II has been named superfluid, in contrast to helium above the lambda point, which behaves like a standard liquid. This characteristic temperature can therefore be considered as a point of second-order phase transition between normal and superfluid phase [31]. A schematic phase diagram (pressure versus temperature) of liquid Helium is shown in Fig. 2.7. One of the crucial properties of superfluids, as shown in [33, 31], is the lack of viscosity, which leads to the dissipationless flow. Apart from that, superfluids do not transport heat or entropy [31]. Therefore, they can flow from a cooler to a hotter region, which leads, e.g., to the *fountain effect* [34].

At this point, it is worth mentioning that the ^{4}He isotope, for which the investigation discussed above has been done, is a bosonic system [31]; however, it turns out

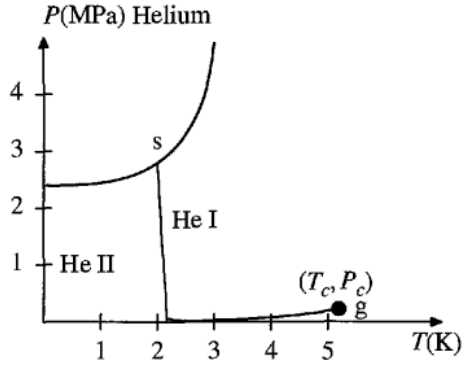

FIGURE 2.7: Phase diagram for ^{4}He [31]. The black circle (labeled as g) corresponds to the gas-liquid critical point, characterized by a temperature T_c and a pressure P_c. This point ends the line separating the gas and liquid phases. The letter s denotes the solid phase.

that superfluidity takes place also in fermionic systems [31]. At first, this phenomenon was observed for ^{3}He in 1972 by Lee, Oscheroff, and Richardson [35], but its properties turned out to be significantly different than those in the bosonic case. Firstly, the temperature of transition in ^{3}He is equal to 2.7 mK [31], which is a few orders of magnitude lower than in ^{4}He. In addition, in fermionic superfluids, one could observe two phase transitions and, as a consequence, three phases: superfluid A, superfluid B, and normal phase [31]. The A phase has a gap that vanishes at some points on the Fermi surface [31]. Later on, this phase has been identified with the Anderson-Brinkman-Morel (ABM) state [36, 37]. On the contrary, the gap in case of B phase is expected to be constant at the whole Fermi surface [31]. This phase, in turn, is now recognized as Balian-Werthamer (BW) state [36, 38]. Physically, the B phase is expected to occur in the regime of low magnetic fields [36] and to be the more stable one [31]. The principal difference between these states is related to the spin combination of particles that create Cooper pairs (which is discussed later in the thesis). Basically, in the ABM state, the spin-triplet pairing is expected to occur, while the BW state corresponds to the spin-singlet pairing [39] (the detailed description of different types of pairing is provided in Sec. 2.4.2). In Fig. 2.8, the phase diagram for ^{3}He is shown. As mentioned, e.g., in [31], the differences between superfluidity in ^{4}He and ^{3}He arise due to the distinct properties of Fermi and Bose statistics. Furthermore, it has been proved that fermionic superfluidity is in fact an analog of superconductivity, but for uncharged particles [31].

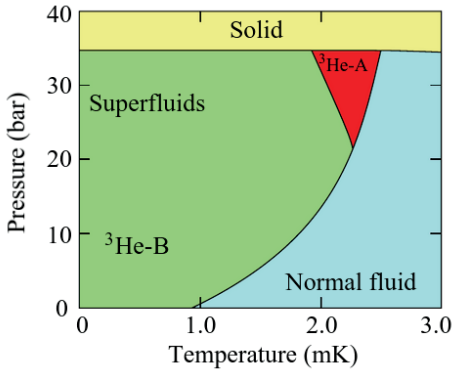

FIGURE 2.8: Phase diagram for ^{3}He [36]. One can see two superfluid phases: A and B.

2.3.1 Bose-Einstein Condensate

Apart from the unusual behaviour of helium II, another significant phenomenon associated with superfluidity is the formation of the so-called Bose–Einstein condensate (BEC) [5]. The origins of this idea date back to 1925, when N. Bose and A. Einstein predicted that an ideal bosonic gas at temperatures close to absolute zero is supposed to create the so-called condensate [40]. Only a few years later, the superfluid properties of ^{4}He, being an example of a bosonic system, were discovered (in 1932 by Keesom and Clusius [30]) and described in detail (in 1938) by Kapitza [32]. As this isotope is a bosonic system, it has been speculated that BEC can be, in fact, an example of a superfluid system [31].

At the beginning, the very existence of BEC in real systems, as well as its possible connection to superfluidity, was a matter of controversy. Bose–Einstein condensation was first predicted for an ideal (non-interacting) Bose gas by Einstein [40], and thus regarded as a purely quantum-statistical phase transition. However, this appeared to contradict real systems, where interactions are inevitably present [41]. London [42] was the first to suggest that superfluid helium might be understood as a manifestation of BEC, but this interpretation was met with scepticism. In particular, Landau questioned the relation between BEC and superfluidity [43, 5], and it was further argued [44] that, because of interactions, a system would crystallize into a solid before Bose–Einstein condensation could occur. A breakthrough came with Bogoliubov's work in 1947 [45], which demonstrated that interactions are not only compatible with condensation but,

in fact, essential for its proper description. Later studies showed that, despite differences between theoretical predictions for the ideal Bose gas and the observed behaviour of superfluid ^{4}He [31], liquid helium indeed exhibits properties analogous to those of a Bose–Einstein condensate in a dilute gas [44].

Basically, in BEC, many particles occupy the same state, which is also the lowest energy state; it also turns out that the condensate coexists with particles in the normal state [31]. However, in contrast to e.g., liquid-gas transition, these phases are expected to be separated in momentum space – particles forming a condensate are expected to have zero momentum (which characterizes the lowest energy state), while the ones in the normal phase have a momentum of finite value [31]. According to [31], the number of particles N_0 in BEC can be estimated within the following formula:

$$N_0 = N\left[1 - \left(\frac{T}{T_c}\right)^{3/2}\right], \tag{2.11}$$

where N denotes the number of particles, T has the meaning of temperature, and T_c – critical temperature, for which bosons start to form the condensate. This temperature can be approximated as [5]:

$$T_c \approx 3.3125\frac{\hbar^2}{mk_B}\left(\frac{N}{V}\right)^{2/3}. \tag{2.12}$$

In Eq. 2.12, V denotes the volume in which particles are placed, m is the mass of a single particle, and k_B is the Boltzmann constant.

As can be seen, the number of particles in the condensate is determined by temperature; the lower it is, the more particles occupy the lowest energy state. What is especially important is that the change of temperature results in modification of the thermal de Broglie wavelength [44], which is a fundamental quantity that allows us to describe the phenomenon of condensation. One can define it as [44]:

$$\lambda = \hbar\sqrt{\frac{2\pi}{mk_BT}}. \tag{2.13}$$

Based on that, one can consider several „configurations" that bosons can create depending on the temperature [44]:

- above critical temperature, one can consider particles as wavepackets of an extent equal to λ from Eq. 2.13. Then, as the de Broglie wavelength becomes comparable to other length scales in the system, quantum effects have to be considered. Later on, as the temperature is lower, the wavelength increases,
- once the temperature becomes approximately equal critical temperature, λ becomes close to the average distance between particles. As a result, these waves start to overlap, which leads to the occupation of the same state by many particles,
- in $T = 0$ pure BEC is expected to be created. In such a case, all the bosons occupy the same state (so a normal phase does not occur in the system).

Analytically, BEC can be described within the Gross-Pitaevskii equation [44, 31]. For the system consisting of N bosons, the many-body wave function can be defined as a product of single-particle (position-dependent) wave functions $\psi(\boldsymbol{r})$ associated with each of the particles [31]. Assuming each particle occupies the same state, we have

$$\Psi_N(\boldsymbol{r}_1, \boldsymbol{r}_2, ..., \boldsymbol{r}_N) = \psi(\boldsymbol{r}_1)\psi(\boldsymbol{r}_2)...\psi(\boldsymbol{r}_N). \tag{2.14}$$

Then, the energy connected with condensate can be written as [46]:

$$E = N \int d\boldsymbol{r} \left[\frac{\hbar^2}{2m} |\nabla\psi(\boldsymbol{r})|^2 + V(\boldsymbol{r})|\psi(\boldsymbol{r})|^2 + \frac{1}{2} N g |\psi(\boldsymbol{r})|^4 \right], \tag{2.15}$$

where $V(\boldsymbol{r})$ means the external potential and g – interaction coupling constant that defines the interaction between particles. Through the minimization of this energy, one can obtain static Gross-Pitaevskii equations. Later on, with respect to the principle of stationary action, time-dependent Gross-Pitaevskii equations can be obtained [46, 44]:

$$\left(-\frac{\hbar^2\nabla^2}{2m} + V(\boldsymbol{r}, t) + g|\Psi(\boldsymbol{r}, t)|^2 \right) \Psi(\boldsymbol{r}, t) = i\hbar \frac{\partial \Psi(\boldsymbol{r}, t)}{\partial t}, \tag{2.16}$$

where we have introduced the condensate wavefunction, which can be defined as $\Psi(\boldsymbol{r}, t) = \sqrt{N}\psi(\boldsymbol{r}, t)$. The static Gross-Pitaevskii equation has the same form, but with time derivative $i\hbar\frac{\partial}{\partial t}$ replaced by chemical potential μ, and dropping time dependence in the wave-function and the external potential.

2.3.2 Two-fluid Model and Landau Velocity

The first attempts to examine the properties of superfluid Helium were made within the two-fluid model, developed consecutively by Tisza and Landau [5, 43]. According to the approach postulated by Tisza, in a superfluid one can distinguish two components [47]:

- normal fluid made of particles that do not form condensate, but carry entropy and can be characterized by some finite viscosity [5, 31]. With this kind of flow, one can associate the following equation [48, 49, 50]:

$$\rho_n \frac{\partial \boldsymbol{v}_n}{\partial t} + \rho_n (\boldsymbol{v}_n \cdot \nabla)\boldsymbol{v}_n = -\frac{\rho_n}{\rho}\nabla P - \rho_s \sigma \nabla T + \eta \nabla^2 \boldsymbol{v}_n, \tag{2.17}$$

  where ρ_n is density of normal component, ρ_s – density of superfluid component, $\boldsymbol{v}_n$ – velocity of normal component. Later on, P denotes pressure, T – temperature, η – viscosity, and σ – entropy,

- superfluid consisting of particles in the form of condensate, which does not exhibit viscosity and therefore does not contribute to heat transport [5, 31]. This flow is described with regard to the formula [48, 49, 50]:

$$\rho_s \frac{\partial \boldsymbol{v}_s}{\partial t} + \rho_s (\boldsymbol{v}_s \cdot \nabla)\boldsymbol{v}_s = -\frac{\rho_s}{\rho}\nabla P + \rho_s \sigma \nabla T. \tag{2.18}$$

  Here, $\boldsymbol{v}_s$ is the superfluid velocity.

As can be seen, Eq. 2.17 has the form of the Navier-Stokes equation (which is the common relation describing the flow of a normal fluid), and Eq. 2.18 is the Euler equation used in the case of superflow [49]. Moreover, total density ρ (being the sum of normal and superfluid density) has to fulfill the continuity equation (being the mass conservation law) [51, 49, 50]:

$$\frac{\partial \rho}{\partial t} + \nabla \cdot \boldsymbol{J} = 0, \tag{2.19}$$

where $\boldsymbol{J}$ denotes the total flow given as [51]:

$$\boldsymbol{J} = \rho_n \boldsymbol{v}_n + \rho_s \boldsymbol{v}_s. \tag{2.20}$$

The behaviour of these two components as a function of temperature is schematically shown in Fig. 2.9 [52]. As can be seen, in the vicinity of zero temperature, almost all the

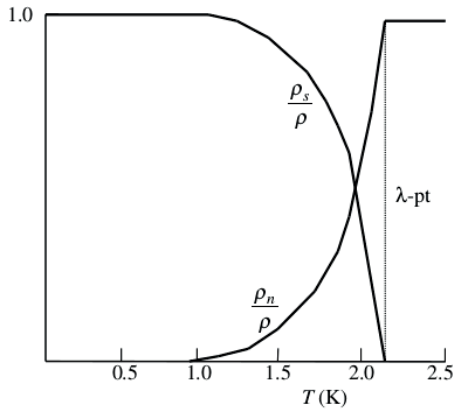

FIGURE 2.9: Superfluid density ρ_s and normal density ρ_n normalized to the total density ρ as a function of temperature [52].

fluid creates the condensate, so $\rho_s \approx \rho$ [31]. As the temperature increases, the contribution of the superfluid component decreases; simultaneously, the fraction of the normal part increases. Once the critical value of lambda point is reached, the system turns into the normal phase, so $\rho_n \approx \rho$ [31].

The two-fluid model, as introduced by Tisza, predicted the existence of two sound modes in superfluids. Omitting the viscosity term, one can obtain the following wave equations [48, 49]:

$$\frac{\partial^2 \rho}{\partial t^2} = \nabla^2 P, \tag{2.21}$$

$$\frac{\partial^2 S}{\partial t^2} = \frac{\rho_s S^2}{\rho_n} \nabla^2 T. \tag{2.22}$$

Based on these equations and assuming that heat capacities at given pressure P in volume C are equal [48], one can derive the relations for first sound speed u_1 and second sound speed u_2 [48, 49]:

$$u_1^2 \approx \left(\frac{\partial P}{\partial \rho}\right)_S, \tag{2.23}$$

$$u_2^2 \approx \frac{TS^2 \rho_s}{C \rho_n} \nabla^2 T. \tag{2.24}$$

The first sound speed is related to fluctuations in the density caused by changes in pressure [48]. On the other hand, there is also a second sound mode, according to which the normal and superfluid components move in antiphase [48], so total density remains constant (at the point, one should mention that explicit formula for second sound speed from Eq. 2.24 has been introduced by Landau in [53]). The second sound mode is usually referred to as entropy wave or temperature wave [31], as it strongly depends on temperature and almost vanishes at the lambda point [48]. With regard to the idea of two sound modes, one can explain some phenomena of non-classical heat transport (such as the fountain effect [31]) with regard to this concept.

Later, the two-fluid model developed by Tisza was reformulated by Landau [5]. Similar in its fundamentals, the difference between these approaches lies in the nature of the normal component [43]. According to Landau's idea, there are no excitations in the superfluid fraction, while in the normal one can distinguish collective excitations taking the form of two species of quasiparticles [52, 31]:

- phonons, which appear for low values of wave vector $\boldsymbol{k}$ and energies approximated as $\hbar c\boldsymbol{k}$ (where c denotes the sound speed) [5],
- rotons (for high $\boldsymbol{k}$) with energies $\Delta + \hbar^2(\boldsymbol{k} - \boldsymbol{k}_0)^2/(2m_0^*)$, where $\boldsymbol{k}_0$ and m_0^* are empirical parameters [5].

Therefore, it can be seen that the difference between the approaches by Tisza and Landau lies in the predicted form of excitations. According to the idea of Landau, due to the strong interaction in ^{4}He the single particle excitations (as predicted by Tisza [43]) could not occur [15]. Instead of this, Landau postulated the collective excitations in the form of quasiparticles [43] (which, however, do not have the meaning of physical particles [15]).

Another important quantity introduced by Landau is the characteristic velocity which „separates" the superfluid and normal phases [15, 31]. If this velocity is exceeded, superfluidity is destroyed and, as a consequence, the fluid turns into the normal phase [15, 31]. In order to derive the formula for this characteristic velocity, one should at first consider a particle of mass m moving with momentum $\boldsymbol{p}$ in the stationary (laboratory) rest frame. The energy associated with a particle in the stationary frame is equal to $\boldsymbol{p}^2/2m$ [31]. On the other hand, one can also imagine an additional frame, which moves with velocity $\boldsymbol{v}$. With regard to Galilean invariance [31], it can be seen that the

momentum $\boldsymbol{p}'$ and energy E' of particle in the moving frame are equal [31]:

$$\boldsymbol{p}' = \boldsymbol{p} - m\boldsymbol{v}, \tag{2.25}$$

$$E' = \frac{(\boldsymbol{p})'^2}{2m} = \frac{(\boldsymbol{p} - m\boldsymbol{v})^2}{2m} = E - \boldsymbol{p}\boldsymbol{v} + \frac{m\boldsymbol{v}^2}{2}. \tag{2.26}$$

Let us consider a macroscopic obstacle (with mass M) placed in the fluid that flows with velocity $\boldsymbol{V}$. In the first, we consider the reference frame that moves together with the fluid. In other words, in this frame, the fluid is at rest. The velocity of the obstacle can be only changed due to the scattering process leading to the creation of quasiparticles in the fluid[15] (here, the quasiparticle excitation is characterized by momentum $\boldsymbol{p}$). Therefore, the total energy of such a system would be equal $E = E_0 + \varepsilon(\boldsymbol{p})$, where E_0 has the meaning of ground state energy and $\varepsilon(\boldsymbol{p})$ is the energy of the quasiparticle.

Next, let us consider a frame attached to the obstacle. This frame moves with velocity $-\boldsymbol{V}$ with respect to the previous one. Combining this with Eq. 2.26 leads to the following relation for the energy E of the fluid with excited quasiparticle:

$$E' = E_0 + \varepsilon(\boldsymbol{p}) + \boldsymbol{p}\boldsymbol{V} + \frac{m\boldsymbol{V}^2}{2}. \tag{2.27}$$

In Eq. 2.27, one can distinguish the part $\varepsilon(\boldsymbol{p}) + \boldsymbol{p}\boldsymbol{V}$, which is connected with the contribution from quasiparticle [31]. Therefore, once this expression is negative, creation of quasiparticles with momentum $\boldsymbol{p}$ is energetically favorable and leads to dissipation mechanisms. With the case when $\varepsilon(\boldsymbol{p}) + \boldsymbol{p}\boldsymbol{V} = 0$ one can associate particular velocity $\boldsymbol{V}_c$, called critical velocity [31]:

$$\varepsilon(\boldsymbol{p}) + \boldsymbol{p}\boldsymbol{V}_c = 0, \tag{2.28}$$

where $\varepsilon(\boldsymbol{p})$ denotes the energy of quasiparticle excitation [31], which can be equivalently written as:

$$|\varepsilon(\boldsymbol{p})| = \boldsymbol{p}\boldsymbol{V}_c. \tag{2.29}$$

This leads to the following formula for critical velocity [15, 5]:

$$\boldsymbol{V}_c = \min\left[\frac{|\varepsilon(\boldsymbol{p})|}{\boldsymbol{p}}\right]. \tag{2.30}$$

This critical velocity was first introduced by Landau and is therefore referred to as the Landau velocity.

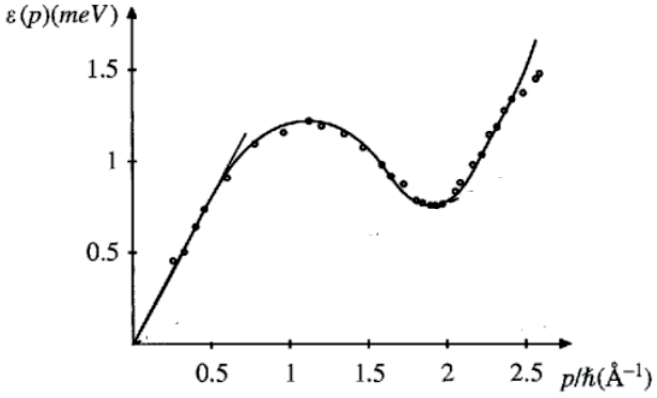

FIGURE 2.10: Quasiparticle energy spectrum for superfluid Helium, based on [31].

The critical velocity is directly connected with the quasiparticle energy spectrum. In Fig. 2.10, the spectrum for superfluid Helium (so for the system investigated by Landau) is presented [31]. In the regime of low momenta, the quasiparticle excitations are expected to take the form of phonons [31, 15]; therefore, this range of energies corresponds to the phonon part of the energy spectrum [5]. In general, the dispersion relation for (low-energy) phonons can be written as [31, 15]:

$$\varepsilon(\boldsymbol{p}) = c\boldsymbol{p}, \tag{2.31}$$

where c is the speed of sound. Therefore, one can associate the straight line from Fig. 2.10 (marked as c) with the phonon part of the spectrum. Substituting Eq. 2.31 into relation for critical velocity (Eq. 2.30) leads to the following result [15]:

$$\boldsymbol{V}_c = \min\left[\frac{c\boldsymbol{p}}{\boldsymbol{p}}\right] = \min[c] = c. \tag{2.32}$$

As can be seen, if the system can excite through phonons generation, the critical velocity is equal to the speed of sound c [15]. In other words, once this velocity is exceeded, quasiparticle excitations in the form of phonons occur in the system, and flow becomes dissipative [31, 15]. On the other hand, if the velocity is smaller than the „boundary" value c, there is no dissipation in the system and the flow can be considered as superflow [15].

To summarize, in each of the momentum limits, if the velocity is smaller than the critical velocity, the fluid flows without dissipation and can therefore be considered as a pure superfluid [15]. When critical velocity is exceeded, quasiparticle excitations start to occur in the system (so it turns into a normal phase). At this point, it is also worth mentioning that the energy spectrum allows one to deduce the properties of superfluid Helium. For weakly interacting BEC, the energy spectrum behaves like $\omega \approx cp$ and next turns into a quadratic dispersion relation [31]. Then, the critical velocity is close to the speed of sound. On the contrary, the energy spectrum of superfluid He looks different due to the presence of the roton minimum (in Fig. 2.10, it appears for $p/\hbar \approx 2$ Å^{-1}). Based on that, it has been assumed that superfluid He is not a weakly interacting system. Furthermore, the critical velocity of superfluid He is smaller than the speed of sound, as the roton minimum in the excitation spectrum allows dissipation to occur at much lower velocities than phonon emission.

The approach presented above can also be extended to fermionic systems described within BCS theory [15]. In such a case, the energy of a quasiparticle is defined as [15]:

$$\varepsilon(\boldsymbol{p}) = \sqrt{\left(\frac{\boldsymbol{p}^2}{2m} - \mu\right)^2 + \Delta^2}. \tag{2.33}$$

Therefore, per analogy to Eq. 2.28, the condition for quasiparticle creation would take the form:

$$\sqrt{\left(\frac{\boldsymbol{p}^2}{2m} - \mu\right)^2 + \Delta^2} + \boldsymbol{p} \cdot \boldsymbol{V} \leq 0. \tag{2.34}$$

As the value of the scalar product of $\boldsymbol{p} \cdot \boldsymbol{V}$ can be in the range $[-pV, +pV]$, here one should consider the boundary case corresponding to $-pV$. This leads to the following form of this condition:

$$\sqrt{\left(\frac{\boldsymbol{p}^2}{2m} - \mu\right)^2 + \Delta^2} - pV \leq 0. \tag{2.35}$$

Then, it can be seen that Eq. 2.35 can be fulfilled for velocities greater that critical velocity V_c:

$$V_c = \sqrt{\frac{1}{m}\left(\sqrt{\mu^2 + \Delta^2} - \mu\right)}. \tag{2.36}$$

In addition, in the case of the BCS system, one can assume that the chemical potential is close to the Fermi energy ($\mu \approx \varepsilon_F$) and the pairing potential is significantly smaller than the Fermi energy ($\Delta \ll \varepsilon_F$) [31]. Moreover, with the Fermi energy, one can also associate a certain velocity (labeled as V_F and equal $\hbar k_F/m$ [15], and $\varepsilon_F = \hbar^2 k_F^2/2m$). This leads to the following simplification of Eq. 2.36:

$$\frac{V_c}{V_F} \approx \frac{1}{2}\frac{\Delta}{\varepsilon_F}. \tag{2.37}$$

Finally, substituting ε_F with $(\hbar^2 k_F^2)/2m$ [31], one can obtain the expression for Landau velocity in BCS systems [15]:

$$V_c \approx \frac{\Delta}{\hbar k_F}. \tag{2.38}$$

Since the excitations in the analyzed case lead to the breaking of Cooper pairs, the Landau velocity is referred to as the pair-breaking velocity. In addition, as it will be shown later in the thesis, in weakly interacting Fermi superfluids, this critical velocity is much smaller than the speed of sound.

2.3.3 The Fundamentals of Bardeen-Cooper-Schrieffer Theory

As it was shown in the previous section, the mechanism of condensation in bosonic systems, as well as their superfluid properties, is well understood. However, such an approach cannot be directly applied in the case of fermions, as they do not condensate directly due to the Pauli principle [15]. Therefore, the process of condensation turns out to be modified as compared to bosons and is connected with Cooper pairs creation, which later on starts to form a condensate [15]. The concept of Cooper pairs is one of the fundamental ideas of Bardeen-Cooper-Schrieffer theory, which was initially raised for superconductive systems, so for systems consisting of charged particles (therefore, the fundamental predictions of this approach are described for electron systems) [54]. Historically, as soon as ^{3}He (being the fermionic system) was discovered by Oscheroff [55], it was postulated that superfluid properties of ^{3}He are in fact analogous to superconductivity described within BCS theory [31, 5]. Indeed, later on, BCS theory has also been applied to the case of superfluids, which are composed of particles that are electrically neutral. In other words, it can be said that superconductivity is, in fact, the form of superfluidity for charged particles [5]. However, one should keep in mind several crucial differences, which are described in the following section (such as the mechanism of Cooper pairs creation [31]). In addition, it should also be stressed that

BCS theory is expected to provide a reliable description for the systems in the regime of weak interactions [31]. However, as shown in this chapter, its extension to the non-uniform case provides a reasonable description of, for example, superfluid nuclear systems.

Electron-Phonon Interaction

In general, one can distinguish three fundamental theorems behind the BCS approach. First of all, they assume the existence of electron-phonon coupling [31], which results in an attractive component in the interaction between electrons [56, 31]. At first, this property seems to be surprising, as the interaction between electrons is, in general, repulsive due to the Coulomb potential [31]. However, it turns out that e.g. in metals (when the electrons are confined in a crystal lattice [31]) these particles should be rather considered as quasiparticles (so the electron is accompanied by exchange correlation hole surrounding it [31]).

The interaction between electrons is altered due to their interaction with phonons [31]; in other words, one can understand this interaction as the exchange of phonons between electrons [54]. According to [5, 57], when the electrons move through the lattice, it becomes distorted, which leads to modulation in electron charge density [31] (in other words, some amount of positive charge is locally created [5]). As a consequence, the potential acting on other electrons in the lattice would be periodically modified with a wavelength equal $2\pi/\boldsymbol{q}$, where $\boldsymbol{q}$ is the wave vector of the phonon [31]. Then, another electron passing through the lattice can feel the positive charge induced by the preceding electron as an attractive potential [31, 5]. Therefore, the interaction resulting from the lattice distortion is mediated by phonons and can be understood as an attractive interaction of these two electrons [5, 58]. Based on that, one can define the effective potential connected with phonon exchange (with wave vector $\boldsymbol{q}$ and frequency ω_q) as [31, 5, 58]:

$$V_{\text{eff}}(\boldsymbol{q},\omega) = |g_{\boldsymbol{q}}|^2 \frac{1}{\omega^2 - \omega_{\boldsymbol{q}}^2}. \tag{2.39}$$

In Eq. 2.39, the term $g_{\boldsymbol{q}}$ is called the electron-phonon vertex and has the meaning of a matrix element describing scattering of an electron from a state of momentum $\boldsymbol{k}$ to momentum $\boldsymbol{k}+\boldsymbol{q}$ [31]. The process of effective interaction between electrons mediated by phonons is schematically shown in Fig. 2.11. According to it, an electron with momentum $\boldsymbol{k}$ is scattered to the state with momentum $\boldsymbol{k}+\boldsymbol{q}$, while the particle with

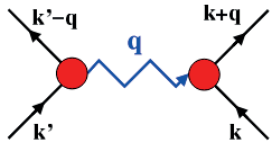

FIGURE 2.11: Effective interaction between electrons due to phonon exchange [58].

momentum k' is scattered to momentum $k' - q$. In addition, the red points correspond to the electron-phonon vertices. One should also mention that in this formula, the screening effect (reducing the repulsive interaction) is also included [31, 5].

Based on that, one can approximate the g_q with the constant g_{eff} independent on q (being the average interaction of g_q over the whole set of q) [31]. In addition, frequency ω_q can be replaced with the Debye frequency of phonons ω_D [31]. This leads to the following formula for the effective interaction potential [31]:

$$V_{\text{eff}}(q, \omega) = |g_{\text{eff}}|^2 \frac{1}{\omega^2 - \omega_D^2}. \tag{2.40}$$

As can be seen, the interaction described within this formula would be attractive for phonon frequencies smaller than ω_D [31, 58, 56].

Cooper Pairs Creation and Pairing Gap

Another fundamental concept of BCS theory is the phenomenon of Cooper pair creation and the associated energy gap. At first, one should recall the idea of the Fermi surface, which is a kind of „boundary" between occupied and unoccupied states (in zero temperature, all the states below the Fermi surface are occupied, while the states above it remain unoccupied) [31]. Such a surface corresponds to a particular energy, known as the Fermi energy, and is labeled as ϵ_F. Commonly, the Fermi surface is considered as a sphere with radius defined by Fermi wave vector k_F equal $\sqrt{2m\epsilon_F}/\hbar$ [31] (so the Fermi surface can be described either in terms of Fermi energy ϵ_F or Fermi momentum k_F) [31]. In other words, all the states with momenta lower than k_F are occupied [31].

At first, the idea of Cooper pair creation was postulated by Cooper, who found that attractive interaction between electrons can be present only close to the Fermi surface

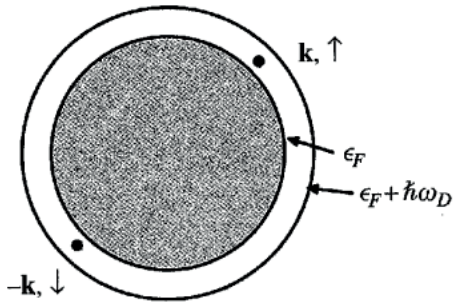

FIGURE 2.12: The schematic idea of Cooper pair creation [31].

[31]. As a consequence, the system of two electrons placed outside of the fully occupied Fermi surface (as shown in Fig. 2.12) has been considered. It turned out that these electrons form a bound state (called Cooper pair) with total momentum equal 0 and interact through electron-phonon interaction [31, 54]. One of these particles is assumed to have momentum $\boldsymbol{k}$ and spin $+1/2$ (denoted as $\uparrow$), while the other one has momentum $-\boldsymbol{k}$ and spin $-1/2$ ($\downarrow$) [31, 54]. In other words, once the state $\boldsymbol{k} \uparrow$ is occupied, the state $-\boldsymbol{k} \downarrow$ would be occupied as well [54]. As mentioned previously, the electron-phonon interaction transfers momentum $\boldsymbol{q} = \boldsymbol{k}' - \boldsymbol{k}$ from one of the electrons to another one [31, 56]. In addition, it should also be recalled that the interaction between electrons can be attractive, unless the frequency of phonons is below Debye phonon frequency ω_D corresponding to energy equal $\hbar\omega_D$ [54] (as shown in Fig. 2.12). Therefore, it can be seen that Cooper pairs can be formed only in a certain range of energies, limited by ϵ_F and $\hbar\omega_D$ [54].

In order to estimate the energy of a Cooper pair, one should first define the two-particle wave function of the electrons creating such a pair [31]:

$$\Psi(\boldsymbol{r}_1, \sigma_1, \boldsymbol{r}_2, \sigma_2) = e^{i\boldsymbol{k}_{\mathrm{CM}} \cdot \boldsymbol{R}_{\mathrm{CM}}} \varphi(\boldsymbol{r}_1 - \boldsymbol{r}_2) \phi_{\sigma_1, \sigma_2}, \tag{2.41}$$

where $\boldsymbol{R}_{\mathrm{CM}}$ is the center of mass of a pair and $\boldsymbol{k}_{\mathrm{CM}}$ means its total momentum (which, as it was said, is imposed to be 0). The term ϕ is the spin wave function, which can be either a spin singlet (for which the total spin of a pair is equal to 0) or a spin triplet (when the total spin is 1) [31]. Once the wave function φ is expanded in plane wave

basis as [31]:

$$\varphi(\boldsymbol{r}_1 - \boldsymbol{r}_2) = \sum_{\boldsymbol{k}} \varphi_{\boldsymbol{k}} e^{i\boldsymbol{k}(\boldsymbol{r}_1 - \boldsymbol{r}_2)}, \tag{2.42}$$

where $\varphi_{\boldsymbol{k}}$ are expansion coefficients, one can insert Eq. 2.41 into Schrödinger equation. It turns into the following formula [31, 56]:

$$E\varphi_{\boldsymbol{k}} = 2\epsilon_{\boldsymbol{k}}\varphi_{\boldsymbol{k}} - |g_{\text{eff}}|^2 \sum_{\boldsymbol{k}'} \varphi_{\boldsymbol{k}'}. \tag{2.43}$$

Again, g_{eff} denotes the effective interaction. In addition, as energies of electrons forming pairs have to be lower than $\hbar\omega_D$, their momenta have to be below $\boldsymbol{k}_F + \omega_D/v$, where v is the Bloch wave group velocity at the Fermi surface [31].

Eq. 2.41 can be solved self-consistently, which gives the following formula for the energy of a Cooper pair [31, 56]:

$$-E = 2\hbar\omega_D e^{-1/\lambda}, \tag{2.44}$$

where λ is the electron-phonon coupling parameter [31]:

$$\lambda = |g_{\text{eff}}|^2 g(\epsilon_F), \tag{2.45}$$

where $g(\epsilon_F)$ is the density at the Fermi surface.

With regard to the idea of Cooper pairs, one can explain the unusual feature of the energy spectrum of superconductors, which is the presence of a so-called energy gap [31, 5, 54]. Such a schematic spectrum is shown in Fig. 2.13, where dashed lines denote energy levels of electrons and holes in the superconductor, and the solid line corresponds to the spectrum of the normal metal [31]. As can be seen, in the case of superconductors, the excitation energy at the Fermi surface is different than zero. In other words, in order to add a single electron to the system, energy equal to Δ is needed [31]. Simultaneously, adding a hole (so removing an electron) requires energy Δ [31]. Therefore, the minimal energy that is necessary to excite the superconductor at Fermi energy (so as to break the pair into two electrons [31]), is equal 2Δ [5, 31]. It is also the energy that is necessary to break one Cooper pair (in other words, 2Δ can be understood as the binding energy of a single pair and, simultaneously, equivalent to the excitation energy of the superconductor) [5, 31, 54].

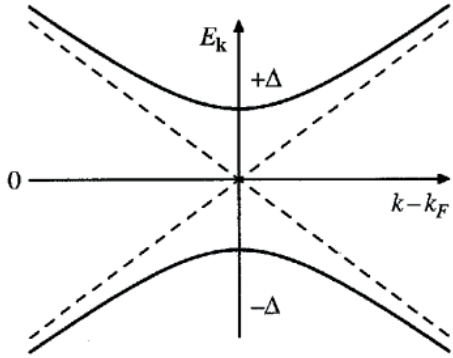

FIGURE 2.13: Quasiparticle energy spectrum in superconductor and normal metal [31].

The energy gap can also be observed in the plot showing the density of states as a function of energy, Fig. 2.14. As can be seen, there is an unoccupied range of energies (denoted as Δ) below and above the Fermi energy (what is important, the energy gap is always localized, around the Fermi energy [31]. The energy gap corresponds to the range of energies, where Cooper pairs can be formed [31].

Coherent State Wave Function

According to [31, 54], it has been realized that all the electrons at the Fermi surface would create Cooper pairs. Therefore, there was a need to formulate a many-particle wave function describing such a state (when all the particles are paired), which is the matter of the last of the fundamental statements of BCS theory, coming from Schrieffer [31]. With regard to it, Cooper pairs form a coherent state described within the BCS (or coherent) wave function [31, 56]. This theorem is based on the Cooper pair creation operator [31]:

$$P_k^\dagger = \psi_{k\uparrow}^\dagger \psi_{-k\downarrow}^\dagger, \tag{2.46}$$

where $\psi_{k\uparrow}^\dagger$ is the creation operator of a spin-up particle with momentum $\boldsymbol{k}$ and $\psi_{-k\downarrow}^\dagger$ – of spin-down particle with momentum $-\boldsymbol{k}$. In the next step, one can define the coherent many-body wave function $|\Psi_{\mathrm{BCS}}\rangle$ as [31, 54]:

$$|\Psi_{\mathrm{BCS}}\rangle = \text{const.} \exp\left(\sum_k \alpha_k P_k^\dagger\right)|0\rangle. \tag{2.47}$$

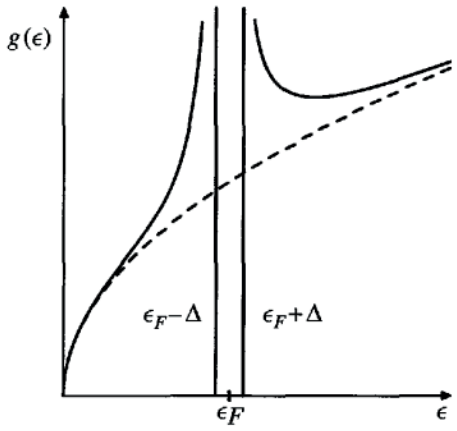

FIGURE 2.14: Density of states as a function of energy in BCS theory [31].

Here, the coefficients α_k are chosen in the way to minimize the energy [31]. In addition, the vacuum state $|0\rangle$ corresponds to the state without Cooper pairs at the Fermi surface [31].

Later on, one should denote that pair operators commute with each other, so $[P_k^\dagger, P_{k'}^\dagger] = 0$ (however, they do not obey commutation rules for bosons, so $[P_k, P_k^\dagger] \neq 1$) [31]. Therefore, wave function from Eq. 2.47 can be rewritten as the product of exponentials over $\boldsymbol{k}$ states [31]:

$$|\Psi_{\mathrm{BCS}}\rangle = \mathrm{const} \prod_k \exp\left(\alpha_k P_k^\dagger\right) |0\rangle. \tag{2.48}$$

Then, one should also recall that $(P_k^\dagger)^2 = 0$, so in Eq. 2.48 the terms including $(P_k^\dagger)^2$ (and higher powers) disappear [31]. This leads to the following form of the wave function [31]:

$$|\Psi_{\mathrm{BCS}}\rangle = \mathrm{const} \prod_k \left(1 + \alpha_k P_k^\dagger\right) |0\rangle. \tag{2.49}$$

According to [31], the normalization constant is equal $1/(1 + |\alpha_k|^2)$. Finally, one can write the expression for the macroscopic wave function describing the system, in which all the particles are paired [31, 54, 56]:

$$|\Psi_{\mathrm{BCS}}\rangle = \prod_k \left(u_k^* + v_k^* P_k^\dagger\right) |0\rangle. \tag{2.50}$$

In Eq. 2.50, the coefficients u_k^* and v_k^* are defined as [31]:

$$u_k^* = \frac{1}{1+|\alpha_k|^2}, \tag{2.51}$$

$$v_k^* = \frac{\alpha_k}{1+|\alpha_k|^2}, \tag{2.52}$$

and are supposed to obey the following constraint [31, 56]:

$$|v_k|^2 + |v_k|^2 = 1. \tag{2.53}$$

As a consequence, it can be seen that the term v_k denotes the amplitude of probability that the pair state is occupied and u_k that it is unoccupied [56].

BCS Equations and Energy Gap Equation

In order to derive equations describing BCS systems, one should start with an expression for the Hamiltonian. Considering only the interaction leading to the creation of Cooper pairs, one can write it as [31]:

$$H = \sum_{k,\sigma} \epsilon_k \psi^\dagger_{k\sigma}\psi_{k\sigma} - |g_{\text{eff}}|^2 \sum_{k,k'} \psi^\dagger_{k\uparrow}\psi^\dagger_{-k\downarrow}\psi_{-k'\downarrow}\psi_{k'\uparrow}. \tag{2.54}$$

On the right side of Eq. 2.54, the first term corresponds to kinetic energy and the second one to the interaction part. However, as this form of Hamiltonian still describes the many-body interacting system, one should find another way of examination instead of solving it explicitly [31]. One of the methods is the minimization of the total energy of the system with regard to coefficients u_k and v_k, which have been introduced in the section about the coherent state (Sec. 2.47) and can be treated as variational parameters [31, 54]. In addition, in order to minimize the energy, one should also assume a fixed number of particles [31].

The energy with regard to u_k and v_k can be obtained by taking the expectation value of each of the terms (kinetic and interacting) in the Hamiltonian, which leads to the following formula [31]:

$$E = 2\sum_k \epsilon_k |v_k|^2 - |g_{\text{eff}}|^2 \sum_{kk'} v_k v^*_{k'} u_{k'} u^*_k. \tag{2.55}$$

To find the minimal energy, the method of Lagrange multipliers can be applied [31]. According to this procedure, one should differentiate the energy from Eq. 2.55 over u_k^* and v_k^* [31]. Additionally, we introduce constraint on number of particles (defined as $N = \sum_k(|v_k|^2 - |u_k|^2 + 1)$), which is controlled through adjustment of chemical potential μ (therefore, μ is a Lagrange multiplier) [31]. This leads to the following equations [31]:

$$(\epsilon_k - \mu)u_k + \Delta v_k = E_k u_k, \tag{2.56}$$

$$\Delta u_k - (\epsilon_k - \mu)v_k = E_k v_k, \tag{2.57}$$

where $\epsilon(\boldsymbol{k})$ is the single particle energy. As can be seen, the parameter of crucial importance, labeled as Δ, is introduced in these equations. It has the meaning of gap parameter and can be expressed in terms of u_k and v_k as [31, 56]:

$$\Delta = |g_{\text{eff}}|^2 \sum_k u_k v_k^*, \tag{2.58}$$

where g_{eff} is the constant describing the strength of the interaction.

The exact expression for Δ can be determined from Eqs. 2.56 - 2.57 [31]. They are commonly written in the matrix form, recognized as the BCS equation [31]:

$$\begin{pmatrix} (\epsilon_k - \mu) & \Delta \\ \Delta^* & -(\epsilon_k - \mu) \end{pmatrix} \begin{pmatrix} u_k \\ v_k \end{pmatrix} = E_k \begin{pmatrix} u_k \\ v_k. \end{pmatrix} \tag{2.59}$$

Based on that, it can be seen that the quantity $\pm E_k$ has the meaning of eigenvalue of the two-by-two matrix on the left side of Eq. 2.59 and $[u_k, v_k]^T$ is its eigenvector [31]. Therefore, the dependence E_k has the physical meaning of energy spectrum in the BCS regime (as shown in Fig. 2.13) [31, 54]:

$$E_k = \sqrt{(\hbar^2 \boldsymbol{k}^2/2m - \mu)^2 + \Delta^2}, \tag{2.60}$$

where the term $\epsilon_k = \hbar^2 \boldsymbol{k}^2/2m$ corresponds to the single particle energy.

Once the expressions for u_k and v_k are obtained from Eq. 2.59 [31]:

$$|u_k|^2 = \frac{1}{2}\left(1 + \frac{\epsilon_k - \mu}{E_k}\right), \tag{2.61}$$

$$|v_k|^2 = \frac{1}{2}\left(1 - \frac{\epsilon_k - \mu}{E_k}\right), \tag{2.62}$$

one can combine them with Eq. 2.58 and rewrite Δ with regard to E_k [31, 56]:

$$\Delta = |g_{\text{eff}}|^2 \sum_k \frac{\Delta}{2E_k}. \tag{2.63}$$

Eq. 2.63 is called the BCS gap equation and can be written equivalently as [31]:

$$1 = \frac{|g_{\text{eff}}|^2}{2} \sum_k \frac{1}{\sqrt{(\hbar^2 \boldsymbol{k}^2/2m - \mu)^2 + \Delta^2}}. \tag{2.64}$$

Based on that, one can obtain the value of Δ describing directly the size of the energy gap [31]. Here, it is also worth noting the nonlinearity of the BCS equations. As can be seen, the coefficients u_k and v_k are included both in the matrix in Eq. 2.59 and in the expression for Δ as well. Therefore, Eq. 2.59 has to be solved in a self-consistent way [56, 31]. This procedure is described in detail in Sec. 3.6.

In superconductive systems, one should also take into consideration the electron-phonon interaction. Therefore, the sum over $\boldsymbol{k}$ in Eq. 2.64 can be replaced with the integral of the density of states at Fermi energy (so, in fact, $g(\epsilon_F)$ from Sec. 2.3.3 concerning Cooper pairs creation) over energy [31]. This results in the following formula (with regard to previously used symbols) [31]:

$$1 = \lambda \ln\left(\frac{2\hbar\omega_D}{|\Delta|}\right), \tag{2.65}$$

which can also be formulated as:

$$|\Delta| = 2\hbar\omega_D e^{-1/\lambda} \tag{2.66}$$

As can be seen, this equation is the same as the formula for the binding energy of a Cooper pair (Eq. 2.44).

Order Parameter

As it has been remarked previously, the fundamental assumption behind the BCS theory discussed in this chapter is the uniformity of the system. In such a case, the gap parameter Δ, as well as quasiparticle wave function amplitudes v_k and u_k, can be considered only as numbers, due to the fact that they do not depend on position. However, in the case of non-uniform systems (described within BdG formalism), these parameters become position-dependent. As a consequence, in such a case, Δ has the meaning of position-dependent order parameter.

In order to interpret the physical meaning of the order parameter, one should come back to the macroscopic wave function of the condensate (Eq. 2.16 in Sec. 2.3.1). It can be written as a function of position in the following form [31]:

$$\Psi(\boldsymbol{r}) = |\Psi(\boldsymbol{r})|e^{i\phi(\boldsymbol{r})} \tag{2.67}$$

In Eq. 2.67, one can distinguish the absolute value of the wave function $|\Psi(\boldsymbol{r})|$ and the phase factor $\phi(\boldsymbol{r})$. The macroscopic wave function has the meaning of an order parameter, which allows us to distinguish the phases [31]. When $|\Psi(\boldsymbol{r})|$, which is a real number, is equal 0, the system is in the normal phase (so there is no phase $\phi(\boldsymbol{r})$). On the other hand, once $|\Psi(\boldsymbol{r})|$ becomes greater than 0, the system is in the superfluid state, and the phase factor can be determined; therefore, it can be considered as a physical parameter describing the system [31]. In the case of superfluids, one can associate the gap parameter Δ with the order parameter, as it takes a nonzero value only for the superfluid phase [31]. This idea has been established by Gor'kov et al. in [59].

Quasiparticles

Coming back to the general formula of Hamiltonian from Eq. 2.54, it can be seen that its interaction term includes four operators. As a consequence, this form of Hamiltonian is not quadratic and therefore cannot be easily solved [60, 61]. Therefore, one should bring this Hamiltonian to the quadratic form, as in such a case it can be diagonalized through the Bogoliubov transformation [60, 61]. In order to tackle this problem, one can apply the method called mean field decoupling [60, 61], which is based on the assumption that higher order fluctuations of the interaction term in Eq. 2.54 can be neglected [60, 61]. Then, one can rewrite Hamiltonian from Eq. 2.54 in the following

quadratic form with regard to the gap parameter [31, 56]:

$$H = \sum_{k,\sigma}(\epsilon_k - \mu)\psi^\dagger_{k\sigma}\psi_{k\sigma} - \sum_k \Delta\psi^\dagger_{-k\downarrow}\psi^\dagger_{k\uparrow} + \Delta^*\psi_{k\uparrow}\psi_{-k\downarrow}, \tag{2.68}$$

where $\Delta = |g_{\text{eff}}|^2 \sum_k \langle\psi_{-k\downarrow}\psi_{k\uparrow}\rangle$. Usually, Eq. 2.68 is written in the matrix form [31]:

$$H = \begin{pmatrix}\psi^\dagger_{k\uparrow} \\ \psi_{-k\downarrow}\end{pmatrix}\begin{pmatrix}(\epsilon_k - \mu) & \Delta \\ -\Delta^* & -(\epsilon_k - \mu)\end{pmatrix}\begin{pmatrix}\psi_{k\uparrow} \\ \psi^\dagger_{-k\downarrow}\end{pmatrix} \tag{2.69}$$

As can be seen, this form of Hamiltonian is quadratic in field operators [31]. Therefore, it can be diagonalized through Bogoliubov transformation [31, 5], being the unitary transformation based on multiplication of the Hamiltonian matrix (from left and right side) by a unitary matrix [31]. In the case of Bogoliubov transformation, the unitary matrix (denoted as B) takes the form [62, 31]:

$$B = \begin{pmatrix}u_k & v^*_k \\ -v_k & u^*_k.\end{pmatrix} \tag{2.70}$$

Once the transformation matrix B is applied to $\psi^\dagger$ and ψ, new creation ($\alpha^\dagger$) and annihilation (α) operators are defined. These new operators can then be expressed in the explicit form [63, 31, 56]:

$$\alpha_{k\uparrow} = u^*_k\psi_{k\uparrow} - v^*_k\psi^\dagger_{-k\downarrow}, \tag{2.71}$$

$$\alpha^\dagger_{-k\downarrow} = v_k\psi_{k\uparrow} + u_k\psi^\dagger_{-k\downarrow}. \tag{2.72}$$

As can be seen, the new operators are linear combinations of $\psi^\dagger$ and ψ. Then, with regard to $\alpha^\dagger$ and α, one can bring the Hamiltonian to the diagonal form [63, 31, 56]:

$$H = \sum_k E_k\left(\alpha^\dagger_{k\uparrow}\alpha_{k\uparrow} + \alpha^\dagger_{-k\downarrow}\alpha_{-k\downarrow}\right), \tag{2.73}$$

which can also be written in the matrix form [31]:

$$H = -\sum_k \left(\alpha^\dagger_{k\uparrow}\alpha_{-k\downarrow}\right)\begin{pmatrix}E_k & 0 \\ 0 & -E_k\end{pmatrix}\begin{pmatrix}\alpha_{k\uparrow} \\ \alpha^\dagger_{-k\downarrow}\end{pmatrix} \tag{2.74}$$

In principle, Hamiltonian from Eq. 2.73 is diagonal, when u_k, v_k and E_k satisfy the BCS equations [63].

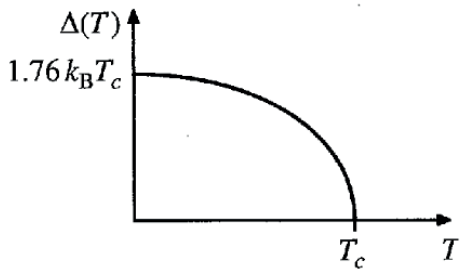

FIGURE 2.15: BCS prediction of Δ as a function of temperature [31].

An essential conclusion arising from this discussion is the physical interpretation of u_k and v_k. The fact that the new operators are the mixture of creation and annihilation operators [31, 56] implies that each of the created/annihilated states is a mixture of quasiparticles – holes and particles, which both can be spin-up (↑) or spin-down(↓) [31]. Therefore, the variables u and v can be understood as wave functions of holes/particles (in other words, the amplitude of probability of occupation of the state by a hole is denoted as $|u_k|^2$ and $|v_k|^2$ – by particle) [31]. As a consequence, each single particle state, primarily described within a certain wave function, corresponds in fact to the two-component vector consisting of quasiparticle wave functions.

Extension of BCS Theory to Finite Temperatures

Later on, one should also make the connection between Δ and the temperature of the BCS system. In general, in finite temperatures gap equation can be modified to the following form [31]:

$$\Delta = |g_{\text{eff}}|^2 \sum_k \frac{\Delta}{2E_k} \tanh\left(\frac{E_k}{2k_B T}\right) \tag{2.75}$$

In the finite temperature case, the occupation of quasiparticle state with energy E_k is determined by the Fermi-Dirac distribution (here the k_B is the Boltzmann constant and T – temperature) [31]. Within the gap equation, one can explicitly estimate the critical temperature at which Δ vanishes [31, 56]. The dependence of the energy gap in the BCS system on temperature is shown in Fig. 2.15. As it can be seen, for temperatures below critical temperature T_c, Δ is nonzero, so the system is in superfluid phase. On the other hand, for temperatures higher than T_c, Δ disappears, which means that the system turns into the normal state. The change from superfluid to normal phase is

a second-order phase transition with Δ being the order parameter [54]. In addition, from the dependence shown in Fig. 2.15, one can obtain the equation for the critical temperature in the BCS regime [31]:

$$k_B T_c = 1.13\hbar\omega_D \exp(-1/\lambda). \tag{2.76}$$

As can be seen, this result is in fact equivalent to the binding energy of the Cooper pair [31]. For temperature equal 0, Eq. 2.76 leads to the value of energy gap 2Δ in BCS regime, which is equal $3.52k_B T_c$ [54, 31, 56].

2.4 Superfluidity in Neutron Star Crust

2.4.1 Historical Introduction

Even before the discovery of pulsars by Jocelyn Bell in 1967, the possibility that the inner matter of neutron stars shows superfluid properties has been raised [5, 15]. At first, Bohr et al. [64], soon after BCS theory was published, showed the connection between superconductivity and excitation spectra of nuclei [5, 12]. As it has been observed, even-even nuclei have higher excitation energy than odd nuclei [5]. This leads to the conclusion that excitation of even-even nuclei was impossible until Cooper pairs (formed of nucleons) were broken [5]. Based on that, the idea of nuclear pairing could have been introduced [12].

Later on, as it has been investigated by Migdal [6], the internal matter of the star has been supposed to contain superfluid matter [5, 15]. This idea has been continued by Ginzburg [65], who has shown that for densities about 10^{13}-10^{15} g/cm^3 the energy gap arises as a result of so-called singlet-state pairing characteristic for the inner crust of neutron star [12] (pairing states are described in details in Sec. 2.4.2). Finally, in a paper by Wolf [66], the superfluid properties of neutron matter in the crust have been shown [15]. Particularly, it has been proved that neutron singlet-state pairing is expected to be dominant in the crust and disappears in the core (as interaction in this state becomes repulsive at core densities) [12]. On the contrary, in the case of protons, the singlet-state interaction becomes attractive in the core, which leads to proton pairing [12]. Later on, it has been shown that neutron pairing in the core is also possible, but in the form of a triplet state [67, 68].

2.4.2 Pairing in Neutron Star Crust and Cooper Pairs Creation

In general, Cooper pairs can be considered as the two-particle bound states [69]. Therefore, despite the fact that standard BCS theory describes pairing in electron systems, Cooper pairs can form in various systems and in many different states, characterized by spin-orbital angular momentum [69]. As mentioned in Sec . 2.4.1, in the neutron star crust, one can observe pairing between strongly interacting nucleons. In addition, according to [69, 15, 70], the behaviour of nucleons in the crust can be successfully approximated by BCS predictions. However, one should point out several differences between pairing taking place in standard systems (consisting of electrons [31]) and in the neutron star crust (called nuclear pairing [5]).

As in neutron star crust pairing takes place in the interacting medium, this phenomenon turns out to be strongly affected by so-called many-body effects (or medium effects) [5]. One of them, called the polarization effect, is connected with the size of the Cooper pair [5]. As well as in standard BCS theory, in nuclear systems it is assumed to be of the order of coherence length [5], which is one of the fundamental length scales in superfluid systems. One can define this quantity as $\xi = (\hbar v_F)/(\pi\Delta)$ [15], where v_F is velocity related to Fermi momentum: $v_F = m\hbar k_F$ [31]. In addition, in nuclear matter, the average distance between nucleons is assumed to be proportional to $1/k_F$ [5]; therefore, it can be seen that the size of the Cooper pair is expected to be significantly larger than the distance between particles [5]. This leads to the polarization effect, which is connected with the presence of so-called spectator nucleons localized between Cooper pairs [5]. These nucleons are supposed to affect the interaction between particles forming a Cooper pair, which results in modification of the value of the pairing gap [5]. In other words, the nucleons participating in pairing effectively "screen" the interaction themselves (a process usually described within the induced interaction model) [70]. Due to this effect, the pairing gap in nuclear systems is expected to be reduced by approximately $(4e)^{1/3}$ [70]. The comparison of the standard BCS energy gap and the values obtained within various methods for the nuclear case (including polarization effect) is shown in Fig. 2.16.

Another important issue that affects the energy gap is the behaviour of neutrons inside clusters [15]. The properties of neutrons bound in a cluster are assumed to be

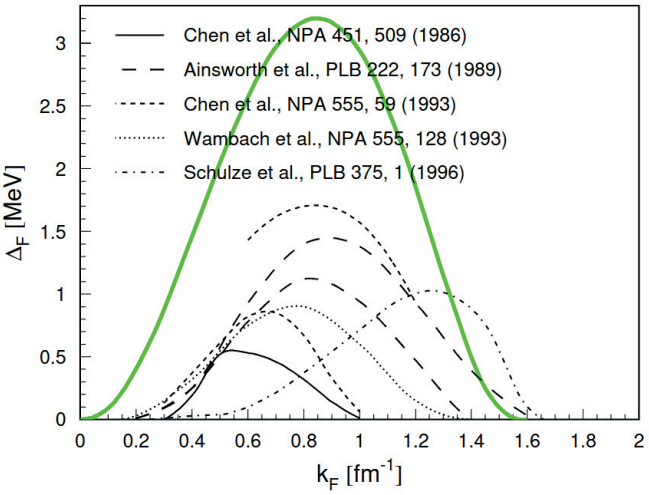

FIGURE 2.16: Spin-singlet pairing gap obtained within different methods, including polarization effect (dashed lines,) compared with BCS prediction (green line) [70].

influenced by free superfluid neutrons surrounding the impurities. Due to the presence of this surrounding medium, pairing of bound neutrons occurs, so that they also become superfluid (this is also known as the proximity effect) [15]. Then, the internal pairing field associated with bound neutrons is supposed to exhibit spatial variations [15, 71]. As a result, the difference in the value of the pairing gap inside and outside of the impurity is indistinct [71]. Consequently, one cannot apply the local density approximation to calculate the pairing field in the clusters (as this approach assumes the matter to be locally homogenous) [15]. At the point, one should also mention the self-energy effect [5], which is described in detail in Ch. 4 concerning effective mass.

Based on the preceding discussion, the phenomenon of nuclear pairing can be considered in a more detailed way. In general, one can describe the pair of nucleons within several quantities [5]:

- total spin of the pair of interacting nucleons. Once the spin of each of the nucleons is denoted as s_1 and s_2, the total spin S is equal $s_1 + s_2$,
- total isospin – using the same notation as above, it reads $T = t_1 + t_2$,
- total angular momentum $L = l_1 + l_2$.

Regarding these parameters, one can expand the gap equation in partial waves [69, 70]. At first, it is convenient to write the gap equation in the following form [72, 70]:

$$\Delta(\boldsymbol{k}) = -\sum_{\boldsymbol{k}'}\langle \boldsymbol{k}|V|\boldsymbol{k}'\rangle \frac{\Delta(\boldsymbol{k}')}{2E(\boldsymbol{k}')}, \tag{2.77}$$

where $E(\boldsymbol{k}')^2$ is equal $(\varepsilon(\boldsymbol{k})-\mu)^2+|\Delta(\boldsymbol{k})|^2$, with $\varepsilon(\boldsymbol{k})$ being single particle energy and μ – chemical potential. The term $\langle \boldsymbol{k}|V|\boldsymbol{k}'\rangle$ denotes the matrix element of nucleon-nucleon potential $V(\boldsymbol{k},\boldsymbol{k}')$ [72]. Then, according to [73], one can decompose the interaction term and the whole gap equation into the following forms:

$$\langle \boldsymbol{k}|V|\boldsymbol{k}'\rangle = 4\pi\sum_{l}(2l+1)P_l(\hat{\boldsymbol{k}}\cdot\hat{\boldsymbol{k}}')V_l(k,k'), \tag{2.78}$$

$$\Delta(\boldsymbol{k}) = \sum_{lm}\sqrt{\frac{4\pi}{2l+1}}Y_{lm}(\hat{\boldsymbol{k}})\Delta_{lm}(k). \tag{2.79}$$

In Eq. 2.78 and Eq. 2.79, the term $Y_{lm}(\hat{\boldsymbol{k}})$ is the spherical harmonic for orbital angular momentum l, m denotes the projection of this momentum along z axis and $P_l(\hat{\boldsymbol{k}}\cdot\hat{\boldsymbol{k}}')$ is the Legendre polynomial [72]. Once the pairing field is expanded in spherical harmonic basis, the interaction can also be expanded in a basis labeled by angular momentum l; in addition, the interaction can be characterized by phase shifts δ. Thus, the pairing gap will depend on the phase shifts δ, so one can associate a pairing gap with each partial wave. In other words, as a result of this decomposition, one can show the connection of Δ with δ.

In nuclear matter in neutron star crust, each partial wave corresponds to a particular pairing channel [74], which is physically represented by spin-angular momentum configuration [69, 7]. For each of these configurations, one can determine the value of the phase shift. As shown, e.g., in [73], a positive phase shift corresponds to an attractive interaction, while a negative value corresponds to a repulsive one [5]. One should also mention that pairing channels are described according to spectroscopic notation: ${}^{2S+1}L_J^*$ [74, 7], where $J = S + L$ is the total angular momentum and $2S+1$ denotes the number of spin states [7]. Therefore, as the total spin S can be equal either 0 or 1, $2S+1$ reaches 1 or 3. These values, in turn, correspond to the so-called singlet or triplet state, respectively [7]. The term L^* has the meaning of the total orbital angular momentum, which in this notation – instead of consecutive values $0, 1, 2...$ – is written as $S, P, D...$

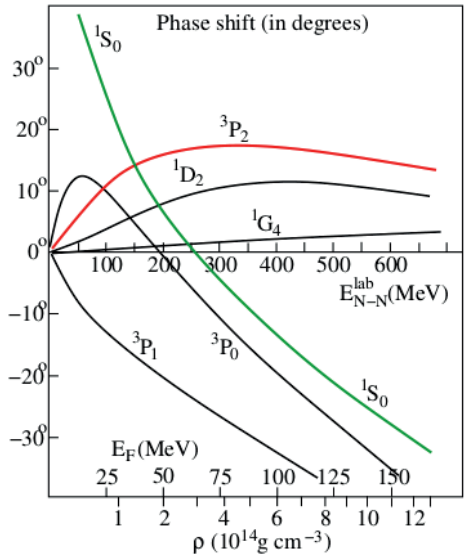

FIGURE 2.17: Phase shift as a function of nucleon-nucleon energy in laboratory frame $E^{\mathrm{lab}}{}_{\mathrm{N-N}}$ (upper part) and density (corresponding to Fermi energy E_F, lower part) for different pairing channels [69], based on [68].

[7]. In addition, the Pauli principle imposes that the sum of the parameters mentioned above (so $S + T + L$) has to be an odd number [7].

As mentioned earlier, one can describe the nature of interaction in a particular pairing channel within the phase shift. Fig. 2.17 shows the dependence of scattering phase shift on energy of interaction between nucleons and density. As pairing requires attractive interaction, it can be seen that in the case of neutron stars, Cooper pairs will be formed in two common configurations, $^1S_0$ and $^3P_2$ (called spin-singlet and spin-triplet states) [69, 7]. They are schematically shown in Fig. 2.18 [69]. As it can be seen, spin-singlet state (denoted as $^1S_0$) has the total spin equal 0 (so the spins of the nucleons are oppositely directed). On the contrary, for a spin-triplet pair ($^3P_2$), the total spin is 1 (so the spins of nucleons in the pair are oriented in the same direction, which leads to four possible combinations of the mutual alignment of spins). Moreover, both for $^1S_0$ and $^3P_2$ the total orbital angular momentum of the pair is equal 0 [7] (as for low energies states with $L = 0$ are expected to be dominant [7]).

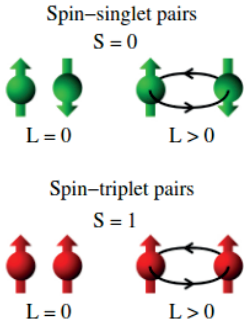

FIGURE 2.18: Spin-singlet and spin-triplet configuration of Cooper pair [69].

At the point, one should come back to Fig. 2.17 and the dependence of phase shift on density. In general, the occurrence of a particular configuration in nuclear matter is determined by the value of the Fermi momentum [69]. Therefore, the contribution of particular configurations to Cooper pair formation depends on density [5, 69]. According to Fig. 2.17, for densities lower than approximately $0.5\rho_0$ [5, 69], ${}^1S_0$ state turns out to be dominant, while for higher densities it is ${}^3P_2$ configuration [5, 69]. As a consequence, in the neutron star crust the superfluid phase is supposed to consist of Cooper pairs in ${}^1S_0$ configuration [7], while in the core the pairs are expected to be created mostly from ${}^3P_2$ states [5].

It is also worth mentioning that in neutron stars, due to the isospin asymmetry of nuclear matter, pairing channels can also be only isospin-asymmetric (so $T = 1$) [7, 5], which leads only to neutron-neutron or proton-proton pairing. The neutron pairing is expected to be the dominant type of pairing at the range of densities corresponding to the inner crust [70]. According to [70, 7, 69], proton pairing is also possible (but in the investigated cases it is close to zero). Fig. 2.19 shows the comparison of pairing gaps obtained for neutron and proton configurations as a function of density. As can be seen, the preferred type of configuration strongly depends on density. As the examination of nuclear pairing is based on standard BCS theory, neutron pairing channels are supposed to be dominant in the crust [7]. This happens due to the fact that for crustal densities, protons are confined in the clusters and therefore cannot form Cooper pairs efficiently [7]. In the deeper layers of the crust (close to the crust-core transition), the density of protons becomes comparable to the density of neutrons in the inner crust [7].

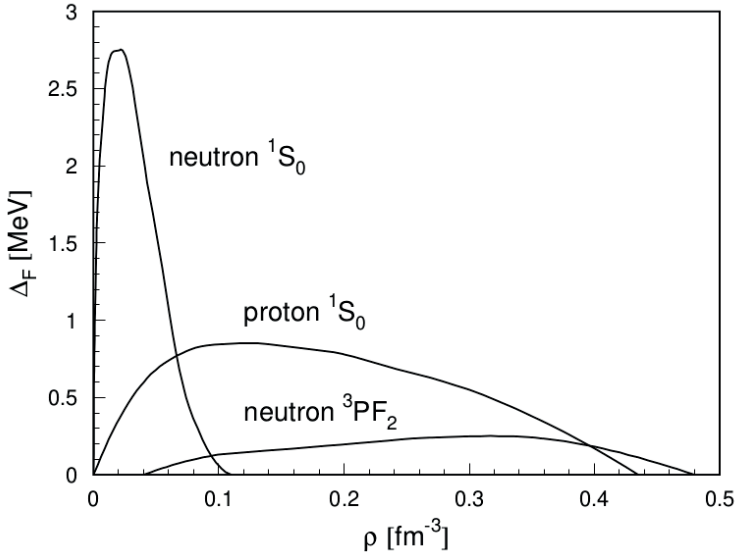

FIGURE 2.19: Pairing gaps for different configurations in neutron star matter as a function of density [70].

In such a case, proton pairing can be observed [70]. Later on, as the density approaches the values characteristic for the core, neutron $^3P_2$ and $^3F_2$ configurations become dominant [7].

At the point, one should also mention that neutron-proton pairing channels, which are isospin-symmetric ($T = 0$), are not expected to appear in neutron stars [7, 5]. This arises from the fact that in such a case, the nuclear matter should also be isospin-symmetric. This, in turn, requires the density of neutrons to be close to the density of protons, which does not take place in the neutron star interior [7, 5].

Temperatures in Neutron Stars

As it was mentioned in Sec. 2.3.1, the occurrence of superfluidity in the system is determined by temperature, as the pairing gap vanishes above some critical temperature [15]. Once it is exceeded, the system returns to its normal phase.

Immediately after its formation, the interior temperature of a neutron star is approximately 10^{12} K [5]. However, it is expected to cool down rapidly, so the final temperature after cooling reaches approximately 10^8-10^{10} K [69]. Taking into consideration the analysis of superfluids from Sec. 2.4, this quantity seems to be much too high for superfluidity to occur. However, one should remember that temperature scales in the neutron star interior should be compared to the typical Fermi temperature defined as [5]:

$$T_F = \frac{\varepsilon_F}{k_B}, \tag{2.80}$$

where ε_F is Fermi energy and k_B is the Boltzmann constant. Based on this equation, one can estimate that in the range of densities characteristic for neutron stars, the Fermi temperature would be of the order 10^{11} K, which is significantly higher than temperatures inside a star. In other words, due to extremely high densities, critical temperatures in neutron stars are also high [69], which allows for the existence of a superfluid phase in their interior.

2.5 Dynamic Properties of Inner Crust Matter

2.5.1 Quantum Vortices

Another important phenomenon connected with superfluidity is the creation of quantum vortices. In order to explain this effect, one should come back to properties described in Sec. 2.3. With regard to classical fluid mechanics, superflow can be considered as potential flow, for which the following relation can be written [31]:

$$\nabla \times \boldsymbol{v}_s = 0. \tag{2.81}$$

According to it, the superflow moving with velocity $\boldsymbol{v}_s$ is irrotational [31]. On the other hand, one can also consider circulation, which is one of the basic properties of any flow. In the considered case, the circulation over any closed path (here labeled as κ) can be defined as the integral of velocity $\boldsymbol{v}_s$ [31]:

$$\kappa = \oint \boldsymbol{v}_s \cdot \, d\boldsymbol{r}, \tag{2.82}$$

In addition, in order to show some important properties of quantum vortices, one should also consider the expression for superfluid velocity where the gradient of phase

is taken into consideration. In order to derive this formula, one can at first take a closer look at the properties of condensate. The expression for contribution to current density coming from condensate (here denoted as j_0) can be written as [31]:

$$j_0 = \frac{\hbar}{2mi}[\Psi^*(\boldsymbol{r})\nabla\Psi(\boldsymbol{r}) - \Psi^*(\boldsymbol{r})\nabla\Psi(\boldsymbol{r})], \tag{2.83}$$

where $\Psi(\boldsymbol{r})$ is the macroscopic wave function of the condensate from Eq. 2.16. Here, the current means the number of particles flowing through a unit area per unit time. However, it does not have the common meaning of electric current, as in this case, the particles are uncharged. Later on, one can rewrite the formula for macroscopic wave function of the condensate as $\Psi(\boldsymbol{r}) = \sqrt{\rho_s(\boldsymbol{r})}e^{i\phi(\boldsymbol{r})}$, where ρ_s means the superfluid density and $\phi(\boldsymbol{r})$ is the phase [31]. Then, after applying the differentiation rule to this formula and inserting the result into Eq. 2.83, one can rewrite j_0 as [31]:

$$j_0(\boldsymbol{r}) = \frac{\hbar}{m}\rho_s(\boldsymbol{r})\nabla\phi(\boldsymbol{r}). \tag{2.84}$$

Taking into account that, by definition, current is equal density times velocity (so $j_0 = \rho_s v_s$), one can derive the relation for superfluid velocity v_s from Eq. 2.84:

$$v_s(\boldsymbol{r}) = \frac{\hbar}{m}\nabla\phi(\boldsymbol{r}). \tag{2.85}$$

Finally, combining Eq. 2.81 and definition of superfluid velocity from Eq. 2.85, one can show that the value obtained within Eq. 2.82 does not depend on the chosen path [75]:

$$\kappa = \oint \frac{\hbar}{m}\nabla\phi(\boldsymbol{r})\ d\boldsymbol{r} = \frac{\hbar}{m}\Delta\phi. \tag{2.86}$$

In Eq. 2.86, the expression $\Delta\phi$ has the meaning of the difference between angles ϕ at the beginning and at the end of integration [75]. As the phase can be defined up to 2π factor (because $e^{i\phi} = e^{i(\phi+2\pi)}$, the phase difference for a closed path can be only a multiple of 2π. As a consequence, for the closed path Eq. 2.86 will always give the same value up to 2π factor. In other words, if the flow goes around any closed path, its contribution to circulation would be equal $\frac{\hbar}{m}\Delta\phi = \frac{\hbar}{m}w2\pi = w\frac{h}{m}$ [75, 31], where w is an integer number. Finally, it can be seen that circulation κ has to be quantized in units of h/m [31]:

$$\kappa = \frac{h}{m}w \tag{2.87}$$

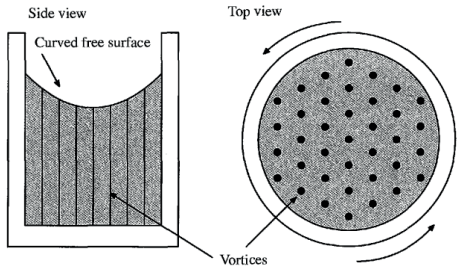

FIGURE 2.20: A sketch of quantum vortices in superfluid [31].

with w being a winding number (which means how many times the phase jumps by 2π around the chosen closed contour) [31, 75].

As it comes up from the analysis presented above, in superfluid systems, a liquid should not react to rotation (for example, a superfluid in a rotating container should not form a meniscus). Contrary to this prediction, one could observe that the surface became curved [31]. As the vortices in a classical sense cannot be present in the system, they must take a quantized form [31]. This mechanism is schematically shown in Fig. 2.20. On the left side of Fig. 2.20, one can see the curved surface of the superfluid. The right side presents the lattice of quantum vortices, which can be imagined as a circulating flow of cylindrical shape.

In general, the "rotation" of a quantum vortex can be described in cylindrical polar coordinates. Then, the condition for irrotationality takes the form [31]:

$$\nabla \times \boldsymbol{v}_s = \frac{1}{r} \det \begin{pmatrix} \boldsymbol{e}_r & \boldsymbol{e}_\phi & \boldsymbol{e}_z \\ \frac{\partial}{\partial r} & \frac{\partial}{\partial \phi} & \frac{\partial}{\partial z} \\ v_r & r v_\phi & v_z \end{pmatrix}. \tag{2.88}$$

In Eq. 2.88, the terms $\boldsymbol{e}_r$, $\boldsymbol{e}_\phi$ and $\boldsymbol{e}_z$ denote the unit vectors in each of direction r, ϕ, z at the point $\boldsymbol{r} = (r, \phi, z)$. The last line of the matrix contains the components of superfluid velocity in each of the directions, so that $\boldsymbol{v}_s = v_r \boldsymbol{e}_r + v_\phi \boldsymbol{e}_\phi + v_z \boldsymbol{e}_z$ [31]. Then, the irrotationality condition requires that [31]:

$$\frac{1}{r} \frac{\partial}{\partial r} (r v_\phi) = 0. \tag{2.89}$$

Based on that, one can define the velocity of the flow around the vortex [31]:

$$\boldsymbol{v}_s = \frac{\kappa}{2\pi r}\boldsymbol{e}_\phi. \tag{2.90}$$

With regard to Eq. 2.90, it can be seen that the condition for irrotationality would be satisfied in the whole region of vortex except from $r = 0$, which corresponds to the core of the vortex [31], where the macroscopic wave function is equal 0 (therefore, the phase in the core is not defined) [31]. Therefore, quantum vortices are commonly understood as topological defects, inside of which the superfluidity is destroyed [5].

In general, if the superfluid rotates together with a cylinder of radius R and angular velocity ω, the total circulation around it would be equal to the integral around the cylinder [31]:

$$\kappa = \oint \boldsymbol{v}_s \; d\boldsymbol{r} = (2\pi R)\omega R. \tag{2.91}$$

Then, as the circulation is quantized, κ should be also equal [31]:

$$\kappa = \frac{h}{m}N_v, \tag{2.92}$$

where N_v denotes the total number of vortices in the superfluid (each of them carrying a quantum h/m of the circulation [75]. This leads to the expression for the number of vortices per unit area [31, 75], which is also known as the Feynman-Onsager formula for vortex density in a rotating superfluid [76, 77]:

$$\frac{N_v}{\pi R^2} = \frac{2m\omega}{h}. \tag{2.93}$$

Here, the term ω is equivalent to the angular velocity of rotation of the star and can therefore be defined as $2\pi/P$, with P being the rotation period [5].

Another important quantity describing vortices in neutron stars is surface vortex density, which can be defined as [78]:

$$\mathcal{N} = \frac{2\omega}{\kappa_v} \approx 6 \cdot 10^3 \left(\frac{1\,\mathrm{ms}}{P}\right) \mathrm{cm}^2, \tag{2.94}$$

where κ_v denotes the quantum of circulation carried by a single vortex. Based on Eq. 2.94, it can be seen that the surface vortex density increases as the star spins up

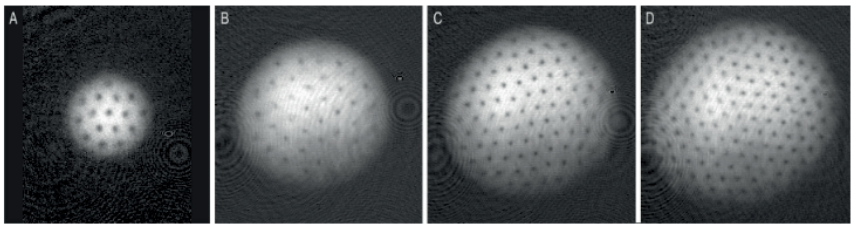

FIGURE 2.21: Vortex lattices containing 16 vortices (a), 32 (b), 80 (c), and 130 (d) [79].

[5]. This comes as a result of the fact that the only possibility for the neutron star to slow down is to expel the vortices out of the inner crust [5]. In addition, one can also define the average distance d between the vortices in the lattice, which can be approximated as $1/\sqrt{\mathcal{N}}$ [78]. As an example, in the case of Vela pulsar (for which $P = 89$ ms), the inter vortex spacing is approximately equal $4 \cdot 10^{-3}$ cm [78]. As reported in [79, 80], the vortex lattice was observed in 2001 in a rotating BEC by the Ketterle group. Fig. 2.21 shows the observed lattices containing different numbers of vortices.

2.5.2 Vortex Filament Model

To describe the dynamics of vortices in neutron star crusts, the Vortex Filament Model (VFM) has been developed [21]. Historically, VFM originates from Schwarz's model, which was developed for a single vortex in superfluid Helium without impurities [21]. Nowadays, VFM provides a description of many-vortex systems moving in the superfluid medium. The model can also be extended to cases where vortices interact with impurities [15]. The assumption behind this model is that all the relevant scales are expected to be much bigger than the core size of the vortex [15].

The quantum vortex in superfluid matter can be described as a so-called filament passing through the fluid [21], as it is schematically shown in the middle panel of Fig. 2.3. In general, VFM is primarily used in studies of quantum turbulence, where it describes the behavior of a vortex line in the presence of other vortices. In the neutron star context, the interaction between vortex and impurity (which is expected to be dominant compared to the vortex-vortex interaction [81, 15]) is of the main interest. Additionally, Fig. 2.22 provides the sketch of the evolution of the vortex line (blue line) in presence of an impurity (red dot). As can be seen, once the impurity approaches the vortex line, it significantly modifies its position due to the various forces acting on the vortex. They

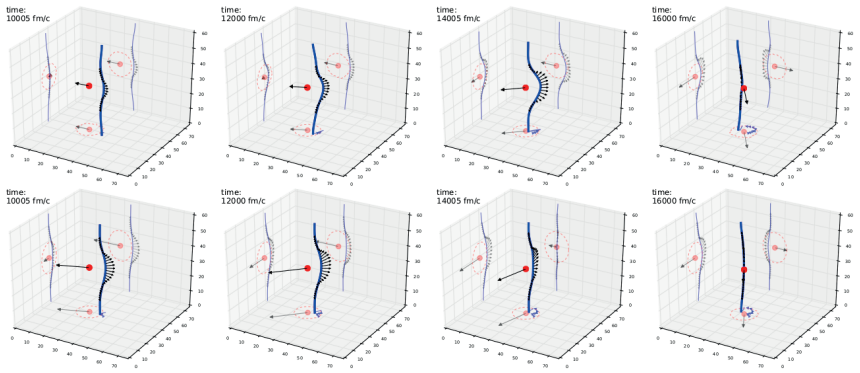

FIGURE 2.22: Interaction of vortex filament with impurity approaching it [82].

are described in detail in the following part of this section.

In general, the movement of vortex lines is possible as a result of forces acting on it (otherwise, they stay „frozen" in the superfluid medium and move together with it) [15]. Usually, this movement is described in the (x, y) plane and the vortex line is assumed to be placed parallel to z axis (which is expected to be valid in case of neutron stars). Then, one can define the auxiliary variable $\boldsymbol{u}$ being a vector of vortex line displacement along z: $\boldsymbol{u}(z,t) = [x(z,t), y(z,t)]$ [81]. It can be understood as a kind of parametrization, describing the coordinates x and y for a particular z. Based on that, one can write the force balance equation [82, 81]:

$$\boldsymbol{F_d} + \boldsymbol{F_m} + \boldsymbol{F_t} = 0 \tag{2.95}$$

with an assumption that the vortex mass is negligible [15, 21].

The forces from Eq. 2.95 arise due to the different contributions of certain components of the crust [15]. In the case of the analyzed system, one can distinguish three significant velocities, which are the velocity of neutron superfluid $\boldsymbol{v_s}$, vortex velocity $\boldsymbol{v_v}$, and velocity of impurities $\boldsymbol{v_p}$ (which is also called velocity of solid crust) [15]. However, it can be seen that in the following relations, only the relative velocities are considered (which is a consequence of the Galilean invariance). One can define the forces as:

- Magnus force (also known as lift force) – it works against pinning force and is

therefore connected with the movement of the vortex through the superfluid neutron matter [21, 15]. It can be defined with regard to the following formula [21, 15]:

$$\boldsymbol{F_m} = \rho_n \boldsymbol{\kappa} \times (\boldsymbol{v_v} - \boldsymbol{v_s}). \tag{2.96}$$

The parameter ρ_n denotes the mass density of the superfluid component (defined as $m_n n$, where m_n is the neutron mass and n means the number density of the neutron background) [82]. Here, it should be stressed that ρ_n is the same as the superfluid density and should not be confused with the density of the normal component. The term $\boldsymbol{\kappa}$ refers to circulation pointed along the vortex [82] and can be defined as a vector along the angular velocity of neutrons (so tangential to the vortex line) normalized to $h/2m_n$ (being the single quantum of circulation carried by one vortex, where $2m_n$ is the mass of Cooper pair) [15]. In general, the vector describing the position of the vortex line core is normal to κ and to the relative velocity $\boldsymbol{v_n} - \boldsymbol{v_v}$ between vortex velocity and superflow velocity [21]. Additionally, the vortex velocity can also be defined as $\partial \boldsymbol{u}/\partial t$ [81]. What is also important, the superflow has two major contributions. Apart from the flow caused in the background matter by the movement of the vortex, one should also consider the self-interaction. As the vortex takes the form of a deformed line, the particular parts of such a line also interact with each other [21], which leads to the contribution to the whole background flow;

- viscous drag force – it is responsible for dissipation that occurs due to the relative motion between the vortex and the whole crust (so, in fact, with the impurities) [15]. In general, one can decompose this force into longitudinal and perpendicular parts in the (x, y) plane. However, in the case of this research, it is assumed that the perpendicular component is equal to 0 [82] and therefore can be omitted in further analysis. Then, the longitudinal component of the drag force can be defined as [15]:

$$\boldsymbol{F_d} = -\mathcal{R}(\boldsymbol{v_v} - \boldsymbol{v_p}) \tag{2.97}$$

with $\mathcal{R}$ being a constant connected with interaction between vortex and crust (so with lattice of impurities and electron gas) [15]. Viscous drag force is also called pinning force [82]. When the velocity of the crust and vortex are equal, vortices are pinned to the crust [15]; in other words, the pinning force is due to vortex-nucleus interaction [82], which will be considered in this thesis. As a consequence, this force leads to mutual friction between the vortex line and

the normal component [15, 21]. However, it should also be mentioned that the vortex-nucleus interaction force is not the only contribution to the pinning. In fact, the structure of the crust (including the number of impurities and the distances between them) influences the pinning as well [15];

- tension force – it is connected with vortex bending. Despite the fact that vortices take the form of straight lines [82], they can be distorted from this shape due to the interaction with impurities during the movement through the medium [21]. Tension force is given as [15, 81]:

$$\boldsymbol{F_t} = T\frac{\partial^2 \boldsymbol{u}}{\partial z^2}. \tag{2.98}$$

In Eq. 2.98, the component T is called tension coefficient defined as $\rho_n \kappa \mathcal{C}_t$ [81, 15], where κ is equal $h/2m_n$ and $\mathcal{C}_t$ is the so-called rigidity coefficient [15]. Its simple estimate is:

$$\mathcal{C}_t \sim \frac{\kappa}{4\pi} \ln \frac{d_v}{r_v} \tag{2.99}$$

where spacing between vortices is denoted as d_v and size of the vortex core as r_v [15].

2.5.3 The Phenomenon of Glitch

As mentioned before, one of the phenomena associated with the rotation of neutron stars is the occurrence of glitches. The history of their examination dates back to 1967, when Jocelyn Bell (a student of Hewish) discovered regular pulses of radio waves [5, 15] during studies of the Vulpecula constellation [5]. Later on, it was realized that this radiation, in fact, comes from rotating neutron stars [12] that emit electromagnetic radiation in the form of regular pulses; therefore, these objects have been named pulsars [5]. In 1974, Hewish received a Nobel Prize for their discovery; however, Bell was not included in the award, which remains a source of controversy [5, 12].

In general, pulses coming from neutron stars are extremely regular (the delays are usually about a few microseconds per year) [15, 83]. Due to e.g. emission of electromagnetic radiation and, possibly, gravitational waves [83], the frequency of rotation turns out to steadily and slowly decrease [83]. However, one can still observe some irregularities, such as sudden spin-ups in the rotational frequency of the pulsar [15,

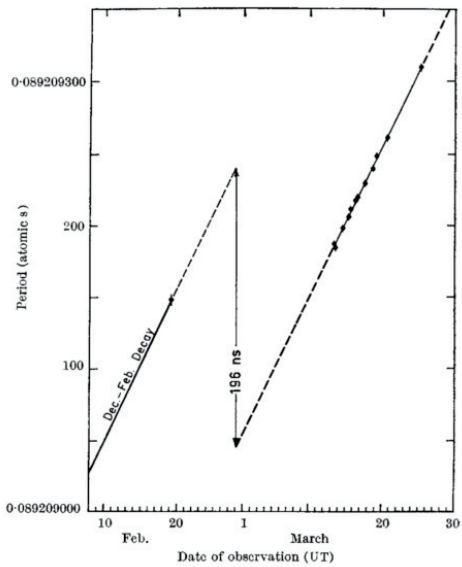

FIGURE 2.23: Period of rotation of Vela pulsar as a function of time [84].

83], which are referred to as glitches. As an example, in Fig. 2.23, the period of rotation with regard to the date of observation for the Vela pulsar is shown [84]. The discontinuity visible in this diagram corresponds to the first glitch in history, observed in 1969 [5]. As can be seen, the period of rotation decreased by about 196 ns. It has also been observed that the glitch is followed by a period of relaxation (lasting usually about a few days [15]), during which the period of rotation comes back to the value before this phenomenon [15]. Another example of a pulsar exhibiting glitches is Crab, for which the frequency of rotation as a function of time is presented in Fig. 2.24 [85]. One of the possible explanations of the phenomenon of glitches is the superfluidity of the internal matter in the inner crust [10, 81, 83]. Therefore, there seems to be a strong connection between glitches and the presence of vortices in the crust. One of the first models within this framework can be found in the work by Anderson [86], where the inner crust is described as a two-fluid system. Then, the neutron matter plays the role of a superfluid component filled with quantum vortices. Protons and electrons are therefore considered as the normal (crustal) component [86] (in addition, the outer crust is also considered as part of the normal component [5]). With each of these components, one can associate the angular velocity of rotation, denoted as Ω_n for the superfluid

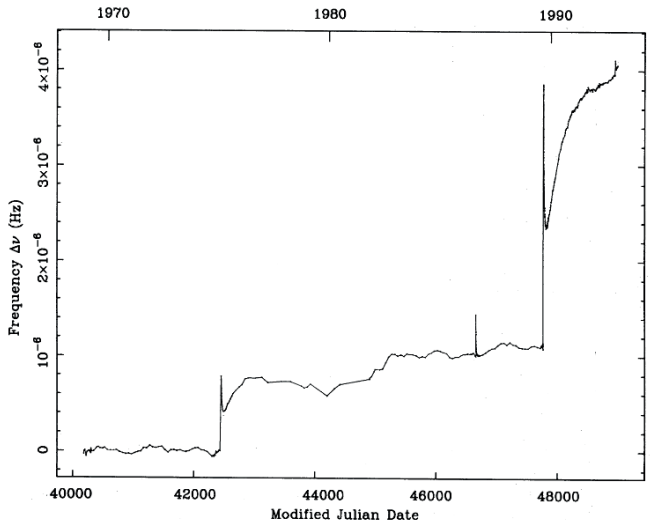

FIGURE 2.24: Frequency of rotation of Crab pulsar as a function of time [85].

neutron component and Ω_c for the normal part. In literature, the subscript n refers to neutrons (so to the superfluid component) and c to charged particles (protons and electrons), which create the normal component.

As it has been mentioned before, one can investigate the properties of neutron stars with regard to the measurements of the electromagnetic radiation, which is emitted by the moving charged particles (so by the normal component). The fundamental quantity that can be measured is the frequency of rotation of the charged component (which, however, does not provide the straightforward information about the movement of the superfluid (neutron) component). The increase in the angular momentum of the charged component reveals itself in the form of a glitch (so, in other words, glitches appear as a result of a change in the velocity of the neutron star). Then, it can be seen that this angular momentum has to be „taken" from the superfluid component. As the circulation is quantized, the angular momentum of vortices can be modified only through the change of their number, so they must have the ability to move through the medium.

Taking the more detailed insight into the mechanism of the glitch, when the normal component spins down, vortices (which are assumed to carry the significant part of

the total angular momentum) try to follow this movement [5]. However, as it was mentioned in Sec. 2.5.2, they are expected to be pinned to the nuclei [81, 83]. Therefore, they cannot move freely and start to work against the deceleration [10, 83]. Consequently, the angular velocity of the superfluid component remains approximately constant, which leads to the difference between the velocity of the normal and superfluid components [81, 5]. Such a difference results in Magnus force, which works against the pinning force [81, 83]. Later on, as the difference between Ω_n and Ω_c exceeds some critical value (in other words, when Ω_n exceeds Ω_c [5]), vortices are unpinned from nuclei, which leads to a sudden decrease in angular velocity [81, 10]. Here, one should also mention the vortex avalanche model, according to which a single unpinned vortex unpins the pinned one and so on [17]. As a consequence, angular momentum is transferred from the fluid to the charged component (in order for total angular momentum to be conserved), which manifests as a glitch. In other words, the phenomenon of glitch is connected with angular momentum exchange between the superfluid and normal component in the inner crust [17, 10].

One of the important quantities in the examination of glitches is their amplitude, which can be described in the framework of the dynamics of the internal matter of the crust [83]. In general, the angular momentum conservation law takes the following form [83, 10, 17]:

$$I_n(\Omega_c + \delta\Omega) + I_c\Omega_c = (I_n + I_c)\Omega. \tag{2.100}$$

In Eq. 2.100, I_n and I_c have the meaning of moments of inertia for the neutron superfluid component (so for the vortex lines as well) and the normal component, respectively. The term $\delta\Omega$, called a lag [83] (or differential rotation [5]), denotes the difference $\Omega_c - \Omega_n$ [83]. Once it reaches some particular value (which, however, cannot be precisely calculated [5]), vortices start to unpin from the crust [5, 83]; this, in fact, corresponds to the situation when the Magnus force exceeds the pinning force [5]. At last, in Eq. 2.100 Ω denotes the common angular velocity, once both of the components recover after a glitch [83] (it is therefore equal to the angular velocity of rotation of the whole star and can be expressed as $2\pi/P$, with P being the period of rotation [5]). Therefore, the quantity $\Omega - \Omega_c$ has the meaning of the size of a glitch [83]; as it can be seen, it depends on the lag arising as a result of the difference in velocities of particular components and on the total moment of inertia $I_n + I_p$ [83]. Considering relations for $\dot{\Omega}_c$ and $\dot{\Omega}_n$, which can be found e.g. in [83], one can obtain the equation for critical lag

$\delta\Omega$ [83]:

$$\delta\Omega = \delta\Omega_0 e^{-t/\tau},\ \tau = \frac{I_c}{I}\frac{1}{2\Omega_n \mathcal{B}}, \tag{2.101}$$

where $\delta\Omega_0$ is the initial value of the lag, t means the time between glitches, τ is the coupling time scale and $\mathcal{B}$ is the mutual friction coefficient denoting the strength of pinning, which is proportional to $\mathcal{R}$ [83].

On the other hand, one should also consider the quantity called glitch activity $\mathcal{A}$. According to [5, 15], it can be defined as:

$$\mathcal{A} = \frac{1}{t}\sum_i \frac{\Delta\Omega_c^i}{\Omega_c}, \tag{2.102}$$

where $\Delta\Omega_c^i$ denotes the rise in the angular velocity of the normal component [5]. Therefore, the term $\Delta\Omega_c^i/\Omega_c$ corresponds to the size of a glitch (or, in other words, its amplitude) normalized to the angular velocity of the normal component Ω_c [87]. In Eq. 2.102, $\sum_i$ denotes the sum of all the amplitudes $\Delta\Omega_c^i/\Omega_c$ occurring in a certain time of observation t [5, 15]. Typically, glitches take the values from $\Delta\Omega_c/\Omega_c \approx 10^{-12}$ to even 10^{-3} [88] (e.g. in case of Crab pulsar [88]).

Combining Eq. 2.101 with the expression for activity from Eq. 2.102 and neglecting entrainment effects, one can obtain the following relation [83, 17]:

$$\frac{I_n}{I_c} = -\frac{\Omega_c}{\dot{\Omega}_c}\mathcal{A}, \tag{2.103}$$

which can be used to estimate the size of a glitch [83]. Alternatively, taking into consideration the entrainment effects (influencing the moment of inertia [10]), one can obtain the formula [83, 10]:

$$\frac{I_n}{I_c} \approx -\frac{\Omega_c}{\dot{\Omega}_c}\mathcal{A}\frac{m^* n}{m_n}, \tag{2.104}$$

where m_n and m_n^* are the neutron mass and its effective mass, respectively.

As it was mentioned before, in order to explain the phenomenon of glitches, one should study the vortex-impurity interaction, which provides an essential input for macroscopic models. Among various parameters (such as activation energy required for the process of unpinning), pinning force (obtained within microscopic calculations) turns

out to be especially important, e.g., in the investigation of the glitch amplitude (being the macroscopic parameter). To illustrate the connection between these quantities, one should first examine the frequency jump associated with the glitch, denoted as $\Delta\nu$. It should fulfill the following relation [89]:

$$2\pi\nu = -\frac{I_n}{I}\langle\Delta\Omega\rangle \tag{2.105}$$

with I being the total moment of inertia. $\Delta\Omega$ is the difference in lag before and after the glitch. Once it cannot be directly measured [89], one can consider the local lag (Ω) instead. The upper limit of this lag (Ω^*) can be defined as:

$$\Omega^* = \frac{f_p(\boldsymbol{r})(1-\epsilon_n(\boldsymbol{r}))}{\kappa\rho_n(\boldsymbol{r})x}, \tag{2.106}$$

where f_p means the pinning force[89]. Based on that, it can be seen that $2\pi\nu$ should obey the following relation [89]:

$$2\pi\nu < \Delta\Omega_{\max} = \frac{I_n}{I}\langle\Omega^*\rangle. \tag{2.107}$$

Then, one can write the explicit formula for the maximal value of glitch amplitude with regard to the pinning force f_p [89]:

$$\Delta\Omega_{\max} = \frac{\pi^2}{I\kappa}\int d\boldsymbol{r}\, r^3 f_p(\boldsymbol{r}). \tag{2.108}$$

Over the years, several approaches have been developed to estimate the pinning force. As shown in [5], research by Anderson [86] has led to calculations considering both realistic pairing gaps [90] and quantum calculations [91]. One of the promising methods is dynamic calculations, first introduced by Bulgac et al. [92] and later developed in [82]. Following this approach, the pinning force is obtained using the dynamic method in this research.

Chapter 3

Theoretical Background – Methodology

3.1 Mean Field Approximation Methods

Nuclear matter in the neutron star crust is, in fact, a many-body interacting system. The crucial problem in describing such systems arises due to the interaction between particles. In general, the position of a particle in such a system is influenced by the positions of all the other particles (in other words, their motion is correlated) [60, 93]). The wave function in the Schrödinger equation depends on position vectors of each of the particles. In addition, the potential term in the Hamiltonian includes the potential describing interaction between all the particles [60]. Although the wave function provides all the necessary information, solving the Schrödinger equation for many-particle systems becomes an extremely complicated and computationally demanding task.

In order to simplify this approach, one can consider the following idea – each of the particles moves in the external potential which is equivalent to the mean interaction with all other particles (so, in other words, this potential models the interaction between particles) [93]. Based on that, one can substitute the potential term in the Schrödinger equation with the so-called mean field potential, which depends explicitly only on the position of the particle, but describes the average interaction with other particles as well [60, 93]. Then, as the mean field Hamiltonian contains only the single-particle terms, the initial many-body problem can be reduced to the single-particle one [60]. This method is known as Mean Field Approximation (MFA).

3.1.1 Hartree-Fock-Bogoliubov Formalism and its Modifications

The fundamental approach used in the analysis of many-body interacting quantum systems in the framework of MFA is the Hartree-Fock (HF) method. Initially, it was developed to describe electronic systems [94] and has been used, for example, in solid-state physics [95]. According to this approach, the many-body wave function can be approximated by a Slater determinant (in the fermionic case) of all the orbitals in the system [94]. Based on that, one can derive the set of equations corresponding to these orbitals and, consequently, wave functions and energies [94].

The extension of the HF method for superfluid systems (so including effects connected with pairing) is called Hartree-Fock-Bogoliubov (HFB) formalism [96]. In order to derive HFB equations, one should assume that Hamiltonian H takes the diagonalized form, Eq. 2.73 [63]. In addition, creation and annihilation operators $\alpha_n^\dagger$ and α_n, coming from Bogoliubov transformation and defining a state described within a set of n quantum numbers, should obey the following commutation rules [63]:

$$[\alpha_n^\dagger, H] = -E_n \alpha_n^\dagger, \tag{3.1}$$

$$[\alpha_n, H] = E_n \alpha_n. \tag{3.2}$$

Later on, one should combine these equations with commutation relations that standard operators $\psi_{n\sigma}^\dagger$ and $\psi_{n\sigma}$ have to fulfill (they can be found e.g. in [63]). Then, the following equations that quasiparticle wave functions are supposed to fulfill can be obtained [63]:

$$\sum_{\sigma'=\{\uparrow,\downarrow\}} \Big(h_{\sigma\sigma'}(\boldsymbol{r}) u_{n\sigma'}(\boldsymbol{r}) + \int d^3\boldsymbol{r}' \Delta_{\sigma\sigma'}(\boldsymbol{r},\boldsymbol{r}') v_{n\sigma'}(\boldsymbol{r}') \Big) = E_n u_{n\sigma}(\boldsymbol{r}), \tag{3.3}$$

$$\sum_{\sigma'=\{\uparrow,\downarrow\}} \Big(- h^*_{\sigma\sigma'}(\boldsymbol{r}) v_{n\sigma'}(\boldsymbol{r}) + \int d^3\boldsymbol{r}' \Delta^*_{\sigma\sigma'}(\boldsymbol{r},\boldsymbol{r}') u_{n\sigma'}(\boldsymbol{r}') \Big) = E_n v_{n\sigma}(\boldsymbol{r}), \tag{3.4}$$

where $h(\boldsymbol{r})$ is the single particle Hamiltonian:

$$h_{\sigma\sigma'}(\boldsymbol{r},\boldsymbol{r}') = \delta_{\sigma\sigma'} \Big(- \frac{\hbar^2}{2m} \nabla^2 + V_\sigma(\boldsymbol{r}) - \mu_\sigma \Big). \tag{3.5}$$

As it can be seen, Eqs 3.3 - 3.4 can be expanded into four equations with regard to spin projection ($\sigma' = \{\uparrow, \downarrow\}$). Usually, such equations are written in the matrix form [63]:

$$\sum_{\sigma'=\{\uparrow,\downarrow\}} \int d^3\boldsymbol{r}' H_{\sigma\sigma'}(\boldsymbol{r},\boldsymbol{r}') \begin{pmatrix} u_{n\sigma'}(\boldsymbol{r}') \\ v_{n\sigma'}(\boldsymbol{r}') \end{pmatrix} = E_n \begin{pmatrix} u_{n\sigma}(\boldsymbol{r}) \\ v_{n\sigma}(\boldsymbol{r}) \end{pmatrix}, \tag{3.6}$$

where $[u_{n\sigma}(\boldsymbol{r}), v_{n\sigma}(\boldsymbol{r})]^T$ is shorthand notation for vector $[u_{n\uparrow}(\boldsymbol{r}), u_{n\downarrow}(\boldsymbol{r}), v_{n\uparrow}(\boldsymbol{r}), v_{n\downarrow}(\boldsymbol{r})]^T$. Then, considering all the possible configurations of spin projections, the Hamiltonian matrix H from Eq. 3.6 can be written as [63]:

$$H(\boldsymbol{r},\boldsymbol{r}') = \begin{pmatrix} h_{\uparrow\uparrow}(\boldsymbol{r},\boldsymbol{r}') & h_{\uparrow\downarrow}(\boldsymbol{r},\boldsymbol{r}') & 0 & \Delta_{\uparrow\downarrow}(\boldsymbol{r},\boldsymbol{r}') \\ h_{\downarrow\uparrow}(\boldsymbol{r},\boldsymbol{r}') & h_{\downarrow\downarrow}(\boldsymbol{r},\boldsymbol{r}') & \Delta_{\downarrow\uparrow}(\boldsymbol{r},\boldsymbol{r}') & 0 \\ 0 & -\Delta^*_{\uparrow\downarrow}(\boldsymbol{r},\boldsymbol{r}') & -h^*_{\uparrow\uparrow}(\boldsymbol{r},\boldsymbol{r}') & h^*_{\uparrow\downarrow}(\boldsymbol{r},\boldsymbol{r}') \\ -\Delta^*_{\downarrow\uparrow}(\boldsymbol{r},\boldsymbol{r}') & 0 & h^*_{\downarrow\uparrow}(\boldsymbol{r},\boldsymbol{r}') & -h^*_{\downarrow\downarrow}(\boldsymbol{r},\boldsymbol{r}') \end{pmatrix}. \tag{3.7}$$

In Eq. 3.7, the terms connected with Δ acting on states with the same spin projection ($\Delta_{\uparrow\uparrow}$ and $\Delta_{\downarrow\downarrow}$) are set to 0, due to the fact that spin-singlet pairing (which is the dominant pairing channel in neutron star crust) couples the states with opposite spin [69]. In addition, it is also imposed that $\Delta \equiv \Delta_{\uparrow\downarrow} = -\Delta_{\downarrow\uparrow}$, which is a consequence of the anticommutation relation.

As it can be seen, the form of Eq. 3.7 leads to integro-differential equations, which turn out to be a significant computational challenge. In order to simplify them, one can make an assumption of a local pairing potential, in which the diagonal part of the pairing potential is expected to be dominant [97]. As a consequence, the pairing potential is considered as a short-range interaction [97]. This idea leads to the following form of pairing potential [98]:

$$\Delta(\boldsymbol{r},\boldsymbol{r}') \approx \Delta(\boldsymbol{r},\boldsymbol{r}')\delta(\boldsymbol{r}-\boldsymbol{r}'). \tag{3.8}$$

Then, instead of considering pairing potential $\Delta(\boldsymbol{r},\boldsymbol{r}')$ one can use the simplified form $\Delta(\boldsymbol{r})$. As a consequence, the integration form Eqs 3.3 - 3.4 can be removed, which results in the following form of Eq. 3.6 for a four-component vector of quasiparticle

wave functions $[u_{n\uparrow}, u_{n\downarrow}, v_{n\uparrow}, v_{n\downarrow}]^T$ [63]:

$$\begin{pmatrix} h_{\uparrow\uparrow} & h_{\uparrow\downarrow} & 0 & \Delta \\ h_{\downarrow\uparrow} & h_{\downarrow\downarrow} & -\Delta & 0 \\ 0 & -\Delta^* & -h^*_{\uparrow\uparrow} & -h^*_{\uparrow\downarrow} \\ \Delta^* & 0 & -h^*_{\downarrow\uparrow} & -h^*_{\downarrow\downarrow} \end{pmatrix} \begin{pmatrix} u_{n\uparrow} \\ u_{n\downarrow} \\ v_{n\uparrow} \\ v_{n\downarrow} \end{pmatrix} = \varepsilon_n \begin{pmatrix} u_{n\uparrow} \\ u_{n\downarrow} \\ v_{n\uparrow} \\ v_{n\downarrow} \end{pmatrix}. \tag{3.9}$$

For brevity, the position dependence of all quantities has been dropped. In Eq. 3.9, called HFB equations, the single particle Hamiltonian h and pairing potential Δ are both position-dependent. At this point, one should also note that HFB equations are nonlinear due to the presence of quasiparticle wave functions in the expression for the Hamiltonian and pairing field. Therefore, as in the BCS case, they must be solved in a self-consistent manner.

3.1.2 Bogoliubov-de Gennes Method

For Eq. 3.9, one can still make some further assumptions, among which one is related to the spin-orbit coupling. In general, this effect is connected with the interaction of orbital angular momentum and spin angular momentum [62]. On the microscopic level, spin-orbit coupling is included as a correction to the single-particle potential in the nuclear shell model, allowing for the explanation of energy level shifts [62, 99]. According to this model, orbital $\boldsymbol{l}$ and spin $\boldsymbol{s}$ angular momenta are coupled [12, 62], which results in a contribution to the nuclear potential proportional to $\boldsymbol{l} \cdot \boldsymbol{s}$ and, further, in the shift in energy [99, 62]. As a result, energy levels that should be theoretically associated with a particular shell can join the shell of a different energy [99, 62]. This property allows, e.g., for a proper explanation of magic numbers [62].

In general, in nuclear systems, the spin-orbit coupling significantly contributes to the nucleon-nucleon interaction [12]. However, in the neutron star crust, the situation becomes different. It turns out to be proportional to the gradient of the density of neutrons and is supposed to be small, as proton impurities are expected to have a diffuse surface [15]. As a result, density is not expected to exhibit large variability, and the spin-orbit term is usually neglected in the case of astrophysical considerations [15].

Furthermore, as mentioned in the previous chapter, the primary pairing channel in the neutron star crust is the spin singlet configuration. Then, in HFB equations, one

can impose $h_{\uparrow\downarrow} = h_{\downarrow\uparrow} = 0$ (so the spin-triplet state, in which nucleons with the same spins are paired, is not included). Another assumption that one can make is the spin symmetry of the system (so the number of states consisting of two spin-up nucleons is the same as the states from spin-down nucleons). According to [100], the spin polarization of nuclear matter is connected with the magnetic field. It turns out that nuclear matter in a neutron star can become polarized for magnetic fields higher than 10^{17} G [100]; however, it turns out that in the neutron star crust, such a field is not higher than 10^{15} G [100], except magnetars, which are not considered here. Therefore, one can consider the spin-symmetric case with $h_{\uparrow\uparrow} = h_{\downarrow\downarrow} = h$. The simplifications mentioned above allow for a significant reduction in the computational cost of numerical simulations. However, in the case of neutron stars, their presence does not significantly affect the reliability of the results.

According to the assumptions above, HFB equations can be reduced to the form for a two-component vector $[u_{n\uparrow}, v_{n\downarrow}]^T$. They are commonly known as BdG equations [63]:

$$\begin{pmatrix} h & \Delta \\ \Delta^* & -h^* \end{pmatrix} \begin{pmatrix} u_{n\uparrow} \\ v_{n\downarrow} \end{pmatrix} = \varepsilon_n \begin{pmatrix} u_{n\uparrow} \\ v_{n\downarrow} \end{pmatrix}, \tag{3.10}$$

with h, Δ, $u_{n\uparrow}$ and $v_{n\downarrow}$ dependent on position. The BdG formalism is one of the most fundamental methods used to describe superconducting systems (and is commonly applied, e.g., in solid-state physics) [63]. Historically, this approach originates from BCS theory, which was developed to describe homogeneous systems (such as an electronic gas) and has since been generalized to the non-uniform case [101]. Moreover, when Δ in Eq. 3.10 is set to 0, the BdG formalism reduces to the Hartree-Fock method, which is commonly used to describe systems in the normal state, where Cooper pairs do not appear.

3.2 Density Functional Theory

Examination of many-body interacting systems in a nonequilibrium state reveals itself as an extremely demanding challenge [102, 103]. Moreover, the problem tends to be even more complicated in the case of time-dependent analysis, where some common methods based on HF formalism do not allow for sufficiently precise quantitative

description [102, 103]. For these reasons, a powerful tool that provides a detailed description combined with an acceptable computational cost has been required. Density Functional Theory (DFT) fulfills these conditions and is therefore widely used in various fields of science, such as quantum chemistry or solid-state physics [103, 102, 104]. Nowadays, it turns out that DFT can be successfully applied to neutron star studies as well [5, 12, 105]. One of the key advantages of this method is its potential extension to superfluid systems [106], which play a major role in various phenomena occurring within the neutron star crust. The main advantage of DFT is the possibility to examine the system without solving Schrödinger equation explicitly. As the energy of the system is expressed in the form of a density functional, the ground state is obtained through minimization of the energy functional over density [104]. This procedure leads to equations formally equivalent to HF or HFB and can therefore be solved using precise computational methods developed for this formalism [107].

3.2.1 Hohenberg-Kohn Theorem

The fundamental theorem that underlies Density Functional Theory is the Hohenberg-Kohn theorem [104, 102, 103]. In general, all the observables describing a certain system can be obtained, as the many-body wave function is known [104]. However, such a function is extremely complicated and therefore needs to be replaced with a simpler quantity that allows for the examination of the system's properties as well. It turns out that instead of the examination of the wave function, one can analyze the density of particles [108, 102, 103, 104]. Historically, this idea has been used for approximate analysis; later, it was shown that such an approach can provide a very detailed description of the system. According to Hohenberg-Kohn theorems, there is a mapping between density and many-body wave function [108, 102, 103]. Therefore, in principle, one can obtain all the information about the system by examining the density only.

Below, the derivation of Hohenberg-Kohn theorems, based on [108, 109, 102, 103], is presented. First of all, for the system consisting of N particles one can write the Schrödinger equation in the form:

$$H\Psi(\sigma_1\boldsymbol{r}_1, ..., \sigma_N\boldsymbol{r}_N) = E(N)\Psi(\sigma_1\boldsymbol{r}_1, ..., \sigma_N\boldsymbol{r}_N), \tag{3.11}$$

where Ψ has the meaning of a many-body wave function that describes the ground state of the system with N particles with spins σ. Then, the density of particles $\rho_\sigma(\boldsymbol{r})$

can be defined with regard to this wave function as follows:

$$\rho_\sigma(\boldsymbol{r}) = N_\sigma \sum_{\sigma_2,...,\sigma_N} \int d^3\boldsymbol{r}_2 ... d^3\boldsymbol{r}_N \, |\Psi(\sigma\boldsymbol{r}, \sigma_2\boldsymbol{r}_2, ..., \sigma_N\boldsymbol{r}_N)|^2. \tag{3.12}$$

In addition, the total density of particles is then equal to the sum of spin-up and spin-down number of particles $\rho(\boldsymbol{r}) = \rho_\uparrow(\boldsymbol{r}) + \rho_\downarrow(\boldsymbol{r})$.

Starting from the information presented above, one can define some important mappings between certain quantities:

- first of all, as external potential is known, it can be shown that V_{ext} can be mapped to state $|\Psi[V_{\text{ext}}]\rangle$ (which is the first Hohenberg-Kohn theorem),
- then, according to Eq. 3.12, a connection between $\Psi[V_{\text{ext}}]\rangle$ and density $\rho[\Psi]$ can be derived (second Hohenberg-Kohn theorem).

One can summarize these properties in the form of the following relation:

$$V_{\text{ext}} \overset{A}{\leftrightarrow} |\Psi[V_{\text{ext}}]\rangle \overset{B}{\leftrightarrow} \rho[\Psi]. \tag{3.13}$$

The crucial feature of the mappings above is their invertibility. In order to show this property in case of mapping labeled as A, one should consider two different external potentials – V_{ext_1} and V_{ext_2} – that are applied to the system and differ more than by some constant C (so $V_{\text{ext}_1} \neq V_{\text{ext}_2} + C$). These potentials refer to different ground states described with many-body wave functions $|\Psi_1\rangle$ and $|\Psi_2\rangle$. With each of these states one can associate the following Schrödinger equation:

$$\begin{aligned} H_1\Psi_1(\sigma_1\boldsymbol{r}_1, ..., \sigma_N\boldsymbol{r}_N) &= (T + V_{\text{ext}_1} + V_{\text{interaction}})\Psi_1(\sigma_1\boldsymbol{r}_1, ..., \sigma_N\boldsymbol{r}_N) \\ &= E_{\text{gs}_1}(N)\Psi_1(\sigma_1\boldsymbol{r}_1, ..., \sigma_N\boldsymbol{r}_N), \end{aligned} \tag{3.14}$$

$$\begin{aligned} H_2\Psi_2(\sigma_1\boldsymbol{r}_1, ..., \sigma_N\boldsymbol{r}_N) &= (T + V_{\text{ext}_2} + V_{\text{interaction}})\Psi_2(\sigma_1\boldsymbol{r}_1, ..., \sigma_N\boldsymbol{r}_N) \\ &= E_{\text{gs}_2}(N)\Psi_2(\sigma_1\boldsymbol{r}_1, ..., \sigma_N\boldsymbol{r}_N). \end{aligned} \tag{3.15}$$

Then, if the equality $|\Psi_1\rangle = |\Psi_2\rangle$ is assumed, one can subtract Eq. 3.14 and Eq. 3.15:

$$(V_{\text{ext}_1} - V_{\text{ext}_2})\Psi_1(\sigma_1\boldsymbol{r}_1, ..., \sigma_N\boldsymbol{r}_N) = (E_{\text{gs}_1}(N) - E_{\text{gs}_2}(N))\Psi_1(\sigma_1\boldsymbol{r}_1, ..., \sigma_N\boldsymbol{r}_N). \tag{3.16}$$

In the next step, one should consider that the action of a potential operator on a certain function results in multiplication of this function (which in this case is the wave function) according to the scheme:

$$(V_{\text{ext}_1} - V_{\text{ext}_2})\Psi_1(\sigma_1\boldsymbol{r}_1, ..., \sigma_N\boldsymbol{r}_N) = \sum_{i=1}^{N}(V_{\text{ext}_1}(\boldsymbol{r}_i) - V_{\text{ext}_2}(\boldsymbol{r}_i))\Psi_1(\sigma_1\boldsymbol{r}_1, ..., \sigma_N\boldsymbol{r}_N). \quad (3.17)$$

Combining Eq. 3.16 and Eq. 3.17, the following relation can be obtained:

$$\sum_{i=1}^{N}(V_{\text{ext}_1}(\boldsymbol{r}_i) - V_{\text{ext}_2}(\boldsymbol{r}_i)) = (E_{\text{gs}_1}(N) - E_{\text{gs}_2}(N)), \quad (3.18)$$

which stands in contrary to the assumption that V_{ext_1} and V_{ext_2} differ more just by a constant. As a consequence, the mapping A from Eq. 3.13 has to be invertible – from V_{ext} one can obtain $|\Psi\rangle$ and vice versa.

Later on, the mapping B of the wave function into the density can also be shown. Again, the many-body system with two external potentials – V_{ext_1} and V_{ext_2} – is considered. Then, according to Eq. 3.11, it can be shown that ground state energies of the system (here denoted as E_{gs_1} and E_{gs_2}, respectively) fulfill the following relations:

$$E_{\text{gs}_1} = \langle\Psi_1|H_1|\Psi_1\rangle < \langle\Psi_2|H_1|\Psi_2\rangle, \quad (3.19)$$

$$E_{\text{gs}_2} = \langle\Psi_2|H_2|\Psi_2\rangle < \langle\Psi_1|H_2|\Psi_1\rangle. \quad (3.20)$$

Then, one should note that the Hamiltonian consists of the kinetic part and terms related to the external and interaction potentials. Therefore, the expression $\langle\Psi_2|H_1|\Psi_2\rangle$ can be written as:

$$\begin{aligned}\langle\Psi_2|H_1|\Psi_2\rangle &= \langle\Psi_2|T + V_{\text{ext}_1} + V_{\text{interaction}}|\Psi_2\rangle \\ &= \langle\Psi_2|T + V_{\text{ext}_2} + V_{\text{ext}_1} - V_{\text{ext}_2} + V_{\text{interaction}}|\Psi_2\rangle,\end{aligned} \quad (3.21)$$

where, in addition, the external potential term was added and subtracted. After that, it can be seen that in Eq. 3.21 the formula for H_2 is hidden:

$$\langle\Psi_2|H_2 - V_{\text{ext}_2} + V_{\text{ext}_1}|\Psi_2\rangle = \langle\Psi_2|H_2|\Psi_2\rangle + \langle\Psi_2|V_{\text{ext}_1} - V_{\text{ext}_2}|\Psi_2\rangle. \quad (3.22)$$

In Eq. 3.22, the part $\langle\Psi_2|H_2|\Psi_2\rangle$ corresponds to the ground state energy connected with V_{ext_2} and the second term can be rewritten:

$$\begin{aligned}\langle\Psi_2|H_2|\Psi_2\rangle + \langle\Psi_2|V_{\text{ext}_1} - V_{\text{ext}_2}|\Psi_2\rangle = E_{\text{gs}_2}(N) + \\ + \sum_{\sigma_1,...,\sigma_N=\{\uparrow,\downarrow\}} \int d^3\boldsymbol{r}_1 ... d^3\boldsymbol{r}_N \sum_{i=1}^{N} (V_{\text{ext}_1}(\boldsymbol{r}_i) - V_{\text{ext}_2}(\boldsymbol{r}_i))|\Psi_2(\sigma_1\boldsymbol{r}_1, ..., \sigma_N\boldsymbol{r}_N)|^2.\end{aligned} \tag{3.23}$$

Then, it should also be considered that:

- wave function $\Psi_2(\sigma_1\boldsymbol{r}_1, ..., \sigma_N\boldsymbol{r}_N)$ is connected with density $\rho_2(\boldsymbol{r})$,
- in the case of fermionic systems, the wave function is expected to be antisymmetric.

After that, the last term in Eq. 3.23 is equal $\int d^3\boldsymbol{r}\,(V_{\text{ext}_1} - V_{\text{ext}_2})\rho_2(\boldsymbol{r})$. With regard to Eq. 3.21, one can write that:

$$\langle\Psi_2|H_1|\Psi_2\rangle = E_{\text{gs}_2}(N) + \int d^3\boldsymbol{r}\,(V_{\text{ext}_1} - V_{\text{ext}_2})\rho_2(\boldsymbol{r}). \tag{3.24}$$

Substituting Eq. 3.19 into Eq. 3.24, the following relation can be obtained:

$$E_{\text{gs}_1}(N) < E_{\text{gs}_2}(N) + \int d^3\boldsymbol{r}\,(V_{\text{ext}_1} - V_{\text{ext}_2})\rho_2(\boldsymbol{r}). \tag{3.25}$$

In the same way, one can derive the analogous dependence for E_{gs_2}:

$$E_{\text{gs}_2}(N) < E_{\text{gs}_1}(N) + \int d^3\boldsymbol{r}\,(V_{\text{ext}_2} - V_{\text{ext}_1})\rho_1(\boldsymbol{r}). \tag{3.26}$$

In addition to this analysis, one can also make another assumption – the wave functions $|\Psi_1\rangle$ and $|\Psi_2\rangle$ are supposed to generate the same density (so $\rho_1(\boldsymbol{r}) = \rho_2(\boldsymbol{r})$). Then, the subtraction of Eq. 3.25 and Eq. 3.26 leads to the following conclusion about ground state energies:

$$E_{\text{gs}_1}(N) - E_{\text{gs}_2}(N) < E_{\text{gs}_2}(N) - E_{\text{gs}_1}(N). \tag{3.27}$$

One can clearly see that Eq. 3.27 leads to a contradiction – as a consequence, the densities have to be different ($\rho_1(\boldsymbol{r}) \neq \rho_2(\boldsymbol{r})$). Moreover, wave function maps to the density, so mapping B also turns out to be invertible (in other words, from wave function one

can obtain density and vice versa). Therefore, the ground state energy can be considered as a functional of density:

$$\langle \Psi[\rho]|H|\Psi[\rho]\rangle = E[\rho]. \tag{3.28}$$

As a consequence of the derivation presented above, the density of particles provides all the information about the ground state of the system. Therefore, all observables can be expressed in terms of density. In other words, the formula from Eq. 3.28 can be applied to any of the observables O (not only to energy):

$$\langle \Psi[\rho]|O|\Psi[\rho]\rangle = O[\rho]. \tag{3.29}$$

Another conclusion derived from the Hohenberg-Kohn approach is the connection between the external potential and density, as both mappings from Eq. 3.13 are invertible. As a consequence, at some fixed external potential, the energy functional $E[\rho]$ reaches a minimum for a density equal to the ground state density ρ_{gs} (and, simultaneously, this minimal energy is the ground state energy of the system). Technically, the process of minimization requires the calculation of the functional derivative of E over ρ, which approaches 0 for minimal energy:

$$\frac{\delta E}{\delta \rho} = 0. \tag{3.30}$$

As mentioned at the beginning of this section, the process of minimization described with Eq. 3.30 leads to equations that can be efficiently solved. What is also important is that the exact form of the external potential does not influence the invertibility of mappings. Therefore, the functional is characteristic for a certain system and can be written in the form $F[\rho]$ that defines the whole system:

$$F[\rho] = E_{V_{\text{ext}}}[\rho] - \int d^3\boldsymbol{r}\, V_{\text{ext}}(\boldsymbol{r})\rho(\boldsymbol{r}) = \langle \Psi[\rho]|(T + V_{\text{interaction}})|\Psi[\rho]\rangle. \tag{3.31}$$

In Eq. 3.31, the term $E_{V_{\text{ext}}}[\rho]$ denotes the total energy of the system, including also the contribution from external potential. Then, subtracting this external part from the total energy brings the functional to its so-called universal form.

3.2.2 Kohn-Sham Formalism

Although the Hohenberg-Kohn method enables a significant simplification of the description of many-body quantum systems, constructing the energy density functional remains a challenge. In general, one can distinguish various classes of energy density functionals $\mathcal{E}[\rho]$; the crucial difference between these classes lies in the way in which density is parametrized (e.g., by orbitals).

In case of normal systems, the most fundamental class is based on Local Density Approximation (LDA) [110, 104], where energy density functional $\mathcal{E}[\rho]$ depends only on normal density $\rho(\boldsymbol{r})$ [110, 104]. Therefore, the energy functional $E[\rho]$ can be expressed through the integral of energy density functional [108, 104]:

$$E[\rho] = \int \mathcal{E}[\rho(\boldsymbol{r})] d\boldsymbol{r}. \tag{3.32}$$

Then, the ground state energy of a system can be obtained through minimization of the energy functional with a constraint on the number of particles defined as [104]:

$$N = \int d^3\boldsymbol{r}\, \rho(\boldsymbol{r}). \tag{3.33}$$

In other words, it is expected to be fixed throughout the entire minimization process, which yields a single algebraic equation.

Additionally, one can also consider a class called Generalized Gradient Approximation (GGA) [104]. In this case, $\mathcal{E}[\rho]$ depends on normal density $\rho(\boldsymbol{r})$ and it's gradient $\nabla\rho(\boldsymbol{r})$, which leads to the following form of energy functional [104]:

$$E[\rho] = \int \mathcal{E}[\rho(\boldsymbol{r}), \nabla\rho(\boldsymbol{r})] d\boldsymbol{r}. \tag{3.34}$$

Once the energy functional is constructed, it is minimized with respect to density according to Eq. 3.30. In this case, the resulting equation is a differential equation due to the presence of the density gradients.

The energy functionals mentioned above are still not precise enough for describing experimental data in fields such as quantum chemistry [104]. This problem can be

overcome with regard to Kohn-Sham formalism (also known as the Meta-GGA approach), in which so-called orbital-dependent functionals are used [104, 102]. According to [104], many Meta-GGA functionals have been constructed through fitting to, e.g., chemical data and with regard to empirical parameters; therefore, they provide a significantly more detailed description than the methods based on standard functionals. In addition, this method leads to equations that are formally equivalent to Hartree-Fock equations [111]; therefore, well-developed computational methods of solving Hartree-Fock equations can be applied. Despite the fact that the Kohn-Sham method is used in the description of systems in the normal state, one can also extend this formalism to superfluid systems, which is discussed in Sec . 3.3.1.

In the discussion of Kohn-Sham methods, one can at first take a closer look at the construction of the energy functional. In general, in Kohn-Sham formalism, it depends on the normal density $\rho(\boldsymbol{r})$ and kinetic density $\tau(\boldsymbol{r})$, and can also depend on the gradients of normal density [104, 102]. However, this dependence is not explicit, as the densities are defined with regard to wave functions $\phi_n(\boldsymbol{r})$ [104], each of them corresponding to n-th orbital (called Kohn-Sham orbital) occupied (due to Pauli principle) by only one particle. In addition, these wave functions are expected to be orthonormal, so for the consecutive functions $\phi_i(\boldsymbol{r})$ the following condition should be fulfilled: $\int d^3\boldsymbol{r}\, \phi_i^*(\boldsymbol{r})\phi_j(\boldsymbol{r}) = \delta_{ij}$ [103]. However, one should note that these wave functions are only auxiliary functions without particular physical meaning (as is the case, e.g., in MFA methods) [104]. Here, they are only used to parametrize densities. According to that, normal density can be written as [104, 102]:

$$\rho(\boldsymbol{r}) = \sum_n |\phi_n(\boldsymbol{r})|^2,\ n = 1, 2, ..., N \tag{3.35}$$

with N being the number of particles. Kinetic density can then be defined as the sum of the derivatives of $\phi_n(\boldsymbol{r})$ [104, 102]:

$$\tau(\boldsymbol{r}) = \sum_n |\nabla\phi_n(\boldsymbol{r})|^2. \tag{3.36}$$

Finally, the energy functional for Meta-GGA takes the generic form [104, 102]:

$$E[\rho] = \int \mathcal{E}[\rho(\boldsymbol{r}), \nabla\rho(\boldsymbol{r}), \tau(\boldsymbol{r})]d\boldsymbol{r}. \tag{3.37}$$

As can be seen, the energy functional used in the Kohn-Sham method depends only implicitly on the density ρ. In addition, one can also show that kinetic density is in fact functional of normal density (so $\tau = \tau[\rho]$), which fulfills the requirement of the Hohenberg-Kohn theorem.

The discussion below concerning Kohn-Sham method is based on [102, 103, 111, 104, 75]. The main idea behind this formalism is to simplify the description of the system of interacting particles by replacing it with a non-interacting one, under the condition that its ground state density is the same as for the initial (interacting) system. Therefore, two systems are considered:

- The first one is the system of interacting particles in an external potential, denoted as $V_{\text{int}}^{\text{ext}}$. This system is characterized by a certain ground state density $\rho_{\text{gs}}(\boldsymbol{r})$.
- Another one is non-interacting system within external potential $V_{\text{non}-\text{int}}^{\text{ext}}$. The fundamental assumption is that it's ground state density $\rho_{\text{non}-\text{int}}(\boldsymbol{r})$ is equal $\rho_{\text{gs}}(\boldsymbol{r})$.

For a non-interacting system, one can write the Hamiltonian (denoted as $H_{\text{non}-\text{int}}$) as a sum of kinetic ($T$) and external potential ($V_{\text{non}-\text{int}}^{\text{ext}}$) terms:

$$H_{\text{non}-\text{int}} = T + V_{\text{non}-\text{int}}^{\text{ext}}. \tag{3.38}$$

As a consequence, the energy functional for the non-interacting case (marked as $E_{\text{non}-\text{int}}$) takes the general form:

$$E_{\text{non}-\text{int}}[\rho] = \langle \Psi[\rho] | (T + V_{\text{non}-\text{int}}^{\text{ext}}) | \Psi[\rho] \rangle. \tag{3.39}$$

In other words, the energy functional $E_{\text{non}-\text{int}}[\rho_{\text{non}-\text{int}}]$ describes the non-interacting system in external potential $V_{\text{non}-\text{int}}^{\text{ext}}$ with regard to many body wave function $\Psi[\rho_{\text{non}-\text{int}}]$.

Later, one should consider the variation of the energy functional with respect to density. In case of the interacting system (for which the energy functional is denoted as $E_{\text{int}}[\rho]$), this variation leads to the following relation:

$$\frac{\delta E_{\text{int}}[\rho]}{\delta \rho} = \frac{\delta T}{\delta \rho} + V_{\text{int}}^{\text{ext}}(\boldsymbol{r}) + \frac{\delta E_{\text{interaction}}}{\delta \rho}, \tag{3.40}$$

with $E_{\text{interaction}}$ describing the part of the energy functional connected with two-body interaction. For a non-interacting system, the variation of the energy functional takes

the form:

$$\frac{\delta E_{\text{non-int}}[\rho]}{\delta \rho} = \frac{\delta T}{\delta \rho} + V^{\text{ext}}_{\text{non-int}}(\boldsymbol{r}). \tag{3.41}$$

Based on the Hohenberg-Kohn theorem, it can be seen that finding $V^{\text{ext}}_{\text{non-int}}$ allows one to obtain $\rho_{\text{non-int}}(\boldsymbol{r})$ equivalent to $\rho_{\text{gs}}(\boldsymbol{r})$. According to Eq. 3.40 and Eq. 3.41, one can define this potential as:

$$V^{\text{ext}}_{\text{non-int}} = V^{\text{ext}}_{\text{int}}(\boldsymbol{r}) + \frac{\delta E_{\text{interaction}}}{\delta \rho}. \tag{3.42}$$

In the part $\delta E_{\text{interaction}}/\delta\rho$ one can distinguish two important terms:

- Hartree term:
$$V_H(\boldsymbol{r}) = \int d^3\boldsymbol{r}\; V_{\text{interaction}}(\boldsymbol{r}, \boldsymbol{r}')\rho(\boldsymbol{r}'), \tag{3.43}$$
- correlation term (together with Fock exchange term): $\delta E_{\text{corr}}[\rho]/\delta\rho$, where $E_{\text{corr}}[\rho]$ is the part of the energy functional connected with correlations.

Finally, one can write the expression for $V^{\text{ext}}_{\text{non-int}}$, which will be called the Kohn-Sham potential later on, and denoted as V_{KS}, as follows:

$$V_{\text{KS}} \equiv V^{\text{ext}}_{\text{int}}(\boldsymbol{r}) + \int d^3\boldsymbol{r}\; V_{\text{interaction}}(\boldsymbol{r}, \boldsymbol{r}')\rho(\boldsymbol{r}') + \frac{\delta E_{\text{corr}}[\rho]}{\delta \rho}. \tag{3.44}$$

By construction, the non-interacting systems placed in such a potential attain the same ground state density as the interacting system. While in the case of electronic systems, it is convenient to split this potential into Hartree and exchange terms, as shown above, in general, it can be written in compact form (without distinguishing between Hartree and exchange terms):

$$V_{\text{KS}} = \frac{\delta E[\rho]}{\delta \rho}. \tag{3.45}$$

This potential is the potential for non-interacting systems, which, however, generates the same ground state density as for the interacting system. Once it is obtained, one can apply it in the minimization procedure; one can also recall that in this method, densities are parametrized by wave functions. Therefore, the minimization of the energy functional (which, for a moment, we assume is known) is performed over ϕ_n:

$$\frac{\delta E}{\delta \phi_n} = 0. \tag{3.46}$$

In detail, the minimization procedure is carried out using the Lagrange multiplier method. With regard to it, one should at first construct the following equation:

$$\Omega = E - \sum_{i,j} \kappa_{ij} \left(\langle \phi_i | \phi_j \rangle - \delta_{ij} \right), \tag{3.47}$$

where κ is the Lagrange multiplier. The constraint for this procedure assumes the orthogonality of wave functions ϕ_i and ϕ_j. Then, the variational derivative of Ω over ϕ_n or ϕ_n^* should be considered. As an example, the relation:

$$\frac{\delta \Omega}{\delta \phi_n^*} = 0 \tag{3.48}$$

leads to the following formula:

$$\frac{\delta \Omega}{\delta \phi_n^*} = \frac{\delta E}{\delta \phi_n^*} - \sum_j \kappa_{nj} \phi_j = 0. \tag{3.49}$$

In Eq. 3.49, $\delta E / \delta \phi_i$ corresponds to $h\phi_n$ with $h = -\frac{\hbar^2 \nabla^2}{2m} + V_{\mathrm{KS}}$ being the single particle Hamiltonian with Kohn-Sham potential included. Later on, one should introduce the unitary transformation matrix U:

$$U \kappa_{nj} U^\dagger = \varepsilon_n \delta_{nj}, \tag{3.50}$$

which transforms κ_{nj} to the diagonal form. The variable ε_n means the single-particle eigenenergy. Once U is applied to the equation resulting from Eq. 3.49:

$$h\phi_n = \sum_j \kappa_{nj} \phi_j, \tag{3.51}$$

one can get the following equation:

$$U \, h \, U^\dagger \varphi_n = \sum_j \varepsilon_n \delta_{nj} \varphi_j \tag{3.52}$$

with φ_j being wave functions corresponding to particular eigenenergies ε_n. Finally, Eq. 3.52 leads to the Kohn-Sham equations for a system of non-interacting particles:

$$\Big(-\frac{\hbar^2}{2m} \nabla^2 + V_{\mathrm{KS}}(\boldsymbol{r}) \Big) \phi_n(\boldsymbol{r}) = \varepsilon_n \phi_n(\boldsymbol{r}), \tag{3.53}$$

where ε_n means eigenfunction corresponding to certain wave function ϕ_n. By solving these equations and combining with Eq. 3.35 and Eq. 3.36, one can obtain the ground state densities, and next evaluate the ground state energy Eq. 3.37. What is especially important is that Eq. 3.53 is formally equivalent to the HF equations and therefore can be solved using techniques developed for problems described within the Hartree-Fock approach.

In addition, density of particles $\rho(\boldsymbol{r})$ from Eq. 3.35 can be redefined according to the following correction:

$$\rho(\boldsymbol{r}) = \sum_n \theta(\mu - \varepsilon_n)|\phi_n(\boldsymbol{r})|^2. \tag{3.54}$$

In Eq. 3.54, θ is the Heaviside function, which in this case favors the particles with energies below a certain cutoff energy (corresponding to a particular chemical potential μ). Additionally, replacing the step function with the Fermi-Dirac distribution extends this formalism to finite temperatures.

To summarize, Kohn-Sham method maps an interacting system into a system of non-interacting particles in V_{KS} potential. In the case of many-body interacting systems, instead of solving the Schrödinger equation explicitly, one can postulate the energy functional and minimize it over the density or wave functions associated with a particular orbital. This process leads to equations analogous to HF equations (where, in order to consider the interaction between particles, the Kohn-Sham potential should be included). Once they are solved, one can obtain the ground state density from which all the information about the system can be extracted.

3.3 Density Functional Theory for Superfluid Systems

As mentioned before, the DFT method can be applied in various fields of science, including superfluid systems. However, in contrast to standard formulations, in such a case, the formalism must be extended to properly capture the superfluid effects. One of the reasons for which DFT cannot be used in nuclear systems in its fundamental form is the presence of strong interactions between particles (in other words, particles are expected to be self-bound) [5]. Therefore, the Hohenberg-Kohn theorem cannot be applied directly, as it requires the particles to be gathered by an external potential (not by an intrinsic type of interaction, as occurs in the nuclear case). Another difficulty

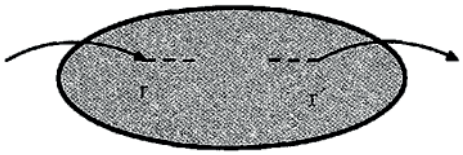

FIGURE 3.1: Schematic view of creation and annihilation of particles in the condensate [31].

is connected with symmetry breaking. As it has been pointed out in [5], in the standard DFT method, the symmetry-breaking solutions are not allowed in the Hohenberg-Kohn method (the energy can be minimized only by a density that allows the ground state to fulfill the symmetry condition). However, symmetry-breaking solutions are crucial in the case of superfluid systems, as they are obtained due to the presence of a pairing potential [5]. As a consequence, there was a need to accommodate the standard DFT formalism to the superfluid case.

Off-diagonal Long Range Order

At first, one can consider the effects arising from the interaction between particles. One of the crucial phenomena connected with such interaction is called off-diagonal long-range order (ODLRO) [31, 112, 113]. Firstly, this concept was introduced for bosons in [114] and further discussed in [115]. In case of such systems, one can start from the investigation of the one-body density matrix [31, 112, 113]:

$$\rho_1(\boldsymbol{r}-\boldsymbol{r}') = \langle \psi^\dagger(\boldsymbol{r})\psi(\boldsymbol{r}')\rangle, \tag{3.55}$$

where $\psi^\dagger(\boldsymbol{r})$ and $\psi(\boldsymbol{r}')$ are field operators. Physically, $\psi(\boldsymbol{r}')$ means that the particle is created at position $\boldsymbol{r}'$ out of the condensate (it is removed from it) and $\psi^\dagger(\boldsymbol{r})$ denotes the annihilation of particle at position $\boldsymbol{r}$ in the condensate (which means that the particle is absorbed into condensate) [31, 112]. This process is schematically shown in Fig. 3.1. It turns out that the presence of condensate gives a nonzero contribution to this density matrix, even if $|\boldsymbol{r}-\boldsymbol{r}'|$ approaches infinity:

$$\langle \psi^\dagger(\boldsymbol{r})\psi(\boldsymbol{r}')\rangle \xrightarrow{|\boldsymbol{r}-\boldsymbol{r}'|\to\infty} \neq 0, \tag{3.56}$$

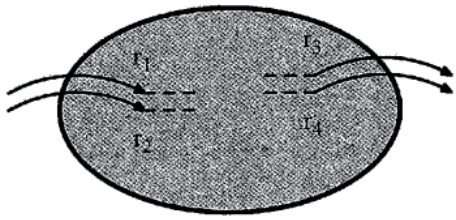

FIGURE 3.2: Schematic view of creation and annihilation of a fermionic pair in the condensate [31].

which is known as ODLRO [31, 112]. This effect appears in the condensate due to its coherence [31, 112]. Therefore, the presence of ODLRO is connected with the creation of BEC in the system and can be assumed as its characteristic property [31, 112]. Consequently, the behavior of ODLRO enables us to distinguish between the superfluid and normal phases.

Later, Yang [116] demonstrated that the phenomenon of ODLRO can also be observed in fermionic systems [113, 31]. As mentioned in [31], in such a case, ODLRO corresponds to the idea of a macroscopic wave function defined for Cooper pairs, which can create a condensate. Consequently, in fermionic systems, one can examine ODLRO for Cooper pairs. In contrast to bosons (for which one-body density matrix has been considered), here one can take a closer look at the density matrix for pairs [31]:

$$\rho_1(\boldsymbol{R}-\boldsymbol{R}') = \langle \varphi^\dagger(\boldsymbol{R})\varphi(\boldsymbol{R}')\rangle. \tag{3.57}$$

In Eq. 3.57, $\varphi(\boldsymbol{R}')$ anihilates the pair from position $\boldsymbol{R}'$ and $\varphi^\dagger(\boldsymbol{R})$ creates a pair at position $\boldsymbol{R}$. According to [31, 113, 116], the density matrix from Eq. 3.57 can be written in the form of a two-particle density matrix:

$$\rho_2(\boldsymbol{r}_1\sigma_1, \boldsymbol{r}_2\sigma_2, \boldsymbol{r}_3\sigma_3, \boldsymbol{r}_4\sigma_4) = \langle \psi^\dagger_{\sigma_1}(\boldsymbol{r}_1)\psi^\dagger_{\sigma_2}(\boldsymbol{r}_2)\psi_{\sigma_3}(\boldsymbol{r}_3)\psi_{\sigma_4}(\boldsymbol{r}_4)\rangle. \tag{3.58}$$

Here, the particle at position $\boldsymbol{r}_1$ is localized close to the particle at $\boldsymbol{r}_2$; in other words, they are assumed to create a pair, as well as particles at $\boldsymbol{r}_3$ and $\boldsymbol{r}_4$. According to Eq. 3.58, the pair $\boldsymbol{r}_1, \boldsymbol{r}_2$ is created in the condensate, while another pair $(\boldsymbol{r}_3, \boldsymbol{r}_4)$ is removed from it. This idea is illustrated in Fig. 3.2. As well as in the case of bosons, the behavior of the matrix Eq. 3.58 allows us to observe the difference between superfluid and normal

systems. In the superfluid state, this expression tends to take a nonzero value, as the distance between pairs $|\boldsymbol{R}-\boldsymbol{R}'|$ approaches infinity [31]:

$$\langle\varphi^{\dagger}(\boldsymbol{R})\varphi(\boldsymbol{R}')\rangle \xrightarrow{|\boldsymbol{R}-\boldsymbol{R}'|\to\infty} \neq 0. \tag{3.59}$$

On the contrary, in the case of normal systems, this expression would always be zero [31]. Based on this, it can be seen that in the case of superfluids, another type of density must be introduced to account for the finite value of ODLRO.

Oliveira-Gross-Kohn Theorem

The idea of introducing another type of density is the clue of the Oliveira-Gross-Kohn theorem [117, 118, 113]. According to this, a finite value of ODLRO would be associated with a nonzero value of this density, referred to as anomalous density. It can be defined as follows [117, 118]:

$$\nu_{\uparrow\downarrow}(\boldsymbol{r},\boldsymbol{r}') = \langle\psi_{\downarrow}(\boldsymbol{r}')\psi_{\uparrow}(\boldsymbol{r})\rangle. \tag{3.60}$$

The notation $\nu_{\uparrow\downarrow}$ corresponds to the fact that anomalous density is antisymmetric, so it couples only the states with opposite spins; therefore, $\nu_{\sigma\sigma'}(\boldsymbol{r},\boldsymbol{r}') = -\nu_{\sigma'\sigma}(\boldsymbol{r},\boldsymbol{r}')$ [119]. In Eq. 3.60, the variables $\boldsymbol{r}$ and $\boldsymbol{r}'$ denote the position of particles in a Cooper pair.

With regard to this new density, the limit of expression for one-body density matrix for Cooper pairs (Eq. 3.57) can be written in the following way [119]:

$$\lim_{|\boldsymbol{R}-\boldsymbol{R}'|\to\infty}\rho_1(\boldsymbol{R}-\boldsymbol{R}') = \nu^{*}_{\uparrow\downarrow}(\boldsymbol{R})\nu_{\uparrow\downarrow}(\boldsymbol{R}'). \tag{3.61}$$

The presence of additional density arising from the superfluid properties of the system leads to significant modification in the part of the energy functional connected with the external potential. In addition to the potential coupling to normal density, one should also include another part connected with potential coupling to anomalous density [117, 118]. Then, the part of the energy functional corresponding to this new contribution to external pairing potential can be written in the general form as $E[\nu]$ [117, 118]:

$$E[\nu] = -\frac{1}{2}\sum_{\sigma,\sigma'=\{\uparrow,\downarrow\}}\int d^3\boldsymbol{r}\int d^3\boldsymbol{r}'\left(\Delta^{\mathrm{ext}*}_{\sigma\sigma'}(\boldsymbol{r},\boldsymbol{r}')\nu_{\sigma\sigma'}(\boldsymbol{r},\boldsymbol{r}') + \Delta^{\mathrm{ext}}_{\sigma\sigma'}(\boldsymbol{r},\boldsymbol{r}')\nu^{*}_{\sigma\sigma'}(\boldsymbol{r},\boldsymbol{r}')\right), \tag{3.62}$$

where $\Delta^{\text{ext}}_{\sigma\sigma'}(\boldsymbol{r}, \boldsymbol{r}')$ means the external pairing potential coupling to anomalous density. At this point, one should consider the antisymmetric properties of anomalous density, which lead to the antisymmetry of the pairing potential. As a consequence, its symmetric part cancels out and does not contribute to the expression from Eq. 3.62.

Hohenberg-Kohn and Kohn-Sham Methods for Superfluids

The discussion in this section is based on [117, 118, 119].

As well as normal systems, superfluids can also be analyzed with regard to Hohenberg-Kohn and Kohn-Sham theorems. In the case of the Hohenberg-Kohn method, it can be shown that the normal density ρ and the anomalous density ν map to the external potential coupling to ρ (which is denoted as V) and to the one connected with ν (which is Δ), respectively. Then, the energy functional would change its form; for superfluids, it would be the functional of two densities, ρ and ν. As a consequence, minimization of the energy functional E has to be done over normal and anomalous density separately, which leads to the following equations:

$$\frac{\delta E}{\delta \rho} = 0. \tag{3.63}$$

$$\frac{\delta E}{\delta \nu} = 0. \tag{3.64}$$

Analogously to the normal state, these relations allow us to obtain ground state normal density ρ_{gs} and anomalous density ν_{gs}. Based on that, one can also define the universal functional dependent on both of these densities:

$$F[\rho, \nu] = E_{V,\Delta}[\rho, \nu] - E_V[\rho] - E_\Delta[\nu] = \langle \Psi[\rho, \nu] | (T + V_{\text{interaction}}) | \Psi[\rho, \nu] \rangle, \tag{3.65}$$

where $E_{V,\Delta}[\rho, \nu]$ means the total energy of the system in the field of two external potentials connected with normal and anomalous density. The component $E_V[\rho]$ denotes the part of the energy functional connected with the external potential, and $E_\Delta[\nu]$ with the external pairing.

The Kohn-Sham method for superfluids maps an interacting system into a non-interacting one in potentials V^{ext} and Δ^{ext}. As in the normal case, this approach also allows us to replace the potentials of an interacting system with the corresponding quantities of

a non-interacting one, thereby obtaining the ground state densities. Per analogy to Eq. 3.38, the Hamiltonian of a non-interacting superfluid system (denoted as $H_{\text{non-int}}$) can be written as:

$$\begin{aligned} H_{\text{non-int}} = &\sum_{\sigma=\{\uparrow,\downarrow\}} \int d^3\boldsymbol{r}\, \psi^\dagger_\sigma(\boldsymbol{r}) \Big[-\frac{\hbar^2}{2m}\nabla^2 + V^{\text{ext}}_{\text{non-int},\,\sigma}(\boldsymbol{r}) - \mu_\sigma \Big] \psi_\sigma(\boldsymbol{r}) + \\ &+ \sum_{\sigma,\sigma'=\{\uparrow\downarrow\}} \int d^3\boldsymbol{r} \int d^3\boldsymbol{r}' \Big(\Delta^{\text{ext}}_{\text{non-int},\,\sigma\sigma'}(\boldsymbol{r},\boldsymbol{r}') \psi^\dagger_\sigma(\boldsymbol{r}) \psi^\dagger_{\sigma'}(\boldsymbol{r}') + \\ &+ \Delta^{\text{ext}*}_{\text{non-int},\,\sigma\sigma'}(\boldsymbol{r},\boldsymbol{r}') \psi_\sigma(\boldsymbol{r}) \psi_{\sigma'}(\boldsymbol{r}') \Big). \end{aligned} \tag{3.66}$$

In Eq. 3.66 one can distinguish kinetic term $(-(\hbar^2\nabla^2)/2m)$ and the part connected with external potential coupling to normal density (here, it is $V^{\text{ext}}_{\text{non-int},\,\sigma}(\boldsymbol{r}) - \mu_\sigma$ with the chemical potential explicitly included. Additionally, the second line of Eq. 3.66 describes the part of the Hamiltonian connected with the external potential for anomalous density. As it can be seen, it has been separated to two parts: $\Delta^{\text{ext}}_{\text{non-int},\,\sigma\sigma'}(\boldsymbol{r},\boldsymbol{r}')$ and $\Delta^{\text{ext}*}_{\text{non-int},\,\sigma\sigma'}(\boldsymbol{r},\boldsymbol{r}')$, as Δ is complex quantity.

On the other hand, one can also write the Hamiltonian for an interacting superfluid system. Here, Hamiltonian is denoted as H_{int} and external potential as $V^{\text{ext}}_{\text{int},\,\sigma}(\boldsymbol{r})$. In addition, there is also the term $V^{\text{interaction}}_{\sigma\sigma'}(\boldsymbol{r},\boldsymbol{r}')$ connected with the interaction potential:

$$\begin{aligned} H_{\text{int}} = &\sum_{\sigma=\{\uparrow,\downarrow\}} \int d^3\boldsymbol{r}\, \psi^\dagger_\sigma(\boldsymbol{r}) \Big[-\frac{\hbar^2}{2m}\nabla^2 + V^{\text{ext}}_{\text{int},\,\sigma}(\boldsymbol{r}) - \mu_\sigma \Big] \psi_\sigma(\boldsymbol{r}) + \\ &+ \sum_{\sigma,\sigma'=\{\uparrow\downarrow\}} \int d^3\boldsymbol{r} \int d^3\boldsymbol{r}' \Big(\Delta^{\text{ext}}_{\text{int},\,\sigma\sigma'}(\boldsymbol{r},\boldsymbol{r}') \psi^\dagger_\sigma(\boldsymbol{r}) \psi^\dagger_{\sigma'}(\boldsymbol{r}') + \\ &+ \Delta^{\text{ext}*}_{\text{int},\,\sigma\sigma'}(\boldsymbol{r},\boldsymbol{r}') \psi_\sigma(\boldsymbol{r}) \psi_{\sigma'}(\boldsymbol{r}') \Big) + \\ &+ \frac{1}{2} \sum_{\sigma,\sigma'=\{\uparrow,\downarrow\}} \int d^3\boldsymbol{r} \int d^3\boldsymbol{r}'\, \psi^\dagger_\sigma(\boldsymbol{r}) \psi^\dagger_{\sigma'}(\boldsymbol{r}')\, V^{\text{interaction}}_{\sigma\sigma'}(\boldsymbol{r},\boldsymbol{r}')\, \psi_{\sigma'}(\boldsymbol{r}') \psi_\sigma(\boldsymbol{r}). \end{aligned} \tag{3.67}$$

As the Hamiltonians for interacting and non-interacting systems are defined, one can extract the Kohn-Sham potentials. What is important is that, in the superfluid case, there would be two of them, corresponding to different densities. Therefore, following

the standard scheme, one can obtain the Kohn-Sham potential:

$$V^{\text{ext}}_{\text{non-int},\,\sigma}(\boldsymbol{r}) = V^{\text{ext}}_{\text{int},\,\sigma}(\boldsymbol{r}) + \sum_{\sigma'=\{\uparrow\downarrow\}} \int d^3\boldsymbol{r}'\, V^{\text{interaction}}_{\sigma\sigma'}(\boldsymbol{r},\boldsymbol{r}')\rho_{\sigma'}(\boldsymbol{r}') + \frac{\delta E_{\text{corr}}[\rho,\nu]}{\delta\rho} \tag{3.68}$$

as before, and by analogy:

$$\Delta^{\text{ext}}_{\text{non-int},\,\sigma\sigma'}(\boldsymbol{r},\boldsymbol{r}') = \Delta^{\text{ext}}_{\text{int},\,\sigma\sigma'}(\boldsymbol{r},\boldsymbol{r}') + V^{\text{interaction}}_{\sigma\sigma'}(\boldsymbol{r},\boldsymbol{r}')\nu_{\sigma\sigma'}(\boldsymbol{r},\boldsymbol{r}') + \frac{\delta E_{\text{corr}}[\rho,\nu]}{\delta\nu}. \tag{3.69}$$

Once these potentials are calculated, one can minimize the energy functional for a non-interacting system (which in this case can be written as $\langle\Psi[\rho,\nu]|H_{\text{non-int}}|\Psi[\rho,\nu]\rangle$) with regard to Eq. 3.63 and Eq. 3.64. As a result, densities equivalent to ground state densities of an interacting system are obtained. One can also note that the $\Delta^{\text{ext}}_{\text{non-int}}$, will be indicated as a Kohn-Sham paring potential Δ_{KS}, and its general definition is

$$\Delta_{\text{KS}} = -\frac{\delta E}{\delta\nu^*}. \tag{3.70}$$

3.3.1 Superfluid Local Density Approximation

Another issue that has to be considered in the case of superfluid systems is the construction of a proper energy functional. In general, it can be done with regard to Superfluid Local Density Approximation (SLDA), remaining in the spirit of the Kohn-Sham method for the normal state [120, 105]. Per analogy to the Meta-GGA approach, which overcomes the limitations of Hartree-Fock formalism, SLDA improves the HFB method and allows it to be applied to superfluid systems [105].

In the case of superfluids, the energy functional also includes anomalous density and current. Therefore, the energy functional takes the form [120, 105]:

$$E = \int \mathcal{E}[\rho_\sigma(\boldsymbol{r}), \tau_\sigma(\boldsymbol{r}), \boldsymbol{j}_\sigma(\boldsymbol{r}), \nu(\boldsymbol{r})]d\boldsymbol{r}. \tag{3.71}$$

As the superfluid system is a mixture of particles and holes, the densities from Eq. 3.71 are parametrized by wave functions of quasiparticles. In case of superfluids, one can distinguish the following densities [105, 121, 120]:

- normal density:

$$\rho_\sigma(\boldsymbol{r}) = \sum_{|E_n|<E_c} |v_{n\sigma}(\boldsymbol{r})|^2\, f_\beta(-E_n), \tag{3.72}$$

- kinetic density:

$$\tau_\sigma(\boldsymbol{r}) = \sum_{|E_n|<E_c} |\nabla v_{n\sigma}(\boldsymbol{r})|^2 \, f_\beta(-E_n). \tag{3.73}$$

  In momentum space, the right side of Eq. 3.73 can be written as $\sum_{\boldsymbol{k}} \boldsymbol{k}^2 |v_\sigma(\boldsymbol{k})|^2$, where $|v_\sigma(\boldsymbol{k})|^2$ corresponds occupation probabilities,

- current density:

$$\boldsymbol{j}_\sigma(\boldsymbol{r}) = \sum_{|E_n|<E_c} \mathrm{Im}\left[v_{n\sigma}(\boldsymbol{r}) \nabla v^*_{n\sigma}(\boldsymbol{r})\right] \, f_\beta(-E_n), \tag{3.74}$$

- anomalous density:

$$\nu(\boldsymbol{r}) = \sum_{|E_n|<E_c} \Big(u_{n\uparrow}(\boldsymbol{r}) v^*_{n\downarrow}(\boldsymbol{r}) - u_{n,\downarrow}(\boldsymbol{r}) v^*_{n\uparrow}(\boldsymbol{r}) \Big) \, f_\beta(-E_n). \tag{3.75}$$

  As mentioned earlier, anomalous density (related to Cooper pairs creation) has been introduced to describe the correlations between quasiparticles with opposite spin projections and momenta.

In the formulas above, the summation is done over n orthogonal orbitals (each of them can be occupied only by one quasiparticle); however, only orbitals with energies under the cutoff energy E_c are included [105]. The component f_β denotes the Fermi-Dirac distribution and is responsible for modeling the finite temperature effects [3]:

$$f_\beta(E) = \left[1 + \exp\left(\frac{E}{k_B T}\right)\right]^{-1}. \tag{3.76}$$

Later on, as well as in the standard Kohn-Sham procedure described in Sec. 3.2.2, one should minimize the energy functional over wave functions u and v (as the densities in Eq. 3.71 are expressed by these wave functions):

$$\frac{\delta E}{\delta v_{n\downarrow}} = 0, \tag{3.77}$$

$$\frac{\delta E}{\delta u_{n\uparrow}} = 0.$$

As a result, BdG equations from Eq. 3.10 can be obtained. Consequently, in the superfluid case, the expression for the single-particle Hamiltonian h includes variational

derivatives of the functional over certain types of density and takes the following form [121]:

$$h_\sigma = -\nabla \frac{\delta E}{\delta \tau_\sigma} \nabla + \frac{\delta E}{\delta \rho_\sigma} - \frac{i}{2} \left\{ \frac{\delta E}{\delta \boldsymbol{j}_\sigma}, \nabla \right\} \tag{3.78}$$

where $\{\cdot, \cdot\}$ has the meaning of anticomutator. Beside Kohn-Sham potential $\frac{\delta E}{\delta \rho_\sigma}$, one can note appearance of additional potentials $\frac{\delta E}{\delta \tau_\sigma}$ and $\frac{\delta E}{\delta \boldsymbol{j}_\sigma}$, which demonstrates that SLDA assumes even more complex forms of functionals, as compared to standard Kohn-Sham functional. Pairing potential is equivalent to Δ_{KS}.

3.3.2 Time-Dependent Density Functional Theory in Superfluid Systems

After certain modifications, DFT can also be applied to time-dependent problems. An extension of the standard DFT formalism into the time-dependent case is called the Runge-Gross theorem and considered an analog of the Hohenberg-Kohn theorem for static problems [102, 104]. The discussion below concerning the general statements of Runge-Gross theorem and time-dependent Kohn-Sham equations is based on [122, 104, 123, 118, 124, 119].

Runge-Gross Theorem

Taking a closer look at the Runge-Gross theorem, one should at first consider two external potentials dependent both on position and time: $V_{\mathrm{ext}}(\boldsymbol{r}, t)$ and $V_{\mathrm{ext}'}(\boldsymbol{r}, t)$ acting on a particular many-body system. Per analogy to static case, where these potentials were supposed to differ by more than a constant, here they are supposed to be different by more than some function of time: $V_{\mathrm{ext}'}(\boldsymbol{r}, t) \neq V_{\mathrm{ext}}(\boldsymbol{r}, t) + f(t)$. Based on that, one should consider the time evolution of densities $\rho(\boldsymbol{r}, t)$ and $\rho'(\boldsymbol{r}, t)$ from the initial state $|\Psi(t = 0)\rangle$ in these potentials. With regard to the Runge-Gross theorem, it turns out that – as well as in static systems – two different potentials cannot generate the same density. In other words, two potentials acting on the system require two different densities that generate (separately) each of them. Here, these potentials are denoted as $V_{\mathrm{ext}}(\boldsymbol{r}, t)$ and $V_{\mathrm{ext}'}(\boldsymbol{r}, t)$ with densities $\rho(\boldsymbol{r}, t)$ and $\rho'(\boldsymbol{r}, t)$ connected with each of them, respectively. Therefore, there is a mapping between potentials and densities

corresponding to them:

$$V_{\text{ext}}(\boldsymbol{r},t) + f(t) \leftrightarrow e^{-if(t)}|\Psi(\boldsymbol{r},t)\rangle \leftrightarrow \rho(\boldsymbol{r},t). \tag{3.79}$$

Additionally, this mapping is defined up to an unknown, time-dependent phase factor. However, when observables are computed, this phase factor cancels out due to the combination of the wave function and its complex conjugation that is used during such calculations. The Runge-Gross theorem proves the invertibility of the mapping between potentials and densities – then, for any observable O, one can construct the time-dependent functional of density:

$$O(t) = O[\rho, \Psi_0](t) = \langle \Psi[\rho, \psi_0](t)|O(t)|\Psi[\rho, \Psi_0]\rangle = O[\rho, \Psi_0](t). \tag{3.80}$$

In contrast to the static case, such a functional depends not only on density, but also on the wave function Ψ_0 describing the initial state (at the beginning of time evolution – in other words, $\Psi_0 = \Psi(t = 0)$. In addition, the continuity equation: $\partial\rho(\boldsymbol{r},t)/\partial t + \nabla \cdot \boldsymbol{j}(\boldsymbol{r},t) = 0$ is used when proving the Runge-Gross theorem (and has to be fulfilled).

3.3.3 Time-dependent Kohn-Sham Equations

Once the mapping between potential and density is defined, one can also derive the time-dependent version of the Kohn-Sham method. As previously mentioned, it is evident that one can define the potential for a non-interacting system, from which the density of an interacting system can be obtained. In the time-dependent description, the Kohn-Sham potential also acquires time dependence:

$$V_{\text{KS}}(\boldsymbol{r},t) = \frac{\delta E[\rho]}{\delta\rho}(\boldsymbol{r},t). \tag{3.81}$$

Also, the density is supposed to be time-dependent:

$$\rho(\boldsymbol{r},t) = \sum_n |\phi_n(\boldsymbol{r},t)|^2. \tag{3.82}$$

Then, one can write the time-dependent Kohn-Sham equation with regard to the Kohn-Sham potential (denoted as V_{KS} and equivalent to $V^{\text{ext}}_{\text{non-int}}$) in the following form:

$$\Big(-\frac{\hbar^2}{2m}\nabla^2 + V_{\text{KS}}(\boldsymbol{r},t)\Big)\varphi_n(\boldsymbol{r},t) = i\hbar\frac{\partial}{\partial t}\varphi_n(\boldsymbol{r},t). \tag{3.83}$$

As well as for static systems, the time-dependent Kohn-Sham formalism can also be extended to superfluid systems with regard to the idea of quasiparticles. In such a case, normal and anomalous densities can be expressed through time-dependent wave functions $u_n(\boldsymbol{r},t)$ and $v_n(\boldsymbol{r},t)$:

$$\rho_\sigma(\boldsymbol{r},t) = \sum_n |v_{n\sigma}(\boldsymbol{r},t)|^2, \tag{3.84}$$

$$\nu_{\sigma\sigma'}(\boldsymbol{r},\boldsymbol{r}',t) = \sum_n v^*_{n\sigma}(\boldsymbol{r},t)u_{n\sigma}(\boldsymbol{r}',t). \tag{3.85}$$

As in the superfluid case, two types of densities can be distinguished; one can also define two separate potentials coupling to each of them. The first of these potentials is the already mentioned Kohn-Sham potential (connected with normal density), and another one is the pairing potential coupling to anomalous density. One can write the time-dependent versions of these potentials (V^{KS} and Δ^{KS}, respectively) as follows:

$$V^{\mathrm{KS}}_\sigma(\boldsymbol{r},t) = V^{\mathrm{ext}}_{\mathrm{int},\,\sigma}(\boldsymbol{r},t) + \sum_{\sigma'=\uparrow\downarrow}\int d^3\boldsymbol{r}'\; V^{\mathrm{interaction}}_{\sigma\sigma'}(\boldsymbol{r},\boldsymbol{r}')\rho_{\sigma'}(\boldsymbol{r}',t) + \frac{\delta E_{\mathrm{corr}}[\rho,\nu,t]}{\delta\rho}, \tag{3.86}$$

$$\Delta^{\mathrm{KS}}_{\sigma\sigma'}(\boldsymbol{r},\boldsymbol{r}',t) = \Delta^{\mathrm{ext}}_{\mathrm{int},\,\sigma\sigma'}(\boldsymbol{r},\boldsymbol{r}',t) + V^{\mathrm{interaction}}_{\sigma\sigma'}(\boldsymbol{r},\boldsymbol{r}')\nu_{\sigma\sigma'}(\boldsymbol{r},\boldsymbol{r}',t) + \frac{\delta E_{\mathrm{corr}}[\rho,\nu,t]}{\delta\nu}. \tag{3.87}$$

Finally, the time-dependent version of the Kohn-Sham equations for superfluids can be written as:

$$\sum_{\sigma'=\{\uparrow\downarrow\}}\Big(h_{\sigma\sigma'}(\boldsymbol{r},t)u_{\sigma'}(\boldsymbol{r},t) + \int d^3\boldsymbol{r}'\Delta^{\mathrm{KS}}_{\sigma\sigma'}(\boldsymbol{r},\boldsymbol{r}',t)v_{n\sigma'}(\boldsymbol{r}',t)\Big) = i\hbar\frac{\partial}{\partial t}u_\sigma(\boldsymbol{r},t), \tag{3.88}$$

$$\sum_{\sigma'=\{\uparrow\downarrow\}}\Big(-h^*_{\sigma\sigma'}(\boldsymbol{r},t)v_{\sigma'}(\boldsymbol{r},t) + \int d^3\boldsymbol{r}'\Delta^{*\,\mathrm{KS}}_{\sigma\sigma'}(\boldsymbol{r},\boldsymbol{r}',t)u_{n\sigma'}(\boldsymbol{r}',t)\Big) = i\hbar\frac{\partial}{\partial t}v_\sigma(\boldsymbol{r},t). \tag{3.89}$$

Adiabatic Approximation

In Eqs. 3.88 - Eq. 3.89, the crucial simplification called adiabatic approximation has been applied. In general, the energy functional depends on both the initial state and the entire time evolution, which is known as the memory effect [102, 123, 124]. This, in turn, leads to the much more complex form of energy functional than in the static case [102]:

$$E(t) = \int_0^t dt' \int \mathcal{E}[\Psi_0,\rho(\boldsymbol{r},t'),...]d\boldsymbol{r}. \tag{3.90}$$

In Eq. 3.90, the integral over dt' is responsible for terms connected with time evolution. Although the memory effect is permitted within the Runge-Gross theorem [124], it is evident that time-dependent KS equations do not depend on memory terms. Therefore, one can apply these equations only when this effect is neglected; consequently, memory terms cannot be included in energy functionals as well.

To simplify the problem, one can apply the adiabatic approximation [102, 123, 124]. This theorem states that in the case of very slow evolution, the system is always close to the ground state [102, 123, 124]. Then, it can be described within the formalism used for the static case, which means that the energy functional used in static calculations can be applied to the dynamic case. Technically, once the dependence of the energy functional on Ψ_0 and memory effects is neglected, one can use the same functional in time-dependent calculations as in the static case. Due to these approximations, the functional from Eq. 3.90 reduces to the form used in static calculations.

In order to make a further simplification of Eqs. 3.88 - Eq. 3.89, an approach called Local Pairing Field Approximation (LPFA) can be applied. Then, one can write the time-dependent version of the HFB equations in the following form [106]:

$$\begin{pmatrix} h_{\uparrow\uparrow}(\boldsymbol{r},t) & h_{\uparrow\downarrow}(\boldsymbol{r},t) & 0 & \Delta(\boldsymbol{r},t) \\ h_{\downarrow\uparrow}(\boldsymbol{r},t) & h_{\downarrow\downarrow}(\boldsymbol{r},t) & -\Delta(\boldsymbol{r},t) & 0 \\ 0 & -\Delta^*(\boldsymbol{r},t) & -h^*_{\uparrow\uparrow}(\boldsymbol{r},t) & -h^*_{\uparrow\downarrow}(\boldsymbol{r},t) \\ \Delta^*(\boldsymbol{r},t) & 0 & -h^*_{\downarrow\uparrow}(\boldsymbol{r},t) & -h^*_{\downarrow\downarrow}(\boldsymbol{r},t) \end{pmatrix} \begin{pmatrix} u_{n\uparrow}(\boldsymbol{r},t) \\ u_{n\downarrow}(\boldsymbol{r},t) \\ v_{n\uparrow}(\boldsymbol{r},t) \\ v_{n\downarrow}(\boldsymbol{r},t) \end{pmatrix} = i\hbar\frac{\partial}{\partial t} \begin{pmatrix} u_{n\uparrow}(\boldsymbol{r},t) \\ u_{n\downarrow}(\boldsymbol{r},t) \\ v_{n\uparrow}(\boldsymbol{r},t) \\ v_{n\downarrow}(\boldsymbol{r},t) \end{pmatrix}, \tag{3.91}$$

In the case of this research, the chemical potential in Eq. 3.91 is already included in the single-particle Hamiltonian h. Later on, Eq. 3.91 can be simplified in the same way as in the static case, i.e., due to the lack of the spin-orbit term. As a result, the following form of time-dependent HFB equations can be obtained [105, 125, 126]:

$$\begin{pmatrix} h(\boldsymbol{r},t) & \Delta(\boldsymbol{r},t) \\ \Delta^*(\boldsymbol{r},t) & -h^*(\boldsymbol{r},t) \end{pmatrix} \begin{pmatrix} u_n(\boldsymbol{r},t) \\ v_n(\boldsymbol{r},t) \end{pmatrix} = i\hbar\frac{\partial}{\partial t} \begin{pmatrix} u_n(\boldsymbol{r},t) \\ v_n(\boldsymbol{r},t) \end{pmatrix}. \tag{3.92}$$

3.3.4 DFT in Nuclear Systems

The discussion presented above concerns the general case of superfluid systems, so for one type of superfluid component. However, one should point out that in the case of nuclear matter (being a proton-neutron mixture), all these equations can be obtained both for protons and neutrons [5]. Consequently, in such a case, one should consider separate potentials (including pairing fields) for protons and neutrons. In addition, the energy functional in the case of nuclear systems (which is the main focus of the following section) will depend on densities of protons and neutrons as well [5].

3.4 Energy Functionals

Despite the fact that fundamental theorems of DFT allow to obtain the ground state energy without solving Schrödinger equation, one of the significant difficulties still lies in the construction of the energy functional. Since it cannot be explicitly calculated, there is a need to postulate it in a form that depends on the particular system. In this section, the energy functional for the nuclear case is discussed.

In each energy functional, one can distinguish contributions from various types of energy (each of them being also a functional of certain density). In the most fundamental functionals (arising from the standard BdG theorem), only kinetic and pairing terms are included [5]. However, in the case of proton-neutron matter, one should also consider the complex interactions between nucleons and the Coulomb interaction as well [105, 5, 127]. The first attempt to include the contribution related to interaction in the functional was made by Brink and Boecker in [128]. Later on, another classes of functionals, such as Gogny and Skyrme, have been developed [127]. In the Skyrme method [129] (historically first introduced [62]), the functionals are assumed to be local [127], allowing for significantly increased efficiency in calculations. On the contrary, in the approach by Gogny [130, 131], the density dependence of interaction, together with the spin-orbit term, has been included. The interaction, which is considered a finite-range one [62], is recognized as the Gogny force [132]. It has been introduced due to the difficulties encountered in examining pairing interactions in nuclei within the Skyrme approach [62]. Nevertheless, due to the technical advantages, the Skyrme class has recently been one of the widely used in the investigation of nuclear systems [133].

3.4.1 Skyrme Functional

One of the crucial features of Skyrme functionals is the approximation of nuclear interaction by a zero-range potential $\delta(\boldsymbol{r}_{12})$ and its derivatives [62, 127]. This approximation leads to a quantity known as the effective interaction, also referred to as the pseudopotential [62, 127]. In order to introduce it, one should at first describe a system of two interacting nucleons with position vectors $\boldsymbol{r}_1$ and $\boldsymbol{r}_2$, for which the following quantities can be defined [62, 127]:

- average distance between nucleons $\boldsymbol{r}$:

$$\boldsymbol{r} = \frac{\boldsymbol{r}_1 + \boldsymbol{r}_2}{2}, \tag{3.93}$$

- relative distance $\boldsymbol{r}_{12}$:

$$\boldsymbol{r}_{12} = \boldsymbol{r}_1 - \boldsymbol{r}_2, \tag{3.94}$$

- relative momentum operator $\boldsymbol{k}_{12}$:

$$\boldsymbol{k}_{12} = -i\hbar\frac{\nabla_1 - \nabla_2}{2}, \tag{3.95}$$

- spin-exchange operator:

$$P_\sigma = \frac{1}{2}(1 + \boldsymbol{\sigma}_1 \cdot \boldsymbol{\sigma}_2). \tag{3.96}$$

Then, with regard to a certain number of parameters, the formula for Skyrme effective interaction v_{12} can be written in the general form [62, 127, 134]:

$$\begin{aligned} v_{12} = {} & t_0(1 + x_0 P_\sigma)\delta(\boldsymbol{r}_{12}) + \frac{1}{2}t_1(1 + x_1 P_\sigma)[\boldsymbol{k}_{12}^{\dagger 2}\,\delta(\boldsymbol{r}_{12}) + \delta(\boldsymbol{r}_{12})\boldsymbol{k}_{12}^2] \\ & + t_2(1 + x_2 P_\sigma)\boldsymbol{k}_{12}^\dagger \cdot \delta(\boldsymbol{r}_{12})\boldsymbol{k}_{12} + \frac{1}{6}t_3(1 + x_3 P_\sigma)\delta(\boldsymbol{r}_{12})\rho^\alpha\left(\frac{\boldsymbol{r}_1 + \boldsymbol{r}_2}{2}\right) \\ & + iW_0(\boldsymbol{\sigma}_1 + \boldsymbol{\sigma}_2) \cdot \boldsymbol{k}_{12}^\dagger\,\delta(\boldsymbol{r}_{12})\boldsymbol{k}_{12} \end{aligned} \tag{3.97}$$

with ρ being normal density, α, t_i, x_i and W_0 are parameters. The parameters t_i correspond to the zero-range limit of the Gogny force [127].

The Skyrme energy density functional, denoted as $\mathcal{E}_{\text{Sky}}$, corresponds to the effective Skyrme interaction from Eq. 3.97. In $\mathcal{E}_{\text{Sky}}$ one can distinguish two parts containing

either odd or even terms [134, 127]:

$$\mathcal{E}_{\text{Sky}} = \sum_{l=0,1} (\mathcal{E}_l^{\text{even}} + \mathcal{E}_l^{\text{odd}}) \tag{3.98}$$

with l being the index for isoscalars and isovectors. Isoscalars denote the sum of certain quantities obtained for protons and neutrons (as an example, total density can be understood as an isoscalar, as it corresponds to the sum of densities of protons and neutrons). On the other hand, isovectors refer to the difference between quantities defined for certain species of particles (for example, isovector density would be equivalent to the difference of densities of protons and neutrons) [134, 127].

Time-even densities and currents are expected to be even with regard to time reversal; similarly, time-odd parts are odd then. To distinguish between time-odd and time-even components, it is useful to express densities and currents (which can be extracted from density and anomalous density matrices) in coordinate space. According to that, one can derive the following quantities (index q denotes either protons or neutrons, so $q = p, n$) [134, 127, 5]:

- normal density:

$$\rho_q(\boldsymbol{r}, t) = \sum_{\sigma=\{\uparrow,\downarrow\}} \rho_q(\boldsymbol{r}, \sigma; \boldsymbol{r}, \sigma; t), \tag{3.99}$$

- kinetic density:

$$\tau_q(\boldsymbol{r}, t) = \sum_{\sigma=\{\uparrow,\downarrow\}} \int d^3\boldsymbol{r}' \delta(\boldsymbol{r} - \boldsymbol{r}') \nabla \cdot \nabla' \rho_q(\boldsymbol{r}, \sigma; \boldsymbol{r}', \sigma; t), \tag{3.100}$$

- current density (or momentum density vector):

$$\boldsymbol{j}_q(\boldsymbol{r}, t) = -\frac{i}{2} \sum_{\sigma=\{\uparrow,\downarrow\}} \int d^3\boldsymbol{r}' \delta(\boldsymbol{r} - \boldsymbol{r}') (\nabla - \nabla') \rho_q(\boldsymbol{r}, \sigma; \boldsymbol{r}', \sigma; t), \tag{3.101}$$

- anomalous density:

$$\nu_q(\boldsymbol{r}, t) = \sum_{\sigma=\{\uparrow,\downarrow\}} \nu_q(\boldsymbol{r}, \sigma; \boldsymbol{r}, \sigma; t), \tag{3.102}$$

As can be seen, the quantities defined above are the coordinate-space version of densities and currents included, e.g., in the SLDA functional from Eq. 3.71. Based on that, one can also consider their modifications [134, 127, 5]:

- spin density pseudovector:

$$\boldsymbol{s}_q(\boldsymbol{r},t) = \sum_{\sigma,\sigma'=\{\uparrow,\downarrow\}} \rho_q(\boldsymbol{r},\sigma;\boldsymbol{r},\sigma';t)\boldsymbol{\sigma}_{\sigma'\sigma}, \tag{3.103}$$

- spin kinetic density pseudovector:

$$T_q^{\mu}(\boldsymbol{r},t) = \sum_{\sigma=\{\uparrow,\downarrow\}} \int d^3\boldsymbol{r}'\delta(\boldsymbol{r}-\boldsymbol{r}')\nabla\cdot\nabla'\rho_q(\boldsymbol{r},\sigma;\boldsymbol{r}',\sigma';t)\boldsymbol{\sigma}^{\mu}_{\sigma'\sigma}, \tag{3.104}$$

- spin current density pseudotensor:

$$J_{q\mu}^{\nu}(\boldsymbol{r},t) = -\frac{i}{2}\sum_{\sigma=\{\uparrow,\downarrow\}} \int d^3\boldsymbol{r}'\delta(\boldsymbol{r}-\boldsymbol{r}')(\nabla_{\mu}-\nabla'_{\mu})\rho_q(\boldsymbol{r},\sigma;\boldsymbol{r}',\sigma';t)\boldsymbol{\sigma}^{\nu}_{\sigma'\sigma}, \tag{3.105}$$

- tensor kinetic density pseudovector:

$$F_{q\mu}(\boldsymbol{r},t) = \frac{1}{2}\sum_{\sigma=\{\uparrow,\downarrow\}}\sum_{\nu}\int d^3\boldsymbol{r}'\delta(\boldsymbol{r}-\boldsymbol{r}')(\nabla_{\mu}\nabla'_{\nu}+\nabla'_{\mu}\nabla_{\nu})\rho_q(\boldsymbol{r},\sigma;\boldsymbol{r}',\sigma';t)\boldsymbol{\sigma}^{\nu}_{\sigma'\sigma}. \tag{3.106}$$

In equations above, $\boldsymbol{\sigma}$ denotes Pauli spin matrices with $\mu,\nu = 1,2,3$ being tensor indices. Then, the time-even part of the functional can be defined as follows [134, 127, 5]:

$$\begin{aligned}\mathcal{E}_{\text{even}} = {} & C_l^{\rho}\rho_l^2 + C_l^{\Delta\rho}\rho_l\Delta\rho_l + C_l^{\tau}\rho_l\tau_l + C_l^{\Delta J}\rho_l\nabla\cdot\boldsymbol{J}_l + C_l^{J}\sum_{\mu,\nu}J_{l,\mu\nu}J_{l,\mu\nu} \\ & + \frac{1}{2}C_l^{Tr(J)}\Big(\sum_{\mu}J_{l,\mu\mu}\Big)^2 + \frac{1}{2}C_l^{J^2}\sum_{\mu,\nu}J_{l,\mu\nu}J_{l,\nu\mu}\end{aligned} \tag{3.107}$$

Here, expression $\boldsymbol{J}_q(\boldsymbol{r},t)$ means spin-orbit and is used to approximate spin current density tensor [134, 127, 5]:

$$\boldsymbol{J}_{q\rho}(\boldsymbol{r},t) = \sum_{\mu,\nu}\epsilon_{\rho\mu\nu}J_q^{\mu,\nu}(\boldsymbol{r},t), \tag{3.108}$$

where $\epsilon_{\rho\mu\nu}$ is Levi-Civita symbol. Similarly, the time-odd part can be written as [134, 127, 5]:

$$\begin{aligned}\mathcal{E}_{\text{odd}} = & C_l^s s_l^2 + C_l^{\Delta s} \boldsymbol{s}_l \cdot \Delta \boldsymbol{s}_l + C_l^T \boldsymbol{s}_l \cdot \boldsymbol{T}_l + C_l^j \boldsymbol{j}_l^2 + C_l^{\nabla j} \boldsymbol{s}_l \cdot \nabla \times \boldsymbol{j}_l \\ & + C_l^{\nabla \boldsymbol{s}} (\nabla \cdot \boldsymbol{s}_l)^2 + C_l^F \boldsymbol{s}_l \cdot \boldsymbol{F}_l.\end{aligned} \tag{3.109}$$

In Eq. 3.109, time-odd quantities $\boldsymbol{j}_q(\boldsymbol{r},t)$, $\boldsymbol{s}_q(\boldsymbol{r},t)$, $\boldsymbol{T}_q(\boldsymbol{r},t)$ and $\boldsymbol{F}_q(\boldsymbol{r},t)$ are included. However, once the analyzed case conserves time-reversal symmetry, these densities and currents (and, as a consequence, the whole time-odd contribution to the functional) are expected to vanish [134]. In the case when time-reversal symmetry is broken, time-odd quantities would also contribute to the Skyrme functional [127].

In Eq. 3.107 and Eq. 3.109 the coefficients C come from fitting to experimental data. However, in most versions of Skyrme functionals, tensor terms are neglected, so $C_l^F = C^{\nabla s} = 0$, as well as C_l^T [134, 5]. Furthermore [134, 5]:

- gauge invariance imposes the following connections between time-odd and time-even quantities:

$$C_l^j = -C_l^\tau,\ C_l^J = -C_l^T,\ C_l^{\nabla j} = C_l^{\nabla J},\ C_l^{\mathrm{Tr}(J)} = -C_l^F = C_l^{J^2}, \tag{3.110}$$

- additionally, self-interactions have to be neglected, which leads to the following relations:

$$\begin{aligned}& C_0^n + C_1^n + C_0^s + C_1^s = 0, \\ & C_0^\tau + C_1^\tau + C_0^T + C_1^T = 4(C_0^{\Delta n} + C_1^{\Delta n} + C_0^{\Delta s} + C_1^{\Delta s}), \\ & 4(C_0^{\nabla s} + C_1^{\nabla s}) + C_0^F + C_1^F = 0, \\ & C_0^\tau + C_1^\tau - 2(C_0^T + C_1^T) - (C_0^F + C_1^F) - 4(C_0^{\nabla s} + C_1^{\nabla s}) = 0.\end{aligned} \tag{3.111}$$

Taking into account the Skyrme contribution to the energy functional, one can finally obtain the nuclear single-particle Hamiltonian. It consists of local potentials being functional derivatives of the energy functional E over certain densities/currents [127, 5]:

$$h_q = U_q - \nabla \cdot B_q \nabla - \frac{i}{2}\left\{\boldsymbol{W}_q, \nabla\sigma\right\} + \boldsymbol{S}_q \cdot \boldsymbol{\sigma} - \nabla \cdot (\boldsymbol{\sigma} \cdot \boldsymbol{C}_q)\nabla - \frac{i}{2}\left\{\boldsymbol{A}_q, \nabla\right\}. \tag{3.112}$$

In Eq. 3.112, the expression $\{\boldsymbol{W}_q, \nabla\sigma\}$ is equal $\sum_{ij}\{W_{ij}, \nabla_i\sigma_j\}$ and $B_q = \hbar^2/2m_q^*$ with m_q^* being effective mass. Based on that, one can distinguish the following potentials [127, 5]:

- time-even:
$$U_q = \frac{\delta E}{\delta\rho_q},\ B_q = \frac{\delta E}{\delta\tau_q},\ \boldsymbol{W}_q = \frac{\delta E}{\delta \boldsymbol{J}_q}, \tag{3.113}$$
- time-odd:
$$\boldsymbol{A}_q = \frac{\delta E}{\delta \boldsymbol{j}_q},\ \boldsymbol{S}_q = \frac{\delta E}{\delta \boldsymbol{s}_q},\ \boldsymbol{C}_q = \frac{\delta E}{\delta \boldsymbol{T}_q}. \tag{3.114}$$

As it was mentioned before, once time-reversal symmetry is conserved, time-odd potentials vanish; therefore, the only contribution to the Hamiltonian comes from time-even potentials. In addition, in nuclear community the potential U_q is used instead of V_{KS}.

3.4.2 Pairing Energy

Another important part of the energy functional is connected with pairing energy. In this case, only the interaction between particles of the same type is considered (so only between neutrons or between protons), as in neutron stars, protons and neutrons are expected to occupy different Fermi surfaces. Therefore, it turns out that neutron-proton pairing can be neglected [7]. What is especially important is that the pairing energy considered separately from the kinetic part becomes divergent (in other words, only the sum of these two components gives a finite value) [97, 135], so these terms can be considered only together. The problem of divergence in pairing energy is discussed in a section devoted to regularization methods (Sec. 3.4.3).

In general, pairing contribution to SLDA-type energy density functional (denoted as $\mathcal{E}_{\mathrm{pair}}$) is calculated within the following formula [136, 137]:

$$\mathcal{E}_{\mathrm{pair}} = \sum_{q=\{n,p\}} v^q_{\mathrm{pair}}[\rho_p(\boldsymbol{r}), \rho_n(\boldsymbol{r})]\nu_q(\boldsymbol{r})\nu_q^*(\boldsymbol{r}), \tag{3.115}$$

where the index q has the meaning of isospin, as pairing energy can be obtained both for protons p and neutrons n. In Eq. 3.115, the component v^q_{pair} denotes the two-body

pairing effective force dependent on density [136, 137]:

$$v^q_{\text{pair}}[\rho_n(\boldsymbol{r}), \rho_p(\boldsymbol{r})] = \frac{1}{4} f^\pi_q v^{\pi q}[\rho_n(\boldsymbol{r}), \rho_p(\boldsymbol{r})], \tag{3.116}$$

where f^π_q is the factor connected with symmetry breaking between protons and neutrons. The pairing strength turns out to be different for protons and neutrons due to the Coulomb effects and charge-symmetry breaking [136, 138]; in addition, it also depends on the parity of nuclei [139]. Therefore, f^π_q can take one of the values: f^+_n, f^-_n, f^+_p or f^-_p, depending on the properties of the nuclei. In the nuclear matter investigated here, f^π_q is set to 1. Another component, $v^{\pi q}[\rho_n(\boldsymbol{r}), \rho_p(\boldsymbol{r})]$ is the pairing strength fitted to ${}^1S_0$ type of pairing and for particular densities of protons and neutrons (in other words, it allows to reproduce the pairing gap in uniform neutron matter) [140, 138].

3.4.3 Brussels-Montreal Skyrme Functionals

In principle, the energy density functionals concerning Skyrme interaction are constructed through fitting the parameters from Eq. 3.97 to experimental data [141], which can be done in various ways. As a consequence, one can recognize many different series of these functionals [141]. In general, the fitting procedure can be done with regard to realistic interactions using many-body methods [133], but from the practical point of view, it turns out to be an extremely difficult task. Therefore, phenomenological functionals are widely used [141, 142]. At this point, it should be stressed that in nuclear physics, apart from the functionals based on effective nucleon-nucleon interactions (such as Skyrme or Gogny), genuine energy functionals (which are not based on any potential) are also used [142]. Among them, one can point out, e.g., Fayans [143], SeaLL1 [144], or BCPM [145] functionals [142].

One of the series of Skyrme-based energy density functionals which can be applied for astrophysical systems is Brussels-Montreal Skyrme (BSk) class [141]. What distinguishes it from other classes is the way in which the coefficients in Eq. 3.97 are obtained. In BSk, they are derived from both fitting to experimental data and from the results of many-body calculations (regarding realistic forces) as well [139, 146, 147]. Among the parameters connected with experimental data, one can distinguish, e.g., atomic masses (for nuclei with number of protons and neutrons larger than 8) from Atomic Mass Evaluation (AME) [148, 149], charge radii, and incompressibility [150].

What is also important, certain corrections to energy have been included. Phenomenological Wigner correction is connected with the contribution of light nuclei and nuclei with Z close to N [5, 141]. Another modifications are connected with the rotational and vibrational spurious collective energy [138], which removes the spurious center-of-mass energy [141, 151] and the finite size of the proton (which influences both the charge radius and energy) [141]. The Coulomb exchange has been neglected, due to which Coulomb correlations and charge-symmetry breaking are not considered in the further calculations [152]. On the other hand, from many-body calculations, the equation of state of neutron matter, ${}^1S_0$ pairing gaps, and effective masses could have been incorporated [141].

BSK functionals have received many versions, which are consecutively numbered [141, 5]:

- in functionals BSk16-17 fitting to realistic ${}^1S_0$ pairing gaps (without self-energy) has been applied [138],
- BSk18: spurious spin-isospin instabilities have been removed [153],
- BSk19-21: fitting to realistic equations of state for neutron matter [136],
- BSk22-26: fitting to different symmetry energies [154],
- BSk27*: optimal fitting to 2012 AME[155] has been used [156],
- BSk28-29: generalized spin-orbit coupling has been included [139].

In BSk30-32 parametrization (which is of special interest in the case of this research), direct fitting to realistic ${}^1S_0$ pairing gaps in homogeneous nuclear matter from [147] is used. In addition, in the formula for pairing strength, an additional surface term has been included, as well as self-energy effects [5, 139]. What is especially important is that the general form of BSk31 functional also includes the spin-orbit coupling; however, as it has been explained in the theoretical introduction, in the case of neutron star matter, one can neglect this contribution [139].

In the calculations discussed in this thesis, the BSk31 parametrization has been adopted. As mentioned in [3], in the formula for effective Skyrme interactions (Eq. 3.97), in the normal part, the terms t_1 and t_2 are density-dependent [139], as well as the contact

interaction in the pairing part [157]. The explicit form of the functional can be written as:

$$E = \int \mathcal{E}(\boldsymbol{r})\, d\boldsymbol{r}, \tag{3.117}$$

with energy density [3, 138]:

$$\begin{aligned}&\mathcal{E}[\rho_q(\boldsymbol{r}), \nabla\rho_q(\boldsymbol{r}), \tau_q(\boldsymbol{r}), \boldsymbol{j}_q(\boldsymbol{r}), \nu_q(\boldsymbol{r})] = \\ &\frac{\hbar^2}{2m_q}\tau_q + \mathcal{E}_\rho(\rho_q) + \mathcal{E}_{\Delta\rho}(\rho_q, \nabla\rho_q) + \mathcal{E}_\tau(\rho_q, \tau_q, \boldsymbol{j}_q) + \mathcal{E}_\pi(\rho_q, \nabla\rho_q, \nu_q) + \mathcal{E}_{\mathrm{Coul}}(\rho_p).\end{aligned} \tag{3.118}$$

Here, the term q denotes isospin (protons p or neutrons n), as there are two species of nucleons in the system. In Eq. 3.118, the terms $\mathcal{E}_\rho$, $\mathcal{E}_{\Delta\rho}$, and $\mathcal{E}_\tau$ have a similar structure as the corresponding parts in the nuclear energy density functional $\mathcal{E}_{\mathrm{Sky}}$. In other words, $\mathcal{E}_{\mathrm{Sky}}$ is treated as a starting point for further modification. The consecutive components of the BSk31 functional have the following interpretation [3, 138]:

- $(\hbar^2/2m_q)/\tau_q$ – this part has the meaning of kinetic energy density; the variable m_q corresponds either to neutron or proton mass and τ_q – to the kinetic density,
- $\mathcal{E}_\rho$ is connected with properties of uniform nuclear matter for a particular density – therefore, it depends on normal density and describes interactions of the nucleon with its background,
- $\mathcal{E}_{\Delta\rho}$ – it is the correction arising from nonuniformities of the system (in other words, with spatial fluctuations of normal density),
- $\mathcal{E}_\tau$ – this part is connected with effective mass of nucleon – it changes as the nucleon moves through the medium; depending on the density of the background, the velocity of movement (and, as a consequence, also effective mass of nucleon) would also be modified; in other words, $\mathcal{E}_\tau$ is connected with momentum-dependent interactions,
- $\mathcal{E}_\pi$ – refers to pairing energy,
- $\mathcal{E}_{\mathrm{coul}}$ is connected with the Coulomb interaction.

The contributions to the nuclear energy density functional can be written with regard to coefficients from [158]:

$$\mathcal{E}_\rho = \sum_{l=0,1} C_l^\rho[\rho]\rho_l^2, \tag{3.119}$$

$$\mathcal{E}_\tau = \sum_{l=0,1} C_l^\tau[\rho](\rho_l\tau_l - j_l^2), \tag{3.120}$$

$$\mathcal{E}_{\Delta\rho} = \sum_{l=0,1} C_l^{\Delta\rho}\rho_l\Delta\rho_l + C_l^{\nabla\rho}[\rho]\Delta\rho_l. \tag{3.121}$$

The components marked as C in equations above can be expressed through the parameters used in the description of effective Skyrme interaction (Eq. 3.97). Their particular values come from [139].

The part of the functional connected with pairing can be written as [139]:

$$\begin{aligned}\mathcal{E}_\pi = &\frac{1}{4}f_n^\pm v^{\pi n}[\rho_n(\boldsymbol{r}),\rho_p(\boldsymbol{r})] + \kappa_n|\nabla\rho_n|^2\nu_n^2 + \\ &+ \frac{1}{4}f_p^\pm v^{\pi p}[\rho_n(\boldsymbol{r}),\rho_p(\boldsymbol{r})] + \kappa_p|\nabla\rho_p|^2\nu_p^2.\end{aligned} \tag{3.122}$$

In Eq. 3.122, components for neutrons (n) and protons (p) have be distinguished. The term $\frac{1}{4}f_q^\pm v^{\pi q}[\rho_n(\boldsymbol{r}),\rho_p(\boldsymbol{r})]$ corresponds to pairing interaction from Eq. 3.116. The particular values of this component have been chosen in order to reproduce the pairing gaps in ${}^1S_0$ state from [147] (the explicit formulas for pairing strength can be found, e.g., in [137, 157]). In addition, Eq. 3.122 includes also additional parameter κ_q [139].

The single-particle Hamiltonian can be obtained from the BSk31 energy density functional through derivatives of this functional over certain densities. In the considered case, one can write the expression for Hamiltonian h_q as [3, 138]:

$$h_q = U_q^\rho + U_q^{\Delta\rho} + U_q^\tau + U_q^\pi - \nabla B_q\nabla - \frac{i}{2}\Big\{\boldsymbol{A}_q, \nabla\Big\}. \tag{3.123}$$

In Eq. 3.123, scalar potentials U_q are defined through functional derivatives of a particular part of the functional $\mathcal{E}$ over normal density ρ_q and its gradient $\Delta\rho_q$ [3, 138]:

$$U_q^\rho = \frac{\partial\mathcal{E}_\rho}{\partial\rho_q}, \tag{3.124}$$

$$U_q^{\Delta\rho} = \frac{\partial\mathcal{E}_{\Delta\rho}}{\partial\rho_q} - \nabla\cdot\frac{\partial\mathcal{E}_{\Delta\rho}}{\partial(\nabla\rho_q)} + \Delta\frac{\partial\mathcal{E}_{\Delta\rho}}{\partial(\Delta\rho_q)}, \tag{3.125}$$

$$U_q^\tau = \frac{\partial\mathcal{E}_\tau}{\partial\rho_q}, \tag{3.126}$$

$$U_q^{\pi} = \frac{\partial \mathcal{E}_{\pi}}{\partial \rho_q} - \nabla \cdot \frac{\partial \mathcal{E}_{\pi}}{\partial (\nabla \rho_q)}. \tag{3.127}$$

Since U_q^{π} turns out to be small compared to other contributions, it can be neglected in further calculations [3]. Moreover, in Eq. 3.123 the field B_q contains both the kinetic term and and the derivative of $\mathcal{E}_{\tau}$ over kinetic density τ_q [3]:

$$B_q = \frac{\hbar^2}{2m_q} + \frac{\partial \mathcal{E}_{\tau}}{\partial \tau_q}. \tag{3.128}$$

The component $\boldsymbol{A}_q$ has the meaning of vector potential, which arises due to the presence of current $\boldsymbol{j}_q$. Therefore, it is the functional derivative of $\mathcal{E}_{\tau}$ over this current [3]:

$$\boldsymbol{A}_q = \frac{\partial \mathcal{E}_{\tau}}{\partial \boldsymbol{j}_q}. \tag{3.129}$$

Explicit formulas for the potentials and fields contributing to the Hamiltonian with regard to coefficients from the effective Skyrme interaction can be written as [3, 138]:

$$B_q = \frac{\hbar^2}{2m_q} + C_0^{\tau}\rho + C_1^{\tau}(\rho_q - \rho_{q'}) \tag{3.130}$$

$$\boldsymbol{A}_q = -2C_0^{\tau}\boldsymbol{j} - 2C_1^{\tau}(\boldsymbol{j}_q - \boldsymbol{j}_{q'}) \tag{3.131}$$

$$U_q^{\rho} = \frac{dC_0^{\rho}}{d\rho}\rho_n^2 + \frac{dC_1^{\rho}}{d\rho}(\rho_q - \rho_{q'})^2 + 2\rho C_0^{\rho} + 2(\rho_q - \rho_{q'})C_1^{\rho} \tag{3.132}$$

$$\begin{aligned} U_q^{\tau} = {} & C_0^{\tau}\tau + C_1^{\tau}(\tau_q - \tau_{q'}) + \frac{dC_0^{\tau}}{d\rho}(\rho\tau - \boldsymbol{j}^2) + \\ & + \frac{dC_1^{\tau}}{d\rho}\left[(\rho_q - \rho_{q'})(\tau_q - \tau_{q'}) - (\boldsymbol{j}_q - \boldsymbol{j}_{q'})^2\right] \end{aligned} \tag{3.133}$$

$$\begin{aligned} U_q^{\Delta\rho} = {} & 2C_0^{\Delta\rho}\Delta\rho + 2C_1^{\Delta\rho}(\Delta\rho_q - \Delta\rho_{q'}) + \frac{dC_0^{\nabla\rho}}{d\rho}\Delta\rho + \frac{dC_1^{\nabla\rho}}{d\rho}(\Delta\rho_q - \Delta\rho_{q'}) + \\ & + \boldsymbol{\nabla} \cdot \left(\frac{dC_0^{\nabla\rho}}{d\rho}\boldsymbol{\nabla}\rho\right) + \boldsymbol{\nabla} \cdot \left(\frac{dC_0^{\nabla\rho}}{d\rho}\boldsymbol{\nabla}(\rho_q - \rho_{q'})\right) \end{aligned} \tag{3.134}$$

The index q' has the meaning of complementary species of nucleon (e.g., for q being protons, q' denotes neutrons and vice versa).

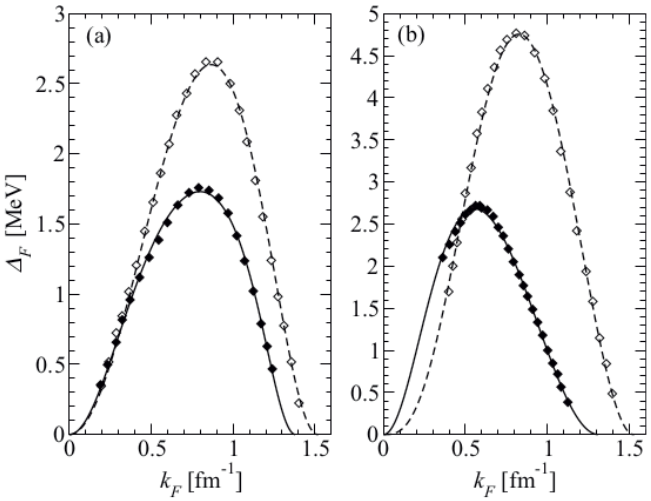

FIGURE 3.3: $^1S_0$ pairing gap in pure neutron matter (a) and symmetric neutron matter (b) with fitted values [139].

Fitting Details

As mentioned before, the parameters of functionals are fitted to experimental data and the results of many-body calculations; in other words, these parameters are constrained by them. Due to the fact that the properties of nuclear matter in neutron stars are close to those of neutron matter, one can use the results of experiments on pure neutron matter to set constraints on the parameters of functionals [5, 139]. As mentioned before, the parameters of functionals are determined to fit realistic $^1S_0$ pairing gaps. Fig. 3.3 shows the $^1S_0$ pairing gap in pure neutron matter (a) and symmetric neutron matter (b) from [147] with fitted values (marked as filled symbols with self-energy effects and empty symbols without these effects) [139]. In the fitting of BSk30-32 functionals, the values of pairing gap with self-energy effects have been used [139].

One of the fundamental quantities describing neutron matter is energy per nucleon e; its dependence on neutron density is known as the equation of state (EoS) [136]. In general, it can be written as a function of nuclear matter density ρ and charge asymmetry parameter η (equal $(\rho_n - \rho_p)/\rho$) in the following form [136, 5]:

$$e(\rho,\eta) = e(\rho,\eta=0) + e^{(1)}_{\rm sym}(\rho)\eta^2 + \mathcal{O}(\eta^2), \tag{3.135}$$

where $e(\rho, \eta = 0)$ is energy per nucleon of symmetric neutron matter (e_{SNM}) and $e^{(1)}_{\mathrm{sym}}(\rho)$ means symmetry energy (which is the difference between energy per nucleon in symmetric and pure neutron matter). In addition, one can also define another type of symmetry energy $e^{(2)}_{\mathrm{sym}}(\rho)$, which describes the energy cost of sustaining an isospin-asymmetry in the neutron matter [159]:

$$e^{(2)}_{\mathrm{sym}}(\rho) = e(\rho, \eta = 1) - e(\rho, \eta = 0) \tag{3.136}$$

Due to the presence of quadratic and higher order terms in η, $e^{(1)}_{\mathrm{sym}}(\rho)$ and $e^{(2)}_{\mathrm{sym}}(\rho)$ are not exactly equal [136]. However, in case of almost pure neutron matter (so for $\eta \approx 1$) and for densities close to saturation density $\rho_0 \approx 0.16$ fm $^{-3}$, one can make an assumption that $e^{(1)}_{\mathrm{sym}}(\rho) \approx e^{(2)}_{\mathrm{sym}}(\rho)$ [5]. According to [5, 160, 161], one can expand e_{SNM} and $e^{(1)}_{\mathrm{sym}}(\rho)$ into the following forms:

$$e_{\mathrm{SNM}}(\rho) \equiv e(\eta, \eta = 0) = a_v + \frac{1}{18} K_v \epsilon^2 - \frac{1}{162} K_{\mathrm{sym}} \epsilon^3 + \mathcal{O}(\epsilon^4), \tag{3.137}$$

$$e^{(1)}_{\mathrm{sym}}(\rho) = J + \frac{1}{3} L \epsilon + \frac{1}{18} K_{\mathrm{sym}} \epsilon^2 + \mathcal{O}(\epsilon^3), \tag{3.138}$$

where $\epsilon = (\rho - \rho_0)/\rho_0$. In Eqs. 3.137 - 3.138, one can find several new quantities, such as isoscalar quantities [5, 160, 161, 162]:

- volume parameter:

$$a_v \equiv e_{\mathrm{SNM}}(\rho = \rho_0), \tag{3.139}$$

- incompressibility:

$$K_v = 9\rho_0^2 \frac{d^2 e_{\mathrm{SNM}}}{d\rho^2}|_{\rho=\rho_0}. \tag{3.140}$$

Furthermore, these equations also include quantities known as isovector parameters [5, 160, 161, 162]:

- symmetry energy coefficient:

$$J \equiv e^{(1)}_{\mathrm{sym}}(\rho = \rho_0), \tag{3.141}$$

- slope of this energy:

$$L = 3\rho_0 \frac{de^{(1)}_{\mathrm{sym}}}{d\rho}|_{\rho=\rho_0} \tag{3.142}$$

- its curvature:

$$K_{\mathrm{sym}} = 9\rho_0^2 \frac{d^2 e_{\mathrm{sym}}^{(1)}}{d\rho^2}|_{\rho=\rho_0}. \tag{3.143}$$

Then, Eq. 3.135 can be written with regard to these quantities as follows [5]:

$$e(\rho,\eta) \approx a_v + \left(J + \frac{1}{3}Le\right)\eta^2 + \frac{1}{18}\left(K_v + \eta^2 K_{\mathrm{sym}}\right)\epsilon^2. \tag{3.144}$$

Each of the neutron matter constraints can be obtained with regard to particular experimental results [5]:

- saturation density ρ_0 and volume parameter a_v, extracted with regard to charge-density distributions from e.g. [163], together with nuclear masses from [148], are expected to be close to 0.15-0.16 fm^{-3} and -16 $\pm$ 1 MeV, respectively,

- incompressibility K_v can be constrained by compression-mode giant resonances [164, 165]. As predicted in [150], the values of K_v are assumed to reach 240 $\pm$ 10 MeV,

- isovector parameters are set by various experiments of nuclear physics, such as heavy ion collision, giant resonances in heavy nuclei, or measurements of neutron skin thickness [139]. Based on that, J can be constrained from 25 to 35 MeV and L from 25 to 115 MeV [139]. As an example, Fig. 3.4 shows the constraints on these symmetry energy coefficients. The constraints from heavy ion collisions are marked as *HIC*, from giant dipole resonance - as *GDR*, and *Sn neutron thickness* mean the measurements of neutron skin thickness in thin isotopes [139]. The white area in the middle of the plot represents the intersection of these constraints and can therefore be considered the permitted range of values for J and L. The stars denote the predictions of BSk30-32 functionals, and the dashed line corresponds to the predictions obtained within another BSk functionals [136]. In the particular case of BSk30-32 functionals, fits are constrained to symmetry coefficient J equal 30, 31, and 32 MeV [139]. As a consequence, three different interactions are obtained, and the functionals describing these interactions are labeled BSk30, BSk31, and BSk32 [139]. As estimated by [166], the value of K_{sym} is expected to be in the range from -500 MeV to 300 MeV. However, these values are still uncertain [5].

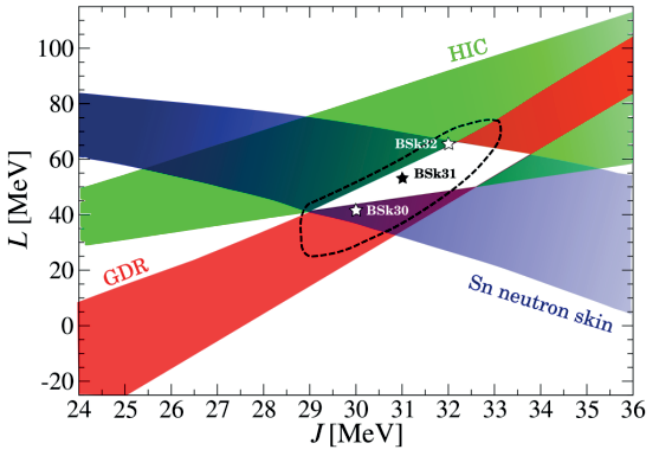

FIGURE 3.4: Constraints on the symmetry energy coefficients [139].

Predictions of BSk30-32 Functionals

At this point, one can take a closer look at the predictions of BSk30-32 functionals and the comparison with other widely recognized results. In Fig. 3.5, some important quantities obtained for pure neutron matter within various approaches are shown. Fig. 3.5a presents the equation of state (EoS) for pure neutron matter (energy per neutron e as a function of neutron density n) for BSk30-32 functionals. These results are compared with Quantum Monte Carlo calculations [167] (the dark-shaded part) and chiral effective field theory calculations [168] (the light-shaded part). In addition, the series denoted as APR refers to the results from [169], while LS2 and LS3 represent the realistic EoS from [170]. In Fig. 3.5b, symmetry energy as a function of neutron density is presented. The BSk31 predictions are compared with results of many-body calculations from [147] (denoted as EBHF). Due to the fact that saturation density considered in [147] is different from that in BSk31, results marked with red line (*BSk31*) have been shifted with regard to this difference and plotted with blue line (*BSk31 with* Δn*=0.016* fm^{-3}) [139]. Another important result is the effective mass of the nucleon, being one of the free parameters of fitting [139]. Fig. 3.5c shows nucleon effective masses (M^*/M) as a function of neutron density n for different asymmetry parameters η. Again, the effective masses calculated within BSk30-32 functionals (where t_1 and t_2 terms are density-dependent) are compared with the EBHF (Extended Brueckner-Hartree-Fock) approach. For all the quantities plotted in Fig. 3.5, the predictions of BSk functionals

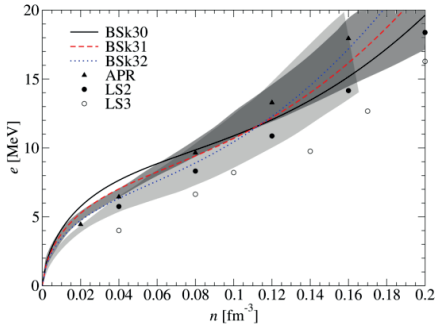

(A) Equation of state for neutron matter obtained within BSk30-32 functionals and other approaches [139].

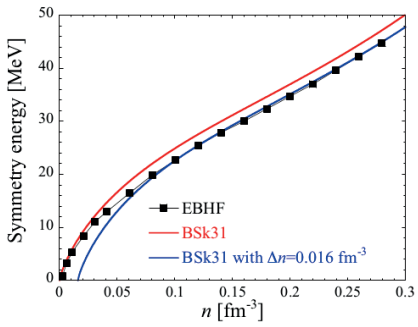

(B) Symmetry energy for neutron matter obtained within BSk31 functional and EBHF approach [139].

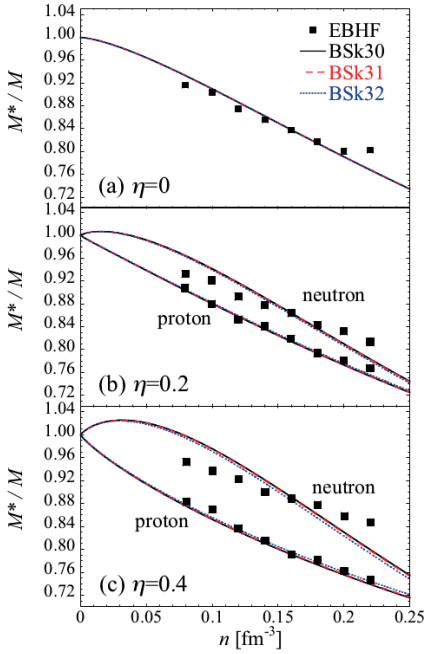

(C) Nucleon effective masses for symmetric nuclear matter (a) and two asymmetric cases (b,c) obtained within BSk30-32 functionals and EBHF approach [139].

FIGURE 3.5: Comparison of equation of state, symmetry energy, and nucleon effective masses as a function of density for neutron matter obtained with BSk functionals and other approaches [139].

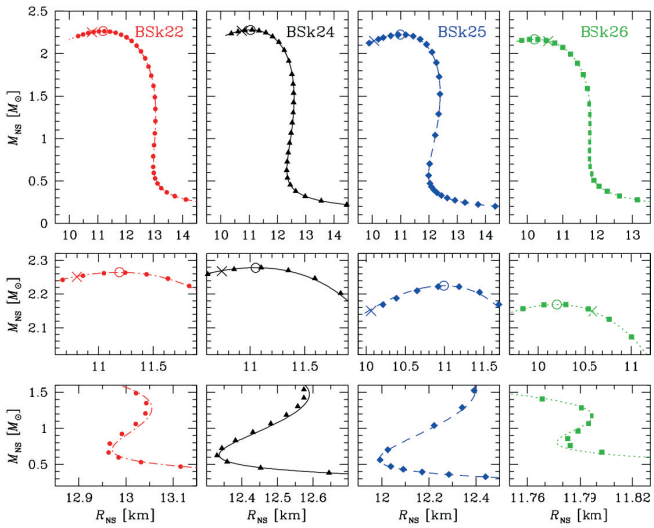

FIGURE 3.6: Mass-radii diagram of non-rotating neutron stars obtained with BSk functionals and analytical calculations [171].

are in good agreement with the results from other approaches.

Apart from the constraints mentioned above, one can also consider the astrophysical ones. In principle, the functionals have to provide a reliable description of neutron stars with certain geometrical parameters, among which mass and radius have the greatest influence [5, 139]. Mass of neutron star can be obtained for a given EoS with regard to Tolman-Oppenheimer Volkoff equations [5, 159], while the radius can be estimated from the analysis of gamma rays emitted from the star [166]. One of the results commonly discussed in the case of astrophysical constraints is the mass-radii diagram. An example of such a plot, obtained with regard to BSk22-26 functionals, is shown in Fig. 3.6. Here, the predictions of BSk functional are marked with symbols and analytical results from [171] – with line. It can be seen that the BSk functionals admit the existence of neutron stars heavier than two solar masses.

Regularization Methods

The following discussion, concerning the renormalization scheme, is based on [135, 97, 121].

At this point, one should also discuss an important problem coming from the local pairing field approximation. Although it simplifies the description, it also causes divergence in the pairing potential. Coming back to Eq. 3.85 and inserting formulas for u and v for e.g. uniform system, it can be seen that for $|\boldsymbol{r}-\boldsymbol{r}'|$ approaching 0, anomalous density behaves as $1/|\boldsymbol{r}-\boldsymbol{r}'|$. In other words, its diagonal part becomes divergent, so the local pairing field cannot be defined. Essentially, this effect is associated with an increase in the Cooper pair wave function as the distance between the particles approaches the radius of interaction. Therefore, it can be seen that the problem of divergence appears for high momenta corresponding to small distances between $\boldsymbol{r}$ and $\boldsymbol{r}'$, which makes the problem universal. Indeed, it takes place either in finite or infinite systems, as well as in inhomogeneous matter. In order to eliminate the problem of divergence, one should make some additional assumptions that keep the pairing field finite. This procedure is called regularization.

In general, various methods of regularization exist, depending on the particular system. In some cases, e.g., for ultracold atoms, a specific value of momentum (called the cutoff momentum k_c) is set. It leads to the energy cutoff $E_c = \frac{\hbar^2 k_c^2}{2m}$, so that only the orbitals with energies under this value would contribute to anomalous density. Then, one can write the expression for such a modified anomalous density ν^{reg} as:

$$\nu^{\text{reg}}_{\uparrow\downarrow}(\boldsymbol{r}) = \sum_{|E_n|<E_c} v^*_{n\uparrow}(\boldsymbol{r}) u_{n\downarrow}(\boldsymbol{r}). \tag{3.145}$$

This must be supplemented with a redefinition of the pairing potential, which in the nuclear case takes the form:

$$\Delta(\boldsymbol{r}) = -v^{\pi q}[\rho_n, \rho_p](\boldsymbol{r})\, \nu^{\text{reg}}_{\uparrow\downarrow}(\boldsymbol{r}), \tag{3.146}$$

In addition, an energy cutoff in the quasiparticle or single-particle energy spectrum must be introduced [141]. This leads to the following form of gap equation for the uniform system [138]:

$$\Delta_q = -\frac{1}{8\pi^2}\left(\frac{2M^*_q}{\hbar^2}\right)^{3/2} v^{\pi q}[\rho_n, \rho_p]\, \Delta_q \int_\Lambda d\epsilon \frac{\sqrt{\epsilon}}{\sqrt{(\epsilon-\mu_q)^2+\Delta_q^2}}. \tag{3.147}$$

In the integral on the right side of the equation, the phenomenological value of Δ_q is used. The integration is done over a certain subspace Λ corresponding to the energy cutoff. One can approximate this integral (I_q) within the following formula [137]:

$$I_q = \sqrt{\epsilon_F^q}\left[2\ln\left(\frac{2\epsilon_F^q}{\Delta_q}\right) + \Lambda\left(\frac{\epsilon_\Lambda}{\epsilon_F^q}\right)\right], \tag{3.148}$$

where ϵ_F^q is the Fermi energy and ϵ_Λ means some value of the quasiparticle/single particle cut-off energy. In our case, we set $\epsilon_\Lambda = E_c$, which in the next step is related to the momentum cut-off scale k_c (equal π/D_x, where D_x is the lattice constant). This, in turn, reflects the resolution scale we use in the calculation. In Eq. 3.148, function Λ is [137]:

$$\Lambda(x) = \ln(16x) + 2\sqrt{1+x} - 2\ln(1+\sqrt{1+x}) - 4. \tag{3.149}$$

Based on that, one can derive the formula for pairing strength $v^{\pi q}[\rho_n, \rho_p]$ [137]:

$$v^{\pi q}[\rho_n, \rho_p] = -8\pi^2\left(\frac{\hbar^2}{2M_q^*}\right)^{3/2}\frac{1}{I_q}. \tag{3.150}$$

3.5 Summary

Here, the short summary of the formulas used in this thesis is provided [3].

BSk31 energy density functional is:

$$\begin{aligned}&\mathcal{E}[\rho_q(\boldsymbol{r}), \nabla\rho_q(\boldsymbol{r}), \tau_q(\boldsymbol{r}), \boldsymbol{j}_q(\boldsymbol{r}), \nu_q(\boldsymbol{r})] = \\ &\frac{\hbar^2}{2m_q}\tau_q + \mathcal{E}_\rho(\rho_q) + \mathcal{E}_{\Delta\rho}(\rho_q, \nabla\rho_q) + \mathcal{E}_\tau(\rho_q, \tau_q, \boldsymbol{j}_q) + \mathcal{E}_\pi(\rho_q, \nabla\rho_q, \nu_q) + \mathcal{E}_{\mathrm{Coul}}(\rho_p).\end{aligned} \tag{3.151}$$

with the following terms:

$$\mathcal{E}_\rho = \sum_{l=0,1} C_l^\rho[\rho]\rho_l^2, \tag{3.152}$$

$$\mathcal{E}_\tau = \sum_{l=0,1} C_l^\tau[\rho](\rho_l\tau_l - \boldsymbol{j}_l^2), \tag{3.153}$$

$$\mathcal{E}_{\Delta\rho} = \sum_{l=0,1} C_l^{\Delta\rho}\rho_l\Delta\rho_l + C_l^{\nabla\rho}[\rho]\Delta\rho_l. \tag{3.154}$$

$$\begin{aligned}\mathcal{E}_\pi = &\frac{1}{4} f_n^{\pm} v^{\pi n}[\rho_n(\boldsymbol{r}), \rho_p(\boldsymbol{r})] + \kappa_n |\nabla \rho_n|^2 \nu_n^2 + \\ &+ \frac{1}{4} f_p^{\pm} v^{\pi p}[\rho_n(\boldsymbol{r}), \rho_p(\boldsymbol{r})] + \kappa_p |\nabla \rho_p|^2 \nu_p^2.\end{aligned} \tag{3.155}$$

In Eq. 3.155, the terms $f_n^{\pm}$ and $f_p^{\pm}$ are set to 1. Densities, which can be calculated both for protons p or neutrons n (so, in the following relations, $q = n, p$), are defined as:

- normal density:
$$\rho_q(\boldsymbol{r}) = 2 \sum_{|E_n|<E_c} |v_{n\downarrow}(\boldsymbol{r})|^2 \, f_\beta(-E_n), \tag{3.156}$$
- kinetic density:
$$\tau_q(\boldsymbol{r}) = 2 \sum_{|E_n|<E_c} |\nabla v_{n\downarrow}(\boldsymbol{r})|^2 \, f_\beta(-E_n), \tag{3.157}$$
- current density:
$$\boldsymbol{j}_q(\boldsymbol{r}) = 2 \sum_{|E_n|<E_c} \mathrm{Im}\left[v_{n\downarrow}(\boldsymbol{r}) \nabla v^*_{n\downarrow}(\boldsymbol{r})\right] \, f_\beta(-E_n), \tag{3.158}$$
- anomalous density:
$$\nu_q(\boldsymbol{r}) = 2 \sum_{|E_n|<E_c} u_{n\uparrow}(\boldsymbol{r}) v^*_{n\downarrow}(\boldsymbol{r}) \left(f_\beta(-E_n) - f_\beta(E_n)\right). \tag{3.159}$$

The factor 2 in front of the formulas for densities corresponds to the spin degeneracy of protons/neutrons. In general, with regard to Fermi-Dirac functions f_β, one can model temperature effects. However, this thesis only considers zero-temperature cases.

Single particle Hamiltonian takes the form:

$$h_q = U_q^\rho + U_q^{\Delta\rho} + U_q^\tau + U_q^\pi - \nabla B_q \nabla - \frac{i}{2}\left\{\boldsymbol{A}_q, \nabla\right\}, \tag{3.160}$$

where potentials are defined as:

$$U_q^\rho = \frac{\partial \mathcal{E}_\rho}{\partial \rho_q}, \tag{3.161}$$

$$U_q^{\Delta\rho} = \frac{\partial \mathcal{E}_{\Delta\rho}}{\partial \rho_q} - \nabla \cdot \frac{\partial \mathcal{E}_{\Delta\rho}}{\partial(\nabla \rho_q)} + \Delta \frac{\partial \mathcal{E}_{\Delta\rho}}{\partial(\Delta \rho_q)}, \tag{3.162}$$

$$U_q^\tau = \frac{\partial \mathcal{E}_\tau}{\partial \rho_q}, \tag{3.163}$$

$$B_q = \frac{\hbar^2}{2m_q} + \frac{\partial \mathcal{E}_\tau}{\partial \tau_q}, \tag{3.164}$$

$$\boldsymbol{A}_q = \frac{\partial \mathcal{E}_\tau}{\partial \boldsymbol{j}_q}. \tag{3.165}$$

The Hamiltonian can also be written referring explicitly to densities:

$$h_q = -\nabla \frac{\partial \varepsilon}{\partial \tau_q} \nabla + \frac{\partial \varepsilon}{\partial \rho_q} - \left(\mu_q - V_q^{\text{ext}}\right) - \frac{i}{2}\left\{\frac{\partial \varepsilon}{\partial \boldsymbol{j}_q} - \hbar \boldsymbol{v}_q^{\text{ext}}, \nabla\right\}, \tag{3.166}$$

where $\boldsymbol{v}_q^{\text{ext}}$ is external velocity field. Pairing potential is defined as:

$$\Delta_q = -2\frac{\partial \varepsilon}{\partial \nu_q^*} + \Delta_q^{\text{ext}}. \tag{3.167}$$

Here, the subscript ext denotes the external potential coupling either to normal density (V^{ext}) or anomalous density (Δ^{ext}). Pairing potential can also be written as:

$$\Delta_q(\boldsymbol{r}) = -v^{\pi q}[\rho_n, \rho_p](\boldsymbol{r})\ \nu_{\uparrow\downarrow}^{\text{reg}}(\boldsymbol{r}), \tag{3.168}$$

with $\nu_{\uparrow\downarrow}^{\text{reg}}(\boldsymbol{r})$ being the renormalized anomalous density:

$$\nu_{\uparrow\downarrow}^{\text{reg}}(\boldsymbol{r}) = \sum_{|E_n|<E_c} v_{n\uparrow}^*(\boldsymbol{r}) u_{n\downarrow}(\boldsymbol{r}). \tag{3.169}$$

and $v^{\pi q}[\rho_n, \rho_p]$ the constant defining pairing strength:

$$v^{\pi q}[\rho_n, \rho_p] = -8\pi^2 \left(\frac{\hbar^2}{2M_q^*}\right)^{3/2} \frac{1}{I_q}. \tag{3.170}$$

The integral I_q is defined as:

$$I_q = \sqrt{\epsilon_F^q}\left[2\ln\left(\frac{2\epsilon_F^q}{\Delta_q}\right) + \Lambda\left(\frac{E_c}{\epsilon_F^q}\right)\right], \tag{3.171}$$

with the term Λ:

$$\Lambda(x) = \ln(16x) + 2\sqrt{1+x} - 2\ln(1+\sqrt{1+x}) - 4. \tag{3.172}$$

3.6 Technical Framework – W-BSk Toolkit

The technical aspects of examining nuclear matter in neutron stars are of crucial importance. In order to analyze such systems, there was a need to implement the theoretical formulas of DFT and TDDFT for nuclear superfluid matter (discussed in Chap. 3) in the code and perform numerical simulations. The software developed and used in this research, called W-BSk Toolkit [172], implements DFT (for static problems) and TDDFT (in studies of time evolution of the system) with regard to BSk31 functional. In principle, this framework allows for solving the equations that have a structure analogous to BdG equations. As it inherits from W-SLDA Toolkit [173, 174, 175], W-BSk shares most of its technical facilities. The crucial difference lies in the energy functional implemented in the code. In W-SLDA, which can be used, e.g., in the investigation of ultracold atom systems, one can apply such functionals as SLDA, ASLDA (asymmetric SLDA for spin-imbalanced systems), or SLDAE (extended SLDA, in which various regimes of interaction can be studied) [174, 75]. In the W-BSk Toolkit, one can investigate spin-symmetric nuclear matter using the BSk31 functional.

In addition, one of the major problems arising in the analysis of superfluid many-body systems is the number of quasiparticle wave functions that have to be evolved. As pointed out in [174], their number can be of the order 10^5-10^6; in addition, the equations including these wave functions are connected through densities, which leads to the enormous computational challenge [174]. Therefore, numerical simulations must be performed on supercomputers, which provide sufficient computational power to handle the large number of equations that need to be solved.

The general method of W-BSk calculations discussed here is based on [176, 177]. All functions that depend on spatial coordinates are represented in a discrete Cartesian space, meaning that all functions evolved during simulations are discretized on the lattice. It is described within the following parameters:

- the size of the lattice in each direction is written as N_x, N_y, and N_z, respectively,
- the lattice spacing is denoted as D_x, D_y, D_z.

Then, any three-dimensional function $f(x,y,z)$ can be discretized as follows:

$$f(x,y,z) = f(x_0 + lD_x, y_o + mD_y, z_0 + nD_z), \tag{3.173}$$

where $l = 0, 1, 2, ..., N_x - 1$, $m = 0, 1, 2, ..., N_y - 1$ and $n = 0, 1, 2, ..., N_z - 1$. The terms x_0, y_0, and z_0 correspond to the origin of the reference frame and are usually set to 0. Later on, we assume periodic boundary conditions:

$$f(x, y, z) = f(x + L_x, y, z), \tag{3.174}$$
$$f(x, y, z) = f(x, y + L_y, z), \tag{3.175}$$
$$f(x, y, z) = f(x, y, z + L_z). \tag{3.176}$$

in which $L_x = N_x D_x$, $L_y = N_y D_y$ and $L_z = N_z D_z$ is the length of the box in each direction. Based on that, the components in the Fourier transforms can be discretized:

$$k_l^{(d)} = \begin{cases} \frac{2\pi}{L_d} l, & l = 0, 1, ..., \frac{N_d}{2} - 1, \\ \frac{2\pi}{L_d}(l - N_d), & l = \frac{N_d}{2}, \frac{N_d}{2} + 1, ..., N_d - 1, \end{cases} \tag{3.177}$$

where d represents the particular direction: $d = x, y, z$. This, in turn, allows us to compute the functional derivatives with regard to the spectral methods. The r-th derivative of the function f (which in this case corresponds to e.g. quasiparticle wave functions) in the x direction can be calculated as:

$$\frac{d^r f}{dx^r} = \frac{1}{L_x L_y L_x} \sum_{lmn} \left(i k_l^{(x)} \right)^r \tilde{f}_{lmn} \exp\left[i \left(k_l^{(x)} x + k_m^{(y)} y + k_n^{(z)} z \right) \right]. \tag{3.178}$$

In Eq. 3.178, the term $\tilde{f}$ denotes the discrete Fourier component (which can be calculated with Fast Fourier Transform).

From the user's perspective, there are four main files in the W-BSk package, which can be edited before the simulation:

- *input.txt*, which is the first file read by the solver during computation. Depending on the code type, one can set various tags. In the case of static code, one can modify, for example, the convergence conditions, which include the minimum difference between energies and the number of particles calculated in consecutive iterations. Once the differences are smaller than this threshold value, the algorithm converges (so the energy obtained in this particular step is the ground state value). One can also set the maximum number of iterations, spin symmetry of the system, temperature, and quantities connected with the chosen procedure of diagonalization (linear mixing or Broyden algorithm). For time-dependent

code, e.g. length of the trajectory or the time step between consecutive iterations can be modified,

- *predefines.h* – here, the dimensions of the computational lattice are set,
- *problem-definition.h* – in this file, the particular physical problem is defined. Among various functions, one can modify, for example, the external potential, pairing potential, velocity field, and densities,
- *logger.h* – allows to determine the quantities that will be printed in the output files.

The W-BSk Toolkit was first introduced in [3], along with details of its construction. Additionally, the repository providing all the settings necessary to reproduce the results from this paper can be found in [178].

3.6.1 Static Problems

The description of the numerical procedure described in this section is based on [179, 180].

Initially, one can gain insight into the self-consistent procedure for obtaining the ground state of the system. Technically, it can be achieved by solving equations with a structure similar to the BdG equations, as shown in Eq. 3.10. At this point, one should remind that they are highly nonlinear, as the potentials included in the Hamiltonian depend on densities and, consequently, also on quasiparticle wave functions. From the mathematical perspective, it corresponds to the so-called fixed point problem, which can be written as:

$$K[\boldsymbol{\varphi}] = \boldsymbol{\varphi}. \tag{3.179}$$

In this relation, K (which is called a map) denotes the left side of Eq. 3.10 divided by ε_n. In general, such problems are solved within iterative algorithms, where in each of the steps a solution vector is obtained (the shorthand notation for this vector is $\boldsymbol{\varphi}$). The solution obtained in a given iteration provides the initial conditions for calculations in the next step, until the system reaches its lowest energy state. At such a moment, the algorithm converges, which means that in the i-th iteration $|\boldsymbol{\varphi}_i < K[\boldsymbol{\varphi}_i]| < \epsilon$, where ϵ is some arbitrarily chosen constraint.

In this particular case, the solution $\boldsymbol{\varphi}$ from Eq. 3.179 corresponds to the set of densities for both species of nucleons (neutrons n and protons p): $\boldsymbol{\rho} = [\rho_n, \rho_p, \tau_n, \tau_p, \nu_n, \nu_p, \boldsymbol{j}_n, \boldsymbol{j}_p]$. This can be written in shorthand notation as $\boldsymbol{\rho} = [\rho_q, \tau_q, \nu_q, \boldsymbol{j}_q]$ with $q = n, p$. Then, the map K represents the following operations:

- at first, based on some input values of densities $\boldsymbol{\rho}_{\text{in}} = [\rho_q^{\text{in}}, \tau_q^{\text{in}}, \nu_q^{\text{in}}, \boldsymbol{j}_q^{\text{in}}]$, potentials from Eqs. 3.161 - Eq. 3.165 are computed and inserted into expression for Hamiltonian (Eq. 3.166). Pairing potential is computed from Eq. 3.167 with regard to the proper functional derivative,
- then, Hamiltonian matrix (Eq. 3.10) is constructed and diagonalized. Based on that, wave functions are extracted and inserted to Eqs. 3.156 - 3.159 for densities. Then, the output densities $\boldsymbol{\rho}_{\text{out}} = [\rho_q^{\text{out}}, \tau_q^{\text{out}}, \nu_q^{\text{out}}, \boldsymbol{j}_q^{\text{out}}]$ are obtained,
- usually, we search for a solution with the requested number of particles. Therefore, in the next step, the input chemical potential μ_{in}^q is modified in order to keep the number of particles conserved. For example, if the number of particles is smaller than initially imposed N_{req}^q, the chemical potential increases (and vice versa). The output value of chemical potential in particular iteration μ_{out}^q can be written as:

$$\mu_{\text{out}}^q = \mu_{\text{in}}^q + \frac{\alpha_\mu}{N_{\text{req}}^q}\left[N_{\text{req}}^q - \int \rho(\boldsymbol{r})\, d\boldsymbol{r}\right], \tag{3.180}$$

  where N_{req}^q means the requested number of particles. As a result, the number of particles matches the expected value in the consecutive iteration.

The self-consistent solution corresponds to the following condition: $|\boldsymbol{\rho}_{\text{in}} - \boldsymbol{\rho}_{\text{out}}| < \epsilon$, where ϵ is the constant parameter set at the beginning of calculations. In general, solving the fixed point problem is typically accomplished using either the linear mixing method or the Broyden algorithm. In the linear mixing, the n-th solution is approximated as:

$$\rho_{n+1} = \alpha K[\rho_n] + (1 - \alpha)\rho_n \tag{3.181}$$

where α is the mixing parameter taking the values from 0 to 1. In the Broyden algorithm, one can obtain the solution by finding a root of the following equation:

$$K[\rho] - \rho = 0. \tag{3.182}$$

In this method, the Jacobian matrix is estimated based on a selected number of previous iterations.

At this point, it should be mentioned that in practical applications, instead of checking the difference directly for densities, the change of energy is considered. As energies are computed from densities (there is a mapping between these quantities), it can be seen that changes in densities have to induce changes in energies, which are easier to interpret. The accuracy of the energy extraction of the initial state is of the order of keV per nucleon [3].

3.6.2 Time-Dependent Problems

The procedure described in this section is based on [75, 176, 181, 182, 183].

In general, the time-dependent HFB equations (Eq. 3.92) can be written in the short-hand form (to simplify notation in this section, we set $\hbar = 1$):

$$i\frac{\partial \varphi_n(\boldsymbol{r},t)}{\partial t} = \mathcal{H}(\boldsymbol{\varphi},t)\varphi_n(\boldsymbol{r},t), \tag{3.183}$$

where $\mathcal{H}$ is the Hamiltonian matrix dependent on the whole set of eigenfunctions: $\boldsymbol{\varphi} = [\varphi_1, \varphi_2, ...]$ and on time as well (through the time-dependent external potentials). The solution of Eq. 3.183 reads:

$$\varphi_n(\boldsymbol{r},t) = \mathcal{T}\exp\left[-i\int_0^{t'}\mathcal{H}(\boldsymbol{\varphi},t')dt'\right]\varphi_n(\boldsymbol{r},0) \tag{3.184}$$

with $\mathcal{T}$ being the time-ordering operator, and $\varphi_n(\boldsymbol{r},0)$ the initial solution (the ground state obtained within the self-consistent procedure from Sec . 3.6.1). When the external potentials do not depend on time (so when $\mathcal{H}(\boldsymbol{\varphi},t)$ becomes $\mathcal{H}(\boldsymbol{\varphi})$), the quasiparticle state evolution can be written as:

$$\varphi_n(\boldsymbol{r},t) = \exp(-iE_nt)\varphi_n(\boldsymbol{r},0). \tag{3.185}$$

Based on this formula, it can be seen frequency of oscillations in time depends on the energy of orbitals (the rapidity increases with their energy). In order to mild these fluctuations, one can bring Eq. 3.183 to the following form with regard to the so-called

instantaneous energy $\langle \mathcal{H}(\boldsymbol{\varphi}, t)\rangle_n$:

$$i\frac{\partial \varphi_n(\boldsymbol{r}, t)}{\partial t} = \left[\mathcal{H}(\boldsymbol{\varphi}, t) - \langle \mathcal{H}(\boldsymbol{\varphi}, t)\rangle_n\right] \varphi_n(\boldsymbol{r}, t). \tag{3.186}$$

The solutions of Eq. 3.183 and Eq. 3.186 are the same up to the phase factor, which cancels out during the computation of densities. Then, the phase factor is suppressed, and all the orbitals fluctuate with similar frequency. This allows the selection of an integration time step Δt that assures accurate computation for all orbitals.

For time integration, in W-BSk Adams-Bashforth-Moulton (ABM) algorithm is adopted. It is one of the multistep methods that allows for improving the stability of integration. In order to apply this algorithm, one can write Eq. 3.186 (which is, in fact, an equation of motion) in the following way:

$$\dot{\boldsymbol{\varphi}} = \boldsymbol{f}(\boldsymbol{\varphi}, t), \tag{3.187}$$

where $\boldsymbol{f} = -i[\mathcal{H}(\boldsymbol{\varphi}, t) - \langle \mathcal{H}(\boldsymbol{\varphi}, t)\rangle_n]\boldsymbol{\varphi}(\boldsymbol{r}, t)$. With regard to the notation commonly used in the ABM method, it can be written that $f_k \equiv f(\boldsymbol{\varphi}_k, k\Delta t)$ and $\boldsymbol{\varphi}_k \equiv \varphi(k\Delta t)$, where Δt is the time integration step. In the ABM algorithm, the integration procedure consists of two steps: predictor and corrector. In case of DFT-based simulations, the combination of the 5th-order predictor:

$$\begin{aligned}\boldsymbol{\varphi}_k^{(p)} = \boldsymbol{\varphi}_{k-1} &+ \frac{1901}{720}\Delta t \boldsymbol{f}_{k-1} - \frac{2774}{720}\Delta t \boldsymbol{f}_{k-2} + \\ &+ \frac{2616}{720}\Delta t \boldsymbol{f}_{k-3} - \frac{1274}{720}\Delta t \boldsymbol{f}_{k-4} + \frac{251}{720}\Delta t \boldsymbol{f}_{k-5}\end{aligned} \tag{3.188}$$

and 5-th order corrector:

$$\begin{aligned}\boldsymbol{\varphi}_k = \boldsymbol{\varphi}_{k-1} &+ \frac{251}{720}\Delta t \boldsymbol{f}(\boldsymbol{\varphi}_k^{(p)}, k\Delta t) + \frac{646}{720}\Delta t \boldsymbol{f}_{k-1} - \frac{264}{720}\Delta t \boldsymbol{f}_{k-2} + \\ &+ \frac{106}{720}\Delta t \boldsymbol{f}_{k-3} - \frac{19}{720}\Delta t \boldsymbol{f}_{k-4}\end{aligned} \tag{3.189}$$

is the most efficient one.

Apart from the ABM method, in W-BSk software, a few first steps are calculated within

a single-step integrator method based on the Taylor expansion of the evolution operator:

$$\begin{aligned}\varphi_n(\boldsymbol{r}, t+\Delta t) &= \mathcal{T}\exp\left[-i\int_t^{t+\Delta t}\mathcal{H}(\boldsymbol{\varphi}, t')dt'\right]\varphi_n(\boldsymbol{r}, t) = \\ &\approx \exp\left[-i\mathcal{H}\left(\boldsymbol{\varphi}, t+\frac{\Delta t}{2}\right)\Delta t\right]\varphi_n(\boldsymbol{r}, t) = \\ &\approx \sum_{k=0}^{r}\frac{(-i\Delta t)^k}{k!}\left[\mathcal{H}\left(\boldsymbol{\varphi}, t+\frac{\Delta t}{2}\right)\right]^k\varphi_n(\boldsymbol{r}, t).\end{aligned} \tag{3.190}$$

In this expansion, the order of truncation r has to be equal to the order of the corrector in the ABM algorithm, which is set to 5 in this case. Based on that, the state for the midtime $(t + \Delta t/2)$ is obtained with regard to the predictor:

$$\varphi_n^{(p)}(\boldsymbol{r}, t+\frac{\Delta t}{2}) \approx \sum_{k=0}^{r}\frac{\left(-i\frac{\Delta t}{2}\right)^k}{k!}\left[\mathcal{H}(\boldsymbol{\varphi}, t)\right]^k\varphi_n(\boldsymbol{r}, t). \tag{3.191}$$

Later on, the integration step is proceeded with the corrector of the following form:

$$\varphi_n(\boldsymbol{r}, t+\Delta t) \approx \sum_{k=0}^{r}\frac{(-i\Delta t)^k}{k!}\left[\mathcal{H}\left(\boldsymbol{\varphi}^{(p)}, t+\frac{\Delta t}{2}\right)\right]^k\varphi_n(\boldsymbol{r}, t). \tag{3.192}$$

As the Hamiltonian is explicitly used $2r$ times in each time step of integration, this method is significantly slower than the ABM algorithm, which applies the Hamiltonian twice per time step. However, in the ABM method, there is a need to store the previous values of $\boldsymbol{f}_k$, which leads to higher memory consumption compared to the algorithm based on Taylor expansion.

3.6.3 Supercomputing

The calculations described above require significant computational power and must therefore be performed on supercomputers. The computational power of such machines is typically expressed in flops (floating-point operations per second) and can be enhanced with the aid of GPUs (graphics processing units). Such structures enable significantly faster calculations and are typically programmed in the CUDA language [176, 75]. Due to their great capabilities, they are commonly used in time-dependent

simulations, which often turn out to be very time-consuming [75]. Static calculations are conducted both on the CPUs (central processing units) of the supercomputer (which are programmed in C99 language) and GPUs, using the ELPA library for diagonalization [75]. The time-dependent calculations are executed entirely on GPUs.

The calculations, being the core of this thesis, have been performed on the supercomputers:

- Piz Daint in Swiss National Supercomputing Centre, Zurich (Switzerland) with 25.326 petaflops [184],
- LUMI in Center for Science, Kajaani (Finland) with 380 petaflops [185].

Chapter 4

Linear Movement of Impurity in Neutron Matter

This chapter is based on results published in: D. Pęcak, A. Zdanowicz, N. Chamel, P. Magierski and G. Wlazłowski, *Time-Dependent Nuclear Energy-Density Functional Theory Toolkit for Neutron Star Crust: Dynamics of a Nucleus in a Neutron Superfluid*, Phys. Rev. X 14, 041054 (2024).

4.1 Effective Mass – The State of The Art

One of the fundamental quantities that should be considered in models of the inner crust is the effective mass of impurity. The idea of this parameter comes from solid state physics, as it turned out that the behavior of electrons in a crystal lattice turns out to be different than, e.g., in vacuum due to the Bragg scattering [15]. Per analogy to such systems, the internal matter of neutron star crust can be considered as a lattice of impurities immersed in the superfluid neutrons [15, 186]. As well as in the case of electrons in solids, bare mass does not describe the properties of impurities properly [15]. Therefore, another parameter, called the effective mass, has been introduced. The following sections present some of the methods for estimating the effective mass of impurities in superfluid neutron matter.

4.1.1 The Geometrical Model

Considering the movement of impurity in the neutron medium, one should take into account that it is not only surrounded by neutrons, but some of them are also bound to the impurity [15, 3, 186]. Therefore, one cannot separate the impurity from the neutron background and analyze its movement without taking into consideration the influence

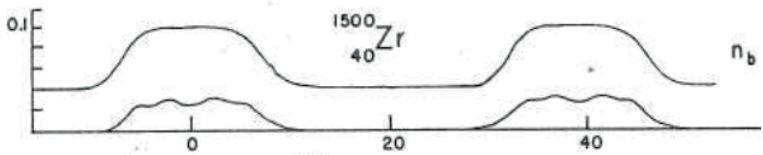

FIGURE 4.1: Density distribution of the of a system of impurities immersed in the medium (the geometrical model) [24].

of these bound neutrons; the cluster is supposed to be penetrable for neutrons, which also affects its properties [3]. Moreover, one should also mention that the interaction of impurity with the surrounding neutron matter can result in various dissipation mechanisms (such as energy flow between proton clusters and neutron matter) [3], which also has an impact on the estimation of the mass of impurity. Effective mass takes into account not only the inertia of impurity, but also the influence of the neutrons surrounding it [3, 187] and therefore allows for a proper description of the neutron star crust. Among various models that allow for estimating the effective mass of impurity, the geometrical one seems to be one of the most intuitive. According to this idea, a system of impurities immersed in the medium can be described with the density distribution, as shown in Fig. 4.1. In principle, in order to estimate the effective mass of the impurity, one can simply integrate the density distribution over position.

The geometrical approach can be considered as an example of a semi-classical method [3]. In such a case, the effective mass of the impurity is connected only with protons and neutrons bound in the cluster (so the influence of free neutrons surrounding the impurity is neglected). The number of bound neutrons N_b can be estimated according to the formula [3]:

$$N_b = \int (\rho_n(\boldsymbol{r}) - \rho_{bn})\, d\boldsymbol{r} \tag{4.1}$$

where ρ_{bn} means the density of background neutrons (this density is also called bulk density). The effective mass can be calculated as [3]:

$$M_{\text{eff}} = Zm_p + N_b m_n, \tag{4.2}$$

where Z is the number of protons and m_p is the proton mass, N_b means the number of bound neutrons and m_n is the neutron mass. When the background density approaches zero (which corresponds to the case of nuclei in the vacuum), $N_b = N$, where N is the number of neutrons.

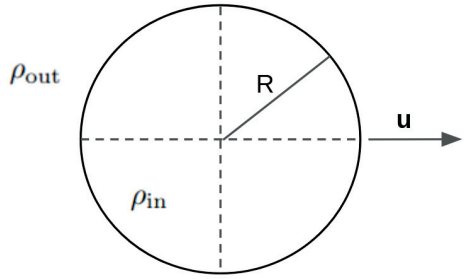

FIGURE 4.2: The schematic view of the investigated system: spherical impurity of density ρ_{in} moving with constant velocity $\boldsymbol{u}$ through the superfluid medium of density ρ_{out}.

4.1.2 The Hydrodynamic Approach

The effective mass of impurity has also been considered within the hydrodynamic approach [187, 188, 189], where impurity of mass M is considered as a sphere of sharp radius R and constant density, moving through a superfluid medium with the constant velocity $\boldsymbol{u}$. The density inside of impurity is denoted as ρ_{in} and ρ_{out} outside of it. This system is sketched in Fig. 4.2. It is assumed that impurity moves through the medium with velocity $\boldsymbol{u}$ and nucleons are treated as an irrotational and incompressible fluid [187]. Such a system can be analyzed with regard to velocity fields and potential fields associated with them [187].

In this model, velocity field $\boldsymbol{v}(\boldsymbol{r},t)$ corresponds to potential field $\Phi(\boldsymbol{r},t)$ according to the formula [99, 187]:

$$\boldsymbol{v}(\boldsymbol{r},t) = \nabla\Phi(\boldsymbol{r},t). \tag{4.3}$$

Moreover, the matter is supposed to be incompressible, so [99]:

$$\nabla \cdot \boldsymbol{v}(\boldsymbol{r},t) = 0. \tag{4.4}$$

Later on, one can define the potential field related to the velocity of internal matter of impurity and to the medium outside of it [187]. In the following analysis, the potential field inside the impurity (for any distance r, measured from the center of the impurity, smaller than the radius of the impurity R, $r < R$) is denoted as Φ_{in} and Φ_{out} (for $r > R$) – outside of it. As a consequence of the continuity requirement [187], these potentials

have to fulfill the Poisson equations:

$$\nabla^2 \Phi_{\text{in}} = 0 \text{ for } r < R, \tag{4.5}$$

$$\nabla^2 \Phi_{\text{out}} = 0 \text{ for } r > R. \tag{4.6}$$

In the next step, one can define the boundary conditions (using radial coordinate r vector $\boldsymbol{n}$ normal to the surface of impurity) [188, 187]:

- velocity field has to be continuous at the „boundary" of impurity:

$$\Phi_{\text{in}}|_{r=R} = \Phi_{\text{out}}|_{r=R}, \tag{4.7}$$

- conservation of mass requires that:

$$\rho_{\text{in}} \left(\frac{\partial \Phi_{\text{in}}}{\partial r}\bigg|_{r=R} - \boldsymbol{n} \cdot \boldsymbol{u} \right) = \rho_{\text{out}} \left(\frac{\partial \Phi_{\text{out}}}{\partial r}\bigg|_{r=R} - \boldsymbol{n} \cdot \boldsymbol{u} \right), \tag{4.8}$$

- the field outside of impurity is supposed to disappear, as r approaches infinity:

$$\Phi_{\text{out}}|_{r \to \infty} = 0. \tag{4.9}$$

Solving Eqs. 4.5 - 4.6 with the boundary conditions mentioned above leads to the following expressions for velocity potentials [187]:

$$\Phi_{\text{in}} = \frac{1 - \kappa'}{2\kappa' + 1} \boldsymbol{u} \cdot \boldsymbol{r}, \tag{4.10}$$

$$\Phi_{\text{out}} = \frac{1 - \kappa'}{2\kappa' + 1} \left(\frac{R}{r} \right)^3 \boldsymbol{u} \cdot \boldsymbol{r}, \tag{4.11}$$

where $\kappa' = \rho_{\text{out}}/\rho_{\text{in}}$. The difference between the potential field inside and outside of the impurity arises due to the presence of the impurity, which distorts the superflow of the background neutrons [82].

Later on, one can consider the kinetic energy associated with this system [187]:

$$T = \frac{1}{2} m_n \int_V \rho(\boldsymbol{r}) \, |\nabla \Phi(\boldsymbol{r})|^2 \, d^3\boldsymbol{r}, \tag{4.12}$$

where m_n means the mass of a nucleon. The integral can be divided into two parts: integration for $r < R$ (inside the impurity) and $r > R$ (outside the impurity). Then, with regard to the divergence theorem [20]:

$$\int_V |\nabla\Phi|^2 \, d\boldsymbol{r} = \oint_S \Phi\nabla\Phi \cdot d\boldsymbol{S}, \tag{4.13}$$

one can write the expression for the kinetic energy of the impurity [187]:

$$T = \frac{1}{2} m_n \, \rho_{\text{in}} \oint_S \Phi_{\text{in}} \frac{\partial\Phi_{\text{in}}}{\partial r} \, dS - \frac{1}{2} m_n \, \rho_{\text{out}} \oint_S \Phi_{\text{out}} \frac{\partial\Phi_{\text{out}}}{\partial r} \, dS, \tag{4.14}$$

where as S we have selected the surface of the nucleus. The minus sign in front of the second term reflects that vectors $\nabla\Phi$ and $d\boldsymbol{S}$ have opposite directions. Then, once the boundary conditions are applied to Eq. 4.14, one can obtain the following formula for kinetic energy [187]:

$$T = \frac{1}{2} m(\rho_{\text{in}} - \rho_{\text{out}}) \oint_S \Phi_{\text{in}}|_{r=R} \boldsymbol{u} \cdot \boldsymbol{n} \, dS \tag{4.15}$$

which, after substitution of expression for internal potential from Eq. 4.10, leads to [187]:

$$T = \frac{2}{3} \pi R^3 m \, \rho_{\text{in}} \frac{(1-\kappa')^2}{2\kappa' + 1} u^2. \tag{4.16}$$

One can compare this result with the common formula for kinetic energy: $M_{\text{eff}} u^2/2$, where M_{eff} denotes the effective mass of impurity in the neutron matter. Then, one can obtain this parameter from the relation [187]:

$$M_{\text{eff}} = \frac{4}{3} \pi R^3 m_n \frac{(\rho_{\text{in}} - \rho_{\text{out}})^2}{\rho_{\text{in}} + 2\rho_{\text{out}}}. \tag{4.17}$$

The predictions of these formulas will be confronted with fully microscopic results later in this section.

4.2 Effective Mass within Density Functional Theory

4.2.1 Methodology

In this section, a novel method for obtaining the effective mass of an impurity in superfluid neutron matter is presented. In contrast to other theoretical approaches, this

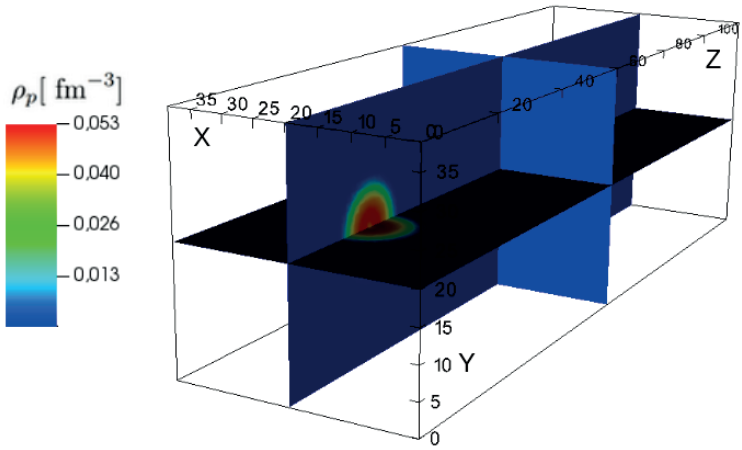

FIGURE 4.3: Initial setup of the simulated system for density 0.006 fm^{-3}: the impurity is placed close to the end of the box. During the simulation, it moves along z axis.

method enables the extraction of this parameter using a minimal number of assumptions. As the simulations are based on DFT, they are expected to provide precise and reliable results.

The initial configuration of the simulated system for exemplary density 0.006 fm^{-3} is shown in Fig. 4.3 as a three-dimensional box. The colorbar on the left side corresponds to the density of protons (ρ_p) in units of fm^{-3} (which takes the highest value in the middle of the impurity). In general, the main aim of this part of the research was to investigate the behavior of single nuclei of zirconium (with $Z = 40$), as it turns out to be the most stable one from all the isotopes that are present in the crust. In the simulated system, the impurity is placed close to the end of the box. The nuclei are immersed in the sea of superfluid neutrons; therefore, far from impurity, the density of neutrons reaches the value of the so-called bulk (or background) density. It is also worth mentioning that free neutrons forming neutron matter can be considered part of the nucleus. Then, such a nucleus is extremely neutron-rich. In these calculations, impurity is expected to be permeable to neutrons, which corresponds to the real structure of the inner crust. Then, in the vicinity of impurity, one cannot precisely define whether the neutrons belong to the impurity or to the background.

In order to make the following part of this chapter clearer, the list of densities used

in the analysis is provided:

- nuclear (crustal) density $\bar{\rho}$: average density of nucleons (including both protons and neutrons) corresponding to the particular depth in the crust. In the following part of the thesis, it is also referred to, in short, as density,
- background (bulk) density of neutrons ρ_{bn}: density of neutrons far from impurity (for numerical reasons, in the calculations it was set to the value in the corner of the box),
- density of protons: $\rho_p(\boldsymbol{r})$,
- total density of neutrons: $\rho_n(\boldsymbol{r})$.

Static Calculations

Numerical procedure consists of three main steps: obtaining ground state solution, calculating wave functions for the initial state, and, finally, time evolution of the system in the presence of the external electric field. Finding a ground state solution involves solving static HFB equations with a constraint on the number of particles (the procedure of obtaining the ground state solution is described in detail in Sec. 3.6). While the number of protons is set to 40, the number of neutrons is chosen to obtain the expected density far from impurity (such density will be later called the bulk density of neutrons). These calculations were performed on a lattice with the following dimensions:

- grid: 32 x 32 x 32 (which means 32 lattice points in each direction),
- lattice spacing: 1.25 x 1.25 x 1.25 (distance (in fm) between consecutive points of lattice).

As a result, the entire system can be considered a three-dimensional box with dimensions 40 fm x 40 fm x 40 fm, containing a single impurity at its center.

Calculations described here were performed for several densities corresponding to different locations in the crust. In general, in the lowest energy state, density distributions (densities as a function of distance from the center of the box) of particular species of nucleons are expected to be spherically symmetric. Indeed, the obtained solutions fulfilled this assumption. Fig. 4.4 shows an exemplary distribution for neutrons, protons, and total density of nucleons calculated for a nuclear density $\bar{\rho} = 0.015$ fm^{-3}. The

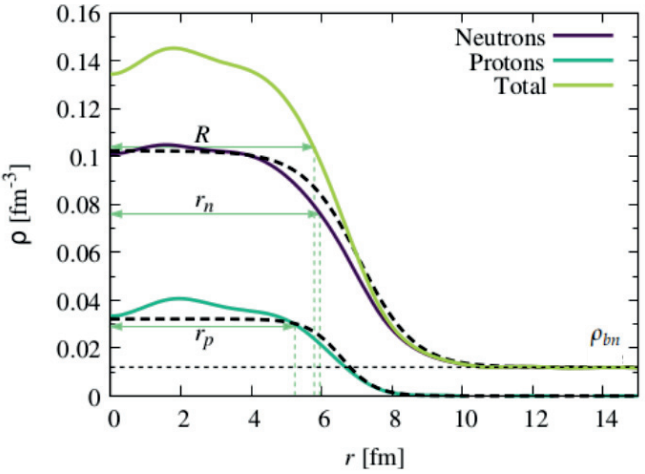

FIGURE 4.4: Density profile for $\bar{\rho} = 0.015$ fm^{-3} [3]. Solid lines show the results of the static DFT method, dashed lines correspond to the results of Thomas-Fermi calculations from [190]. Arrows denote the radius of neutrons r_n, protons r_p, and the whole impurity R obtained from Eq. 4.18. ρ_{bn} is the background density of neutrons far from impurity.

variables r_n, r_p, and R denote (respectively) the radius of neutrons, protons, and the whole impurity. These quantities were obtained as the root-mean-square radius within the following relation:

$$R = \langle R^2 \rangle = \frac{\int \rho(\boldsymbol{r}) r^2 d\boldsymbol{r}}{\int \rho(\boldsymbol{r}) d\boldsymbol{r}}. \tag{4.18}$$

While calculating the radius of the whole impurity, $\rho(\boldsymbol{r})$ had the meaning of the sum of densities of protons and neutrons with subtracted bulk density of neutrons (so $\rho = \rho_n + \rho_p - \rho_{bn}$). Similarly, in the case of the radius of neutrons, ρ was equivalent to $\rho_n - \rho_{bn}$ (therefore, it corresponds to the density of neutrons bound in the cluster from the geometrical case). For the radius of protons, $\rho = \rho_p$.

As can be seen in Fig. 4.4, the bulk density of neutrons saturates to the expected value far from the impurity. On the contrary, in the region close to the center of impurity, all the densities reach maximal values due to the contribution of the density of protons. To compare the obtained results with predictions of other methods, calculations in the frame of the semi-classical model (based on Thomas-Fermi calculations in spherical Wigner-Seitz cells and presented in [190]) are also provided and marked with dashed lines. The visible discrepancies come from phenomena that were not included in the

semi-classical model, such as shell and pairing effects [190]. As a consequence, density profiles coming from this approach are almost constant in the middle of the box. Since the results obtained using the DFT method are fully microscopic, they can be considered the most accurate. Nevertheless, the comparison of dynamic predictions with the semi-classical ones demonstrates their correctness.

As the ground state was obtained, the box was extended in z direction to in order to provide enough space for movement of impurity. In this case, the z dimension equal 120 fm (corresponding to a grid of size 96 with lattice spacing 1.25 fm) was expected to provide enough space for the movement. The additional space in the box was filled with neutrons of density equal to their bulk density in the previous step. The wave functions obtained at this stage of simulations correspond to wave functions (for protons and neutrons) for time equal 0: $[u_{n\uparrow}(\boldsymbol{r},0), v_{n\downarrow}(\boldsymbol{r},0)]$. Starting from these wave functions, time evolution could have been proceeded.

Time-dependent Calculations

In the time-dependent simulations, an electric field in direction of z axis has been applied. Here, it took the form of an external potential:

$$V_p^{\text{ext}} = -\frac{1}{Z}\boldsymbol{F}\cdot\boldsymbol{r}, \tag{4.19}$$

where Z is the number of protons and $\boldsymbol{r}$ means position. Electric force $\boldsymbol{F}$ is connected with electric field E as $\boldsymbol{F} = Ze\boldsymbol{E}$ with e being the charge of an electron. As the force has been expected to act only in z direction, the only component of electric field is the z-th one (so $\boldsymbol{E} = [0,0,E_z]$). In the code, the electric field has been turned on gradually according to the following scheme:

$$E_z(t) = \begin{cases} 0 \text{ for } t < t_1, \\ E_z\, s(t-t_1, t_2-t_1) \text{ for } t_1 < t < t_2, \\ E_z \text{ for } t_2 < t. \end{cases} \tag{4.20}$$

At the time denoted as t_1, the electric field starts to rise and reaches its expected value at time t_2. The function s that switches on the field can be written as:

$$s(t, \Delta t) = \frac{1}{2}\left\{1 + \tanh\left[\tan\left(\pi\frac{t}{\Delta t} - \frac{\pi}{2}\right)\right]\right\}, \tag{4.21}$$

where $\Delta t = t_2 - t_1 = 10$ fm/c.

Effectively, the electric field acts only on protons, as they are the only charged components in the system. Consequently, the only object that is moved by the electric field is the proton impurity. One of the crucial advantages that stands behind this approach is that there is no need to make an artificial distinction between free and bound neutrons. Such a separation causes various difficulties, as „bound" and „free" neutrons do not have a well-defined meaning. Therefore, if the protocol depends on their densities, the extracted parameter would be highly influenced by the definition of these quantities. On the contrary, the density of protons is a well-defined quantity, as it is localized entirely in the impurity. As a result, it seems more reasonable to define the entire protocol in terms of proton density.

Based on the results of time-dependent calculations, the position of the center of mass of the impurity could have been extracted. Then, its velocity and acceleration have been obtained. Finally, one could calculate the effective mass of the cluster from the II law of dynamics.

4.2.2 Effective Mass from Linear Movement of Impurity

As mentioned above, the crucial quantity extracted from dynamical simulations is the position of the impurity's center of mass. It can be defined with regard to the density of protons ρ_p in the following way:

$$\boldsymbol{R}(t) = \frac{1}{Z}\int \rho_p(\boldsymbol{r}, t)\, \boldsymbol{r}\, d\boldsymbol{r}. \tag{4.22}$$

The dependence of $\boldsymbol{R}$ on time for exemplary density 0.006 fm^{-3} is shown in Fig. 4.5. Each of the lines corresponds to a particular force, $F = ZeE_z$, acting on the impurity. Based on these results, the velocity of the center of mass could have been obtained as:

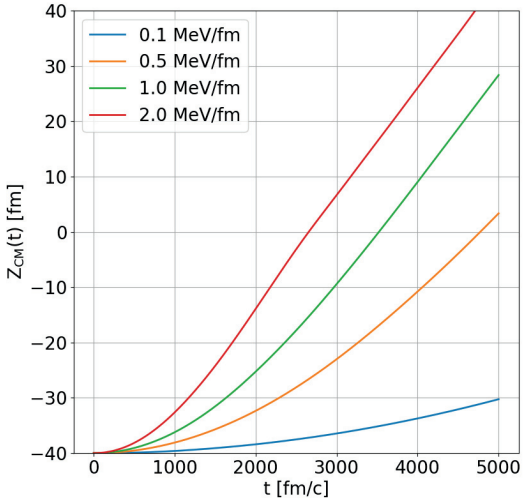

FIGURE 4.5: Position of center of mass $\boldsymbol{R}$ of impurity as a function of time for electric forces: 0.1, 0.5, 1.0, and 2.0 MeV/fm for density 0.006 fm^{-3}.

$$\boldsymbol{v}(t) = \frac{d\boldsymbol{R}}{dt}. \tag{4.23}$$

One should keep in mind that the velocity calculated within this equation corresponds in fact to the z-component of velocity, as this is the only direction in which the electric field is applied (so $\boldsymbol{v} = [0, 0, \boldsymbol{v}_z(t)]$).

Let us take a closer look at the plot of velocity. As an example, in Fig. 4.6 velocity of impurity v (in units of c) as a function of time (fm/c) for different electric forces (in MeV/c) and for nuclear density $\bar{\rho} = 0.006$ fm^{-3} is shown. As can be seen, one can distinguish different regimes of motion:

- first of them (for times below $\approx$ 1000 fm/c), marked as a, is the limit in which velocity arises linearly, which is a characteristic feature of dissipationless flow. Based on this part, the extraction of effective mass was possible,
- when time exceeds 1000 fm/c (regions b and **c**), velocity arises significantly slower (so, in other words, its linear behavior is disrupted). Therefore, mechanisms of dissipation are expected to occur within the system.

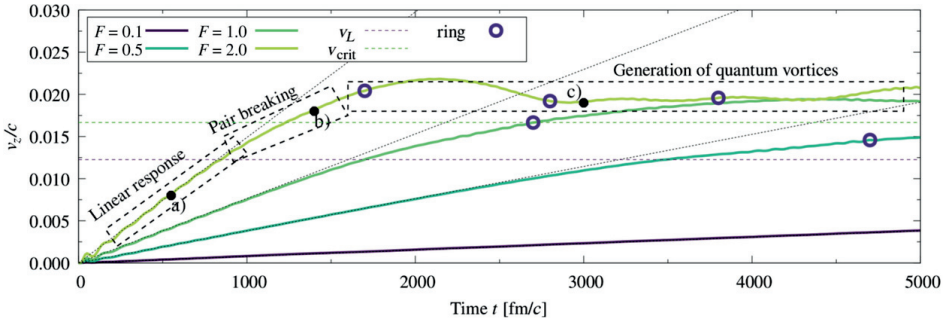

FIGURE 4.6: Velocity of center of mass of impurity as a function of time for nuclear density $\bar{\rho} = 0.006$ fm^{-3} corresponding to background density of neutrons $\rho_{bn} \approx 0.0045$ fm^{-3}. Solid lines show the results of time-dependent DFT calculations for different electric forces (in MeV/fm). Dotted lines correspond to the fitting to the linear part of the plot. Dashed lines denote the threshold velocities: Landau (blue) and critical (green). Circles indicate the time moments for which quantum vortices have been detected. In addition, the regions in which the linear movement of impurity and mechanisms of dissipation (pair breaking and generation of quantum vortices) have been observed are indicated and marked with letters.

First of all, one can make the connection between the dissipationless movement of impurity at the beginning of the simulation and the superfluid properties of the system. In principle, superflow can occur in this system only for velocities below a certain threshold level, which is the Landau velocity (marked in the figure with the dashed line and denoted as v_L). Then, the impurity can move through the medium without any friction. In such case, according to II law of dynamics, one can extract the effective mass M_{eff} from relation $\boldsymbol{F} = M_{\text{eff}}\, \boldsymbol{a}_z$, where $\boldsymbol{a}_z$ is the z-component of acceleration (which also can be extracted from numerical results as $\boldsymbol{a}_z(t) = d\boldsymbol{v}_z(t)/dt$). In practice, this has been achieved by linear fitting (denoted in Fig. 4.6 by black dashed lines) to the initial part of the plot, where the velocity increases linearly. Simultaneously, once the Landau velocity is exceeded, the process of destruction of superfluidity begins, which means that Cooper pairs start to break down. Later on, once the critical velocity (marked with the green dashed line and denoted as v_{crit}) is reached, the mechanism of dissipation changes from Cooper pair breaking to generation of vortex rings (in the figure, the blue circles denote the time at which vortices have been detected). It should also be pointed out that locally (in the nearest surroundings of impurity), the system turns into the normal phase once the critical velocity is reached. This, in turn, results in the movement of the impurity with approximately constant velocity. However, as

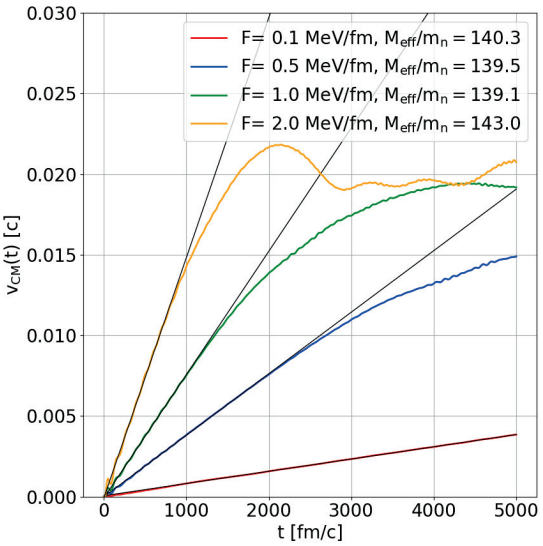

FIGURE 4.7: Velocity of center of mass v of impurity as a function of time for electric forces: 0.1, 0.5, 1.0, and 2.0 MeV/fm for density 0.006 fm^{-3}. The legend provides the effective masses extracted for each of the forces. The fitting lines are marked in black.

the rest of the system remains superfluid, one can still observe some specific effects, such as the creation of quantum vortices far from the impurity. Additionally, the critical velocity can be considered as the limiting velocity in the system. As one can see in Fig. 4.6, the velocity of impurity barely exceeds the value of v_{crit}.

The effective mass has been extracted systematically for each of the external forces. In Fig. 4.7, the plot of velocity as a function of time for density 0.006 fm^{-3} is shown. In addition, effective masses extracted from linear fitting (the fitting lines are marked with black) for different forces are presented in the legend. To determine the value of this parameter for a particular density, the average of the effective masses obtained for the two middle forces has been calculated. Another issue is related to uncertainty estimation. The error of effective mass estimation has been assumed to be the range between the effective mass for the smallest force and the effective mass for the given density (obtained as the average of the results of two forces in the middle). In the case of density 0.006 fm^{-3}, the following result have been obtained:

- external force 0.1 MeV/fm: effective mass 140.3 (in units of neutron mass m_n),

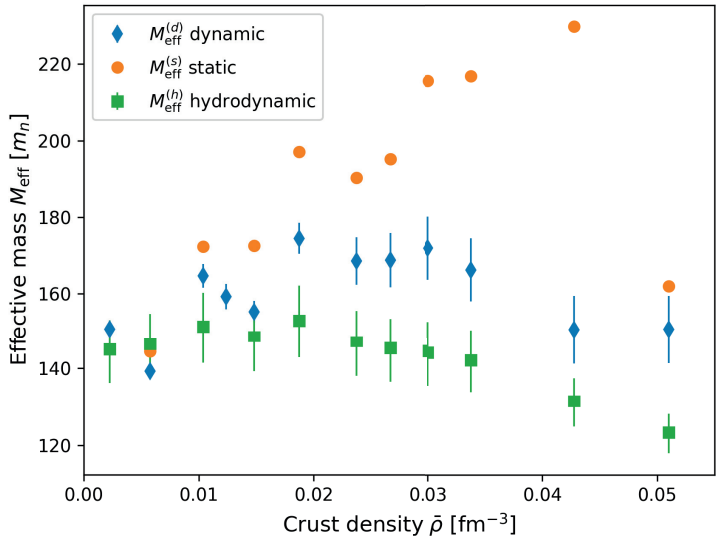

FIGURE 4.8: Effective mass of impurity extracted within various methods as a function of nuclear density [3]. The series denoted as *static* has been obtained within the semi-classical formula from Eq. 4.2, *hydrodynamic* results have been obtained with Eq. 4.17, and *dynamic* – within the dynamic method discussed in this chapter.

- 0.5 MeV/fm: 139.5 m_n,
- 1.0 MeV/fm: 139.1 m_n,
- 2.0 MeV/fm: 143.0 m_n.

Then, the effective mass was calculated as the average of the results for 0.5 MeV/fm and 1.0 MeV/fm: $(139.5\ m_n + 139.1\ m_n/2$, which gives 139.3 m_n. The error bar is expected to be equal: 140.3 m_n − 139.3 m_n = ±1.0 m_n (effective mass for the force 0.1 MeV/fm - final effective mass for this density).

Fig. 4.8 shows the effective mass extracted for different nuclear densities and within various approaches. In the limit of low densities (below 0.01 fm^{-3}), the effective mass calculated within the dynamic approach is in good agreement with results obtained using other methods. However, the discrepancy arises with density. In the case of a static approach, the reason for this difference lies in the estimation of the number of

bound neutrons, estimated with regard to Eq. 4.1. Then, according to Eq. 4.2, it can be seen that the number of bound neutrons and, consequently, also the effective mass, increases with density (while in the dynamic approach, such a dependence cannot be clearly observed). As a result, it turns out that the influence of free neutrons cannot be neglected.

On the other hand, the main difference between the hydrodynamic and dynamic methods is connected with the radius of impurity, which in hydrodynamics is expected to be precisely defined. Therefore, the hydrodynamic effective mass tends to be shifted in relation to dynamic results. Moreover, the only effect connected with the interaction between the impurity and the surrounding medium is the excitation of the superfluid, while many others (such as Cooper pair breaking or various dissipation mechanisms) can also affect the obtained value of the effective mass.

4.2.3 Mechanisms of Dissipation

As mentioned before, the acceleration of impurity leads to the loss of superfluid properties of the medium surrounding it. When the velocity of the impurity exceeds the Landau velocity, its kinetic energy is high enough to be transferred to the medium; simultaneously, the impurity's movement is no longer linear, and various dissipation mechanisms (such as Cooper pair breaking and the creation of quantum vortices) occur in the system. This results in a transition from a superfluid to a normal phase, which is, however, a gradual process during which both phases can coexist. Consequently, the main channel of dissipation depends on the velocity of the impurity.

The velocity of impurity impacts one of the fundamental quantities describing superfluid systems, which is called condensation energy. As it has been widely discussed in Chap. 2, condensation is a characteristic phenomenon taking place in the case of bosons, which at very low temperatures tend to form a condensate (where all the particles occupy the lowest energy state). However, it turns out that the same behaviour can also be observed in the case of fermions, where Cooper pairs condense to the ground state (then, the total momentum and spin of each pair is equal to 0). The energy associated with such a process is called condensation energy; when superfluidity in the system is destroyed and Cooper pairs are broken, the condensation energy decreases.

In general, the energy E of the uniform system in the frame of BCS theory can be written as [31]:

$$E = E_{\mathrm{FFG}} - \frac{3}{8}\frac{N|\Delta_n|^2}{\varepsilon_{Fn}}, \tag{4.24}$$

where ε_{Fn} is Fermi energy of neutrons equal $\hbar^2(3\pi^2\rho_n)^{2/3}/(2m_n^*)$ with m_n^* being effective mass of neutron, N is the number of particles (neutrons) and E_{FFG} corresponds to the energy of free Fermi gas. The second component on the right side of Eq. 4.24 is connected with the emergence of Cooper pairs in the system (so when $\Delta \neq 0$). Their presence lowers the energy by the amount $\frac{3N\Delta^2}{8\varepsilon_F}$, called the condensation energy, with respect to the energy of a Fermi gas in the normal state. Based on that, within local density approximation (so with an assumption that at each point of the system, it can be treated locally as uniform), one can extend Eq. 4.24 to the case of a non-uniform system. Then, the expression for condensation energy that has been used in this research can be written as [31]:

$$E_{\mathrm{cond}}(\boldsymbol{r},t) \approx \int \frac{3}{8}\frac{|\Delta_n(\boldsymbol{r},t)|^2}{\varepsilon_{Fn}(\boldsymbol{r},t)}\rho(\boldsymbol{r},t)d\boldsymbol{r}, \tag{4.25}$$

where now all quantities are computed locally. One way to examine various mechanisms of dissipation is to analyze the velocity of impurity and the behavior of condensation energy as a function of time. In Fig. 4.9a) velocity of impurity v_z (in units of Landau velocity v_L) as a function of time is presented; panel b) shows the condensation energy E_{cond} in corresponding time [3]; both of these quantities have been calculated for various average densities shown in the legend. As can be seen, as long as the velocity of impurity rises linearly, the condensation energy is fairly constant. Later on, once the Landau velocity is exceeded, the condensation energy begins to decrease, indicating that Cooper pairs are breaking and providing a dissipation channel in this velocity regime.

At this point, one should also make a few additional remarks about superfluidity in the discussed system. First of all, it is important that superfluidity is not definitely destroyed when the velocity of impurity becomes larger than the Landau velocity. According to [191, 192], superfluid and normal phases can coexist in the system also for higher velocities, unless the velocity of the impurity remains lower than the so-called critical velocity. It can be written with regard to Landau velocity in the following way

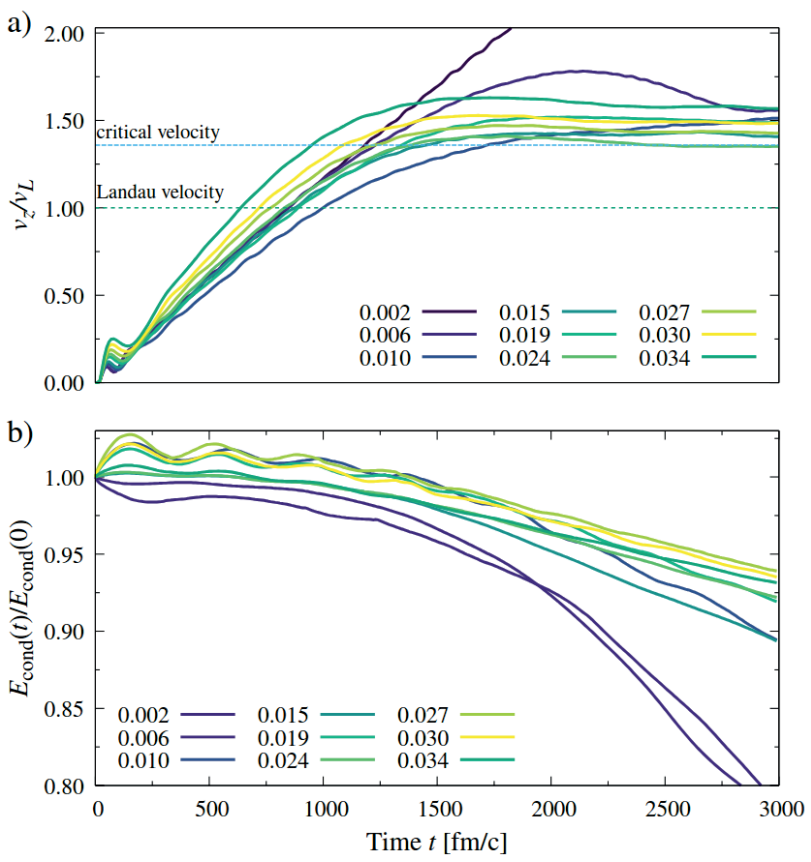

FIGURE 4.9: a) Velocity of impurity v_z in units of Landau velocity v_L, b) condensation energy E_{cond} with respect to the initial value $E_{\text{cond}}(0)$ as a function of time [3]. These quantities are presented for different nuclear densities, as remarked in the legend. In panel a), critical velocity is marked with a blue dotted line and Landau velocity with a green dashed line.

[191, 192]:

$$v_{\text{crit}} = \frac{\exp(1)}{2} v_L. \tag{4.26}$$

This velocity is understood as a limit, above which the superfluid phase cannot exist, and the system entirely turns into the normal state [191, 192]. Moreover, for velocities higher than the Landau velocity, superfluid matter shows some specific properties, usually referred to as gapless superfluidity. In such a case, despite the fact that the pairing potential takes a nonzero value, there is no gap in the energy spectrum, unless the velocity of the impurity remains lower than v_C [191, 192]. As shown in Fig. 4.9, in our simulations, this is also the maximum velocity that the impurity can reach. Despite the fact that Eq. 4.26 was derived within the assumption that the system is uniform, it turns out that this velocity provides a reliable description for nuclear matter as well.

In general, the propagation of impurity causes the movement in the neutron background fluid as well. Therefore, it has been examined whether the local velocity field of neutrons exceeds the Landau velocity. The evolution of the velocity field around the impurity for an exemplary density 0.006 fm^{-3} and external force 2.0 MeV/fm is illustrated in Fig. 4.10. Each of the subfigures shows the ratio between the velocity field of neutrons and the Landau velocity for a few chosen time moments. The velocity field was computed as $j_n(\boldsymbol{r})/\rho_n(\boldsymbol{r})$, where j_n is the neutron current and ρ_n the neutron density [3]. The meaning of the colorbars is the following:

- when the ratio is smaller than 1 (blue colors in the plots), the velocity field of neutrons is below the Landau velocity,
- later on, once the velocity field reaches this threshold value, the ratio is plotted in white,
- after that, when the velocity field is higher than the Landau velocity, the ratio is marked in red.

The Cooper pair breaking (corresponding to the moment at which Landau velocity is exceeded) starts to take place in the nearest surroundings of impurity. In addition, in the range of velocities higher than the Landau velocity but still below the critical velocity, vortex rings around the impurity could have been detected. Therefore, it can be assumed that the presence of vortex rings prevents the impurity from movement with a velocity greater than the critical velocity.

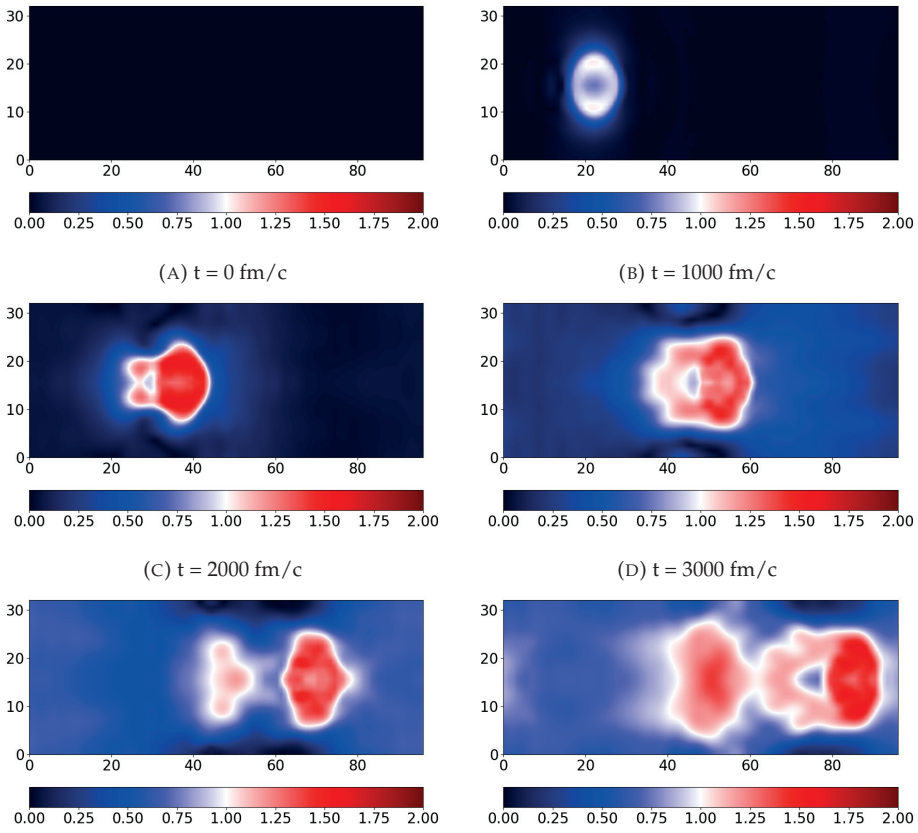

(A) t = 0 fm/c

(B) t = 1000 fm/c

(C) t = 2000 fm/c

(D) t = 3000 fm/c

(E) t = 4000 fm/c

(F) t = 5000 fm/c

FIGURE 4.10: Evolution of ratio of velocity field and Landau velocity for density 0.006 fm^{-3} for time moments: 0, 1000, 2000, 3000, 4000, and 5000 fm/c.

Fig. 4.11 (for density 0.006 fm^{-3} and external force 2.0 MeV/fm) provides an insight into the phenomena of vortex ring nucleation. In the figure, the red sphere represents the proton impurity. The bottom layer shows the neutron pairing field (denoted in the colorbar legend as $|\Delta|$), the blue background (ρ_n) represents neutron density, and the black arrow indicates the direction of the constant electric field. In panel a) (corresponding to the time moment of the simulation equal 3000 fm/c), one can observe the vortex ring (black circle) forming around the impurity and moving in tandem with it. Later on, as it is shown in panel b) (for time 4000 fm/c), another vortex ring appears in the system. Then, the vortices detach from the impurity and are left behind it. Therefore, it can be seen that the vortex can either move together with the impurity or separately as well.

In general, the external force does work and therefore produces a certain amount of excessive energy, which can be transferred through various channels. At the beginning of the trajectories, this energy is distributed in the form of kinetic energy of the impurity, resulting in its linear motion. Once the velocity of the impurity reaches the critical velocity, the velocity of the nucleus cannot increase anymore. Then, the additional energy, instead of being transferred into kinetic energy of impurity, is converted into topological excitations in the form of vortex rings, whose velocities have to be smaller (or equal) than the velocity of the impurity. Assuming that the vortex ring has a round shape and its radius is much larger than the coherence length, the velocity can be estimated, for example, within the hydrodynamic approach [193]:

$$v_{\mathrm{vr}}(r) = \frac{1}{4\pi r}\frac{h}{2m_n}\Big(\ln\frac{8r}{r_{\mathrm{core}}} - \alpha\Big). \tag{4.27}$$

In Eq. 4.27, $h/2m_n$ means quantum of circulation, r – radius of the ring, α – constant dependent on the chosen vortex model (here 1/2), and r_{core} – radius of the vortex core (equal coherence length). The obtained velocity can be compared with several different characteristic velocities extracted for this system, such as critical and Landau velocity, sound speed, and velocity of impurity (for different forces), at which the vortex ring is created. This comparison (where velocities are shown in units of speed of light c) is shown in Fig. 4.12. The speed of sound presented in this figure has been calculated as $\rho_{bn}(dP/d\rho_{bn})$. The term ρ_{bn} means the background density of neutrons and the pressure P is obtained from $\rho_{bn}^2(dE/d\rho_b n)$ (where E is the total energy per nucleon in uniform neutron matter) [194]. In the case of the investigated system, vortex rings

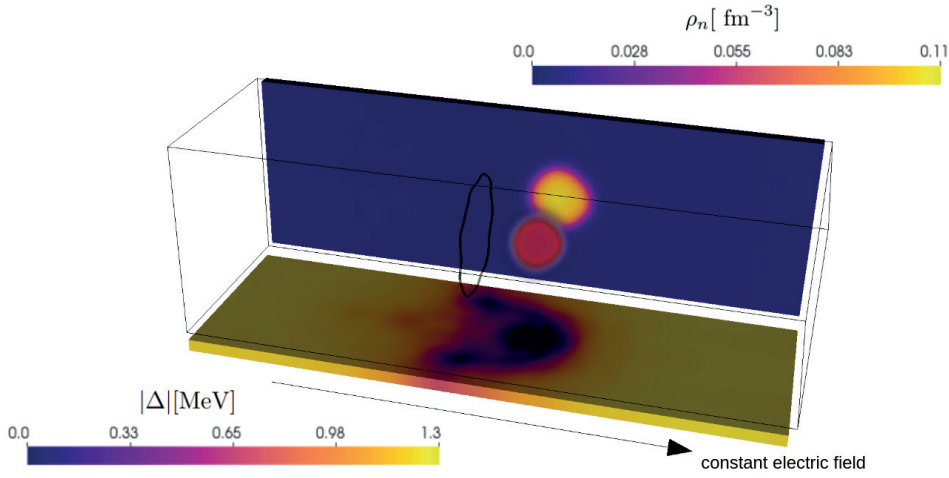

(A) t = 3000 fm/c

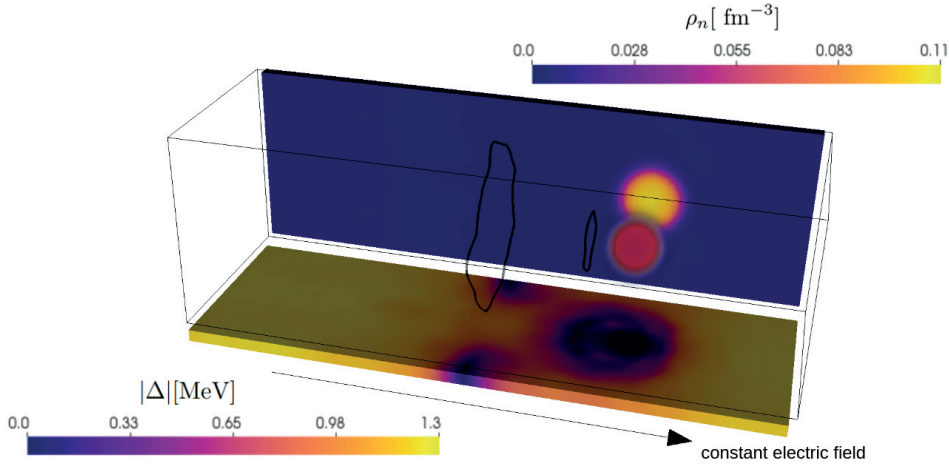

(B) t = 4000 fm/c

FIGURE 4.11: Impurity dynamics for nuclear density $\bar{\rho} = 0.006$ fm^{-3} and electric force 2.0 MeV/fm. For t = 3000 fm/c, the vortex rings is nucleated and moves together with the impurity. At t = 4000 fm/c, another vortex ring occurs, and the impurity starts to move separately from the vortices, which are left behind it.

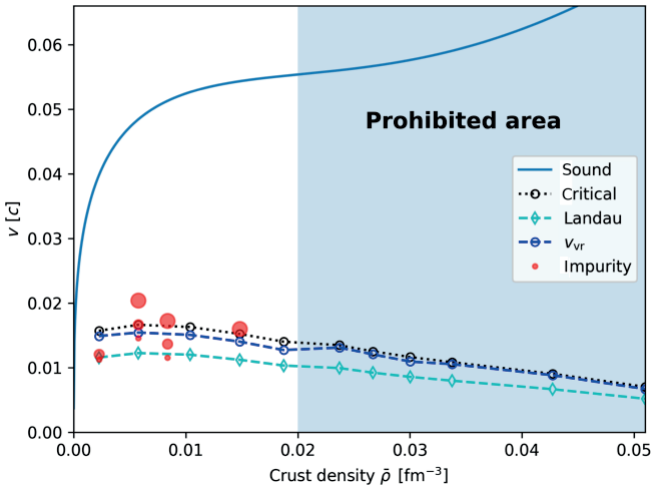

FIGURE 4.12: Characteristic velocities computed for the considered system as a function of density [3]. Sound velocity (solid blue line) has been calculated as $\rho_{bn}(dP/d\rho_{bn})$, critical velocity (black circles) with Eq. 4.26, Landau velocity (green circles) with Eq. 2.38, velocity of vortex ring with Eq. 4.27 and velocity of impurity as $M_{\text{eff}}v^2/2$ (where M_{eff} is effective mass of impurity and v its velocity computed from Eq. 4.23).

appear only for densities below 0.02 fm^{-3}, which is related to the relationship between the coherence length and the size of the impurity. As both of them depend on density, one can show that for a density of 0.02 fm^{-3}, the coherence length (which also defines the size of the vortex core) takes a larger value than the size of the impurity. Therefore, it is clear that the radius of the created ring cannot be smaller than the coherence length (so, equivalently, the size of the vortex core), which happens for densities above 0.02 fm^{-3}. In Fig. 4.12, the region of densities in which vortices cannot be nucleated is marked as *prohibited area*. Indeed, in none of the calculations have the vortices been detected in this area.

4.3 Summary

To summarize, this chapter is focused on the following issues:

- First of all, a new method of extracting the effective mass of impurity has been developed and discussed. This approach is free from various assumptions and

therefore provides a detailed and reliable description of the impurity properties immersed in the neutron medium.

- The campaign of numerical simulations using cutting-edge software, W-BSk Toolkit, has been performed. These calculations have been performed systematically for various densities corresponding to different depths in the neutron star crust.
- The results obtained within this method have been compared with predictions of other approaches, which, in contrast, rely on various assumptions. Despite this, the parameters extracted using this novel method are in reasonable agreement with quantities obtained from other well-established methods, such as hydrodynamic.
- The time-dependent approach also allows for providing deeper insight into the mutual interaction and friction between the impurity and the medium. The process of destroying superfluidity, with regard to Landau velocity and condensation energy, has been discussed.
- It has been identified that kinetic energy from moving impurity can be transferred to the medium in various ways. It has been proven that the process of energy transfer can take the form of either Cooper pair breaking or nucleation of vortices in the medium.
- It has been checked that vortices can be injected into the medium when particular additional constraints are satisfied. These conditions correspond to the geometrical properties of the vortices, which can be created in the form of rings.

Chapter 5

Oscillations of Impurity in Neutron Matter

This chapter is based on results published in a paper: A. Zdanowicz, D. Pęcak, P. Magierski, G. Wlazłowski, *Dynamical scheme for computing the mass parameter of a system in a medium*, Phys. Rev. C 112, 045804, 2025.

In general, the effective mass described in the previous chapter belongs to the wider class of so-called mass parameters, which are the crucial quantities for each effective model. The method discussed in Chap. 4, based on the analysis of the impurity's movement through the medium, was specifically designed to extract the effective mass and represents a cutting-edge approach in the field of neutron star studies. However, one can find examples of other quantities that cannot be extracted within the framework of this method, such as mass parameters describing the spatial deformation of the impurity. Therefore, there was a need to find an alternative method that allows for the extraction of other mass parameters as well. The approach discussed in this chapter is based on properties of oscillations. In the first order, this new method has been applied to extract the effective mass of the impurity. This allowed us to demonstrate consistency with the results from the previous chapter, thereby proving the correctness of the method. Later, a mass parameter describing the deformation of the impurity was determined.

On the more general level, effective mass can be understood as a particular quantity from the whole group of so-called mass parameters connected with the inertia of impurity [62]. According to that, in the case of the analyzed system (impurity in neutron matter), one can also distinguish another type of mass parameters, which are connected with the changes of shape of a cluster [99, 195]. This modification of shape

can be observed, for example, in the form of spatial oscillations [99, 195]. Therefore, the mass parameter associated with the change of shape can be obtained through an analysis of these oscillations. The modifications of shape are usually referred to as multipole modes [195], depending on the shape of the impurity. In this case, the quadrupole mode is analyzed.

5.1 Model of Collective Motion

As it was noted in Chap. 2, impurities immersed in the sea of superfluid neutrons can also be considered as very neutron-rich nuclei. Therefore, methods derived from studies of heavy nuclei can also be applied to neutron star crusts. Moreover, this proton-neutron matter forms a many-body system in which interactions between particles play a crucial role. Therefore, in such systems, one can observe various effects that do not occur, e.g., in light nuclei [195]. One of such phenomena is called collective motion, in which the movement of a large number of particles results in large amplitude oscillations of certain multiple moments (which are therefore called collective variables, as they describe a particular example of collective motion) [62, 195]. These large amplitude collective motions (LACM) result in various effects, among which one can consider spatial deformation of nuclei [99, 195]. This deformation of nuclei results in oscillations of the collective variable corresponding to the multiple moment connected with a particular type of deformation [195]. In general, the change of shape of impurity is usually referred to as surface vibration [99, 195]. However, one should also mention other types of collective motion, such as surface rotation [99, 195]; combining these effects together leads to the rotation-vibration model.

The fundamental quantity used in the description of deformation is a shape parametrization, defined by the radius of the impurity. In the most basic analysis, the impurity is considered a liquid drop with a constant density and a sharp radius. Then, one can parametrize the shape of such a nuclear surface with regard to spherical harmonics $Y_{\lambda\mu}(\theta,\phi)$ in the following way [99, 195]:

$$R(\theta,\phi,t) = R_0\Big(1 + \sum_{\lambda=0}^{\infty}\sum_{\mu=-\lambda}^{\lambda} \alpha^*_{\lambda\mu}(t) Y_{\lambda\mu}(\theta,\phi)\Big), \tag{5.1}$$

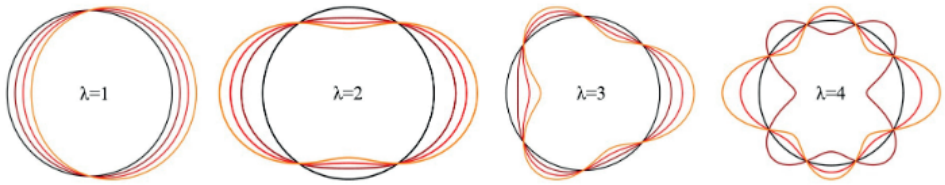

FIGURE 5.1: Deformation of impurity depending on value of λ [195]. The consecutive colors (from darker to lighter ones) denote the subsequent steps of deformation of impurity, as the deformation parameter $\alpha_{\lambda\mu}$ increases.

where R_0 means radius of undeformed (spherical) impurity with the same volume as the deformed one [195]. The crucial time-dependent quantity $\alpha_{\lambda\mu}$, called shape parameter, is the collective variable describing deformation [195, 99]. Here, its complex conjugation $\alpha^*_{\lambda\mu}$ is used; according to properties of spherical harmonics, which imply that $Y^*_{\lambda\mu}(\theta,\phi) = (-1)^\mu Y_{\lambda-\mu}(\theta,\phi)$, the shape parameter has to fulfill the relation [99]:

$$\alpha_{\lambda\mu} = (-1)^\mu \alpha^*_{\lambda-\mu}. \tag{5.2}$$

Depending on the value of λ, $\alpha_{\lambda\mu}$ refers to a particular multiple-mode connected with a certain shape of impurity [195]. The first few modes are schematically shown in Fig. 5.1. The parameter λ equal 1 is connected with translational motion of impurity (so with the shift of its center of mass) [195, 99]. This mode is called dipole moment and does not refer directly to any type of deformation [195]; thus, it does not contribute to nuclear excitations [99]. Later on, one can distinguish, e.g., quadrupole moment for $\lambda = 2$, octupole for $\lambda = 3$, and hexadecupole for $\lambda = 4$; the moments of higher order are expected to be irrelevant in the case of low-energy excitations [195]. In the previous chapter, the mode corresponding to $\lambda = 1$ has been considered. The method presented here is, in fact, an extension of the approach from Chap. 4 to the arbitrary mode. It is demonstrated for $\lambda = 1$ (so when the effective mass is calculated) and $\lambda = 2$, as it turns out that the crucial contribution to deformation comes from the quadrupole mode [195, 99]. In the second order, one can also consider the fundamental asymmetric mode, which is the octupole deformation (not analyzed in this chapter) [195, 99]. The consecutive hexadecupole moment is expected to appear only as an admixture to the quadrupole mode [195]. In addition, one should also mention a mode corresponding to $\lambda = 0$, which is called the monopole mode [99]. Despite the fact that the spherical harmonic Y_{00} is constant, a nonzero value of α_{00} can be observed [99]; therefore,

some deformation has to take place. In the case of the monopole mode, the volume of the whole impurity increases [99]. However, the monopole mode is expected to be a high-energy one and does not contribute to low-energy excitations [99]. Therefore, the quadrupole mode would be the only one considered in the following discussion.

In the description of deformation, one can start from a closer look into Eq. 5.1. In the case of the quadrupole moment, this formula takes the form [99]:

$$R(\theta,\phi,t) = R_0\Big(1 + \sum_{\mu=-2}^{2} \alpha^*_{2\mu}(t) Y_{2\mu}(\theta,\phi)\Big). \tag{5.3}$$

According to this formula, the surface of impurity is described (in laboratory frame) by five independent deformation parameters $\alpha_{2\mu}$: α_{20} (which is real according to Eq. 5.2) and real and imaginary parts of α_{21} and α_{22} [99]. However, it seems to be more intuitive to investigate deformation in the impurity frame when the coordinate system is connected with the axes of symmetry of the impurity (called principal axes) [195, 99]. The shape parameters in such an approach are labeled as a_μ. Due to the symmetry of impurity, one can assume that $a_1 = a_{-1} = 0$ and $a_2 = a_{-2}$; then, Eq. 5.3 can be expressed with regard to just two deformation parameters, a_0 and a_2, and takes the following form [195]:

$$R(\theta',\phi',t) = R_0\Big(1 + a_0(t) Y_{20}(\theta',\phi') + a_2(t) Y_{2,2}(\theta',\phi') + a_2(t) Y_{2,-2,}(\theta',\phi')\Big). \tag{5.4}$$

Coming back to Eq. 5.1, one can derive the formula for the rate of change of radius:

$$\frac{dR}{dt} = R_0 \sum_{\lambda,\mu} \dot{\alpha}^*_{\lambda\mu}\, Y_{\lambda\mu}(\theta,\phi). \tag{5.5}$$

In fact, it describes the velocity of oscillations of the surface of impurity. With such oscillations, one can connect particular kinetic energy, which can be written within the common formula [99]:

$$T = \frac{1}{2} \sum_{\lambda,\mu} M_\lambda |\dot{\alpha}^*_{\lambda\mu}|^2, \tag{5.6}$$

where M_λ is the collective mass parameter.

5.1.1 The Concept of Mass Parameter

The primary objective of this part of the research is to extract mass parameters in relation to specific collective variables. In general, in the process of constructing any effective model, one should at first distinguish degrees of freedom associated with collective variables (which are later on denoted as Q). Such variables should be chosen in a way that allows for the investigation of the quantity of interest (in this case, mass parameters are examined). Based on these collective variables, one can define the Hamiltonian used in equations of motion. In this particular case, they describe the movement of impurity, which can be analyzed in terms of oscillations of a collective variable associated with a specific type of movement. Within such an analysis, one can extract a particular mass parameter.

In general, whenever an effective model is constructed, one can start with a Hamiltonian of a generic form (denoted here by E to maintain consistency with DFT notation):

$$E_Q = \frac{M_Q \dot{Q}^2}{2} + V(Q), \tag{5.7}$$

where the part $M_Q\dot{Q}^2/2$ corresponds to the kinetic term (in which the mass parameter is included) and $V(Q)$ – to the potential one. Therefore, the construction of a Hamiltonian requires both the mass parameter and the potential. However, it should be stressed that this form of Hamiltonian seems to be a proper choice only when the Q variable does not couple to other ones. In general, in the Hamiltonian, the dissipative term, which describes the coupling of Q with other degrees of freedom, should also be included. Therefore, the proper choice of collective variable is of special importance; its dependence on the other degrees of freedom should be as small as possible. Then, the dissipative term in the Hamiltonian can be neglected.

In addition, it is also worth noting that this research focuses on investigating the kinetic term; however, the potential term $V(Q)$ can also be extracted. This can be done with regard to the potential energy surface (also known as energy landscape), which is a standard method, e.g., in studies of dynamics of chemical reactions [196] and nuclear reactions [197, 198]. In general, it allows us to describe the potential energy as a function of chosen degrees of freedom [196]. Therefore, the energy surface can be

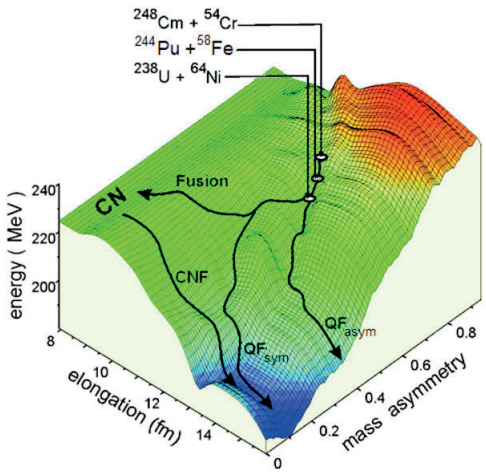

FIGURE 5.2: Exemplary potential energy surface [199].

multidimensional, as shown, e.g., in Fig. 5.2, where the energy depends on the elongation of nuclei and mass asymmetry for different nuclear reactions [199]. It should also be remarked that the examination of the potential term is done within static calculations, by minimizing energy with given constraints on collective variables. On the contrary, in the case of mass parameters, there is no well-established methodology for their extraction. However, as these parameters describe the dynamical properties of the system, it turns out to be easier to obtain them within a time-dependent approach, as advocated in this work.

The choice of collective variable depends on the specific case. Here, the position of the center of mass of the impurity and the quadrupole moment have been chosen. Based on the analysis of the first of these parameters, one can extract effective mass; then, compared to the results from [3], one can verify the correctness and effectiveness of the presented method. The second of the chosen collective variables – quadrupole moment – turns out to be an important parameter in neutron star studies. According to [82], quadrupole deformation of nuclei arises as a result of the interaction of the impurity with the vortex. Therefore, examination of the quadrupole moment can provide a significant contribution to the effective model of the crust.

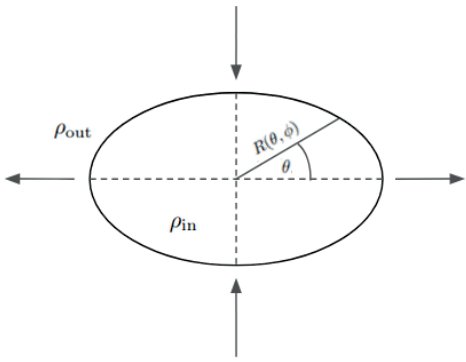

FIGURE 5.3: Schematic view of the system analyzed within the hydrodynamic approach [20]. The arrows denote the directions in which the shape of impurity can be modified (in other words, the nuclei can be either flattened or elongated).

5.1.2 Mass Parameter within Hydrodynamic Approach

One of the well-known methods for calculating the mass parameter is based on the hydrodynamic approach. As well as in calculations from Sec. 4.1.2, the impurity is considered as a sphere of sharp radius and constant density ρ_{in} immersed in the superfluid medium of density ρ_{out} [187, 188]. The radius of impurity can be written with regard to spherical harmonics and therefore depends on angles θ and ϕ. The analyzed system is schematically shown in Fig. 5.3. The arrows that are drawn in this figure show the direction of deformation – in this case, the impurity changes its shape from spherical to ellipsoidal. Similarly to the calculation of effective mass from Sec. 4.1.2, one can investigate this system with regard to the irrotational fluid model. It enables us to define the velocity fields in terms of the potential fields.

In the next step, one can define the boundary conditions, which are analogous to the ones from Sec. 4.1.2. First of all, Eq. 4.7 imposes that the potential field has to be continuous (so $\Phi_{in}|_{r=R_0} = \Phi_{out}|_{r=R_0}$) [188, 187], where R_0 is radius of spherical impurity. The condition Eq. 4.8 concerning conservation of mass [188, 187], in this case, modifies to form where the velocity field of impurity v is replaced with the rate of change of its radius dR/dt:

$$\rho_{in}\left(\frac{\partial\Phi_{in}}{\partial r}\bigg|_{r=R_0} - \frac{dR}{dt}\right) = \rho_{out}\left(\frac{\partial\Phi_{out}}{\partial r}\bigg|_{r=R_0} - \frac{dR}{dt}\right). \tag{5.8}$$

The last condition is connected with the asymptotic behaviour of the velocity field outside of the impurity: $\Phi_{\text{out}}|_{r\to\infty} = 0$ [187].

As well as in the previous chapter, solving Eqs. 4.5 - 4.6 with regard to the boundary conditions allows us to obtain formulas for potential fields with regard to spherical harmonics $Y_{\lambda\mu}$ [20]:

$$\Phi_{\text{in}} = \sum_{\lambda,\mu} \beta_{\lambda\mu}\, r^{\lambda}\, Y_{\lambda\mu}, \tag{5.9}$$

$$\Phi_{\text{out}} = \sum_{\lambda,\mu} \gamma_{\lambda\mu}\, r^{-\lambda-1}\, Y_{\lambda\mu}. \tag{5.10}$$

In Eq. 5.9 and Eq. 5.10, the variables $\beta_{\lambda\mu}$ and $\gamma_{\lambda\mu}$ denote the coefficients of expansion into spherical harmonic series. The components r^{λ} and $r^{-\lambda-1}$ have the meaning of expansion functions and provide the dependence of the potential field on the distance. As the potential field outside of impurity is assumed to approach 0 for $r \to \infty$, the expansion functions have to take the form $r^{-\lambda-1}$ to fulfill this condition. As the field inside of the impurity does not have to obey any constraints, one can apply the standard polynomial expansion, where the functions are of the form r^{λ}. Then, one should substitute the formula for the rate of change of radius (Eq. 5.5), together with expressions for Φ_{in} and Φ_{out} (from Eqs. 5.9 - 5.10), into Eq. 5.8. This leads to the following equations for coefficients β and γ used in equations for potential fields:

$$\beta_{\lambda\mu} = \frac{1}{R_0^{\lambda-2}} \frac{\kappa - 1}{\kappa\lambda + (\lambda + 1)} \dot{\alpha}^{*}_{\lambda\mu}, \tag{5.11}$$

$$\gamma_{\lambda\mu} = R_0^{\lambda+3} \frac{\kappa - 1}{\kappa\lambda + (\lambda + 1)} \dot{\alpha}^{*}_{\lambda\mu}. \tag{5.12}$$

In Eq. 5.12 there is the auxiliary variable $\kappa = \rho_{\text{in}}/\rho_{\text{out}}$.

At this point, one can come back to the formula for kinetic energy from Eq. 4.14. One should also take into account that the deformation is assumed to be small enough to set the boundary of the integral to a sphere of radius R_0. This leads to the following form of Eq. 4.14 [20]:

$$T = \frac{1}{2} m_n\, \rho_{\text{in}} \int_{r=R_0} \Phi_{\text{in}} \frac{\partial \Phi_{\text{in}}}{\partial r} R_0^2\, d\Omega - \frac{1}{2} m_n\, \rho_{\text{out}} \int_{r=R_0} \Phi_{\text{out}} \frac{\partial \Phi_{\text{out}}}{\partial r} R_0^2\, d\Omega, \tag{5.13}$$

In the next step, one can insert the expression for fields Φ_{in} and Φ_{out} into the formula for kinetic energy. This results in the following equation [20]:

$$T = \frac{1}{2} m_n \, \rho_{\text{out}} (\kappa - 1)^2 \, R_0^5 \sum_{\lambda,\mu} \frac{1}{\kappa\lambda + (\lambda + 1)} |\dot{\alpha}^*_{\lambda\mu}|^2. \tag{5.14}$$

Comparing Eq. 5.14 with the common expression for kinetic energy (Eq. 5.6), one can obtain the equation for mass parameter [20]:

$$M_\lambda = m_n \, \rho_{\text{out}} (\kappa - 1)^2 \, R_0^5 \, \frac{1}{\kappa\lambda + (\lambda + 1)}. \tag{5.15}$$

As it was mentioned in Sec. 5.1, the parameter λ corresponds to a particular multiple mode. Therefore, in the case of quadrupole mode, one can write an expression for the mass parameter M_2 as:

$$M_2 = m_n \, \rho_{\text{out}} (\kappa - 1)^2 \, \frac{R_0^5}{2\kappa + 3}. \tag{5.16}$$

In the next step, one should obtain the radius R_0. As it corresponds to undeformed (spherical) impurity, it can be calculated from the general formula for density equal $m_n \, \rho_{\text{in}}$:

$$m_n \, \rho_{\text{in}} = \frac{M_{\text{CM}}}{V}, \tag{5.17}$$

where M_{CM} is the effective mass of impurity and V – its volume, defined as $(4/3)\pi R_0^3$. Then, R_0 can be calculated as:

$$R_0 = \left(\frac{3 M_{\text{CM}}}{4\pi \, m_n \, \rho_{\text{in}}} \right)^{1/3}. \tag{5.18}$$

The mass parameter obtained through the procedure described above is directly related to the deformation parameter $\alpha^*_{\lambda\mu}$. However, in practical applications, especially when DFT is used, it is preferable to work with deformation parameters calculated from densities. One of them is the quantity called quadrupole moment, quantified by Q_{20} and defined as [200]:

$$Q_{20}(t) = \int (3z^2 - r^2) \rho_p(\boldsymbol{r}, t) \, d\boldsymbol{r}, \tag{5.19}$$

where z means the coordinate along z axis and $\boldsymbol{r}$ is the coordinate describing position of impurity. In this case, the quadrupole moment is defined only with respect to the

density of protons (the same approach has been applied in calculations from Chap. 4). As a result, the whole protocol is constructed with regard to the well-defined quantities.

It is convenient to link the mass parameter obtained for deformation parameter $\alpha^*_{\lambda\mu}$ (Eq. 5.16) to the analogous quantity for quadrupole moment Q_{20}. It can be assumed that Q_{20} and $\alpha^*_{\lambda\mu}$ are proportional to each other through the certain coefficient C:

$$Q_{20} = C\alpha_{20}. \tag{5.20}$$

This coefficient, according to [201], can be written as:

$$C = \sqrt{\frac{5}{16\pi}}\frac{M_{\mathrm{CM}}}{m_n}R_0^2. \tag{5.21}$$

Combining the connection between Q_{20} and α_{20} from Eq. 5.20 with formula for kinetic energy from Eq. 5.6, the mass parameters for α_{20} and Q_{20} would be proportional with regard to C^2. As a consequence, the mass parameter for the quadrupole mode (denoted as $M_{Q_{20}}$) can be calculated as:

$$M_{Q_{20}} = \frac{M_2}{C^2}, \tag{5.22}$$

which leads to the equation [20]:

$$M_{Q_{20}} = \frac{16\pi m_n^3}{5M_{\mathrm{CM}}^2}\rho_{\mathrm{out}}(\kappa-1)^2\frac{R_0}{2\kappa+3}. \tag{5.23}$$

The formula from Eq. 5.23 has been used in calculations presented in Sec. 5.2.2.

5.2 Mass Parameters within Density Functional Theory

The discussion and equations in this section are based on [20].

As well as in the analysis from Chap. 4, the method presented here is based on numerical calculations performed within time-dependent DFT. Therefore, the main challenge is the proper construction of scheme that extracts the mass parameters related to the given collective variable, as defined through Eq. 5.7. First of all, Q should be a

functional of density:

$$Q(t) = Q[\rho(\boldsymbol{r}, t)]. \tag{5.24}$$

This assumption is directly connected with the postulated form of energy, which is also a functional of density. In other words, one can obtain the energy of the system in such a form only when the collective variable is a functional of density as well. In addition, only small fluctuations of Q around the equilibrium value are considered. As a consequence, the expression for potential can be approximated with regard to the following formula:

$$V(Q) \approx \frac{1}{2} M_Q \omega_Q^2 (Q(t) - Q_0)^2. \tag{5.25}$$

The potential takes the form of a harmonic oscillator. The variable Q_0 is the value around which the system fluctuates, so $Q(t) = Q_0 + \delta Q(t)$. In other words, Q_0 can be considered as the value for which $V(Q)$ reaches the minimal value. When only small fluctuations around this minimum are considered, their dynamics can be accurately approximated by those of a harmonic oscillator, which justifies the use of this approximation.

The term ω_Q corresponds to the frequency of oscillations of the collective variable, which is in fact the characteristic frequency of the harmonic oscillator (in other words, $Q(t)$ oscillates according to the harmonic oscillator model). Consequently, with regard to the frequency of oscillations of the collective variable, one can obtain the energy of the mode from the relation $E_Q = \hbar\omega_Q$. However, extraction of the mass parameter, denoted as M_Q in Eq. 5.25, requires some further modifications. In general, it cannot be extracted explicitly from this equation when no external driving is applied to the system. The same problem occurs, for example, in a standard oscillator like a pendulum, where mass cannot be extracted solely from the frequency of oscillations, as one quantity extracted from simulations (e.g., the frequency of oscillations) allows for the calculation of only one parameter describing the system (such as energy). Therefore, in order to obtain the mass parameter, one should introduce some additional external perturbation. In this case, it takes the form of an external harmonic potential coupling to the collective variable; then, based on the behavior of $Q(t)$ over time, the mass parameter can be extracted. In other words, one can always add an external force in the form of a harmonic oscillator potential $\frac{1}{2}k(Q(t) - Q_0)^2$ to the system and observe its behaviour, once the control parameter k is modified. In such a case, the total energy of

the system can be written as:

$$E'_Q(t) = \frac{M_Q \dot{Q}^2}{2} + V(Q) + \frac{k}{2}(Q(t) - Q_0)^2 = E_Q(t) + \frac{k}{2}(Q(t) - Q_0)^2, \tag{5.26}$$

where k is some arbitrary coefficient and first two terms (denoted by E_Q) have the meaning of the energy without external potential. In this modified case, and assuming small amplitude fluctuations, the potential term would take the form:

$$V'(Q) \approx \frac{1}{2} M_Q \omega^2(k)(Q(t) - Q_0)^2. \tag{5.27}$$

Once the additional external force is applied, the system consists of two harmonic oscillator potentials: the internal and the external ones. As a consequence, the frequency of harmonic oscillations ω becomes dependent on the control parameter k in the following way:

$$\omega^2(k) = \omega_Q^2 + \frac{k}{M_Q}. \tag{5.28}$$

In other words, for each k, a different value of ω is associated. The parameter ω_Q means the frequency of oscillations extracted in the case when no external potential is applied (so for $k = 0$). By measuring how these oscillations change as we modify the control parameter k, we can extract the mode's energy ($\hbar\omega_Q$) and the associated mass parameter.

Note that, if the collective variable is appropriately chosen, the energy of the system, described by the energy density functional, can be approximated by the effective expression E_Q. In this case, analogously to the analysis of the linear motion of an impurity, the BSk31 functional is employed. Consequently, the effective energy E_Q in Eq. 5.26 is equivalent to the energy derived from the BSk functional.

More technically, the calculations that allow for the extraction mass parameter are performed within the following protocol:

- first of all, during static calculations, the ground state is prepared. Later on, such a state with a certain initial value of Q (corresponding to $Q(t = 0)$) would be used in dynamic simulations,

- for each of the investigated densities, numerical simulations based on the time-dependent DFT method are performed for different values of k. What is important is that this parameter is chosen arbitrarily in a way that allows for obtaining small-amplitude oscillations. Moreover, as the expression for energy (Eq. 5.26) includes also the additional term coming from external perturbation of the collective variable, the single-particle Hamiltonian $h(\boldsymbol{r}, t)$ should be modified as well. Therefore, as the total potential U_q (acting either on protons or neutrons) is equivalent to the functional derivative of energy from Eq. 5.26 over normal density ρ_q:

$$U_q = \frac{\delta E'}{\delta \rho_q}, \tag{5.29}$$

  and the modified single-particle Hamiltonian $h'(\boldsymbol{r}, t)$ takes the form:

$$h'(\boldsymbol{r}, t) = h(\boldsymbol{r}, t) + k(Q(t) - Q_0)\frac{\delta Q}{\delta \rho}, \tag{5.30}$$

- then, for each value of k, frequency of oscillations is extracted;
- later on, from the linear fitting to the relation described with Eq. 5.28 (with $1/M_Q$ and ω_Q as fitting parameters), the mass parameter M_Q can be extracted.

Within such a procedure, one can extract both the energy of a particular mode and the corresponding mass parameter.

As mentioned before, the collective variable $Q(t)$ is expected to show harmonic oscillations; by analysing these oscillations, one can extract the mass parameter. In the ideal case, no damping should be present in the system. However, despite the fact that the collective variable is chosen in a way to be as independent of other degrees of freedom as possible, there would always be some coupling between them. In other words, the energy can flow from one chosen degree of freedom to another. As a consequence, oscillations of the collective variable may become damped. To provide a more realistic description of the oscillations and improve the accuracy of the parameter extraction, formulas for a damped oscillator have been employed. In other words, as the collective variable cannot be ideally independent, it seems to be more reliable to describe the oscillations within the damped oscillator model. In such a case, the dependence of the

collective variable on time can be written as:

$$Q(t) = Ae^{-\gamma t}\sin(\omega_d\, t + \varphi), \tag{5.31}$$

where A has the meaning of amplitude of oscillations, γ – dissipation coefficient, ω_d – frequency of oscillations and φ – phase.

At this point, one should also make a few further remarks about the phenomenon of damping, which is directly connected with the lifetime of oscillations. Due to the suppressing properties of the medium surrounding impurity, the oscillations of $Q(t)$ can be observed only for some finite time; in other words, they are expected to show damping described by the coefficient γ. According to that, it turns out that the frequency of oscillations extracted directly from the results of the simulation is the frequency of damped oscillations (denoted as ω_d). On the other hand, the formula from Eq. 5.28 describes the general dependence of ω^2 on k, where damping is not included. The connection between the frequency of damped (ω_d) and undamped (ω) oscillations can therefore be defined by the following relation:

$$\omega^2 = \omega_d^2 + \gamma^2. \tag{5.32}$$

Then, once ω_d and γ are obtained from simulation, one can compute ω, and next use it to extract the mode's energy ($\hbar\omega$) and the mass parameter (M_Q).

5.2.1 Center of Mass Oscillations

As well as in the case of research from Chap. 4, in order to extract the mass parameter, simulations in the frame of time-dependent DFT were performed. Technically, the numerical procedure and analysis of the obtained results included the following main steps:

- first of all, a ground state solution within static calculations was obtained. In this case, the size of the grid was set to N_x x N_y x N_z = 32 x 32 x 64 lattice points with spacing 1.25 x 1.25 x 1.25 (in fm) – such dimensions provided enough space for impurity to oscillate,
- later on, the obtained system was evolved with applied external driving and with an initial impurity displacement set to 1 fm. As illustrated in Fig. 5.4, showing

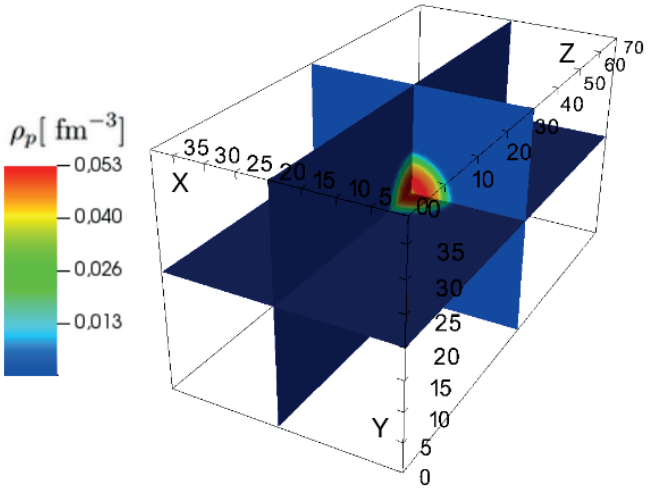

FIGURE 5.4: 3D view of the initial setup in simulations of center of mass oscillations for density 0.006 fm^{-3}: the impurity placed in the center of the box.

the initial configuration of the system for exemplary density 0.006 fm^{-3}, 1 fm is a small amplitude compared to the size of the impurity, which is considered the typical size scale in this research. To extract the effective mass, the initial amplitude had to be small enough to minimise effects associated with dissipation. On the other hand, in order to study dissipation mechanisms (discussed in detail in Sec. 5.2.1), calculations for larger amplitudes (10 fm) were also performed.

Simulations were performed for each of the examined densities at different values of the control parameter k. The time length of each trajectory has been set to 10000 fm/c. Then, the position of the center of mass, Z_{CM}, as a function of time have been recorded. Based on that, one could extract the frequency of oscillations ω and analyze the dependence of ω^2 on k systematically for the whole range of chosen densities. These results allowed us to extract the mass parameter with regard to Eq. 5.28. From linear fitting to $\omega^2(k)$, one could obtain M_{CM} as the inverse of the slope of the fitted line.

In the first analyzed case, the chosen collective variable is the position of the center of mass of the impurity. Based on that, one can extract the effective mass and compare it with the results from Chap. 4, which allows one to demonstrate the correctness of this method. As impurity is requested to oscillate only along z axis, the position of

center of mass Z_{CM} can be written as:

$$Z_{\mathrm{CM}}(t) = \frac{1}{N_p} \int z\, \rho_p(\boldsymbol{r}, t)\, d\boldsymbol{r}, \tag{5.33}$$

where N_p means the number of protons in the cluster (obtained as $N_p = \int \rho_p(\boldsymbol{r})\, d\boldsymbol{r}$). As well as in the case of the quadrupole moment (Eq. 5.19), the center of mass is defined with regard to the density of protons. Calculations were performed for the total number of protons to be 40.

In case of center of mass oscillations, the energy functional from Eq. 5.26 should be modified to:

$$E'(t) = E_{\mathrm{BSk}} + \frac{k}{2}(Z_{\mathrm{CM}}(t) - Z_0)^2, \tag{5.34}$$

with Z_0 being the position around which the impurity oscillates and k the control parameter for the external driving (which controls the dynamics of oscillations). Once the energy of the system is expressed with regard to Eq. 5.34, the impurity evolves according to the following mean-field potential:

$$U_p = \frac{\delta E'}{\delta \rho_p} = U_{p,\mathrm{BSk}} + k(Z_{\mathrm{CM}} - Z_0)\frac{z}{N_p}. \tag{5.35}$$

It should be mentioned that this new potential attains extra time dependence, as the position of the center of mass is a function of time ($Z_{\mathrm{CM}}(t)$). Fig. 5.5 shows the position of the impurity in consecutive time moments for density 0.006 fm^{-3}. The arrow means the direction of movement of impurity, a solid black cross denotes the center of the box, a dashed black cross corresponds to the point, around which impurity oscillates, and a magenta line – to the slope of potential proportional to z/N_p. One can see that it varies in time, which is a result of the impact of additional harmonic driving. This potential moves the impurity and, consequently, generates the oscillations. According to Eq. 5.30, the potential from Eq. 5.35 contributes to the modified Hamiltonian in the form of a force, as $\boldsymbol{F} = -\nabla U_p$. This force can be written as:

$$\boldsymbol{F} = -\nabla U_p \sim \left[0, 0, -\nabla U_{p,\mathrm{BSk}} - \frac{k(Z_{\mathrm{CM}}(t) - Z_0)}{N_p}\right], \tag{5.36}$$

where $\nabla U_{p,\mathrm{BSk}}$ means the nuclear force (included in the functional) and $k(Z_{\mathrm{CM}}(t) - Z_0)(z/N_p)$ is the contribution coming directly from the external force. Such a force is

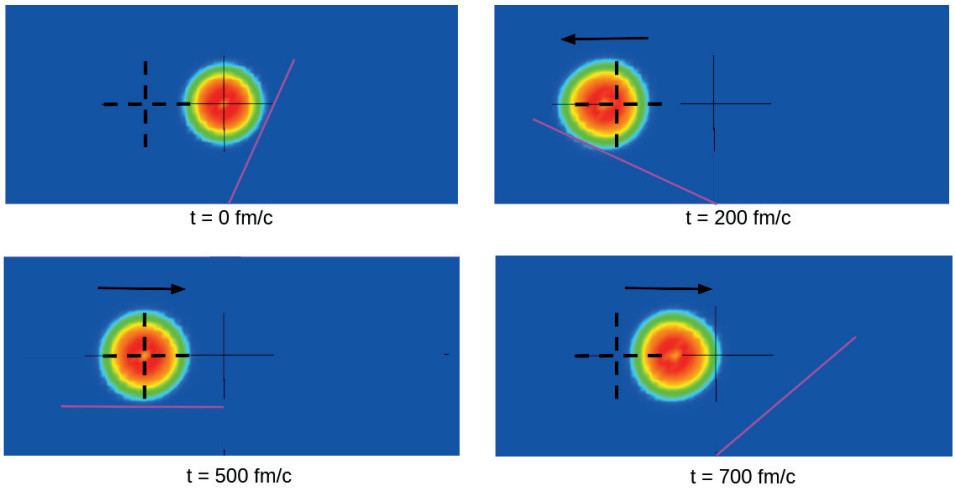

FIGURE 5.5: Time evolution of position of impurity in the external potential, arising from harmonic driving, for density 0.006 fm^{-3}. The variable ρ_p in the legend corresponds to the density of protons.

constant in space and acts only on protons, but its strength is time-dependent (due to the time dependence of the center of mass position). Due to the impact of this force, the impurity can be moved through the medium without any modifications in its density distribution.

Effective Mass from Analysis of Oscillating Impurity

The recorded oscillations and checks based on tracking of energy conservation are presented in Fig. 5.6 (which shows the results for exemplary densities and k values for amplitude 1 fm) and in Fig. 5.7 (presenting the data for amplitude 10 fm). For each density, in the upper panels, the percentage change in total energy is shown. At the lower panels, the position of the center of mass of impurity with regard to its initial position, denoted as $Z_{\mathrm{CM}} - Z_0$ (in units of fm) as a function of time for (in fm/c) for a certain value of k is shown. In each of the plots of $Z_{\mathrm{CM}}(t) - Z_0$, the orange line shows the results from the simulation, and the green one corresponds to the fit. The percentage change of energy takes values of the order from 10^{-2}% to 10^{-4}%. Based on that, one can assume that the total energy is conserved with good quality and remains almost constant throughout the entire evolution. Therefore, the performed simulations

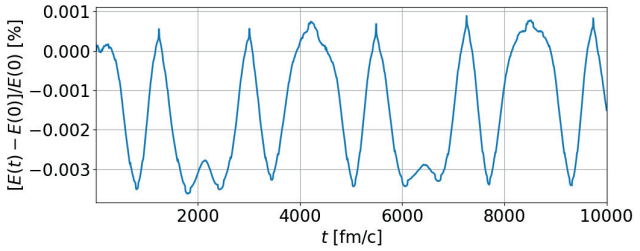

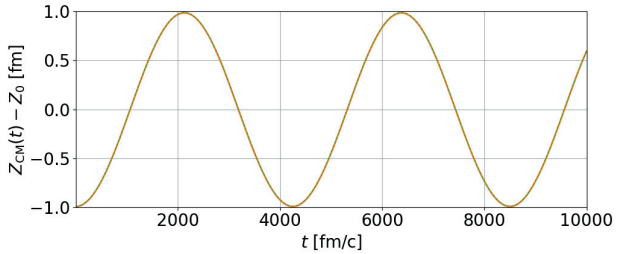

(A) $\bar{\rho} = 0.010$ fm^{-3}, $k = 0.24$

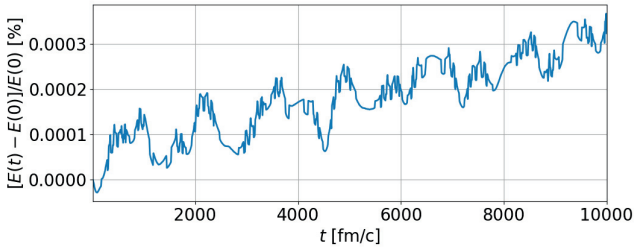

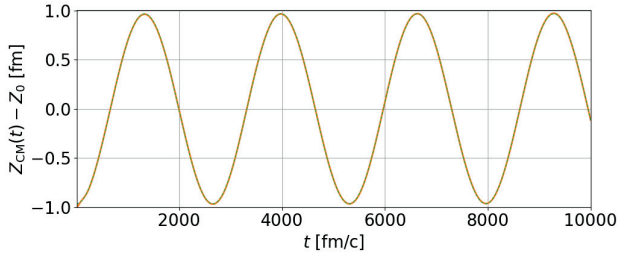

(B) $\bar{\rho} = 0.034$ fm^{-3}, $k = 0.40$

FIGURE 5.6: Percentage change of total energy of oscillating impurity (upper panels) and oscillations of center of mass of impurity (lower panels) for amplitude equal 1 fm for densities 0.010 fm^{-3} and 0.034 fm^{-3}.

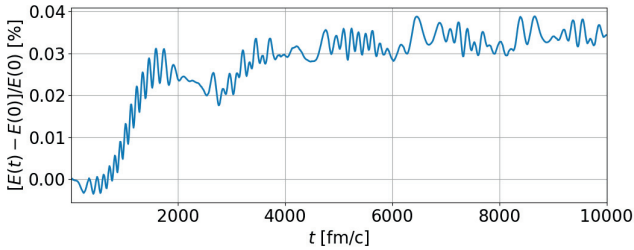

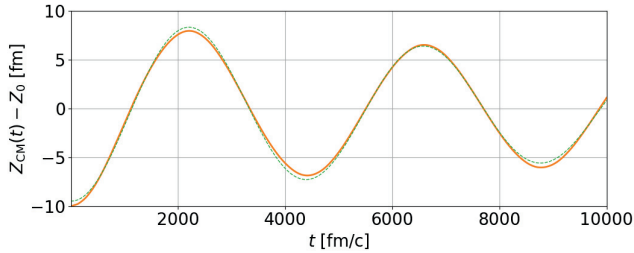

(A) $\bar{\rho} = 0.010$ fm^{-3}, $k = 0.24$

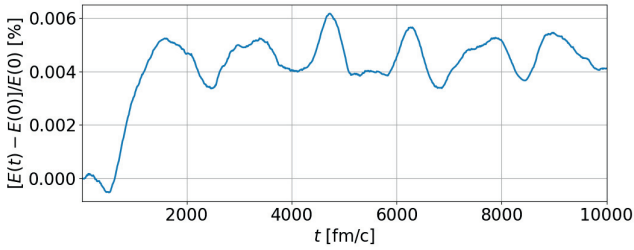

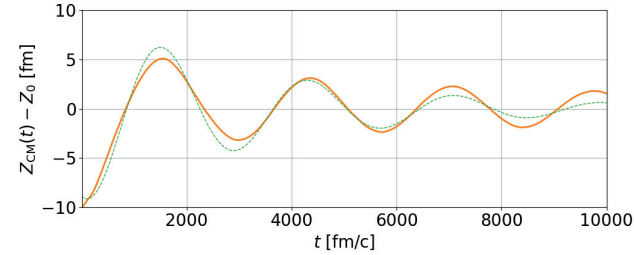

(B) $\bar{\rho} = 0.034$ fm^{-3}, $k = 0.37$

FIGURE 5.7: Percentage change of total energy of oscillating impurity (upper panels) and oscillations of center of mass of impurity (lower panels) for amplitude equal 10 fm for densities 0.010 fm^{-3} and 0.034 fm^{-3}.

can be considered reliable.

Once these results have been obtained, one could extract the effective mass with respect to the following protocol:

- from the simulations, the dependencies $Z_{\mathrm{CM}} - Z_0(t)$ for different values of k have been recorded,
- the formula for damped harmonic oscillator: $Q(t) = Ae^{-\gamma t}\sin(\omega_d\, t + \varphi)$ (Eq. 5.31) has been fitted to each of the plots $Q(t) = Z_{\mathrm{CM}} - Z_0(t)$,
- from this fitting, one could obtain the frequency of damped oscillations ω_d and damping coefficient γ,
- then, one could calculate frequency of undamped oscillations as: $\omega^2 = \omega_d^2 + \gamma^2$ (Eq. 5.32),
- finally, fitting to the relation: $\omega^2(k) = \omega_Q^2 + \frac{k}{M_Q}$ (Eq. 5.28) could have been done. From this formula, one could extract the mass parameter M_Q related to the center of mass oscillations.

The method described above is illustrated in Fig. 5.8 (where data for an exemplary density of the inner crust $\bar{\rho} = 0.015$ are shown). In panel a), one can see the change of position of the center of mass of impurity ($Z_{\mathrm{CM}} - Z_0$, in units of fm) as a function of time (in fm/c) for amplitude 1 fm and a few exemplary values of k. Later on, panel b) of Fig. 5.8 shows the squared frequency of oscillations (ω^2 extracted directly from results of simulations in units of $\mathrm{c}^2/\mathrm{fm}^2$) for different k (in units of $\mathrm{MeV}/\mathrm{fm}^2$); the frequencies from panel b) correspond to k from panel a). As it was expected, the consecutive values of ω^2 follow the linear dependence from Eq. 5.28.

At this point, one should also take a closer look at the point of intercept obtained from $\omega^2(k)$. Once the theoretical dependence from Eq. 5.28 is fitted to $\omega^2(k)$, it can be seen that for k equal 0 the corresponding frequency (called later ω_{CM}) is also 0. This feature arises from properties of the Hamiltonian, which is translational invariant. As a consequence, the energy of the system remains the same, no matter where the impurity is localized (unless there is no external potential, which happens when $k = 0$). On the other hand, since the impurity has to be placed at some arbitrarily chosen position, the

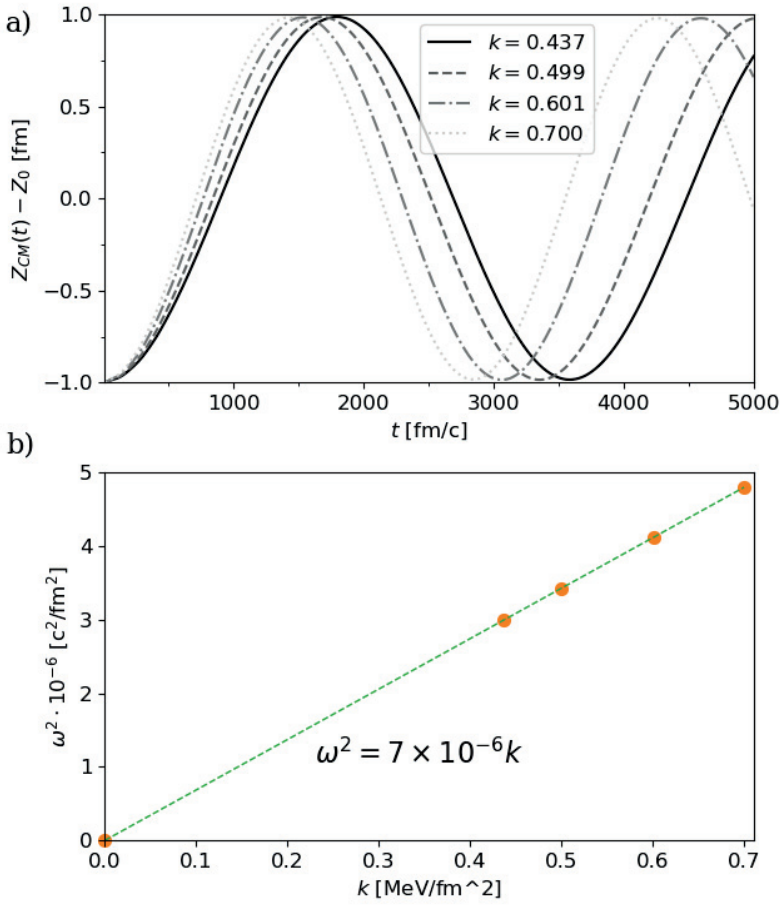

FIGURE 5.8: a) Time evolution of $Z_{\mathrm{CM}} - Z_0$ for different values of k. b) Squared frequency of oscillations as a function of k [20].

translational symmetry of the system is broken. This, in fact, corresponds to the phenomenon of spontaneous symmetry breaking, when the Hamiltonian is translational invariant, but the solution is not [202, 203]. As a consequence of this phenomenon, a zero-energy mode (called Goldstone mode) is induced [203].

According to the Goldstone theorem, spontaneous breaking of global and continuous symmetry results in the mode of vanishing energy, as the wave number of this mode approaches zero [202]. It requires, however, that some translational symmetry be intact [202], as is the case, e.g., for the Hamiltonian in the analyzed case. The Goldstone theorem can be explained with regard to Noether's statement [202], according to which for any continuous global symmetry there must exist a current, which is locally conserved due to the local continuity equation. As a consequence, excitations at nonzero wave number in the form of gapless modes are expected to occur in the system [202]. Therefore, the presence of a zero-energy mode (for which the frequency, here denoted as ω_{CM}, is equal to 0) is a consequence of the Goldstone theorem. Due to this property, in case of center of mass oscillations, it is possible to extract the effective mass from a run executed only for a single value of k. However, in this research, we follow the protocol with fitting to $\omega^2(k)$ dependence.

Fig. 5.9 shows the effective mass (in units of neutron mass m_n) calculated for different densities and in the frame of various approaches. In Fig. 5.9, one can distinguish the following sets of data:

- orange triangles denote effective mass extracted from analysis of oscillations of impurity for small amplitude of oscillations, which in this case has been set to 1 fm. As verified in the simulations, for such an amplitude, the oscillations remained undamped, indicating that the Landau velocity was not exceeded. Moreover, this value is smaller than the size of impurity, which (according to Chap. 4) varies from 5 to 10 fm depending on density;
- green squares mark the effective mass extracted within the same approach, but for a higher amplitude of oscillations (10 fm), for which the Landau velocity is exceeded. More detailed analysis of such a case is presented in Sec. 5.2.1,
- blue diamonds mean the results calculated with regard to the method described in Chap. 4 (together with uncertainties).

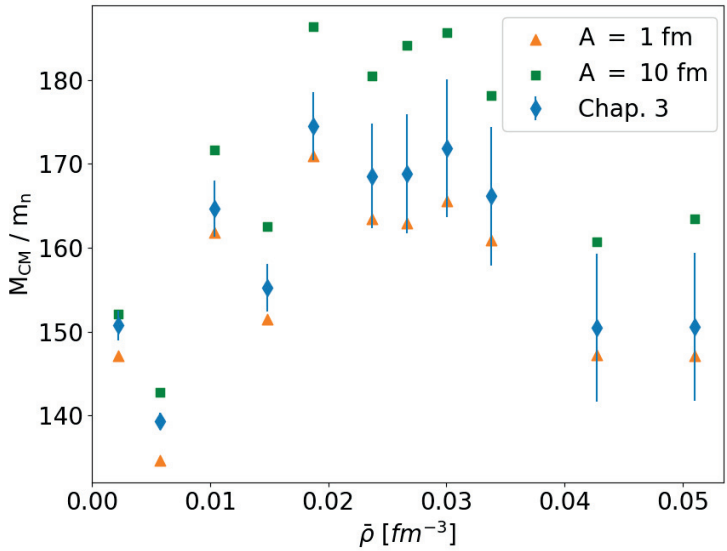

FIGURE 5.9: Effective mass obtained from oscillations of impurity, compared with the results of the method from Chap. 4 [20].

The effective masses calculated for small oscillation amplitudes are in good agreement with the values obtained within the framework of the dynamic approach. Although both methods are based on the same numerical framework, the approach discussed in this section proves to be a more universal method. In the case of linear movement of impurity, the effective mass is the only parameter that can be extracted in the proposed way. On the contrary, the approach described in this chapter can also be applied to other collective variables (such as the quadrupole moment) and therefore allows for the study of various properties of the system.

Dissipation

As mentioned before, the value of the amplitude of oscillations should be properly chosen due to the various mechanisms of dissipation that manifest themselves in the form of damped oscillations. For the analysis of dissipation mechanisms, the initial amplitude Z_0 equal to 10 fm was chosen. Such an amplitude is much larger than the size of the impurity and can therefore be considered as a large value, for which dissipation should be observed. On the contrary, for amplitude equal 1 fm (which is much

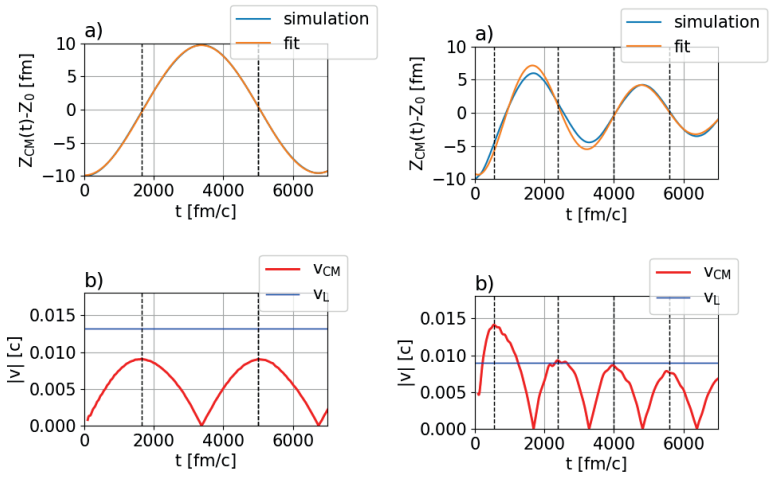

(A) $\bar{\rho} = 0.002$ fm^{-3} (B) $\bar{\rho} = 0.027$ fm^{-3}

FIGURE 5.10: a) Oscillations of the center of mass of impurity as a function of time – data from simulation with fitted curve. b) Velocity of the center of mass with a horizontal line corresponding to the Landau velocity for densities 0.002 fm^{-3} and 0.027 fm^{-3}.

smaller than the size of the impurity), almost no damping occurs (the value of γ_{CM} can be considered as negligibly small). Fig. 5.10 shows some interesting effects connected with dissipation for exemplary densities 0.002 fm^{-3} and 0.027 fm^{-3} (here, the part of the trajectory from 0 to 7 000 fm/c is shown). In each of the figures, panel a) presents oscillations of the position of the center of mass as a function of time. Blue line shows the dependence obtained directly from simulation, and orange dashed line denotes the curve fitted to these results (in this case, the model of damped harmonic oscillator described with Eq. 5.31 has been fitted to the data). Panel b) presents the velocity of the center of mass (extracted as the derivative of Z_{CM} over time and plotted with a red line). The vertical dashed lines correspond to particular moments at which velocity reaches a local maximum; additionally, in panel b), the horizontal blue line represents the Landau velocity for the analyzed density.

Considering the position of the center of mass, the damping can be observed for density 0.027 fm^{-3} at the beginning of the trajectory; later on, the amplitude of oscillations decreases less and less rapidly. The moments of greatest damping correspond to the time steps at which the velocity of the impurity exceeds the Landau velocity. On the

other hand, when the Landau velocity is not exceeded, damping is also smaller (in other words, the amplitude decreases less in subsequent cycles compared to the initial times). As it was mentioned in Chap. 4, Landau velocity can be considered as a kind of „border" distinguishing dissipative and non-dissipative regimes; once Landau velocity is exceeded, destruction of superfluidity begins, and dissipation is supposed to occur in the system. In this case, such a property can be observed in the form of damped oscillations (the higher the velocity is, the stronger the damping becomes). In contrast, in the case of density 0.002 fm^{-3}, the velocity of the impurity is always lower than the Landau velocity. Therefore, dissipation is not expected to take place in the system; indeed, one cannot observe damped oscillations for this density.

One should also keep in mind that predictions connected with Landau velocity and destruction of superfluidity are well studied only for uniform systems; the exact behaviour in the case of neutron star crust is therefore unsure. Despite the fact that the mechanisms of dissipation discussed in this section are in good agreement with theory, some phenomena that can be observed arise as a result of possible discrepancies between predictions for uniform systems and real properties of non-uniform ones. For example, at a density of 0.027 fm^{-3} and times above 3000 fm/c, despite the Landau velocity not being exceeded, small damping can still be observed. As in non-uniform systems, Landau velocity does not set the precise „border" between dissipative and non-dissipative states; dissipation effects can still be observed, even though the threshold velocity is not exceeded.

Later on, one can examine the damping coefficient. Fig. 5.11 shows the dissipation parameter γ (denoted in the legend as γ_{CM}) extracted from fitting to the obtained data for different densities and for both of the amplitudes, 1 fm and 10 fm. Initially, one can examine the data for amplitude 10 fm (corresponding to the case where oscillations are suppressed). Then, the damping parameter γ increases with density. For low densities (close to the vacuum state) γ reaches a small value, as in such a case there is no possible channel of dissipation. Consequently, for a zero-density background γ is expected to be equal to 0, as in such case there is no medium to which energy can be transferred from impurity. Later on, while density increases, more energy can be transferred from a cluster to the neutron matter; therefore, γ becomes larger, which can be explained with regard to Landau velocity. On the contrary, for amplitude 1 fm, the values of γ

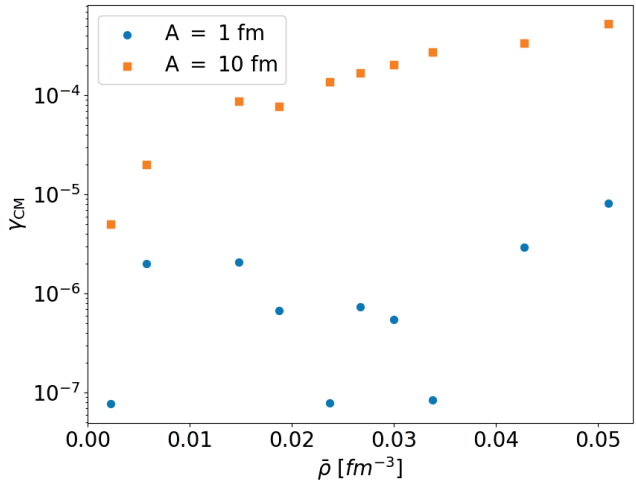

FIGURE 5.11: Damping coefficient extracted from fitting to center of mass oscillations for initial amplitude 1 fm and 10 fm as a function of density.

are small enough to be treated as zero, so for this amplitude, no damping can be observed.

Fig. 5.12 presents a plot of Landau velocity, together with other characteristic velocities, as a function of density. Landau velocity has a peak for lower densities (around 0.006 fm^{-3}); later on, it starts to decrease with density. One can examine this property with regard to Eq. 2.38, where the Landau velocity is described in terms of the pairing field and the Fermi wave vector. In this case, both of these quantities should be defined for neutrons and are denoted as Δ_n and k_{Fn}, respectively. Then, as k_{Fn} is defined through $(3\pi^2\rho_n)^{1/3}$, it is expected to increase with density. On the other hand, Δ_n increases for lower densities and has its maximum around 0.02 fm^{-3} [3]. After that, it starts to decrease with density. Combining these two properties, one can see that the Landau velocity tends to decrease with increasing density. Therefore, it also becomes easier for impurity to exceed this velocity. As a result, dissipation is also stronger in the higher density regime than in the case of lower densities.

In Fig. 5.12, some other important quantities are also presented. Together with Landau velocity, one can also consider the critical velocity mentioned in Chap. 4. As it has

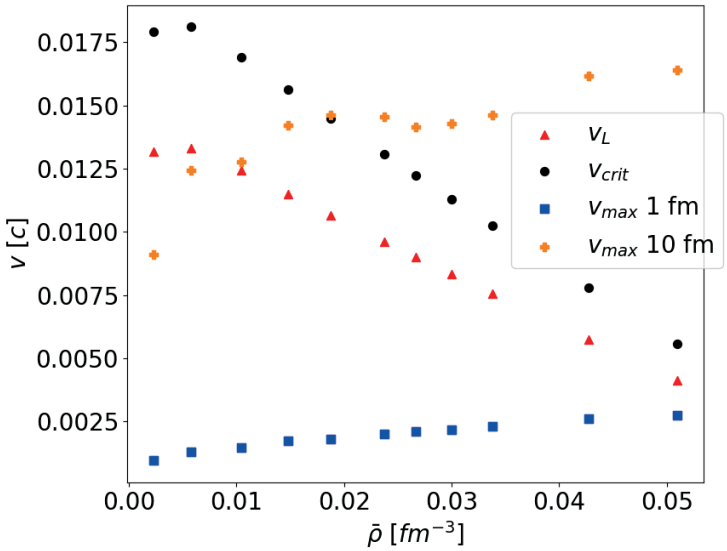

FIGURE 5.12: Landau velocity v_L, critical velocity v_{crit}, maximal velocity for amplitude equal 1 fm (v_{max} 1 fm) and for 10 fm (v_{max} 10 fm) as a function of density of the inner crust.

been shown, this quantity (described within Eq. 4.26) can be considered as a kind of „border", for which superfluidity is destroyed at all [3]. Later on, the maximal velocity for oscillation amplitudes of 1 fm and 10 fm is presented. This quantity has been calculated as $A\omega$, where A is the maximal amplitude of oscillations extracted from simulations and ω – frequency. For amplitude equal 1 fm this velocity does not exceed the Landau velocity; as a consequence, no damping occurs in such case, as the system remains in the superfluid state. On the contrary, for an amplitude equal to 10 fm, the Landau velocity is exceeded for almost all the densities (except for the lowest one). Therefore, for large oscillations, dissipation mechanisms start to occur in the system.

What is also interesting, the damping coefficient takes different values depending on the maximal velocity, which can be controlled by executing calculations for different amplitudes, $v = A\omega$. Fig. 5.13 presents this dependence for exemplary density 0.015 fm^{-3}; dashed line denotes the Landau velocity for this density. As expected, γ_{CM} increases with velocity. The higher the velocity is, the larger the amount of energy is

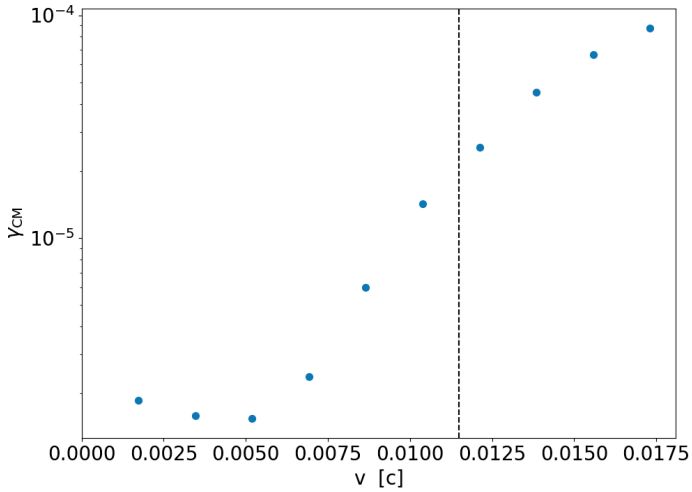

FIGURE 5.13: Damping coefficient as a function of maximal velocity of impurity for density 0.015 fm^{-3}.

distributed to the surrounding medium. Consequently, oscillations become more suppressed.

One can also make a connection between the exceeding of Landau velocity and condensation energy. In Fig. 5.14, panel a) presents two types of energies as a function of time obtained from the simulations:

- condensation energy E_{cond} (blue line) has been calculated from Eq. 4.25,
- energy connected with oscillations of impurity E_{osc} (orange line) has been obtained from the following relation:

$$E_{\text{osc}} = \frac{Mv^2}{2} + \frac{M\omega^2(Z_{\text{CM}} - Z_0)^2}{2}. \tag{5.37}$$

  where M is the effective mass of the impurity from the previous chapter. Other terms in this equation: ω (frequency of oscillations), Z_{CM} (position of the center of mass), and v (velocity of impurity) have been obtained from the results of the simulation.

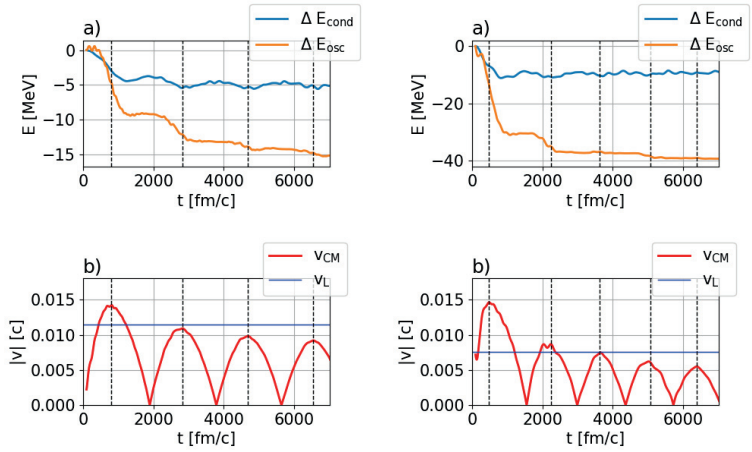

(A) $\bar{\rho} = 0.015$ fm^{-3} (B) $\bar{\rho} = 0.034$ fm^{-3}

FIGURE 5.14: a) Change of condensation energy ΔE_{cond} and change of energy of impurity ΔE_{osc} as a function of time, b) velocity of impurity v_{CM} and Landau velocity v_{L} as a function of time for densities 0.015 fm^{-3} and 0.034 fm^{-3}.

These energies are presented with regard to their initial values. Panel b) shows the velocity of impurity from Fig. 5.12 (red line, labeled in the legend as v_{CM}) and Landau velocity corresponding to the particular density (blue line, v_{L}). Again, vertical dashed lines correspond to time moments at which the Landau velocity reaches the local maximum. The results are shown for the amplitude of oscillations 10 fm, for densities 0.015 fm^{-3} and 0.034 fm^{-3}. The energy associated with oscillations (in which the kinetic energy of the impurity and the potential term related to harmonic oscillations are included) systematically decreases over time, which is related to the decreasing amplitude of the oscillations. Initially, when the Landau velocity is significantly exceeded, a major drop in condensation energy is observed. When superfluidity starts to be destroyed, the number of particles in the condensate decreases, which leads to a drop in the energy of the whole condensate. A similar tendency can also be observed for energy of oscillations. At the moments when velocity approaches the Landau velocity (corresponding to the local maxima in velocity), the drops in energy of oscillations are pronounced and the energy starts to decrease in time. This effect arises from dissipation mechanisms, which suppress the oscillations; consequently, their energy also decreases. In other words, when Landau velocity is exceeded, and dissipation starts

to occur in the system, the amplitude of oscillations becomes smaller and so does their energy.

At this point, one can come back to the results shown in Fig. 5.9. The effective masses calculated for amplitude of oscillations equal to 10 fm are consequently higher than the corresponding values obtained for small amplitudes. However, they follow the same tendency as parameters extracted for small amplitude and from the dynamic approach as well. Therefore, one can consider values for higher amplitudes as an upper bound for the uncertainty of the effective mass extracted using this method. One should also mention that an amplitude equal to 10 fm cannot be considered as a small value (as it has been shown, for such a value, damping occurs in the system). Therefore, the method's assumptions are not fulfilled in such a case. Even though one can see the qualitative agreement of the effective mass extracted for 10 fm with the results obtained for 1 fm (corresponding to a small amplitude of oscillations).

5.2.2 Quadrupole Moment Oscillations

Oscillations of the center of mass of impurity described in the previous section can be considered as the most basic type of oscillations of a collective variable. However, there can also be more sophisticated cases connected with another collective variable, such as the quadrupole moment (quantified by Q_{20}), which is related to the nuclear deformation of the impurity. In other words, one can observe oscillations of this collective variable, which correspond to the modification of the shape of a cluster. The following section of this chapter discusses this type of oscillation for zirconium nuclei (for which the number of protons Z is equal to 40).

In general, when the value of Q_{20} is modified, the nuclei become deformed according to the following scheme:

- when Q_{20} is zero, the shape of the impurity is spherical,
- negative sign of Q_{20} corresponds to oblate shape,
- when Q_{20} is positive, nuclei are deform into prolate shape.

The configurations described above are schematically shown in Fig. 5.15. The value of the quadrupole moment corresponds to the level of deformation – the higher Q_{20} is,

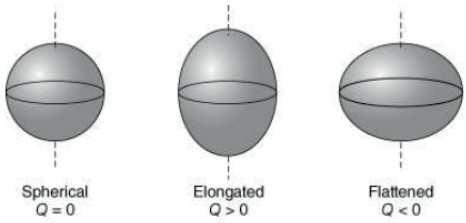

FIGURE 5.15: Spatial deformation of nuclei depending on the sign of the quadrupole moment [204].

the more deformed the nuclei are. As it has been mentioned before, typical values of Q_{20} for deformed nuclei are about 10^3-10^4 fm^2.

As well as in the case of center of mass oscillations, one can define the total energy functional of the system with regard to the collective variable and Eq. 5.26:

$$E' = \frac{M_{Q_{20}}\dot{Q}_{20}^2}{2} + V(Q_{20}) + \frac{k}{2}(Q_{20} - Q_{20_0})^2 = E + \frac{k}{2}(Q_{20} - Q_{20_0})^2, \tag{5.38}$$

where Q_{20_0} is connected with the reference shape of impurity. In this case, the value has been set to 0 (which means that impurity would oscillate around a spherical shape). The variable k corresponds to the control parameter, which determines the strength of external driving. However, in this case, the mass parameter $M_{Q_{20}}$ is connected to the deformation of nuclei; in general, it indicates how easily an impurity can be deformed.

Based on that, the mean-field potential (acting only on protons) applied in dynamical calculations can be written as:

$$U_p = \frac{\delta E'}{\delta \rho_p} = U_{p,\mathrm{BSk}} + kQ_{20}(3z^2 - r^2). \tag{5.39}$$

Technically, in the first step, the static solution (nuclei with small deformation) has been obtained. The initial value of Q_{20} imposed as a constraint in static calculations has been set to 100 fm^2. In general, the ground state has been calculated through constrained minimization with regard to the Lagrange multiplier method. The formula for energy, being a subject of minimization, has been written as:

$$E = E_{\mathrm{BSk}} - \lambda_Q(Q_{20} - Q_{20_0}), \tag{5.40}$$

where λ_Q has the meaning of Lagrange multiplier. During the numerical procedure, the multiplier was updated in each iteration once the ground state energy was obtained, with the desired value of Q_{20}. What is especially important in the case of static calculations is that the variable Q_{20_0} has a slightly different meaning than in the dynamic protocol. In Eq. 5.40, Q_{20_0} means the requested deformation that the nucleus should reach after the procedure of minimization. In other words, in the ground state, impurity was assumed to have some deformation, which in this case has been set to 100 fm^2. Such a ground state solution, with an imposed value of quadrupole moment (i.e., a deformed impurity), served as the starting point for time evolution. Later on, at the beginning of time evolution, the constraint on the deformation was released. As a result, impurity oscillated spontaneously around a spherical shape (in other words, it changed its shape from prolate through spherical to oblate). In both static and dynamic calculations, the investigated system had 32 lattice points in each direction (so N_x x N_y x N_z = 32 x 32 x 32) with a lattice spacing 1.25 x 1.25 x 1.25 (in fm). Fig. 5.16 shows the initial configuration of the simulated system (ρ_n describes the density of neutrons and ρ_p is the density of protons).

As well as in the case of the center of mass, the fundamental results recorded from simulations are the oscillations of the collective variable. Based on that, the mass parameter was calculated. Fig. 5.17 (for nuclear density equal 0.015 fm^{-3}) illustrates this procedure. In panel a), one can see oscillations of the quadrupole moment (in units of fm^2) as a function of time (in fm/c) for several values of k. Panel b) shows the squared frequency ω^2 of oscillations extracted (for each k) from fitting a curve to data from the simulation. As can be seen in panel a), quadrupole moment oscillations can be described in terms of the model of a damped harmonic oscillator, with a starting amplitude equal to the initial value of the quadrupole moment imposed in static calculations (100 fm^2). Therefore, one could fit Eq. 5.31 to the data from the simulation. Later on, as well as in the previous case, from fitting a dependence from Eq. 5.28 to $\omega^2(k)$, one can extract the mass parameter as the inverse of the slope coefficient of the fitted line. In the exemplary case from Fig. 5.17, the mass parameter is approximately 0.10 fm^{-3} and the frequency of quadrupole mode $\omega_{Q_{20}} = 0.1023$ c/fm.

First of all, despite the fact that the initial value of the quadrupole moment has been set in a way that enforces oscillations of small amplitude, damping could have been observed. Therefore, it turns out that quadrupole moment oscillations exhibit a finite

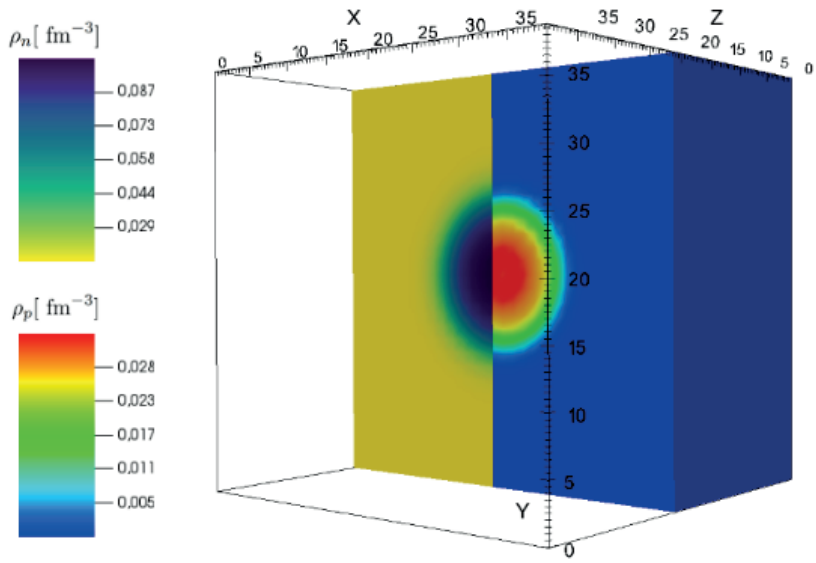

FIGURE 5.16: The initial configuration of the system in the investigation of quadrupole deformation being equal $Q_{20} = 100\,\mathrm{fm}^2$. The deformation is too small to be seen in this image, where the impurity looks spherical [20].

lifetime, which stands in contrast with center of mass oscillations (where, for sufficiently small amplitudes, no dissipation occurred). In addition, in contrast to center of mass oscillations, the intercept appears for ω different than 0. As an example, in case presented in Fig. 5.17 frequency of intercept (denoted as $\omega_{Q_{20}}$) is equal 0.1023 c/fm. The same property has also been observed for all other studied densities; therefore, one can conclude that in the case of quadrupole moment oscillations, the energy mode corresponding to $\omega_{Q_{20}}$ is not the zero-energy Goldstone mode.

With regard to approach presented in Sec. 5.2, for each density mass parameter was extracted. Moreover, the energy of the quadrupole mode (corresponding to the frequency of oscillations $\omega_{Q_{20}}$ extracted from simulations) has been calculated. Both of these results are shown in Fig. 5.18 – panel a) shows energy of the mode (in units of MeV) and panel b) – mass parameter (in MeV/(fm^{2}c^2)). In the case of the mass parameter, apart from the results obtained within the discussed method (denoted as *new method*), quantities extracted in the framework of the hydrodynamic approach are also presented. Both modes' energy and mass parameters decrease with density, in agree-

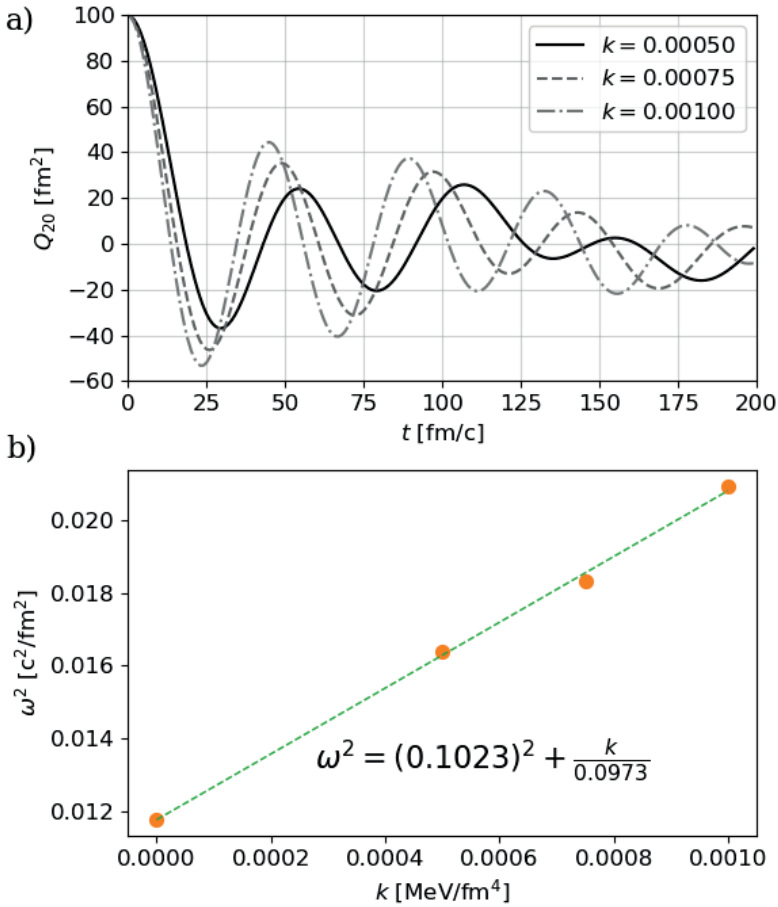

FIGURE 5.17: a) Time evolution of Q_{20} for different values of k. b) Squared frequency of oscillations as a function of k [20].

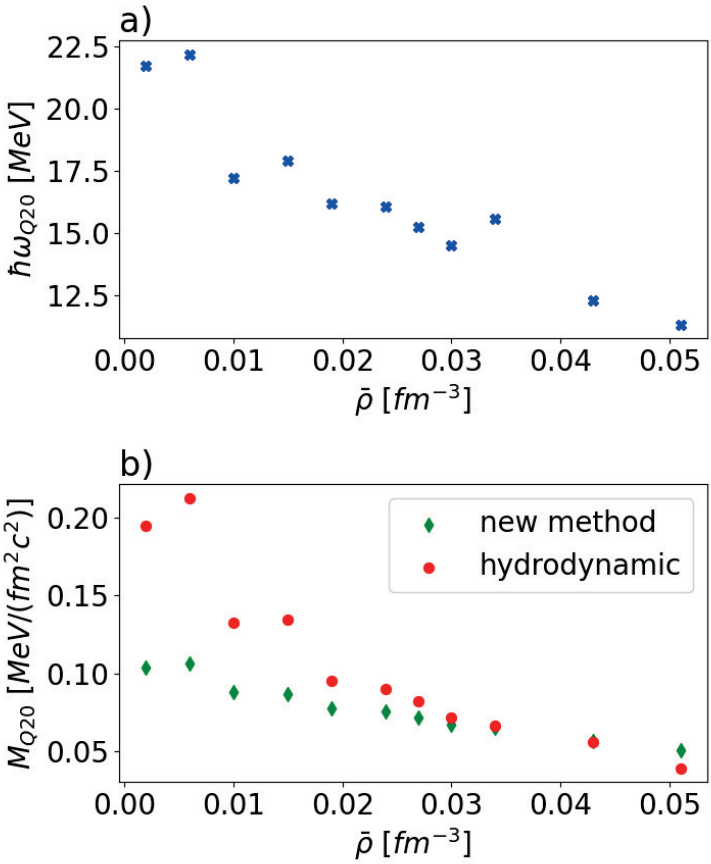

FIGURE 5.18: a) Energy of the mode (where $\omega_{Q_{20}}$ has been extracted from simulations) as a function of density. b) Mass parameter obtained within the general method (labeled as *new method*) and from the hydrodynamic approach (*hydrodynamic*) as a function of density [20].

ment with expectation. According to the theoretical introduction from Sec. 5.2, the quadrupole mass parameter gives information about the susceptibility of the impurity for deformation – the lower this quantity is, the easier it is to modify the shape of a cluster. This feature can be explained in terms of the mode's energy. As it was described in Sec. 2.1, when density is higher, proton clusters start to evolve from spherical impurities into more exotic structures (such as nuclear pasta). As these structures become increasingly complex, their deformation requires less energy. Therefore, as the energy of the mode decreases at higher densities, the mass parameter is expected to be smaller for higher densities.

One should also note the comparison of the mass parameter with the results from the hydrodynamic method (calculated with Eq. 5.23 and indicated in Fig. 5.18 by red dots). In the limit of higher densities (above approximately 0.03 fm^{-3}), hydrodynamic estimation is in good agreement with quantities obtained within dynamical calculations; later on, the lower the density is, the higher the discrepancy one can observe. In general, the hydrodynamic method is expected to work better for higher densities. In the limit of lower densities, the system consists of impurities in the neutron medium, which is close to the vacuum (in other words, there is, in fact, no neutron fluid). However, in the hydrodynamic method, it is assumed that impurities are immersed in some medium. As a consequence, the predictions of hydrodynamic methods in the regime of low densities may not reflect the real properties of the system. On the contrary, for higher densities the amount of neutron fluid increases, so the system starts to "match" the conditions of the hydrodynamic approach.

Another important conclusion is related to the density at which both modes' energy and mass parameters are equal to zero. It can be estimated by fitting a line to the data and finding the point of intercept. The result of this procedure is shown in Fig. 5.19. The density of intercept (denoted as $\bar{\rho}_0$) in both cases is close to 0.09 fm^{-3}. According to [12], this density approximately corresponds to the crust-core transition density. When the density of background neutrons is very high, deformation of proton structures requires almost no energy; therefore, in such a case, the mass parameter and energy of the mode are equal to 0.

In addition, one should also mention that in the case of quadrupole moment oscillations, one can also calculate the damping coefficient, as well as in the case of center

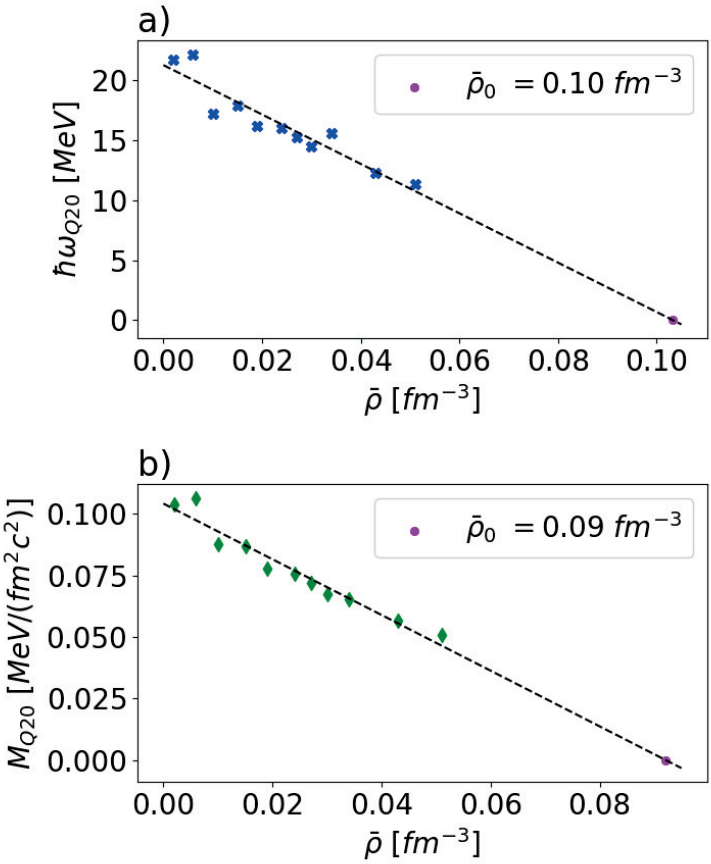

FIGURE 5.19: a) Energy of the mode (where $\omega_{Q_{20}}$ has been extracted from simulations) as a function of density. b) Mass parameter obtained within the general method as a function of density. In both panels, the dashed line has been fitted to the data points. The magenta dot ($\bar{\rho_0}$ in the legend) denotes the density of intercept.

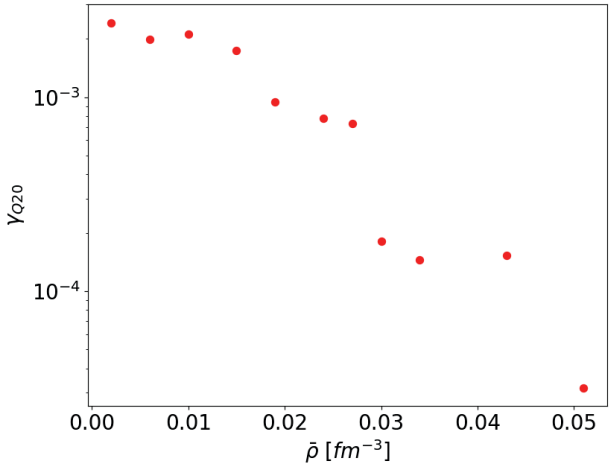

FIGURE 5.20: Damping coefficient as a function of density for $k = 0.01$ Mev/fm^4.

of mass oscillations. Fig. 5.20 presents the dependence of this parameter (labeled as $\gamma_{Q_{20}}$) on density of the inner crust for $k = 0.01$ Mev/fm^4. These results show a different tendency than the damping parameter in the case of center-of-mass oscillations. Here, similarly to the mass parameter, the damping coefficient decreases with density, which is also an expected behaviour. As the density increases, the impurities deform into various exotic structures, ultimately reaching the pasta state. Therefore, once we approach these states, the deformation of impurity should require less energy. Due to that, the spatially modified nucleus would have a longer lifetime of oscillations.

5.3 Summary

In this chapter, the following topics have been considered:

- I have presented a new and general method of extracting the mass parameter of nuclei immersed in the sea of superfluid neutrons in the inner crust of a neutron star. What makes this method a cutting-edge achievement is that it can be applied to each collective variable that can be expressed as a functional of density.

- In this chapter, I have applied this new method to two cases. The first of these was the analysis of center-of-mass oscillations, based on which I extracted the

effective mass (which has also been obtained within the framework of another TDDFT-based approach discussed in the previous chapter). Another investigated quantity was the mass parameter for the quadrupole moment (in this case, the results were unknown).

- The effective masses obtained by this method have been compared with predictions from the previous chapter and turned out to be in very good agreement, which demonstrates the correctness of the general method.
- From the analysis of the oscillations of impurity, one could also get a deeper insight into dissipative processes.
- Next, I have extracted the mass parameter for the quadrupole moment, which is a new contribution to the field of neutron star crust investigation.
- I have also demonstrated that both the mass parameter and mode energy decrease to zero as one approaches the crust-core transition.

The crucial advantage of the presented method that should be highlighted is its applicability in cases where nuclei are surrounded by neutron matter (i.e., in the context of a many-body interacting system). In general, collective mass parameters are usually extracted for impurity localized in vacuum [195], as it is done, e.g., within the adiabatic approximation of the time-dependent HFB method (ATDHFB) [205, 206, 207]. This approach is commonly used in studies of large amplitude collective motion (LACM), where the collective motion of the whole particles in the system is assumed to be significantly slower than the movement of each of the particles considered separately [62]. As an example of the extensions of the ATDHFB method, one can consider the popular cranking approximation [208], introduced in [209] and [210]. Despite this method also allowing for the investigation of large systems (as shown, e.g., in [211] and [212]), it encounters significant challenges related to computational cost. In addition, there is a need to separate quasiparticle wave functions corresponding to the impurity and to the surrounding medium, which also turns out to be a major problem. The dynamic approach discussed in this thesis overcomes the limitations mentioned above and allows for the extraction of mass parameters within well-developed numerical tools [3].

Chapter 6

Vortex-Nucleus Interaction

The last part of this thesis is devoted to the interaction of a vortex with an impurity. The theoretical background of this research is provided in Sec. 2.5 concerning dynamical properties of the inner crust. According to the force balance equation (Eq. 2.95) discussed there, in the neutron star crust, one can distinguish various forces connected with the interaction of vortices and impurities, such as pinning and tension force. This interaction also affects the system's energy and reinforces the change in vortex shape. In addition, the vortex-nucleus interaction causes the deformation of the impurity, which can be described in terms of either the quadrupole or the octupole moment. This chapter focuses on the examination of parameters that describe vortex-nucleus interactions.

6.1 Studies of Vortex-Nucleus Interaction within Various Approaches

6.1.1 Static Calculations of Pinning Energy

As it has been discussed in Sec. 2.5.2, one of the parameters that are crucial in the description of the dynamics of vortices in the neutron star crust is the pinning force. In general, in the crust, the vortex lines cannot move freely, as the interaction with impurities limits their displacement. In other words, one can say that vortices are "pinned" to the lattice of impurities [86, 213]. Therefore, one can introduce the quantity that describes the strength of this pinning, known as the pinning force. In the literature, it is referred to either in terms of force or potential, as, for example, in [214].

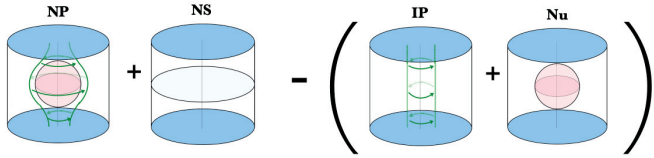

FIGURE 6.1: The sketch of configurations used in the static method of vortex-nucleus interaction studies [214].

The examination of the pinning potential at the microscopic level turns out to be a demanding challenge. As reported in [214], one of the first attempts to tackle this problem has been discussed, e.g., in [91, 215]. There, it has been taken into consideration that the internal structure of the nuclei has a certain influence on their interaction with the vortex. The analogous assumption has been made in the approach presented in [214], where the vortex-nucleus interaction has been investigated in the framework of static calculations. In this approach, the energy of the system is considered separately for a few vortex-nucleus configurations, as shown in Fig. 6.1 [214]. In the static method, the pinning energy is estimated from the binding energy, which is understood as the cost of moving the vortex from the top of the nucleus to infinity [214]. In other words, the binding energy corresponds to the difference between two specific energies: the amount needed to create the vortex at the top of the nucleus and in the uniform matter [214]. In order to estimate the binding energy, with each of the configurations from Fig. 6.1, one can associate a particular energy [214]:

- energy of neutron sea E_{NS} (describing the configuration denoted in Fig. 6.1 as NS, which corresponds to the pure neutron matter),
- energy connected with nucleus E_{N} (configuration Nu, which is an impurity immersed in the neutron matter),
- energy corresponding to interstitial pinning E_{IP} (IP: vortex surrounded by neutron sea),
- nuclear pinning energy E_{NP} (NP: configuration of vortex and nucleus in the neutron matter).

Based on that, one can estimate the binding energy E_{B} as:

$$E_{\mathrm{B}} = E_{\mathrm{NP}} + E_{\mathrm{NS}} - (E_{\mathrm{Nu}} + E_{\mathrm{IP}}) - \lambda_n \left[N_{\mathrm{NP}} + N_{\mathrm{NS}} - (N_{\mathrm{Nu}} + N_{\mathrm{IP}})\right]. \tag{6.1}$$

Here, the correction term $\lambda_n \left[N_{\mathrm{NP}} + N_{\mathrm{NS}} - (N_{\mathrm{Nu}} + N_{\mathrm{IP}})\right]$ (where λ_n means the chemical potential of neutrons and N is number of neutron in each Wigner-Seitz cell) is included in order to keep the fixed number of neutrons [214].

Another important aspect has been raised in [216], where it has been noted that the movement of impurity causes certain displacement of surrounding neutron matter as well. Therefore, one should include this effect in the binding energy through the correction term $K(R)$ (dependent on the vortex-nucleus distance R) [214, 216]:

$$K(R) = \frac{3}{2} M_s \left(\frac{\zeta - 1}{\zeta + 1}\right) \left(\frac{\hbar}{2mR}\right)^2, \tag{6.2}$$

where M_s is the mass of neutron superfluid displaced during the movement of impurity, m is the mass of nucleon and ζ is the ratio of nucleus density ρ_{imp} and density of superfluid neutrons ρ_{bn} (corresponding to the bulk/background density of neutrons from the previous chapters).

In the next order, one can also take an insight into the contribution of nuclear interaction. According to [214], its influence on the pinning energy becomes negligible for sufficiently large distances between vortex and nucleus. Such a critical distance R^* can be estimated as the sum of the radius of impurity R_{imp} and coherence length ξ (corresponding to the size of the vortex core): $R^* \sim R_{\mathrm{imp}} + \xi$ [214]. In addition, it is assumed that the nuclear contribution can be neglected for vortex-nucleus distance R larger than R^*. Then, one can consider the following possibilities [214]:

- for critical distance R^* smaller than the radius of the radius of Wigner-Seitz cell R_{WS} (so when $R^* < R_{\mathrm{WS}}$), it is assumed that at R_{WS} the main correction is the kinetic one (Eq. 6.2). Then, for vortex-nucleus distance R equal R_{WS}, the pinning energy can be calculated from the binding energy as:

$$E_p \approx E_b - K(R_{\mathrm{WS}}), \tag{6.3}$$

- when critical distance R^* is greater than the size of Wigner-Seitz cell ($R^* > R_{\mathrm{WS}}$, the nuclear contribution (and, consequently, also pinning energy) cannot be estimated within the static method due to the vortex-nucleus overlap at R_{WS}.

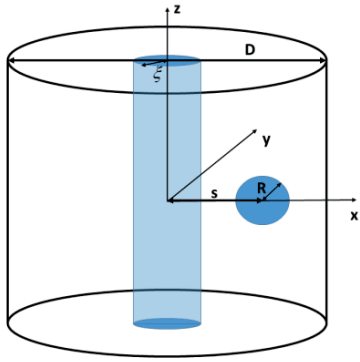

FIGURE 6.2: The schematic view of the investigated system: impurity moving through the neutron medium in the surroundings of the vortex line [82].

To summarize, static calculations enable the estimation of pinning energy under certain assumptions. Firstly, one has to properly choose the configurations from Fig. 6.1 and estimate the critical distance between vortex and nucleus. Then, once the conditions connected with the size of the Wigner-Seitz cell are met, one can finally calculate the pinning energy.

6.1.2 Hydrodynamic Approach

Another way of examining the vortex-impurity interaction is based on hydrodynamic calculations. First attempts to apply this approach to the case of neutron star crust have been described in [216]. In this work, the energy of impurity as a function of vortex-nucleus distance has been investigated [214]; however, in contrast to the static approach, the hydrodynamic method does not consider the structure of the nucleus. Within the approach presented in [216], it has been shown that vortex lines pin to the nuclei for higher nuclear densities (corresponding to the deeper layer of the crust), while in the regime of lower densities, the vortices are repelled from the impurities [214]. Later on, this approach was improved in [217], where the local density approximation was also included.

Within the hydrodynamic approach, one can take a closer look at the energy of the vortex-impurity system, shown schematically in Fig. 6.2 [82]. There, one can see the impurity of radius R moving along the x axis, and the vortex line with core radius ξ

placed along the z axis, in the middle of the $x-y$ plane (so its coordinates in this plane are set to 0). The distance between the vortex and the impurity is denoted as s. The entire system is limited by the potential in the form of a tube (in the figure, the diameter of the entire system, corresponding to the size of the Wigner-Seitz cell), denoted as D.

As well as it has been done, e.g., in the effective mass studies in Sec. 4.1.2, with the impurity and the neutron medium surrounding it, one can associate a particular potential field. The general form of potential fields inside of impurity (Φ_{in}) and outside of it (Φ_{out}) can be written with Eq. 4.10 and Eq. 4.11, respectively. Additionally, in the analyzed case, one should also define the velocity potential for the vortex line, which can be written as $(\kappa/(2\pi))\phi$. The term $\kappa = 2\pi\hbar/2m_n$ is the circulation, and ϕ means the angle in the $x-y$ plane [82]. Again, the potential field inside and outside of the impurity has to fulfill the boundary conditions from Eqs. 4.7 - 4.9 [216, 187, 82].

The impurity is assumed to move with constant velocity $\boldsymbol{u}$. Due to this movement, the velocity potential outside of the nucleus can be modified into the following form [82]:

$$\Phi_{\text{out}}(r,\phi) = \frac{\kappa}{2\pi}\phi + A\frac{(\boldsymbol{r}-\boldsymbol{s})(\frac{\kappa}{2\pi s}\boldsymbol{e}_y - \boldsymbol{u})}{|\boldsymbol{r}-\boldsymbol{s}|^3} \tag{6.4}$$

with $\boldsymbol{e}_y$ being the unit vector along y axis and A a constant. On the other hand, one can define the potential field inside of impurity as [82]:

$$\Phi_{\text{in}}(r,\phi) = B_0 + B_1(\boldsymbol{r}-\boldsymbol{s})\frac{\kappa}{2\pi s}\boldsymbol{e}_y + B_2(\boldsymbol{r}-\boldsymbol{s})\boldsymbol{u}. \tag{6.5}$$

The constants B_0, B_1, B_2 can be obtained from boundary conditions (Eqs. 4.7 - 4.9). After that, the formula for velocity potential inside of impurity can be rewritten into the following equation [82]:

$$\Phi_{\text{in}}(r,\phi) = \left(1+\frac{A}{R^3}\right)(\boldsymbol{r}-\boldsymbol{s})\frac{\kappa}{2\pi s}\boldsymbol{e}_y + \frac{A}{R^3}(\boldsymbol{r}-\boldsymbol{s})\boldsymbol{u}. \tag{6.6}$$

Then, following the analysis from Sec. 4.1.2, one can write the expression for the total energy of the system [82, 216]:

$$E = \frac{1}{2}\rho_{\text{in}}\int_{V_i}(\nabla\Phi_{\text{in}})^2 d^3r + \frac{1}{2}\rho_{\text{out}}\int_{V-V_i-V_{vor}}(\nabla\Phi_{\text{out}})^2 d^3r, \tag{6.7}$$

where the terms V, V_i, and V_{vor} mean the total volume of the system, volume of impurity, and volume of the vortex, respectively. The component ρ_{out} is bulk density of neutrons and $\rho_{\text{in}} = \rho_p + \rho_n$ is the density inside of impurity. Based on that, one can derive the following form of the formula for energy [82]:

$$E = \frac{1}{4\pi}\rho_{\text{out}}\kappa^2 H \ln\left(\frac{D}{2\xi}\right) + \frac{1}{2}\left(\frac{4\pi}{3}R^3\frac{(\rho_{\text{in}}-\rho_{\text{out}})^2}{2\rho_{\text{out}}-\rho_{\text{in}}}\right)u^2 + \\ + 2\pi R^3\frac{\rho_{\text{out}}(\rho_{\text{in}}-\rho_{\text{out}})}{2\rho_{\text{out}}+\rho_{\text{in}}}\left(\frac{\kappa}{2\pi s}\right)^2. \tag{6.8}$$

Here, H denotes the height of the cylinder (potential tube), which can be obtained from the dependence for its volume: $V = \pi D^2 H/4$. On the right side of Eq. 6.8, one can distinguish various components giving rise to the total energy of the system. The first of them corresponds to the contribution of vortex line, the second is connected with the kinetic energy of impurity, and the last one means the contribution to energy coming from vortex-nucleus interaction [82]. The derivative of this last term, denoted as E_{VN}:

$$E_{\text{VN}} = 2\pi R^3\frac{\rho_{\text{out}}(\rho_{\text{in}}-\rho_{\text{out}})}{2\rho_{\text{out}}+\rho_{\text{in}}}\left(\frac{\kappa}{2\pi s}\right)^2 \tag{6.9}$$

over the vortex-nucleus distance s leads to the formula for the interaction force F_{VN}:

$$F_{\text{VN}} = -\frac{dE_{\text{VN}}}{ds} = \frac{d}{ds}\left(2\pi R^3\frac{\rho_{\text{out}}(\rho_{\text{in}}-\rho_{\text{out}})}{2\rho_{\text{out}}+\rho_{\text{in}}}\left(\frac{\kappa}{2\pi s}\right)^2\right) = \\ = -2\frac{\hbar^2}{2m_n}\frac{\rho_{\text{out}}(\rho_{\text{in}}-\rho_{\text{out}})}{2\rho_{\text{out}}+\rho_{\text{in}}}\frac{3M_{\text{eff}}}{4\rho_{\text{in}}m_n}\frac{1}{s^3}. \tag{6.10}$$

In this equation, the term M_{eff} is the effective mass of the impurity. According to [82], for large vortex-nucleus distance s, the dependence of force on this distance is expected to behave like C/s^3 with C being the coefficient:

$$C = 2\frac{\hbar^2}{2m_n}\frac{\rho_{\text{out}}(\rho_{\text{in}}-\rho_{\text{out}})}{2\rho_{\text{out}}+\rho_{\text{in}}}\frac{3M_{\text{eff}}}{4\rho_{\text{in}}m_n}. \tag{6.11}$$

In this chapter, the values of the coefficient C are compared with the predictions of DFT-based calculations.

Another important parameter in the context of vortex-nucleus interaction is the tension force. In principle, this quantity describes the vortex properties connected with

its susceptibility for deformation (in other words, how easy it is to modify the shape of the vortex). Coming back to Eq. 6.8, the energy connected with vortex tension (E_{vort}) corresponds to the first term on the right side of equation [82]

$$E_{\mathrm{vort}} = \frac{1}{4\pi}\rho_{\mathrm{out}}\kappa^2 H \ln\left(\frac{D}{2\tilde{\xi}}\right). \tag{6.12}$$

From this relation, one can calculate the tension force as the derivative of E_{vort} over the height of the cylinder H. Then, the hydrodynamic formula for tension force takes the form: [82, 218, 213]:

$$T = \frac{1}{4\pi}\,\rho_{bn}\,\kappa^2 \ln\left(\frac{D}{2\tilde{\xi}}\right), \tag{6.13}$$

where ρ_{bn} is the density of the superfluid component, which in this case corresponds to the bulk density of neutrons. As the term $\ln\left(\frac{D}{2\tilde{\xi}}\right)$ is expected to be close to 1, Eq. 6.13 can be also written in the approximated form:

$$T \approx \frac{1}{4\pi}\,\rho_{bn}\,\kappa^2, \tag{6.14}$$

which has been used in hydrodynamic-based calculations in the following part of the thesis.

6.2 Vortex-Nucleus Interaction in the Frame of Density Functional Theory

The schematic view of the initial setup of the investigated system (for exemplary density 0.019 fm^{-3}) is shown in Fig. 6.3. The size of the box has been set as follows:

- grid: 64 x 64 x 64 (64 lattice points in each direction),
- lattice spacing: 1.25 x 1.25 x 1.25 (in fm).

As mentioned in the previous chapters, the system consists of an impurity immersed in a neutron medium. At the beginning of the simulations, the impurity is located at position [-20,0,0] (in fm). One can also see the vortex line (the black curve), located initially in the middle of the box (corresponding to coordinates $[x, y] = [0, 0]$) and stretched along the z axis (so its initial length is equal to the z-th dimension of the system). In the dynamic calculations, the impurity was dragged along the x axis to a

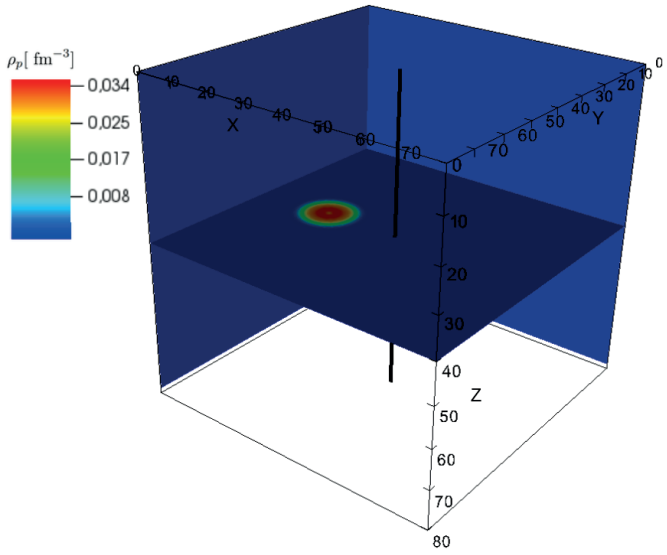

FIGURE 6.3: The initial setup of the investigated system for average density 0.019 fm^{-3}: the impurity immersed in the neutron medium and the vortex line (denoted as the black curve) localized along the z axis.

position of [20,0,0] (in fm) with an approximately constant velocity of 0.002 c. During the movement, the nucleus passed in the vicinity of the vortex line, leading to mutual interaction between them. This process is schematically illustrated in Fig. 6.4 for density 0.019 fm^{-3} (each of the panels corresponds to a particular time moment). In this part of the research, the vortex has been generated directly in the code via the phase imprint method (the procedure is described in detail in [219]). Additionally, the system has been confined within an external potential in the form of a tube. As a result, such a system becomes finite, allowing for the generation of finite angular momentum (and thus, the generation of a vortex). Finally, the motion of the impurity has been induced by a uniform electric field in space. However, in contrast to the calculations in the previous chapters, its direction and strength were time-dependent. The protocol for the force adjustment is described in the next section.

6.2.1 Interaction Force

When an object, such as a nuclear impurity, travels with a constant velocity, based on Newton's principles, we can conclude that the total force acting on the object is equal

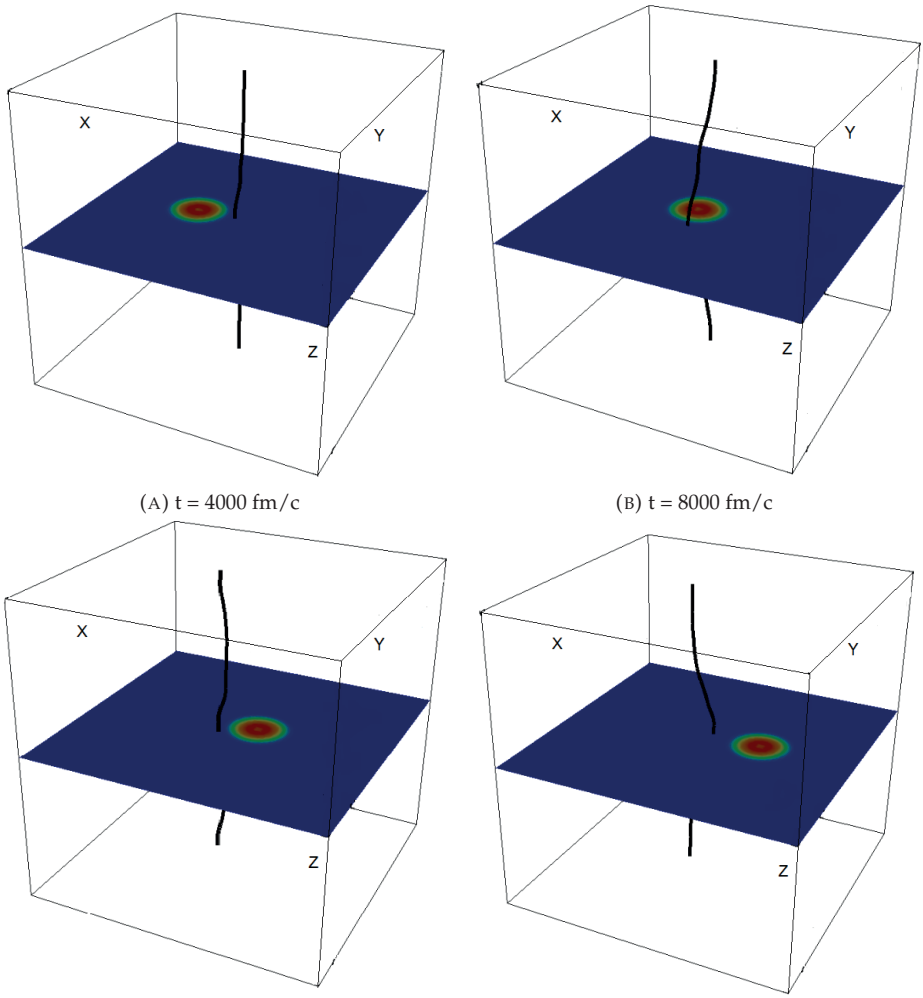

(A) t = 4000 fm/c (B) t = 8000 fm/c

(C) t = 12000 fm/c (D) t = 16000 fm/c

FIGURE 6.4: The time evolution of the vortex-nucleus system for density 0.019 fm^{-3}. Each of the panels shows the system for the particular time moment. The impurity is dragged along x axis, approaches the vortex and passes it. As a result, the vortex line becomes deformed.

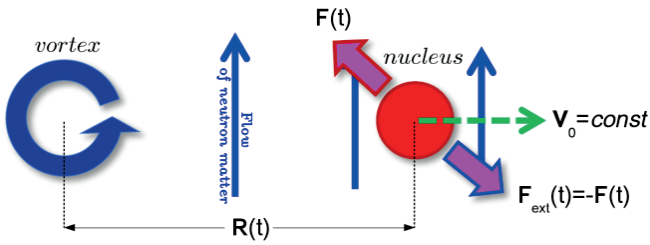

FIGURE 6.5: Schematic procedure of extraction of vortex-nucleus interaction force [82]. The impurity moves with constant velocity v_0 in the $x-y$ plane and passes the vortex line. The interaction force $\boldsymbol{F}$ depends on the distance $\boldsymbol{R}$ between these elements. The external force $\boldsymbol{F}_{\text{ext}}$ is adjusted during calculations in order to maintain the constant velocity of the impurity.

to zero. This statement encapsulates the primary concept underlying the protocol for extracting the vortex-nucleus force in the dynamical approach. The protocol of extraction of this force follows the idea from [82] and is schematically shown in Fig. 6.5. Here, one can see the impurity moving through the medium with a particular constant velocity v_0 in the $x-y$ plane. During this movement, the impurity propagates in the vicinity of the vortex. The interaction between these elements depends on the distance between them (later on denoted as R), which is considered as the smallest distance between the impurity and the vortex line (this quantity is also shown in Fig. 6.6). The vortex-nucleus interaction is represented by the force. As it has been described in [82], when the impurity moves with constant velocity, the forces acting on it have to be in balance. In the analyzed case, one can distinguish the following forces acting on the impurity:

- external force $\boldsymbol{F}_{\text{ext}}$, which is controlled in the code,
- vortex-nucleus interaction force $\boldsymbol{F}_{\text{VN}}$, which we want to extract,
- other dissipative forces. However, if the velocity is much smaller than the Landau velocity, their impact can be neglected.

Therefore, the total force $\boldsymbol{F}_{\text{tot}}$ can be written as the sum of external force and vortex-nucleus interaction force: $\boldsymbol{F}_{\text{tot}} = \boldsymbol{F}_{\text{ext}} + \boldsymbol{F}_{\text{VN}}$. If velocity is constant, then the total force is equal to 0, according to Newton's rules: $\boldsymbol{F}_{\text{tot}} = 0$. Thus, we get the relation between vortex-nucleus interaction force and external force, which reads: $\boldsymbol{F}_{\text{VN}} = -\boldsymbol{F}_{\text{ext}}$. Based on that, one can construct a protocol that generates such an external force as to assure

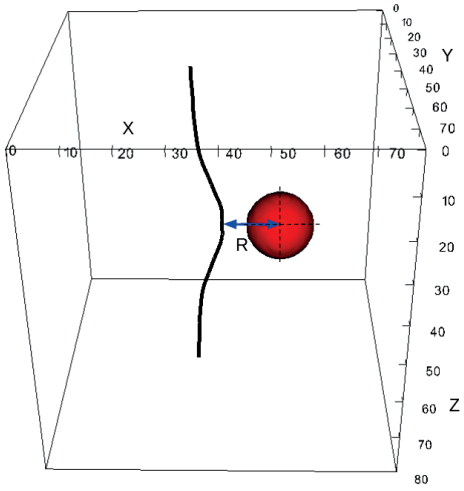

FIGURE 6.6: The definition of the distance R between vortex and impurity. It is considered to be the smallest distance between the center of the impurity and the vortex line, denoted as R and marked with blue arrows. The black curve is the vortex line, and the black cross denotes the center of mass of the impurity.

the movement with constant velocity. What is especially important, this is a very robust approach, as it only utilizes Newton's law and is free from other assumptions, in contrast to the previous methods.

In the code, the external force has been adjusted in each iteration to provide the constant velocity of impurity according to the following formula [82]:

$$\boldsymbol{F}_{\text{ext}}(t+\Delta t) = \boldsymbol{F}_{\text{ext}}(t) - \alpha[\boldsymbol{v}(t) - \boldsymbol{v}_0], \tag{6.15}$$

where $\boldsymbol{v}_0$ is the requested constant velocity of impurity and α is the coefficient of adjustment. The term $\boldsymbol{v}(t)$ is the velocity calculated at time t as time derivative of center of mass position $\boldsymbol{R}(t)$: $\boldsymbol{v}(t) = [\boldsymbol{R}(t) - \boldsymbol{R}(t-\Delta t)]/\Delta t$. In every time step, the force is modified in order to maintain the constant velocity of the impurity As an example, Fig. 6.7 shows the dependence of particular components of velocity in each direction: v_x, v_y, and v_z on time for density 0.015 fm^{-3}. After the initial part of trajectory (during which the velocity of impurity arises due to the impact of electric field), the component of velocity in x direction becomes constant for the rest of the simulation, while v_y and

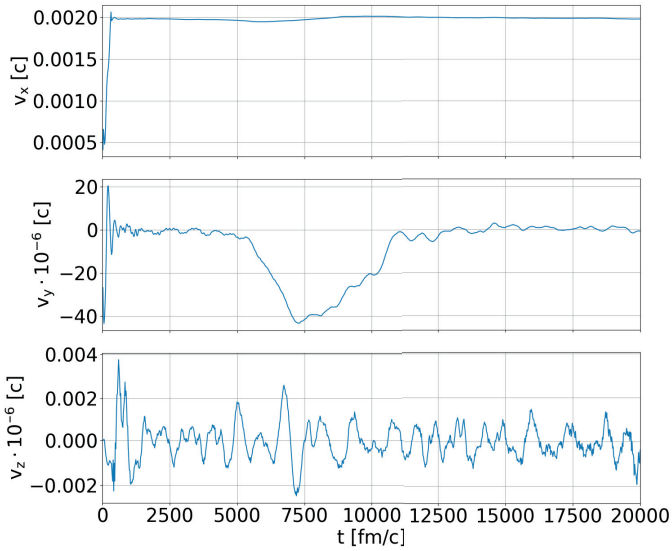

FIGURE 6.7: The components of velocity of impurity as a function of time: a) in x direction, b) in y direction, z) in z direction for density 0.015 fm^{-3}.

v_z are almost zero. From this, it can be inferred that the interaction force is compensated. In addition, the imposed velocity of impurity is significantly smaller than the critical velocity and does not cause phonon excitation (in other words, the dynamics can be assumed to be adiabatic) [82].

Once the interaction force has been extracted from simulations, it could have been decomposed into longitudinal and perpendicular components with respect to the reference frame defined by the relative position of vortex and impurity (so that the longitudinal force acts along this line). Fig. 6.8 demonstrates the procedure of decomposition of the interaction force. Starting from the initial coordinate frame, another one can be defined. The first of the new axes, labeled in the figure as *longitudinal*, corresponds to the line connecting vortex and impurity. Then, another axis is perpendicular to it. In this new coordinate frame, the interaction force can be decomposed into the longitudinal (F_{L}) and perpendicular (F_{P}) parts. The vortex-nucleus distance (denoted as R) is calculated along the longitudinal axis.

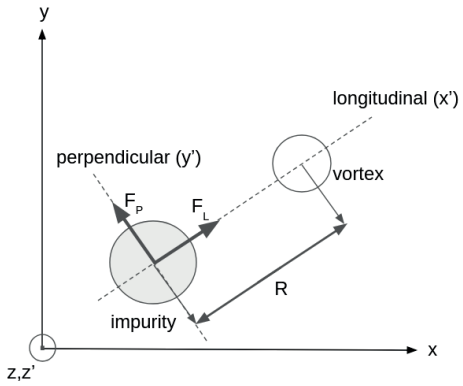

FIGURE 6.8: The sketch of the decomposition of the interaction force between the vortex and the impurity. F_L denotes the longitudinal component (acting along axis labeled as *longitudinal*) and F_P is the perpendicular part (acting along *perpendicular* axis). R denotes the vortex-nucleus distance.

Fig. 6.9a presents the perpendicular and longitudinal components of the vortex-nucleus interaction force F (in MeV/fm) as a function of the distance between vortex and nucleus R (in fm) for density 0.019 fm^{-3}. At this point, it is worth noting that the simulations actually describe two distinct scenarios. As mentioned at the beginning of the chapter, in the first part of the simulation, the impurity approaches the vortex. Later, the nuclei pass in the vicinity of the vortex and move away from it. Therefore, the interaction force from Fig. 6.9a has been calculated for each part of the simulation and then averaged. Fig. 6.9b presents the longitudinal force before averaging, extracted for two cases: when the impurity was approaching and leaving the vortex. In agreement with results reported in the literature, the perpendicular component oscillates around zero (so the interaction takes place along the direction connecting the vortex and the nucleus). Therefore, the only component contributing to the interaction force is the longitudinal one (due to that, in the following part of this chapter, the longitudinal part of the force is referred to, in short, as force). Fig. 6.10 shows the force F as a function of vortex-nucleus distance R for different densities. In the case of this system, a positive value of the force corresponds to a repulsive interaction between the vortex and the nucleus; similarly, a negative sign indicates attraction. Based on these plots, one can take a closer look at the process of impurity movement and its interaction with the vortex. When the distance between vortex and nucleus is small (which corresponds to the situation when the impurity approaches the vortex), the interaction between

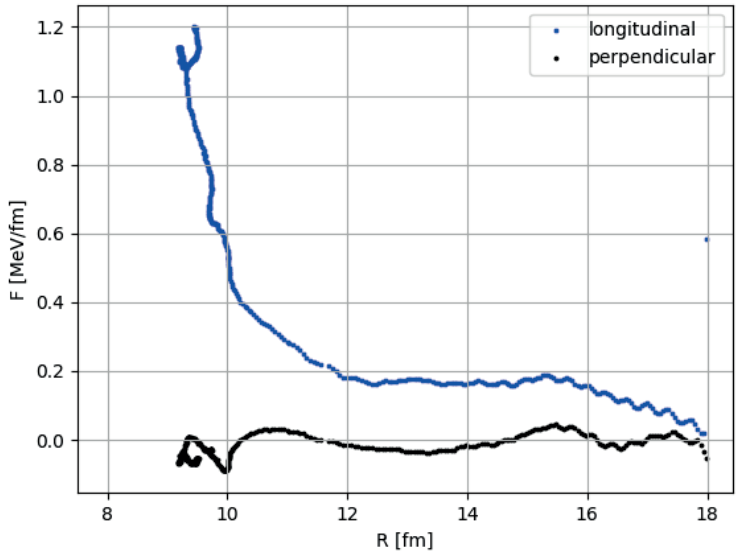

(A) Longitudinal and perpendicular component of force as a function of vortex-nucleus distance for density 0.019 fm^{-3}.

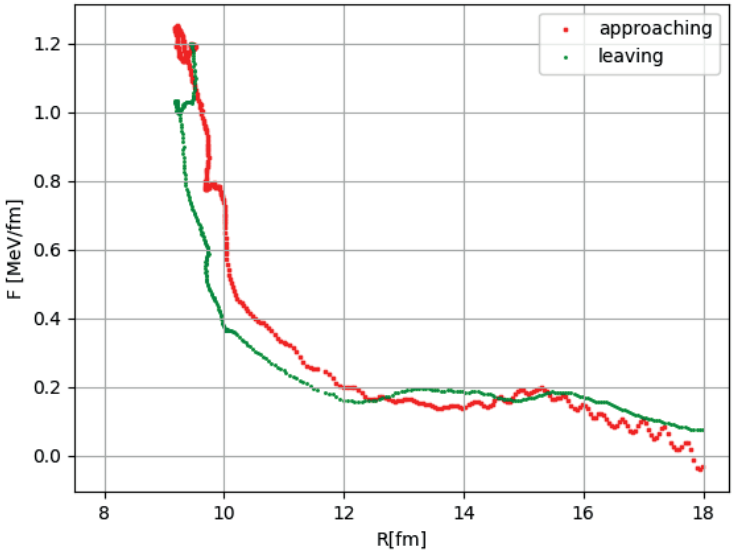

(B) Longitudinal force before averaging for density 0.019 fm^{-3}. The series *approaching* denotes the force extracted in case of impurity approaching the vortex and *leaving* when the nucleus was leaving it.

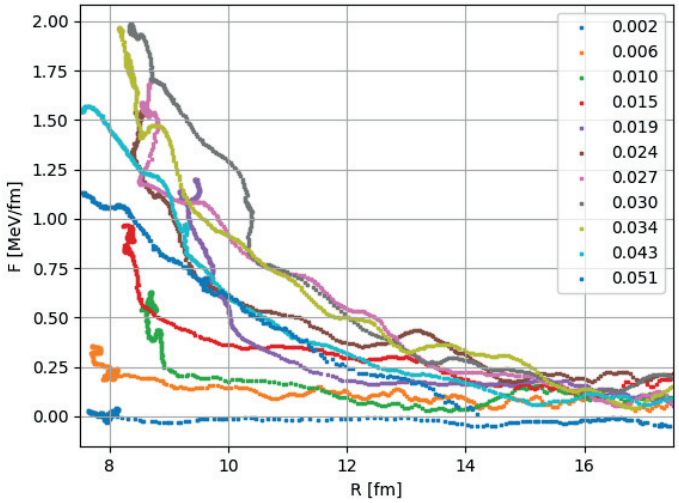

FIGURE 6.10: Longitudinal component of vortex-nucleus force F as a function of vortex-nucleus distance R for densities from 0.002 to 0.051 fm^{-3}.

them is stronger (consequently, the force takes a larger value). Later on, as the distance between the vortex and the nucleus becomes larger (impurity passes the vortex and moves away from it), the force starts to decrease (so the interaction becomes weaker). In addition, the force is always greater than 0, which means that the interaction between impurity and vortex is repulsive for each of the investigated densities [82]. This, in turn, supports the conjecture from [82], where it has been stated that in the neutron star crust, the interaction force is repulsive for every density.

For each of the densities, one can indicate the maximum recorded in the simulation value of the force. Fig. 6.11 presents this value extracted for each of the analyzed densities. For comparison, the value of the interaction force for the vortex-nucleus distance equal to 10 fm is also shown. For densities below 0.030 fm^{-3}, the force increases with density; later on, once this threshold value is exceeded, the force starts to decrease. The same tendency can be observed for the force extracted for a specified vortex-nucleus distance.

In the next order, the C/R^3 dependence has been fitted to the force-distance plots. The

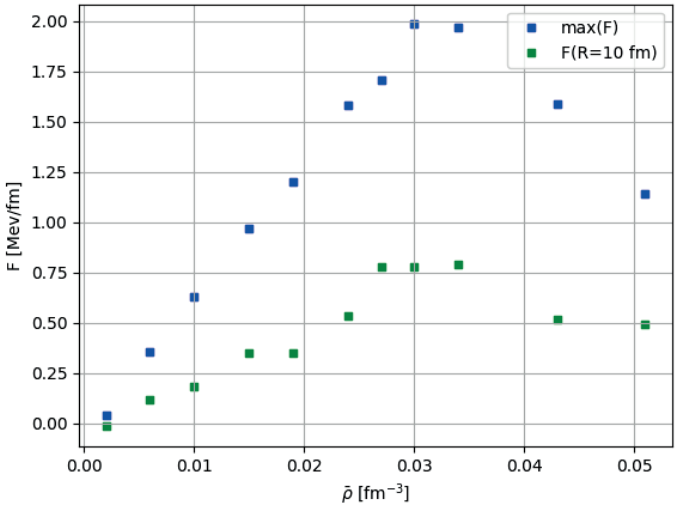

FIGURE 6.11: Maximal measured force and its value for vortex-nucleus distance equal 10 fm for densities from 0.002 to 0.051 fm^{-3}.

fitting procedure has been applied for the range of distances $R = 12 - 17$ fm (being larger than the coherence length). The obtained fitting coefficients have been compared with the values predicted by the hydrodynamic approach (Eq. 6.11) in Fig. 6.12. The error bars obtained during the fitting procedure have been calculated as the square from the variance of the estimated parameter using *curve_fit* function [220]. At first, the evolution of the fitting coefficient obtained from the dynamic method follows the tendency from Fig. 6.11, where the maximal value of the interaction force and its value for $R = 10$ fm as a function of density is shown. Similarly, in the regime of lower densities, the fitting coefficient increases, then reaches the maximum around 0.030 fm^{-3} and starts to decrease. For lower densities, a significant discrepancy is observed between the coefficient obtained from hydrodynamics and dynamic calculations. Later, as the density increases, the parameters obtained through various approaches become consistent. The parameters obtained within the hydrodynamic approach systematically decrease with density; in contrast, the dynamic method shows a maximum at around 0.025 fm^{-3}. At this point, one should underline the qualitative similarity with the calculations concerning the mass parameter (Sec. 5.2.2), where the comparison of the mass parameter for the quadrupole moment obtained with the hydrodynamic and

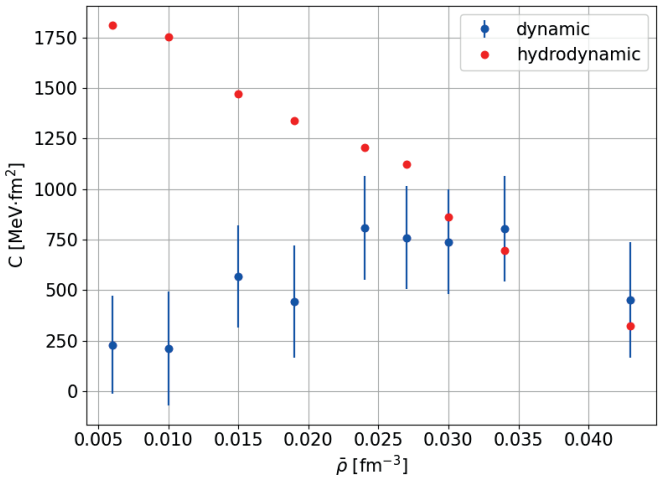

FIGURE 6.12: The fitting coefficient C as a function of density obtained from the hydrodynamic formula (Eq. 6.11) and within the dynamic method.

dynamic approach is provided (panel b of Fig. 5.18). There, as well as in Fig. 6.12, one can see the same trend: for lower densities, the estimation of hydrodynamics is significantly larger than the results obtained from dynamic calculations. Later on, the values extracted from these two approaches become consistent.

6.2.2 Energy of the System and Vortex Length

The next part of the research concerns the energy of the system and the length of the vortex line. In general, one can distinguish various processes that lead to the change in the total energy of the system $\Delta E(t)$ [82]:

- one of them is the vortex-nucleus interaction (dependent on the distance between vortex and impurity $R(t)$) [214, 82]. The process corresponds to a particular change in energy $\Delta E_{\mathrm{VN}}(R(t))$,
- the vortex-nucleus interaction leads to the modification of the shape of the vortex line $\Delta L(t)$. The susceptibility of the vortex with respect to deformations is quantified by the tension force T [218, 213, 82]. This contribution to energy change can be written as $\Delta E_{\mathrm{vort-def}} = T\Delta L(t)$,

- some amount of energy can also be distributed to the impurity and cause its deformation [214, 82]. This change of energy can be quantified by the deformation parameter $Q(t)$ and understood as the internal excitation of impurity: $\Delta E_{\text{def}}(Q(t))$,
- the excitation of the background neutrons can also take place and result in the generation of sound waves or phonons excitation [82]. With this process, one also associates a certain energy change $\Delta E_{\text{background}}(t)$. However, due to the slow movement of impurity, this process can be considered as negligible.

The change of total energy of the system can be schematically written with respect to these contributions in the following form:

$$\Delta E(t) = \Delta E_{\text{VN}}(R(t)) + T\Delta L(t) + \Delta E_{\text{def}}(Q(t)) + \Delta E_{\text{background}}(t). \tag{6.16}$$

In this research, the change in the total energy of the system has been calculated as follows:

- the total energy of the system has been obtained during simulation, based on the formula for the energy density for BSk31 functional (Eq. 3.151),
- the kinetic energy of the impurity has been obtained from the formula: $Mv^2/2$, where M is the effective mass of impurity obtained in Chap. 4 and v is the velocity of center of mass of the nuclei (recorded from the simulations). Then, this kinetic energy has been subtracted from the total energy, which gives the energy denoted as $E(t)$,
- once the initial value of this energy $E(0)$ is subtracted, the change of energy $E(t) - E(0)$ is obtained.

In addition, as mentioned, e.g., in [82], the vortex line becomes deformed due to interaction with impurities. This, in turn, leads to a change of its length with respect to the initial value; such a change of length is referred to as $L(t) - L(0)$. In this thesis, $E(t) - E(0)$ and $L(t) - L(0)$ have been examined both as a function of time and vortex-nucleus distance.

Fig. 6.13 presents the change of energy $E(t) - E(0)$ (in MeV) and change of vortex length $L(t) - L(0)$ (in fm) as a function of time for exemplary density 0.019 fm^{-3}. In the

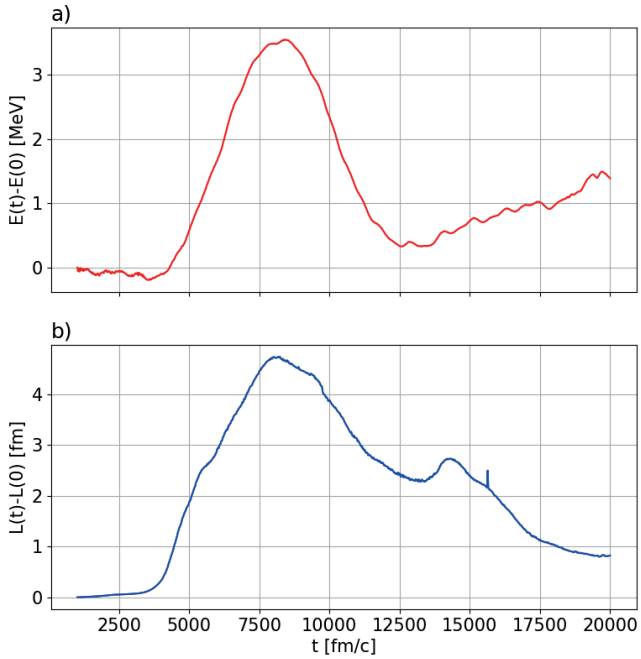

FIGURE 6.13: a) Change of energy $E(t) - E(0)$, b) change of vortex length $L(t) - L(0)$ as a function of time for density 0.019 fm^{-3}.

first part of the simulation, both energy and vortex length increase. This corresponds to the situation in which the impurity approaches the vortex, causing the vortex-nucleus interaction energy to increase, as the interaction is repulsive. This, in turn, affects the vortex, which is evident in the modification of the line's shape. Later on, the energy and length (as well as the interaction force) reach their maximal values, which coincide with the moment where the vortex-nucleus distance R takes the smallest value. Later on, energy and length start to decrease. However, at the end of simulations (when the vortex-nucleus distance is again about 20 fm), neither energy nor vortex length returns to its initial value. This demonstrates that for longer trajectories, the whole process has not been adiabatic, despite the slow movement of impurity.

In addition, one can also examine the dependence of the change of energy and the change of vortex length on the vortex-nucleus distance. These quantities for density 0.019 fm^{-3} are shown in Fig. 6.14. Here, the term $E(R_0)$ denotes the energy and vortex

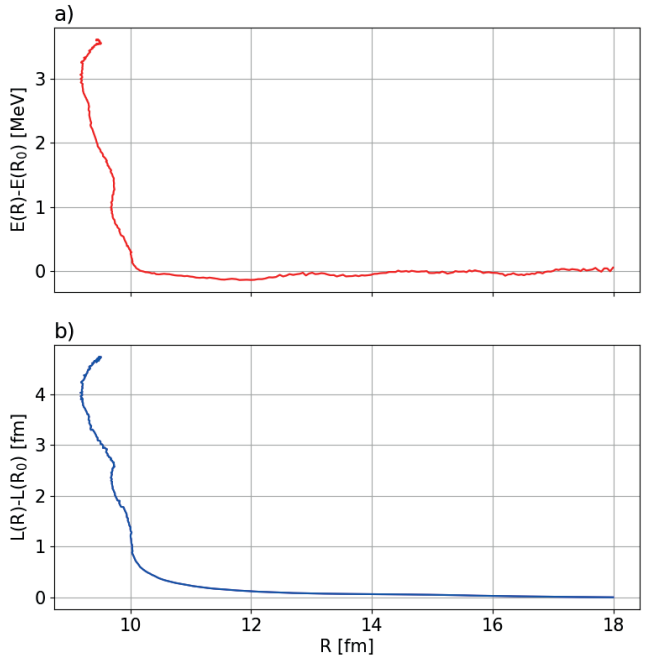

FIGURE 6.14: a) Change of energy $E(R) - E(R_0)$, b) change of vortex length $L(R) - L(R_0)$ as a function of vortex-nucleus distance for density 0.019 fm^{-3}.

length corresponding to the initial vortex-nucleus distance (which has been set to 20 fm). One can see that the energy and vortex length reach their maxima for the smallest distance between vortex and impurity (so when the impurity passes the line).

6.2.3 Pinning Energy and Tension Force

The next part of this research focuses on estimating the pinning energy and tension force. In Fig. 6.15, quantities that are necessary for the estimation of these parameters are marked:

- ΔE_{max} is the maximal change of energy. In principle, it corresponds to the amount of energy that is needed to move the impurity through the medium containing the vortex [214] from a distance $R = 20$ fm (which we assume to be large) to the vicinity of the vortex,

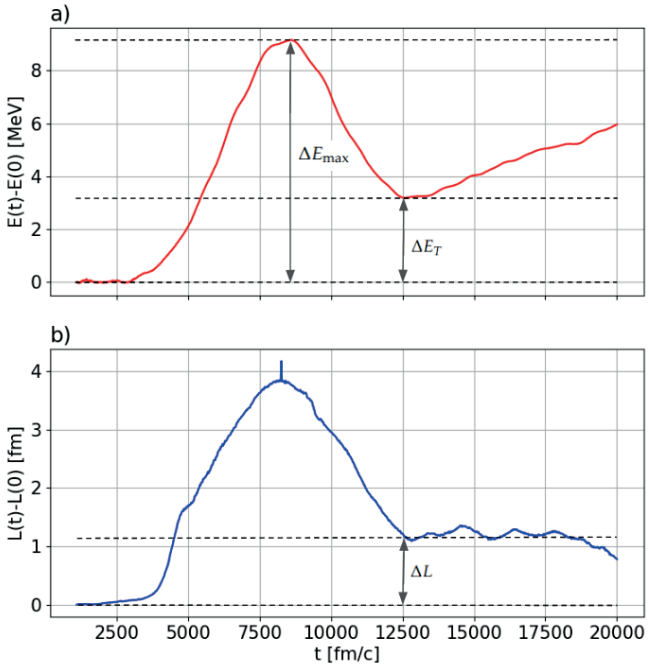

FIGURE 6.15: a) Change of energy and b) change of vortex length as a function of time for exemplary density 0.030 fm^{-3}. ΔE_{max} is the maximal change of energy, ΔE_T means the excitation energy and ΔL the change of vortex length corresponding to ΔE_T.

- ΔE_T is the excitation energy. As one can see, the energy does not return to its initial value even after the impurity passes through the vortex and moves away from it. This difference between initial energy and the level to which it drops after interaction with the vortex is called excitation energy [82]. In the context of vortex-nucleus interaction, some amount of this increase in energy is connected with the change of vortex length (in other words, a certain part of excitation energy can be considered as the energy cost of deformation of the vortex) [218]. The change of vortex length corresponding to this energy is marked as ΔL in the bottom panel.

In addition, we make the following assumptions:

- when the vortex is very close to the impurity, the energy connected with vortex-nuclei interaction dominates over other contributions: $\Delta E_{\text{max}} \approx \Delta E_{\text{VN}}(R) + \ldots$.

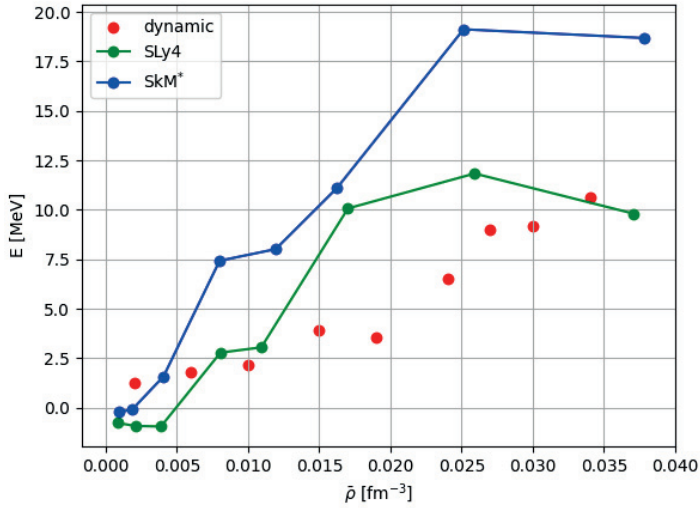

FIGURE 6.16: Pinning energy as a function of density obtained from the DFT-based method (*dynamic method*) together with results from Fig. 5 in [214] for functionals SLy4 and SkM*.

Therefore, it can be assumed that $\Delta E_{\max} \geq \Delta E_{\mathrm{VN}}(R)$, which sets the upper limit for the pinning energy,

- concerning the energy connected with vortex deformation, it is assumed that the energy stored in such deformation dominates over other contributions to the energy: $\Delta E_T \approx T\Delta L + \ldots$. Again, we can set the following condition: $\Delta E_T \geq T\Delta L$, or $T \leq \Delta E_T/\Delta L$, from which the upper limit for the energy connected with vortex deformation is estimated.

Based on that, the pinning energy is estimated as $\Delta E_{\max}$ and the tension force can be estimated by the relation $\Delta E_T/\Delta L$ [218].

Fig. 6.16 provides the comparison of pinning energy calculated in frame of various methods. The results obtained within the dynamic method are compared with results of the static approach from [214], where the pinning energy has been obtained with regard to functionals: SLy4 (green line with data point) and SkM* (blue line with points). Despite the quantitative discrepancies, our results follow the same scheme as

data from [214]. In the regime of lower densities, the pinning energy arises almost linearly for each method; later on, it becomes less rapid. The key issue that needs to be addressed at this point is the relationship between density and the excitations that occur within the system. In principle, as the density increases, the entire process becomes more non-adiabatic, resulting in a larger number of excitations in the final state. Then, contributions to the energy associated with these excitations begin to influence the total energy of the system, so that the interaction energy no longer dominates. Therefore, due to these excitations for densities $\bar{\rho} > 0.035\,\mathrm{fm}^{-3}$, the pinning energy could not be properly estimated within the discussed approach.

Concerning the differences between the results of the DFT-based method and static predictions, it should be pointed out that the protocol of pinning energy extraction provided in [214] differs from the method presented in this thesis. In contrast to the static approach, our dynamic method is, in fact, insensitive to the definition of each configuration considered in the static approach. There, as pointed out in [214], the large differences in energies between each configuration (which may vary from hundreds of keV to tens of MeV [214]) can significantly affect the obtained pinning energy. This, in turn, can cause discrepancies between the results of the static and dynamic methods. In addition, it should also be mentioned that the predictions of a particular method are sensitive to the choice of the functional, which may also cause the difference between the results obtained within the static approach (using SLy4 and SkM* functionals) and the DFT-based method (where the BSk functional has been chosen).

Next, the tension force is considered. The comparison of results from the dynamic and hydrodynamic methods is presented in Fig. 6.17. At low densities, the results of these methods are in good agreement. Later on, for densities ranging from 0.027 to 0.034 fm^{-3}, the dynamic begins to significantly overestimate the value obtained from hydrodynamics. The discrepancies between the hydrodynamic estimation and the results obtained during this research are in agreement with the predictions from [82]. In this paper, it has been demonstrated that in the regime of higher densities, the tension force calculated using the DFT-based method can be significantly larger than the hydrodynamic estimate (in other words, the vortex line is expected to be stiffer in the denser medium). However, as it has been mentioned before (and also in [82]), the tension force obtained from the simulations can be, in fact, considered as the upper limit of this quantity.

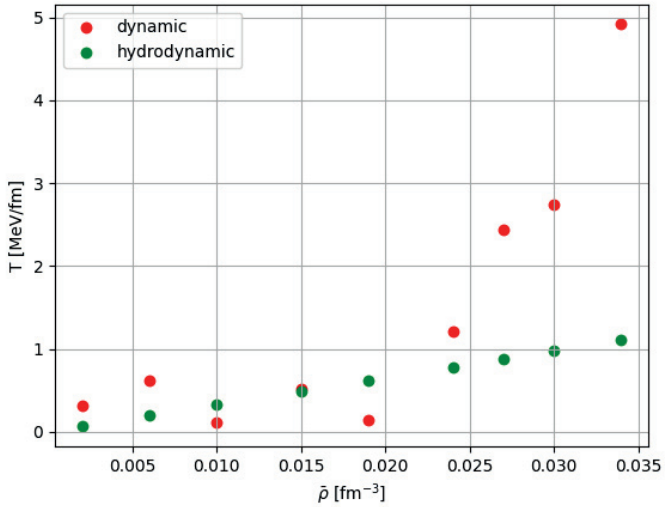

FIGURE 6.17: Tension force as a function of density obtained from the dynamic method (*dynamic*) and within the hydrodynamic formula from [218] (*hydrodynamic*).

6.2.4 Deformation of Impurity

As mentioned in Sec. 5.2.2, at higher densities, the modification of the impurity's shape requires less energy and is therefore one of the possible channels of energy distribution. The deformation of the nucleus is, in turn, induced by the vortex-nucleus interaction [82] and may be an important contribution to the effective model of the vortex-nucleus system. Therefore, the last part of this chapter is devoted to the deformation of impurity. In the investigated system, two types of deformation can be detected: one can be described in terms of a quadrupole moment, while the second is connected with the octupole moment.

At first, the quadrupole deformation has been investigated. Fig. 6.18 shows quadrupole moment Q_{20} (in fm^2) as a function of time (in fm/c). The quadrupole moment turned out to be very small compared to the values typically obtained in nuclear systems (according to [3], they are usually about 10^3-10^4 fm^2). This stands in contrast to the results from [82] and [214], where it has been stated that the Q_{20} deformation is expected to be the main way of deformation. However, one cannot prove it with the calculations

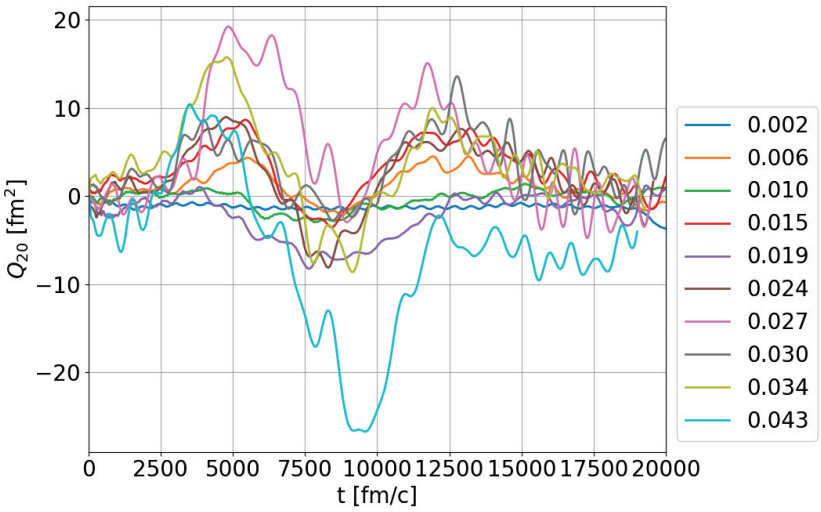

FIGURE 6.18: Quadrupole moment as a function of time for densities from 0.002 to 0.043 fm^{-3}.

based on the BSk functional. Nevertheless, for almost all the densities (except for 0.043 fm^{-3}) Q_{20} takes positive values, which corresponds to the prolate shape of nuclei. This, as reported in [82, 214], is in fact the expected way of deformation. However, for the highest density, one can observe the opposite behaviour (Q_{20} becomes negative). In addition, the maximal absolute value of quadrupole moment increases with density because it costs less energy to deform the impurity in a denser medium.

In the second step, the octupole moment has been analyzed. As can be found, e.g., in [221, 222, 223], the modification of the shape of nuclei connected with this mode is usually referred to as pear-shape deformation. An example of this type of deformation is shown in Fig. 6.19 [221]. In calculations of the octupole moment, it is crucial to properly choose the principal axis, which represents the direction along which the octupole moment would be calculated. In this case, the principal axis is the same as the longitudinal axis in Fig. 6.8. At every time of the trajectory the initial coordinate frame z, y, z is rotated, so that the new frame x', y', z' is obtained. In this new frame, the axis x' corresponds to the vortex-impurity direction and therefore is considered as

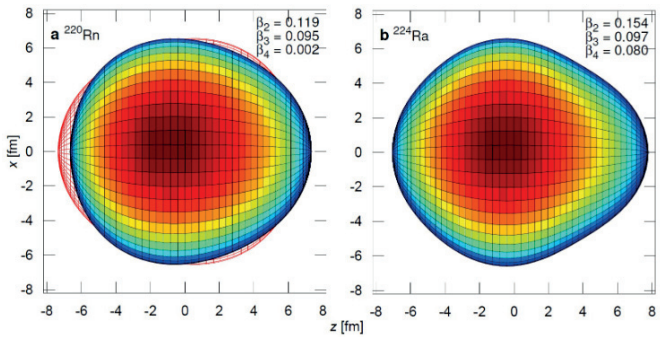

FIGURE 6.19: An example of the octupole deformation for heavy nuclei ^{224}Ra [221].

the new principal axis. Based on that, one can calculate the octupole moment as [222]:

$$Q_{30}(t) = \int \Big(x' \big(2(x')^2 - 3(z')^2 - 3(y')^2 \big) \Big) \rho_p(\boldsymbol{r}, t)\, d\boldsymbol{r} \tag{6.17}$$

where the terms x', y' and z' refer to the axes in the new coordinate frame. Again, the term $\boldsymbol{r}$ is the coordinate describing the position of the impurity.

Fig. 6.20 shows Q_{30} (in fm^3) as a function of time (in fm/c) for various densities. The octupole moment turned out to be significantly larger than the quadrupole and tends to increase with density (which is a similar tendency as in the case of the quadrupole moment). However, as reported in [224], the obtained values are still smaller than typically observed in nuclear matter (on the order of 10^3 fm^3). Despite that, in the investigated case, the octupole moment seems to have a more significant impact on the deformation of the nuclei than the quadrupole moment. This stands in contradiction to the results from [82], where it has been stated that the main contribution to deformation comes from the quadrupole mode. Therefore, the mass parameter connected with the octupole moment could be more useful in collective models of neutron star crust than the mass parameter extracted for the quadrupole mode.

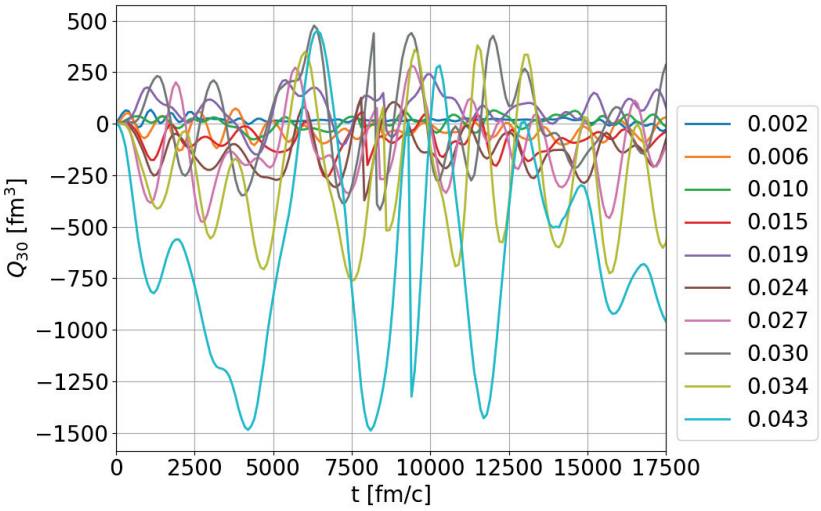

FIGURE 6.20: Octupole moment as a function of time for densities from 0.002 to 0.043 fm^{-3}.

6.3 Summary

In this chapter, the following problems have been examined:

- At first, the vortex-nucleus interaction force as a function of the distance between the vortex and the impurity has been calculated. It has been checked that the interaction is always repulsive. Moreover, the maximal value of the interaction force (as well as its value for a chosen distance) has a maximum for a particular density. This result aligns with other predictions from the literature, which suggest that this effect is linked to the deformation of the nucleus as it moves in the vicinity of the vortex line.

- Later on, it has been analyzed whether the dependence of the interaction force on the vortex-nucleus distance behaves like C/R^3. The coefficient C has been fitted to the data obtained from simulations and compared with the hydrodynamic predictions. The values obtained within these two methods turned out to be in good agreement for larger densities, which is an expected tendency.

- In the next order, the energy and vortex length as a function of time and vortex-nucleus distance have been analyzed. Based on these results, pinning energy and tension force have been calculated and compared with predictions from the literature. The results of the DFT-based method qualitatively agree with those from the hydrodynamic approach, and the observed discrepancies could be reliably explained.
- Finally, the dependencies of quadrupole and octupole moments on time and vortex-nucleus distance have been examined. It has been checked that the main contribution to deformation comes from the octupole mode, while the impact of the quadrupole mode seems to be negligible.

Chapter 7

Summary

The first two chapters of this thesis provide the theoretical background necessary for the research. Chap. 2 is focused on the general insight into the physics of nuclear matter in neutron stars, starting from the description of their internal structure with a special respect to the role of effective models of the crust. Subsequently, the most fundamental information about the phenomenon of superfluidity, including the concept of the Bose-Einstein condensate and the two-fluid model, was provided. The basics of BCS theory, including the mechanism of Cooper pair creation, the concept of order parameter, and quasiparticle wave functions, have also been presented. Later on, the special case of superfluidity in the neutron star crust has been discussed. Finally, the dynamic properties of the inner crust within the framework of the Vortex Filament Model have been tackled. This chapter has been closed with the section concerning the phenomenon of glitches and its connection with the microscopic structure of the crust.

Chap. 3 describes the analytical methods lying behind the numerical software developed during this research. Initially, I discussed the mean-field approximation methods and the basics of Density Functional Theory, along with its extension to superfluid systems. Then, I turned to the topic of energy functionals, with a special emphasis on the BSk functional used in this research. Finally, the description of the new numerical software, W-BSk Toolkit, is provided.

The second part of the thesis is focused on the practical application of the W-BSk Toolkit. Here, this tool has been used to extract the parameters included in effective models of neutron star crust. Chap. 4 concerns the fundamental quantity of every effective model of the neutron star crust, which is the effective mass of impurity. In this research, the cutting-edge method of extracting this parameter, based on dynamic

simulations using time-dependent DFT, has been developed. This novel method enables the investigation of impurities in the surrounding neutron matter, which, until now, has been considered a challenging scientific task requiring various assumptions that have affected the reliability of the results. Here, the new approach combines sophisticated numerical calculations based on the DFT approach with simple physical models, from which one can extract the parameters. The effective mass has been calculated systematically for different nuclear densities, allowing for the examination of the properties of various layers of the crust. The comparison with other well-established methods, such as hydrodynamic, showed that our method provides reliable results. Later, we could also consider various mechanisms of dissipation that occur during the movement of impurities through the surrounding neutron matter. The channels of transfer of kinetic energy of impurity into the neutron matter have been identified and discussed. The process of destroying superfluidity turned out to be connected with interesting phenomena, some of which are not yet known, such as the nucleation of vortex rings.

Despite various advantages of this method, one should point out that it can be applied only in the case of the extraction of the effective mass, which is, in fact, an example of the wider class of mass parameters that need to be included in effective models as well. As another example of the mass parameter, one can point out the quantity that describes the spatial deformation of an impurity, which is described in terms of the quadrupole moment. Therefore, there was a need to develop an alternative method that can be applied to this broader class of mass parameters. In Chap. 5, this new method has been discussed. It is based on the idea of a collective variable associated with a particular mass parameter. Once such a collective variable can be expressed in the form of a density functional, one can extract the corresponding mass parameter based on the time-dependent behaviour of this collective variable. In the first case, the method has been applied to examine the effective mass of the impurity, specifically with regard to its center-of-mass oscillations. Then, the collective variable associated with the effective mass was the position of the center of mass of the impurity. The comparison of the obtained results with the predictions from Chap. 4 revealed the agreement of these two methods. In the next order, with regard to this new method, the processes of dissipation could have also been studied. The other investigated collective variable was the quadrupole moment, which can be used to describe the spatial deformation of the impurity. Based on the oscillations of the quadrupole moment,

the corresponding mass parameter (connected with shape modification) has been extracted, which provides a new contribution to the neutron star crust studies. What is especially important about this new method is its applicability to non-uniform systems. In other recently used methods, the mass parameters can provide reliable results for nuclei in vacuum. Our method, in contrast, overcomes this problem and allows us to investigate the complex system of impurity in the medium.

The last part of the thesis is devoted to vortex-nucleus interaction. In Chap. 6, various parameters describing the interaction between the vortex line and the nucleus passing in the vicinity of the line have been calculated. Again, the DFT-based method has been applied. The first quantity was the interaction force, described as a function of the distance between the vortex and the impurity. It turned out that the strongest interaction occurs at the smallest distance, which is the behavior already predicted in the literature. The comparison with hydrodynamic estimations has also been provided. In the next order, it has been demonstrated that the change in energy of the system is correlated with changes in the vortex length. Based on this, the pinning energy and tension force, being crucial parameters that describe the dynamics of the crust, have been obtained. Here, comparisons with static calculations and hydrodynamic predictions have also been provided. Again, the obtained results follow the predictions of other methods. Finally, different forms of deformation of impurity have been studied. Contrary to recent conclusions from the literature, which have pointed out the quadrupole deformation as the dominant one, it has turned out that the dominant mode of deformation is, in fact, the octupole mode.

Despite the abundance of information obtained during this research, some problems still remain unsolved. One of the open issues is the more detailed investigation of the contribution of the octupole moment to the deformation of the impurity. As the calculations showed that the leading way of deformation is the octupole one, the mass parameter extracted, e.g., from oscillations of the octupole moment, could be more relevant in the collective models of the crust than the mass parameter connected with the quadrupole mode.

In addition, one can also pose the question about the contribution of the non-axial parameters to the octupole deformation. In this research, the description is limited to a single parameter, Q_{30}, which corresponds to the pear-shaped deformation along the

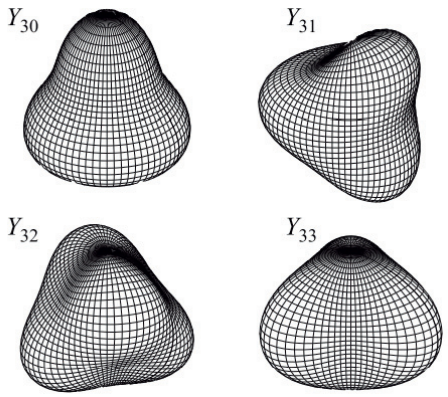

FIGURE 7.1: The non-axial deformations of nuclei with spherical harmonics Y corresponding to each of the possible shapes [225].

principal axis [224]. However, Q_{30} is in fact only one of the contributions to the total octupole deformation, as one can also distinguish another (non-axial) parameter corresponding to various exotic shapes. As an example, Fig. 7.1 shows the shapes, into which the impurity can be deformed for a particular spherical harmonic Y [225]

Summarizing the whole endeavour of this thesis, one should at first point out the importance of numerical simulations, which can be considered as very powerful tools in neutron star research. In fact, they enable the most detailed and reliable description of a quantum many-body system compared to standard methods, such as hydrodynamic approximations. As widely discussed, current approaches encounter various difficulties, either technical or conceptual. On the contrary, the dynamic, DFT-based method presented in this thesis allows overcoming these problems, as it is free of the assumptions that the other methods rely on. Therefore, the obtained results provide a detailed description on the qualitative and quantitative levels. Our results are in good agreement with those of other methods. Due to this, the development of the new software, whose capabilities are demonstrated in this thesis, stands out as a significant achievement in the field of modern neutron star physics. Thanks to this tool, we were able to extract crucial parameters of effective neutron star models and examine various processes occurring in the crust. What is especially important, the software is accessible as open-source. There are also publicly accessible reproducibility packs (via Zenodo [178,

226]), so everyone can reproduce the results (assuming access to a sufficiently powerful supercomputer).

Based on the work presented in this thesis, two papers have already been published [3, 20]. Moreover, we expect that the data collected for vortex-nucleus studies will be further analyzed, which would enable the publication of an additional paper concerning the vortex-nucleus interaction. We believe that this work would make a significant contribution to the field of neutron star studies and open a new chapter in the examination of complex nuclear systems.

Bibliography

[1] V. Graber, N. Andersson, and M. Hogg. "Neutron stars in the laboratory". In: *International Journal of Modern Physics D* 26.08 (Apr. 2017), p. 1730015. ISSN: 1793-6594. DOI: 10.1142/s0218271817300154. URL: http://dx.doi.org/10.1142/S0218271817300154.

[2] J. Piekarewicz. *The Nuclear Physics of Neutron Stars*. 2022. arXiv: 2209.14877 [nucl-th]. URL: https://arxiv.org/abs/2209.14877.

[3] D. Pęcak et al. "Time-Dependent Nuclear Energy-Density Functional Theory Toolkit for Neutron Star Crust: Dynamics of a Nucleus in a Neutron Superfluid". In: *Physical Review X* 14.4 (Dec. 2024). ISSN: 2160-3308. DOI: 10.1103/physrevx.14.041054. URL: http://dx.doi.org/10.1103/PhysRevX.14.041054.

[4] W. Baade and F. Zwicky. "Remarks on Super-Novae and Cosmic Rays". In: *Phys. Rev.* 46 (1 July 1934), pp. 76–77. DOI: 10.1103/PhysRev.46.76.2. URL: https://link.aps.org/doi/10.1103/PhysRev.46.76.2.

[5] V. Allard. "Superfluid dynamics in neutron stars". PhD thesis. Université libre de Bruxelles, 2024.

[6] A. B. Migdal. "Superfluidity and the moments of inertia of nuclei". In: *Nuclear Physics* 13.5 (1959), pp. 655–674. ISSN: 0029-5582. DOI: https://doi.org/10.1016/0029-5582(59)90264-0. URL: https://www.sciencedirect.com/science/article/pii/0029558259902640.

[7] A. Sedrakian and J. W. Clark. "Superfluidity in nuclear systems and neutron stars". In: *The European Physical Journal A* 55.9 (Sept. 2019). ISSN: 1434-601X. DOI: 10.1140/epja/i2019-12863-6. URL: http://dx.doi.org/10.1140/epja/i2019-12863-6.

[8] G. Colò. "Nuclear density functional theory". In: *Advances in Physics: X* 5.1 (2020), p. 1740061. DOI: 10.1080/23746149.2020.1740061.

[9] T. Nakatsukasa et al. "Time-dependent density-functional description of nuclear dynamics". In: *Rev. Mod. Phys.* 88 (4 Nov. 2016), p. 045004. DOI: 10.1103/RevModPhys.88.045004. URL: https://link.aps.org/doi/10.1103/RevModPhys.88.045004.

[10] N. Andersson. "A Superfluid Perspective on Neutron Star Dynamics". In: *Universe* 7.1 (Jan. 2021), p. 17. ISSN: 2218-1997. DOI: 10.3390/universe7010017. URL: http://dx.doi.org/10.3390/universe7010017.

[11] P. Haensel. "Neutron Star Crusts". In: *Physics of Neutron Star Interiors*. Ed. by D. Blaschke, A. Sedrakian, and N. K. Glendenning. Berlin, Heidelberg: Springer Berlin Heidelberg, 2001, pp. 127–174. ISBN: 978-3-540-44578-4. DOI: 10.1007/3-540-44578-1_5. URL: https://doi.org/10.1007/3-540-44578-1_5.

[12] P. Haensel, A. Y. Potekhin, and D. G. Yakovlev. *Neutron stars 1: Equation of state and structure*. Vol. 326. New York, USA: Springer, 2007. DOI: 10.1007/978-0-387-47301-7.

[13] J. G. Hartnett and A. N. Luiten. "Colloquium: Comparison of astrophysical and terrestrial frequency standards". In: *Reviews of Modern Physics* 83.1 (Jan. 2011), 1–9. ISSN: 1539-0756. DOI: 10.1103/revmodphys.83.1. URL: http://dx.doi.org/10.1103/RevModPhys.83.1.

[14] J. M. Lattimer. "Neutron Stars as a Probe of the Equation of State". In: *22nd Texas Symposium on Relativistic Astrophysics*. Ed. by P. Chen et al. Jan. 2004, p. 42.

[15] N. Chamel and P. Haensel. "Physics of Neutron Star Crusts". In: *Living Reviews in Relativity* 11.1 (Dec. 2008). ISSN: 1433-8351. DOI: 10.12942/lrr-2008-10. URL: http://dx.doi.org/10.12942/lrr-2008-10.

[16] M. E. Caplan and C. J. Horowitz. "Colloquium: Astromaterial science and nuclear pasta". In: *Reviews of Modern Physics* 89.4 (Oct. 2017). ISSN: 1539-0756. DOI: 10.1103/revmodphys.89.041002. URL: http://dx.doi.org/10.1103/RevModPhys.89.041002.

[17] S. Zhou et al. *Pulsar Glitches: A Review*. 2022. arXiv: 2211.13885 [astro-ph.HE]. URL: https://arxiv.org/abs/2211.13885.

[18] A. Hewish. "Pulsars and high density physics". In: *Rev. Mod. Phys.* 47 (3 July 1975), pp. 567–572. DOI: 10.1103/RevModPhys.47.567. URL: https://link.aps.org/doi/10.1103/RevModPhys.47.567.

[19] G. Wlazłowski. *Time dependent density functional theory and supercomputing: new prospects formodelling superfudity in neutron stars*. 2019. URL: https://wlazlowski.fizyka.pw.edu.pl/pdfs/2019-SLCJ-Warsaw.pdf.

[20] A. Zdanowicz et al. "Dynamical scheme for computing the mass parameter of a system in a medium". In: *Physical Review C* 112.4 (Oct. 2025). ISSN: 2469-9993. DOI: 10.1103/tz7k-8shj. URL: http://dx.doi.org/10.1103/tz7k-8shj.

[21] M. Tsubota, M. Kobayashi, and H. Takeuchi. "Quantum hydrodynamics". In: *Physics Reports* 522.3 (Jan. 2013), 191–238. ISSN: 0370-1573. DOI: 10.1016/j.physrep.2012.09.007. URL: http://dx.doi.org/10.1016/j.physrep.2012.09.007.

[22] F. Douchin and P. Haensel. "Inner edge of neutron-star crust with SLy effective nucleon-nucleon interactions". In: *Physics Letters B* 485.1–3 (July 2000), 107–114. ISSN: 0370-2693. DOI: 10.1016/s0370-2693(00)00672-9. URL: http://dx.doi.org/10.1016/S0370-2693(00)00672-9.

[23] N. Chamel. "Neutron conduction in the inner crust of a neutron star in the framework of the band theory of solids". In: *Physical Review C* 85.3 (Mar. 2012). ISSN: 1089-490X. DOI: 10.1103/physrevc.85.035801. URL: http://dx.doi.org/10.1103/PhysRevC.85.035801.

[24] J. W. Negele and D. Vautherin. "Neutron star matter at sub-nuclear densities". In: *Nuclear Physics A* 207.2 (June 1973), pp. 298–320. DOI: 10.1016/0375-9474(73)90349-7.

[25] M. Baldo, E. E. Saperstein, and S. V. Tolokonnikov. "A realistic model of superfluidity in the neutron star inner crust". In: *The European Physical Journal A* 32.1 (Apr. 2007), 97–108. ISSN: 1434-601X. DOI: 10.1140/epja/i2006-10356-5. URL: http://dx.doi.org/10.1140/epja/i2006-10356-5.

[26] M. Baldo, E. E. Saperstein, and S. V. Tolokonnikov. "Upper edge of the neutron star inner crust: The drip point and its vicinity". In: *Phys. Rev. C* 76 (2 Aug. 2007), p. 025803. DOI: 10.1103/PhysRevC.76.025803. URL: https://link.aps.org/doi/10.1103/PhysRevC.76.025803.

[27] M. Onsi et al. "Semi-classical equation of state and specific-heat expressions with proton shell corrections for the inner crust of a neutron star". In: *Physical Review C* 77.6 (June 2008). ISSN: 1089-490X. DOI: 10.1103/physrevc.77.065805. URL: http://dx.doi.org/10.1103/PhysRevC.77.065805.

[28] D. van Delft and P. Kes. "The discovery of superconductivity". In: *Physics Today* 63.9 (Sept. 2010), pp. 38–43. ISSN: 0031-9228. DOI: 10.1063/1.3490499. eprint: https://pubs.aip.org/physicstoday/article-pdf/63/9/38/9879861/38_1_online.pdf. URL: https://doi.org/10.1063/1.3490499.

[29] W. Kempinski et al. *Bose–Einstein Condensate – from superfluidity to superconductivity*. URL: https://www.ifmpan.poznan.pl/NCBiR-INNOTECH/documents/from_superfluidity_to_superconductivity.pdf.

[30] W. Keesom and K. Clusius. Proc. Royal Acad. Amsterdam 35 (1932) 307– 320 (Commun. Kamerlingh Onnes Inst. 219e).

[31] J.F. Annett. *Superconductivity, Superfluids and Condensates*. Oxford Master Series in Physics. OUP Oxford, 2004. ISBN: 9780198507567. URL: https://books.google.pl/books?id=WZcXmBrZIc8C.

[32] P. Kapitza. "Viscosity of Liquid Helium below the λ-Point". In: *Nature* (1938). URL: https://doi.org/10.1038/141074a0.

[33] J. Allen and D. Misener. "Flow of Liquid Helium II". In: *Nature* (1938). URL: https://doi.org/10.1038/141075a0.

[34] J. F. Allen and H. Jones. "New Phenomena Connected with Heat Flow in Helium II". In: *Nature* (1938). URL: https://doi.org/10.1038/141243a0.

[35] D. D. Osheroff, R. C. Richardson, and D. M. Lee. "Evidence for a New Phase of Solid He^3". In: *Phys. Rev. Lett.* 28 (14 Apr. 1972), pp. 885–888. DOI: 10.1103/PhysRevLett.28.885. URL: https://link.aps.org/doi/10.1103/PhysRevLett.28.885.

[36] P. Heikkinen. "NMR Techniques at Liquid Helium Temperatures". PhD thesis. June 2010.

[37] P. W. Anderson and W. F. Brinkman. "Anisotropic Superfluidity in He-3: A Possible Interpretation of Its Stability as a Spin-Fluctuation Effect". In: *Phys. Rev. Lett.* 30 (1973), pp. 1108–1111. DOI: 10.1103/PhysRevLett.30.1108.

[38] R. Balian and N. R. Werthamer. "Superconductivity with Pairs in a Relative p Wave". In: *Phys. Rev.* 131 (4 Aug. 1963), pp. 1553–1564. DOI: 10.1103/PhysRev.131.1553. URL: https://link.aps.org/doi/10.1103/PhysRev.131.1553.

[39] P. Coleman. "Retardation and anisotropic pairing". In: *Introduction to Many-Body Physics*. Cambridge University Press, 2015, 542–581.

[40] A. Einstein. "Quantum Theory of a Monoatomic Ideal Gas A translation of Quantentheorie des einatomigen idealen Gases (Einstein, 1924)". In: *Sitzungsberichte der Preußischen Akademie der Wissenschaften* (1924), pp. 261–261.

[41] K. Huang. *Statistical Mechanics*. John Wiley & Sons, 1987.

[42] F. London. "The λ-Phenomenon of Liquid Helium and the Bose-Einstein Degeneracy". In: *Nature* 141 (1938), pp. 643–644. DOI: 10.1038/141643a0.

[43] S. Balibar. "Laszlo Tisza and the two-fluid model of superfluidity". In: *Comptes Rendus Physique* 18.9 (2017). Science in the making: The Comptes rendus de l'Académie des sciences throughout history, pp. 586–591. ISSN: 1631-0705. DOI: https://doi.org/10.1016/j.crhy.2017.10.016. URL: https://www.sciencedirect.com/science/article/pii/S163107051730097X.

[44] W. Ketterle, D. S. Durfee, and D. M. Stamper-Kurn. *Making, probing and understanding Bose-Einstein condensates*. 1999. arXiv: cond-mat/9904034 [cond-mat]. URL: https://arxiv.org/abs/cond-mat/9904034.

[45] N. N. Bogolyubov. "On the theory of superfluidity". In: *J. Phys. (USSR)* 11 (1947), pp. 23–32.

[46] J. Rogel-Salazar. "The Gross–Pitaevskii equation and Bose–Einstein condensates". In: *European Journal of Physics* 34.2 (Jan. 2013), 247–257. ISSN: 1361-6404. DOI: 10.1088/0143-0807/34/2/247. URL: http://dx.doi.org/10.1088/0143-0807/34/2/247.

[47] L. Tisza. "Transport Phenomena in Helium II". In: *Nature* 141 (1938), p. 913. DOI: 10.1038/141913a0.

[48] R. Donnelly. "The Two-Fluid Theory and Second Sound in Liquid Helium". In: *Physics Today* 62 (Mar. 2010). DOI: 10.1063/1.3248499.

[49] L. Tisza. "The Theory of Liquid Helium". In: *Phys. Rev.* 72 (9 Nov. 1947), pp. 838–854. DOI: 10.1103/PhysRev.72.838. URL: https://link.aps.org/doi/10.1103/PhysRev.72.838.

[50] D.R Tilley and J. Tilley. *Superfluidity and Supeerconductivity*. CRC Press, 1990.

[51] I. M. Khalatnikov. *An Introduction To The Theory Of Superfluidity*. CRC Press, 2000. DOI: 10.1201/9780429502897.

[52] W. F. Vinen. "The physics of superfluid helium". In: (2004). DOI: 10.5170/CERN-2004-008.363. URL: https://cds.cern.ch/record/808382.

[53] L. Landau. "Theory of the Superfluidity of Helium II". In: *Phys. Rev.* 60 (4 Aug. 1941), pp. 356–358. DOI: 10.1103/PhysRev.60.356. URL: https://link.aps.org/doi/10.1103/PhysRev.60.356.

[54] J. Bardeen, L. N. Cooper, and J. R. Schrieffer. "Theory of Superconductivity". In: *Phys. Rev.* 108 (5 Dec. 1957), pp. 1175–1204. DOI: 10.1103/PhysRev.108.1175. URL: https://link.aps.org/doi/10.1103/PhysRev.108.1175.

[55] D. D. Osheroff, R. C. Richardson, and D. M. Lee. "Evidence for a New Phase of Solid He^3". In: *Phys. Rev. Lett.* 28 (14 Apr. 1972), pp. 885–888. DOI: 10.1103/PhysRevLett.28.885. URL: https://link.aps.org/doi/10.1103/PhysRevLett.28.885.

[56] M. Tinkham. *Introduction to Superconductivity*. Dover Publications, 2004.

[57] J. Bardeen and D. Pines. "Electron-Phonon Interaction in Metals". In: *Phys. Rev.* 99 (4 Aug. 1955), pp. 1140–1150. DOI: 10.1103/PhysRev.99.1140. URL: https://link.aps.org/doi/10.1103/PhysRev.99.1140.

[58] R. Heid. *Electron-Phonon Coupling in: The Physics of Correlated Insulators, Metals, and Superconductors: Lecture Notes of the Autumn School on Correlated Electrons 2017*. 2017. ISBN: ISBN 978-3-95806-224-5. URL: https://www.cond-mat.de/events/correl17/manuscripts/heid.pdf.

[59] L. Gor'kov and T. Melik-Barkhudarov. "Contribution to the theory of superfluidity in an imper- fect Fermi gas". In: *Sov. Phys. JETP* 40 (1961), pp. 1452–1458.

[60] H. Bruus and K. Flensberg. *Many–Body Quantum Theory in Condensed Matter Physics: An Introduction*. Oxford University Press, Sept. 2004. ISBN: 9780198566335. DOI: 10.1093/oso/9780198566335.001.0001. URL: https://doi.org/10.1093/oso/9780198566335.001.0001.

[61] H. Chunde. "Fermionic Superfluids: The Structure of Polarized Vortices". eng. PhD thesis. Washington State University, 2020, p. 237.

[62] P. Ring and P. Schuck. *The Nuclear Many-Body Problem*. Physics and astronomy online library. Springer, 2004. ISBN: 9783540212065. URL: https://books.google.pl/books?id=PTynSM-nMA8C.

[63] J. X. Zhu. *Bogoliubov-de Gennes method and its applications*. Vol. 924. Springer, 2016.

[64] A. Bohr, B. R. Mottelson, and D. Pines. "Possible Analogy between the Excitation Spectra of Nuclei and Those of the Superconducting Metallic State". In: *Phys. Rev.* 110 (4 May 1958), pp. 936–938. DOI: 10.1103/PhysRev.110.936. URL: https://link.aps.org/doi/10.1103/PhysRev.110.936.

[65] V. L. Ginzburg and D. A. Kirzhnits. "On the Superfluidity of Neutron Stars". In: *Sov. Phys. JETP* 20 (1965), pp. 1346–1348.

[66] R. A. Wolf. "Some Effects of the Strong Interactions on the Properties of Neutron-Star Matter". In: *The Astrophysical Journal* 145 (Sept. 1966), p. 834. DOI: 10.1086/148829.

[67] M. Hoffberg et al. "Anisotropic Superfluidity in Neutron Star Matter". In: *Phys. Rev. Lett.* 24 (14 Apr. 1970), pp. 775–777. DOI: 10.1103/PhysRevLett.24.775. URL: https://link.aps.org/doi/10.1103/PhysRevLett.24.775.

[68] R. Tamagaki. "Superfluid State in Neutron Star Matter. I: Generalized Bogoliubov Transformation and Existence of 3P2 Gap at High Density*)". In: *Progress of Theoretical Physics* 44.4 (Oct. 1970), pp. 905–928. ISSN: 0033-068X. DOI: 10.1143/PTP.44.905. URL: https://doi.org/10.1143/PTP.44.905.

[69] D. Page et al. *Stellar Superfluids*. 2014. arXiv: 1302.6626 [astro-ph.HE]. URL: https://arxiv.org/abs/1302.6626.

[70] U. Lombardo and H. J. Schulze. *Superfluidity in Neutron Star Matter*. 2000. arXiv: astro-ph/0012209 [astro-ph]. URL: https://arxiv.org/abs/astro-ph/0012209.

[71] F. Barranco et al. "Semiclassical approximation to neutron star superfluidity corrected for proximity effects". In: *Physical Review C* 58.2 (Aug. 1998), 1257–1262. ISSN: 1089-490X. DOI: 10.1103/physrevc.58.1257. URL: http://dx.doi.org/10.1103/PhysRevC.58.1257.

[72] S. Maurizio, J. W. Holt, and P. Finelli. "Nuclear pairing from microscopic forces: Singlet channels and higher-partial waves". In: *Physical Review C* 90.4 (Oct. 2014). ISSN: 1089-490X. DOI: 10.1103/physrevc.90.044003. URL: http://dx.doi.org/10.1103/PhysRevC.90.044003.

[73] D. J. Dean and M. Hjorth-Jensen. "Pairing in nuclear systems: from neutron stars to finite nuclei". In: *Reviews of Modern Physics* 75.2 (Apr. 2003), 607–656. ISSN: 1539-0756. DOI: 10.1103/revmodphys.75.607. URL: http://dx.doi.org/10.1103/RevModPhys.75.607.

[74] S. Baroni, A. O. Macchiavelli, and A. Schwenk. "Partial-wave contributions to pairing in nuclei". In: *Physical Review C* 81.6 (June 2010). ISSN: 1089-490X. DOI: 10.1103/physrevc.81.064308. URL: http://dx.doi.org/10.1103/PhysRevC.81.064308.

[75] A. Barresi. "Dynamics of collective modes in superfluid Fermi gases". PhD thesis. Warsaw University of Technology, 2024.

[76] R. Feynmann. "Progress in Low Temperature Physics". In: Elsevier, 1955, pp. 17–53.

[77] L. Onsager. "Statistical hydrodynamics". In: *Il Nuovo Cimento* 6.2 (Mar. 1949), pp. 279–287. DOI: 10.1007/BF02780991.

[78] J. A. Sauls. *Superfluidity in the Interiors of Neutron Stars*. 2019. arXiv: 1906.09641 [astro-ph.HE]. URL: https://arxiv.org/abs/1906.09641.

[79] J. R. Abo-Shaeer et al. "Observation of Vortex Lattices in Bose-Einstein Condensates". In: *Science* 292 (2001), pp. 476 –479. URL: https://api.semanticscholar.org/CorpusID:35348949.

[80] W. Ketterle. "Nobel lecture: When atoms behave as waves: Bose-Einstein condensation and the atom laser". In: *Rev. Mod. Phys.* 74 (4 Nov. 2002), pp. 1131–1151. DOI: 10.1103/RevModPhys.74.1131. URL: https://link.aps.org/doi/10.1103/RevModPhys.74.1131.

[81] M. Hirasawa and N. Shibazaki. *Vortex Configurations, Oscillations and Pinning in Neutron Star Crusts*. 2002. arXiv: astro-ph/0209025 [astro-ph]. URL: https://arxiv.org/abs/astro-ph/0209025.

[82] G. Wlazłowski et al. "Vortex Pinning and Dynamics in the Neutron Star Crust". In: *Physical Review Letters* 117.23 (Nov. 2016). ISSN: 1079-7114. DOI: 10.1103/physrevlett.117.232701. URL: http://dx.doi.org/10.1103/PhysRevLett.117.232701.

[83] B. Haskell and A. Melatos. "Models of pulsar glitches". In: *International Journal of Modern Physics D* 24.03 (Feb. 2015), p. 1530008. ISSN: 1793-6594. DOI: 10.1142/s0218271815300086. URL: http://dx.doi.org/10.1142/S0218271815300086.

[84] V. Radhakrishnan and R. Manchester. "Detection of a Change of State in the Pulsar PSR 0833-45". In: *Nature 222, 228–229* (1969). URL: https://doi.org/10.1038/222228a0.

[85] A. G. Lyne, R. S. Pritchard, and F. Graham Smith. "23 years of Crab pulsar rotational history". In: *Monthly Notices of the Royal Astronomical Society* 265.4 (Dec. 1993), pp. 1003–1012. ISSN: 0035-8711. DOI: 10.1093/mnras/265.4.1003. eprint: https://academic.oup.com/mnras/article-pdf/265/4/1003/3173877/mnras265-1003.pdf. URL: https://doi.org/10.1093/mnras/265.4.1003.

[86] P. W. Anderson and N. Itoh. "Pulsar glitches and restlessness as a hard superfluidity phenomenon". In: *Nature* 256.5512 (July 1975), pp. 25–27. DOI: 10.1038/256025a0.

[87] M. Antonelli, A. Montoli, and P. M. Pizzochero. "Effects of general relativity on glitch amplitudes and pulsar mass upper bounds". In: *Monthly Notices of the Royal Astronomical Society* 475.4 (Jan. 2018), pp. 5403–5416.

[88] E. Gügercinoğlu and M. A. Alpar. "The largest Crab glitch and the vortex creep model". In: *Monthly Notices of the Royal Astronomical Society* 488.2 (July 2019), 2275–2282. ISSN: 1365-2966. DOI: 10.1093/mnras/stz1831. URL: http://dx.doi.org/10.1093/mnras/stz1831.

[89] M. Antonelli, A. Montoli, and P. Pizzochero. "Insights into the physics of neutron star interiors from pulsar glitches". In: (Jan. 2023). DOI: 10.48550/arXiv.2301.12769.

[90] M. A. Alpar. "Pinning and Threading of Quantized Vortices in the Pulsar Crust Superfluid". In: *Astrophysical Journal* 213 (Apr. 1977), pp. 527–530. DOI: 10.1086/155183.

[91] P. Avogadro et al. "Quantum calculation of vortices in the inner crust of neutron stars". In: *Physical Review C* 75.1 (Jan. 2007). ISSN: 1089-490X. DOI: 10.1103/physrevc.75.012805. URL: http://dx.doi.org/10.1103/PhysRevC.75.012805.

[92] A. Bulgac, M. McNeil Forbes, and R. Sharma. "Strength of the Vortex-Pinning Interaction from Real-Time Dynamics". In: *Physical Review Letters* 110.24 (June 2013). ISSN: 1079-7114. DOI: 10.1103/physrevlett.110.241102. URL: http://dx.doi.org/10.1103/PhysRevLett.110.241102.

[93] A. L. Fetter and J. D. Walecka. *Quantum Theory of Many-particle Systems*. Dover Books on Physics. Dover Publications, 2003. ISBN: 9780486428277.

[94] C. D. Sherrill. *An Introduction to Hartree-Fock Molecular Orbital Theory*. 2000. URL: https://vergil.chemistry.gatech.edu/static/content/hf-intro.pdf.

[95] J. C. Slater. "A Simplification of the Hartree-Fock Method". In: *Phys. Rev.* 81 (3 Feb. 1951), pp. 385–390. DOI: 10.1103/PhysRev.81.385. URL: https://link.aps.org/doi/10.1103/PhysRev.81.385.

[96] A. Bulgac. *Hartree–Fock–Bogoliubov Approximation for Finite Systems*. 2000. arXiv: nucl-th/9907088 [nucl-th]. URL: https://arxiv.org/abs/nucl-th/9907088.

[97] A. Bulgac and Y. Yu. "Renormalization of the Hartree-Fock-Bogoliubov Equations in the Case of a Zero Range Pairing Interaction". In: *Physical Review Letters* 88.4 (Jan. 2002). ISSN: 1079-7114. DOI: 10.1103/physrevlett.88.042504. URL: http://dx.doi.org/10.1103/PhysRevLett.88.042504.

[98] S. Kurth et al. "Local Density Approximation for Superconductors". In: *Physical Review Letters* 83 (Sept. 1999). DOI: 10.1103/PhysRevLett.83.2628.

[99] W. Greiner and J. A. Maruhn. *Nuclear Models*. Springer- Verlag Berlin Heidelberg, 1996.

[100] M. Stein et al. "Spin-polarized neutron matter: Critical unpairing and BCS-BEC precursor". In: *Physical Review C* 93.1 (Jan. 2016). ISSN: 2469-9993. DOI: 10.1103/physrevc.93.015802. URL: http://dx.doi.org/10.1103/PhysRevC.93.015802.

[101] W. Cherry et al. "Superconductivity in Metals and Alloys". In: (Feb. 1963), p. 68.

[102] E. Engel and R.M. Dreizler. *Density Functional Theory: An Advanced Course*. Theoretical and Mathematical Physics. Springer Berlin Heidelberg, 2011.

[103] H. Eschring. *The Fundamentals of Density Functional Theory*. Vieweg+Teubner Verlag Wiesbaden, 1996.

[104] C. Fiolhais, F. Nogueira, and M. A. L. Marques. *A Primer in Density Functional Theory*. Springer-Verlag Berlin Heidelberg, 2003.

[105] A. Bulgac. "Time-Dependent Density Functional Theory for Fermionic Superfluids: From Cold Atomic Gases To Nuclei and Neutron Stars Crust". In: *physica status solidi (b)* 256.7 (Apr. 2019). ISSN: 1521-3951. DOI: 10.1002/pssb.201800592. URL: http://dx.doi.org/10.1002/pssb.201800592.

[106] P. Magierski. *The BCS-BEC Crossover and the Unitary Fermi Gas*. Springer Berlin Heidelberg, 2012. ISBN: 9783642219788. DOI: 10.1007/978-3-642-21978-8. URL: http://dx.doi.org/10.1007/978-3-642-21978-8.

[107] P. Echenique and J. L. Alonso. "A mathematical and computational review of Hartree–Fock SCF methods in quantum chemistry". In: *Molecular Physics* (Dec. 2007), 3057–3098. ISSN: 1362-3028. DOI: 10.1080/00268970701757875. URL: http://dx.doi.org/10.1080/00268970701757875.

[108] P. Hohenberg and W. Kohn. "Inhomogeneous Electron Gas". In: *Phys. Rev.* 136 (3B Nov. 1964), B864–B871. DOI: 10.1103/PhysRev.136.B864. URL: https://link.aps.org/doi/10.1103/PhysRev.136.B864.

[109] R. M. Dreizler and E. K. U. Gross. *Density Functional Theory: An Approach to the Quantum Many-Body Problem*. Springer Berlin Heidelberg, 2012. URL: https://books.google.pl/books?id=t6PvCAAAQBAJ.

[110] W. Kohn. "Nobel Lecture: Electronic structure of matter—wave functions and density functionals". In: *Rev. Mod. Phys.* 71 (5 Oct. 1999), pp. 1253–1266. DOI: 10.1103/RevModPhys.71.1253. URL: https://link.aps.org/doi/10.1103/RevModPhys.71.1253.

[111] W. Kohn and L. J. Sham. "Self-Consistent Equations Including Exchange and Correlation Effects". In: *Phys. Rev.* 140 (4A Nov. 1965), A1133–A1138. DOI: 10.1103/PhysRev.140.A1133. URL: https://link.aps.org/doi/10.1103/PhysRev.140.A1133.

[112] A. Colcelli et al. "Finite temperature off-diagonal long-range order for interacting bosons". In: *Physical Review B* 102.18 (Nov. 2020). ISSN: 2469-9969. DOI: 10.1103/physrevb.102.184510. URL: http://dx.doi.org/10.1103/PhysRevB.102.184510.

[113] K. Michielsen and H. D. Raedt. "Off-Diagonal Long-Range Order in Generalized Hubbard Models". In: *International Journal of Modern Physics B* 11 (Jan. 1997), pp. 1311–1335. DOI: 10.1142/S021797929700068X.

[114] O. Penrose. "CXXXVI. On the quantum mechanics of helium II". In: *The London, Edinburgh, and Dublin Philosophical Magazine and Journal of Science* 42.335 (1951), pp. 1373–1377. DOI: 10.1080/14786445108560954.

[115] O. Penrose and L. Onsager. "Bose-Einstein Condensation and Liquid Helium". In: *Phys. Rev.* 104 (3 Nov. 1956), pp. 576–584. DOI: 10.1103/PhysRev.104.576. URL: https://link.aps.org/doi/10.1103/PhysRev.104.576.

[116] C. N. Yang. "Concept of Off-Diagonal Long-Range Order and the Quantum Phases of Liquid He and of Superconductors". In: *Rev. Mod. Phys.* 34 (4 Oct. 1962), pp. 694–704. DOI: 10.1103/RevModPhys.34.694. URL: https://link.aps.org/doi/10.1103/RevModPhys.34.694.

[117] L. N. Oliveira, E. K. U. Gross, and W. Kohn. "Density-Functional Theory for Superconductors". In: *Phys. Rev. Lett.* 60 (23 June 1988), pp. 2430–2433. DOI: 10.1103/PhysRevLett.60.2430. URL: https://link.aps.org/doi/10.1103/PhysRevLett.60.2430.

[118] E.K.U. Gross, R.M. Dreizler, and North Atlantic Treaty Organization. Scientific Affairs Division. *Density Functional Theory*. Language of science. Springer, 1995. ISBN: 9780306449055. URL: https://books.google.pl/books?id=xQy7r1nNYvQC.

[119] P. Magierski. *Superfluidity in Fermi systems within the framework of Density Functional Theory*. 2025. arXiv: 2510.07410 [cond-mat.supr-con]. URL: https://arxiv.org/abs/2510.07410.

[120] A. Bulgac and M. McNeil Forbes. "Time-Dependent Superfluid Local-Density Approximation". In: *Quantum Gases*. Imperial College Press, Mar. 2013, 397–406. DOI: 10.1142/9781848168121_0026. URL: http://dx.doi.org/10.1142/9781848168121_0026.

[121] A. Bulgac. "Local-density-functional theory for superfluid fermionic systems: The unitary gas". In: *Physical Review A* 76.4 (Oct. 2007). ISSN: 1094-1622. DOI: 10.1103/physreva.76.040502. URL: http://dx.doi.org/10.1103/PhysRevA.76.040502.

[122] E. Runge and E. K. U. Gross. "Density-Functional Theory for Time-Dependent Systems". In: *Phys. Rev. Lett.* 52 (12 Mar. 1984), pp. 997–1000. DOI: 10.1103/PhysRevLett.52.997. URL: https://link.aps.org/doi/10.1103/PhysRevLett.52.997.

[123] M. Marques et al. *Fundamentals of Time-Dependent Density Functional Theory*. Vol. 837. Jan. 2012. ISBN: 978-3-642-23517-7. DOI: 10.1007/978-3-642-23518-4.

[124] C. A. Ullrich and Z. h. Yang. "A Brief Compendium of Time-Dependent Density Functional Theory". In: *Brazilian Journal of Physics* 44.1 (July 2013), 154–188. ISSN: 1678-4448. DOI: 10.1007/s13538-013-0141-2. URL: http://dx.doi.org/10.1007/s13538-013-0141-2.

[125] A. Bulgac. "Time-Dependent Density Functional Theory and the Real-Time Dynamics of Fermi Superfluids". In: *Annual Review of Nuclear and Particle Science* 63.1 (Oct. 2013), 97–121. ISSN: 1545-4134. DOI: 10.1146/annurev-nucl-102212-170631. URL: http://dx.doi.org/10.1146/annurev-nucl-102212-170631.

[126] P. Magierski. "Nuclear Reactions and Superfluid Time Dependent Density Functional Theory". In: *Frontiers in Nuclear and Particle Physics: Volume 2*. Bentham Science Publishers, June 2019, 57–71. DOI: 10.2174/978168108764119020008. URL: http://dx.doi.org/10.2174/978168108764119020008.

[127] M. Bender, P. H. Heenen, and P. G. Reinhard. "Self-consistent mean-field models for nuclear structure". In: *Rev. Mod. Phys.* 75 (1 Jan. 2003), pp. 121–180. DOI: 10.1103/RevModPhys.75.121. URL: https://link.aps.org/doi/10.1103/RevModPhys.75.121.

[128] D. M. Brink and E. Boeker. "Effective interactions for Hartree-Fock calculations". In: *Nuclear Physics A* 91.1 (1967), pp. 1–26. ISSN: 0375-9474. DOI: https://doi.org/10.1016/0375-9474(67)90446-0. URL: https://www.sciencedirect.com/science/article/pii/0375947467904460.

[129] T. H. R. Skyrme. "The effective nuclear potential". In: *Nuclear Physics* 9.4 (1958), pp. 615–634. ISSN: 0029-5582. DOI: https://doi.org/10.1016/0029-5582(58)90345-6. URL: https://www.sciencedirect.com/science/article/pii/0029558258903456.

[130] D. Gogny. "Proceedings of the International Confer- ence on Nuclear Physics, Munich". In: ed. by J. de Boer and H. J. Mang. 1973.

[131] D. Gogny. "Proceedings of the International Conference on Nuclear Self Consistent Fields, Trieste". In: ed. by G. Ripka and M. Porneuf. 1975.

[132] J. Dechargé and D. Gogny. "Hartree-Fock-Bogolyubov calculations with the $D1$ effective interaction on spherical nuclei". In: *Phys. Rev. C* 21 (4 Apr. 1980), pp. 1568–1593. DOI: 10.1103/PhysRevC.21.1568. URL: https://link.aps.org/doi/10.1103/PhysRevC.21.1568.

[133] J.E. Drut, R.J. Furnstahl, and L. Platter. "Toward ab initio density functional theory for nuclei". In: *Progress in Particle and Nuclear Physics* 64.1 (Jan. 2010), 120–168. ISSN: 0146-6410. DOI: 10.1016/j.ppnp.2009.09.001. URL: http://dx.doi.org/10.1016/j.ppnp.2009.09.001.

[134] N. Chamel. "Self-interaction errors in nuclear energy density functionals". In: *Physical Review C* 82.6 (Dec. 2010). ISSN: 1089-490X. DOI: 10.1103/physrevc.82.061307. URL: http://dx.doi.org/10.1103/PhysRevC.82.061307.

[135] A. Bulgac. "Local density approximation for systems with pairing correlations". In: *Physical Review C* 65.5 (Apr. 2002). ISSN: 1089-490X. DOI: 10.1103/physrevc.65.051305. URL: http://dx.doi.org/10.1103/PhysRevC.65.051305.

[136] S. Goriely, N. Chamel, and J. M. Pearson. "Further explorations of Skyrme-Hartree-Fock-Bogoliubov mass formulas. XII. Stiffness and stability of neutron-star matter". In: *Physical Review C* 82.3 (Sept. 2010). ISSN: 1089-490X. DOI: 10.1103/physrevc.82.035804. URL: http://dx.doi.org/10.1103/PhysRevC.82.035804.

[137] N. Chamel. "Effective contact pairing forces from realistic calculations in infinite homogeneous nuclear matter". In: *Physical Review C* 82.1 (July 2010). ISSN: 1089-490X. DOI: 10.1103/physrevc.82.014313. URL: http://dx.doi.org/10.1103/PhysRevC.82.014313.

[138] N. Chamel, S. Goriely, and J. M. Pearson. "Further explorations of Skyrme – Hartree – Fock – Bogoliubov mass formulas. IX: Constraint of pairing force to 1S0 neutron-matter gap". In: *Nuclear Physics A* 812.1–4 (Nov. 2008), 72–98. ISSN: 0375-9474. DOI: 10.1016/j.nuclphysa.2008.08.015. URL: http://dx.doi.org/10.1016/j.nuclphysa.2008.08.015.

[139] S. Goriely, N. Chamel, and J. M. Pearson. "Further explorations of Skyrme-Hartree-Fock-Bogoliubov mass formulas. XVI. Inclusion of self-energy effects in pairing". In: *Physical Review C* 93.3, 034337 (Mar. 2016), p. 034337. DOI: 10.1103/PhysRevC.93.034337.

[140] S. Goriely, N. Chamel, and J. M. Pearson. "Skyrme-Hartree-Fock-Bogoliubov Nuclear Mass Formulas: Crossing the 0.6 MeV Accuracy Threshold with Microscopically Deduced Pairing". In: *Physical Review Letters* 102.15 (Apr. 2009). ISSN: 1079-7114. DOI: 10.1103/physrevlett.102.152503. URL: http://dx.doi.org/10.1103/PhysRevLett.102.152503.

[141] N. Chamel et al. "Brussels–Montreal Nuclear Energy Density Functionals, from Atomic Masses to Neutron Stars". In: *Acta Physica Polonica B*. Vol. 46. Zakopane, Poland, Aug. 2014, pp. 349–358. DOI: 10.5506/APhysPolB.46.349. URL: https://in2p3.hal.science/in2p3-01152712.

[142] L. Zurek et al. "Optimized nuclear energy density functionals including long-range pion contributions". In: *Physical Review C* 109.1 (Jan. 2024). ISSN: 2469-9993. DOI: 10.1103/physrevc.109.014319. URL: http://dx.doi.org/10.1103/PhysRevC.109.014319.

[143] P. G. Reinhard and W. Nazarewicz. "Toward a global description of nuclear charge radii: Exploring the Fayans energy density functional". In: *Physical Review C* 95.6 (June 2017). ISSN: 2469-9993. DOI: 10.1103/physrevc.95.064328. URL: http://dx.doi.org/10.1103/PhysRevC.95.064328.

[144] A. Bulgac et al. "Minimal nuclear energy density functional". In: *Physical Review C* 97.4 (Apr. 2018). ISSN: 2469-9993. DOI: 10.1103/physrevc.97.044313. URL: http://dx.doi.org/10.1103/PhysRevC.97.044313.

[145] M. Baldo et al. "Barcelona-Catania-Paris-Madrid functional with a realistic effective mass". In: *Physical Review C* 95.1 (Jan. 2017). ISSN: 2469-9993. DOI: 10.1103/physrevc.95.014318. URL: http://dx.doi.org/10.1103/PhysRevC.95.014318.

[146] L. G. Cao et al. "From Brueckner approach to Skyrme-type energy density functional". In: *Physical Review C* 73.1 (Jan. 2006). ISSN: 1089-490X. DOI: 10.1103/physrevc.73.014313. URL: http://dx.doi.org/10.1103/PhysRevC.73.014313.

[147] L. G. Cao, U. Lombardo, and P. Schuck. "Screening effects in superfluid nuclear and neutron matter within Brueckner theory". In: *Physical Review C* 74.6 (Dec. 2006). ISSN: 1089-490X. DOI: 10.1103/physrevc.74.064301. URL: http://dx.doi.org/10.1103/PhysRevC.74.064301.

[148] G. Audi, A. H. Wapstra, and C. Thibault. "The Ame2003 atomic mass evaluation: (II). Tables, graphs and references". In: *Nuclear Physics A* 729.1 (2003). The 2003 NUBASE and Atomic Mass Evaluations, pp. 337–676. ISSN: 0375-9474. DOI: https://doi.org/10.1016/j.nuclphysa.2003.11.003. URL: https://www.sciencedirect.com/science/article/pii/S0375947403018098.

[149] G. Audi et al. "The Ame2012 atomic mass evaluation". In: *Chinese Physics C* 36.12 (Dec. 2012), p. 1287. DOI: 10.1088/1674-1137/36/12/002. URL: https://doi.org/10.1088/1674-1137/36/12/002.

[150] G. Colò et al. "Microscopic determination of the nuclear incompressibility within the nonrelativistic framework". In: *Phys. Rev. C* 70 (2 Aug. 2004), p. 024307. DOI: 10.1103/PhysRevC.70.024307. URL: https://link.aps.org/doi/10.1103/PhysRevC.70.024307.

[151] M. Bender et al. "Consequences of the center–of–mass correction in nuclear mean–field models". In: *The European Physical Journal A* 7.4 (Apr. 2000), 467–478. ISSN: 1434-601X. DOI: 10.1007/pl00013645. URL: http://dx.doi.org/10.1007/PL00013645.

[152] S. Goriely and J. M. Pearson. "Further explorations of Skyrme-Hartree-Fock-Bogoliubov mass formulas. VIII. Role of Coulomb exchange". In: *Phys. Rev. C* 77 (3 Mar. 2008), p. 031301. DOI: 10.1103/PhysRevC.77.031301. URL: https://link.aps.org/doi/10.1103/PhysRevC.77.031301.

[153] N. Chamel, S. Goriely, and J. M. Pearson. "Further explorations of Skyrme-Hartree-Fock-Bogoliubov mass formulas. XI. Stabilizing neutron stars against a ferromagnetic collapse". In: *Phys. Rev. C* 80 (6 Dec. 2009), p. 065804. DOI: 10.1103/PhysRevC.80.065804. URL: https://link.aps.org/doi/10.1103/PhysRevC.80.065804.

[154] S. Goriely, N. Chamel, and J. M. Pearson. "Further explorations of Skyrme-Hartree-Fock-Bogoliubov mass formulas. XIII. The 2012 atomic mass evaluation and the symmetry coefficient". In: *Phys. Rev. C* 88 (2 Aug. 2013), p. 024308. DOI: 10.1103/PhysRevC.88.024308. URL: https://link.aps.org/doi/10.1103/PhysRevC.88.024308.

[155] G. Audi et al. "The Nubase2012 evaluation of nuclear properties". In: *Chinese Physics C* 36.12 (Dec. 2012), p. 1157. DOI: 10.1088/1674-1137/36/12/001. URL: https://doi.org/10.1088/1674-1137/36/12/001.

[156] S. Goriely, N. Chamel, and J. M. Pearson. "Hartree-Fock-Bogoliubov nuclear mass model with 0.50 MeV accuracy based on standard forms of Skyrme and pairing functionals". In: *Phys. Rev. C* 88 (6 Dec. 2013), p. 061302. DOI: 10.1103/PhysRevC.88.061302. URL: https://link.aps.org/doi/10.1103/PhysRevC.88.061302.

[157] S. Goriely, N. Chamel, and J. M. Pearson. "Skyrme-Hartree-Fock-Bogoliubov Nuclear Mass Formulas: Crossing the 0.6 MeV Accuracy Threshold with Microscopically Deduced Pairing". In: *Physical Review Letters* 102.15 (Apr. 2009).

ISSN: 1079-7114. DOI: 10.1103/physrevlett.102.152503. URL: http://dx.doi.org/10.1103/PhysRevLett.102.152503.

[158] A. Pastore et al. "Linear response theory and neutrino mean free path using Brussels-Montreal Skyrme functionals". In: *Phys. Rev. C* 90 (2 Aug. 2014). DOI: 10.1103/PhysRevC.90.025804. URL: https://link.aps.org/doi/10.1103/PhysRevC.90.025804.

[159] S. Gandolfi et al. "The equation of state of neutron matter, symmetry energy and neutron star structure". In: *The European Physical Journal A* 50.2 (Feb. 2014). ISSN: 1434-601X. DOI: 10.1140/epja/i2014-14010-5. URL: http://dx.doi.org/10.1140/epja/i2014-14010-5.

[160] M. Baldo and G.F. Burgio. "The nuclear symmetry energy". In: *Progress in Particle and Nuclear Physics* 91 (Nov. 2016), 203–258. ISSN: 0146-6410. DOI: 10.1016/j.ppnp.2016.06.006. URL: http://dx.doi.org/10.1016/j.ppnp.2016.06.006.

[161] N. Alam et al. "Strong correlations of neutron star radii with the slopes of nuclear matter incompressibility and symmetry energy at saturation". In: *Physical Review C* 94.5 (Nov. 2016). ISSN: 2469-9993. DOI: 10.1103/physrevc.94.052801. URL: http://dx.doi.org/10.1103/PhysRevC.94.052801.

[162] A. Kumar, H. C. Das, and S. K. Patra. "Incompressibility and symmetry energy of a neutron star". In: *Physical Review C* 104.5 (Nov. 2021). ISSN: 2469-9993. DOI: 10.1103/physrevc.104.055804. URL: http://dx.doi.org/10.1103/PhysRevC.104.055804.

[163] H. De Vries, C. W. De Jager, and C. De Vries. "Nuclear charge - density distribution parameters from elastic electron scattering". In: *Atomic Data and Nuclear Data Tables* 36.3 (1987), pp. 495–536. ISSN: 0092-640X. DOI: https://doi.org/10.1016/0092-640X(87)90013-1. URL: https://www.sciencedirect.com/science/article/pii/0092640X87900131.

[164] J. P. Blaizot. "Nuclear compressibilities". In: *Physics Reports* 64.4 (1980), pp. 171–248. ISSN: 0370-1573. DOI: https://doi.org/10.1016/0370-1573(80)90001-0.

[165] U. Garg and G. Colò. "The compression-mode giant resonances and nuclear incompressibility". In: *Progress in Particle and Nuclear Physics* 101 (2018), pp. 55–95. ISSN: 0146-6410. DOI: https://doi.org/10.1016/j.ppnp.2018.03.001. URL: https://www.sciencedirect.com/science/article/pii/S0146641018300322.

[166] G. F. Burgio et al. "Neutron stars and the nuclear equation of state". In: *Progress in Particle and Nuclear Physics* 120 (2021), p. 103879. ISSN: 0146-6410. DOI: https://doi.org/10.1016/j.ppnp.2021.103879. URL: https://www.sciencedirect.com/science/article/pii/S0146641021000338.

[167] S. Gandolfi, J. Carlson, and S. Reddy. "Maximum mass and radius of neutron stars, and the nuclear symmetry energy". In: *Physical Review C* 85.3 (Mar. 2012). ISSN: 1089-490X. DOI: 10.1103/physrevc.85.032801. URL: http://dx.doi.org/10.1103/PhysRevC.85.032801.

[168] I. Tews et al. "Neutron Matter at Next-to-Next-to-Next-to-Leading Order in Chiral Effective Field Theory". In: *Physical Review Letters* 110.3 (Jan. 2013). ISSN: 1079-7114. DOI: 10.1103/physrevlett.110.032504. URL: http://dx.doi.org/10.1103/PhysRevLett.110.032504.

[169] A. Akmal, V. R. Pandharipande, and D. G. Ravenhall. "Equation of state of nucleon matter and neutron star structure". In: *Physical Review C* 58.3 (Sept. 1998), 1804–1828. ISSN: 1089-490X. DOI: 10.1103/physrevc.58.1804. URL: http://dx.doi.org/10.1103/PhysRevC.58.1804.

[170] Z. H. Li and H. J. Schulze. "Neutron star structure with modern nucleonic three-body forces". In: *Phys. Rev. C* 78 (2 Aug. 2008), p. 028801. DOI: 10.1103/PhysRevC.78.028801. URL: https://link.aps.org/doi/10.1103/PhysRevC.78.028801.

[171] J. M. Pearson et al. "Unified equations of state for cold non-accreting neutron stars with Brussels–Montreal functionals – I. Role of symmetry energy". In: *Monthly Notices of the Royal Astronomical Society* 481.3 (Sept. 2018), pp. 2994–3026. DOI: 10.1093/mnras/sty2413. eprint: https://academic.oup.com/mnras/article-pdf/481/3/2994/25817956/sty2413.pdf. URL: https://doi.org/10.1093/mnras/sty2413.

[172] URL: https://wbsk.fizyka.pw.edu.pl/.

[173] URL: https://wslda.fizyka.pw.edu.pl/.

[174] G. Wlazłowski et al. "Suppressed Solitonic Cascade in Spin-Imbalanced Superfluid Fermi Gas". In: *Physical Review Letters* 120.25 (June 2018). ISSN: 1079-7114. DOI: 10.1103/physrevlett.120.253002. URL: http://dx.doi.org/10.1103/PhysRevLett.120.253002.

[175] A. Bulgac et al. "Quantized Superfluid Vortex Rings in the Unitary Fermi Gas". In: *Physical Review Letters* 112.2 (Jan. 2014). ISSN: 1079-7114. DOI: 10.1103/physrevlett.112.025301. URL: http://dx.doi.org/10.1103/PhysRevLett.112.025301.

[176] G. Wlazłowski et al. "Fermionic quantum turbulence: Pushing the limits of high-performance computing". In: *PNAS Nexus* 3.5 (Apr. 2024). Ed. by C. H. Amon. ISSN: 2752-6542. DOI: 10.1093/pnasnexus/pgae160. URL: http://dx.doi.org/10.1093/pnasnexus/pgae160.

[177] J. Shen, T. Tang, and L.L. Wang. *Spectral Methods: Algorithms, Analysis and Applications*. Springer, Berlin, 2011. URL: http://dx.doi.org/10.1007/978-3-540-71041-7.

[178] D. Pęcak et al. "Dataset and supplement for "Time-dependent nuclear energy-density functional theory toolkit for neutron star crust: dynamics of a nucleus in a neutron superfluid"". In: (Feb. 2024). DOI: 10.5281/zenodo.10724934. URL: https://doi.org/10.5281/zenodo.10724934.

[179] N. D. Woods, M. C. Payne, and P. J. Hasnip. "Computing the self-consistent field in Kohn–Sham density functional theory". In: *Journal of Physics: Condensed Matter* 31.45 (Aug. 2019), p. 453001. ISSN: 1361-648X. DOI: 10.1088/1361-648x/ab31c0. URL: http://dx.doi.org/10.1088/1361-648X/ab31c0.

[180] A. Baran et al. "Broyden's method in nuclear structure calculations". In: *Physical Review C* 78.1 (July 2008). ISSN: 1089-490X. DOI: 10.1103/physrevc.78.014318. URL: http://dx.doi.org/10.1103/PhysRevC.78.014318.

[181] D. A. Rehn et al. "ODE integration schemes for plane-wave real-time time-dependent density functional theory". In: *The Journal of Chemical Physics* 150.1 (Jan. 2019), p. 014101. ISSN: 0021-9606. DOI: 10.1063/1.5056258. eprint: https://pubs.aip.org/aip/jcp/article-pdf/doi/10.1063/1.5056258/15552252/014101_1_online.pdf. URL: https://doi.org/10.1063/1.5056258.

[182] R. W. Hamming. *Numerical Methods for Scientists and Engineers (Dover Books on Mathematics*. Dover Publishing, 1987.

[183] M. Ghrist, B. Fornberg, and J. Reeger. "Stability ordinates of Adams predictor-corrector methods". In: *BIT Numerical Mathematics* 55 (Dec. 2014). DOI: 10.1007/s10543-014-0528-7.

[184] URL: https://www.cscs.ch/computers/piz-daint.

[185] URL: https://lumi-supercomputer.eu/lumi_supercomputer/.

[186] N. Chamel, D. Page, and S. Reddy. "Low-energy collective excitations in the neutron star inner crust". In: *Physical Review C* 87.3 (Mar. 2013). ISSN: 1089-490X. DOI: 10.1103/physrevc.87.035803. URL: http://dx.doi.org/10.1103/PhysRevC.87.035803.

[187] P. Magierski and A. Bulgac. *Nuclear hydrodynamics in the inner crust of neutron stars*. 2003. arXiv: astro-ph/0312644 [astro-ph]. URL: https://arxiv.org/abs/astro-ph/0312644.

[188] P. Magierski. "In-medium ion mass renormalization and lattice vibrations in the neutron star crust". In: *International Journal of Modern Physics E* 13.01 (Feb. 2004), 371–374. ISSN: 1793-6608. DOI: 10.1142/s0218301304002211. URL: http://dx.doi.org/10.1142/S0218301304002211.

[189] N. Martin and M. Urban. "Superfluid hydrodynamics in the inner crust of neutron stars". In: *Physical Review C* 94.6 (Dec. 2016). ISSN: 2469-9993. DOI: 10.1103/physrevc.94.065801. URL: http://dx.doi.org/10.1103/PhysRevC.94.065801.

[190] N. Chamel, J. M. Pearson, and N. N. Shchechilin. "Role of neutron pairing with density-gradient dependence in the semimicroscopic treatment of the inner crust of neutron stars". In: *Phys. Rev. C* 110 (4 Oct. 2024), p. 045808. DOI: 10.1103/PhysRevC.110.045808. URL: https://link.aps.org/doi/10.1103/PhysRevC.110.045808.

[191] V. Allard and N. Chamel. "Gapless superfluidity in neutron stars: Normal-fluid fraction". In: *Phys. Rev. C* 108 (4 Oct. 2023), p. 045801. DOI: 10.1103/PhysRevC.108.045801. URL: https://link.aps.org/doi/10.1103/PhysRevC.108.045801.

[192] V. Allard and N. Chamel. "Gapless superfluidity in neutron stars: Thermal properties". In: *Phys. Rev. C* 108 (1 July 2023), p. 015801. DOI: 10.1103/PhysRevC.108.015801. URL: https://link.aps.org/doi/10.1103/PhysRevC.108.015801.

[193] C. F. Barenghi and R. J. Donnelly. "Vortex rings in classical and quantum systems". In: *Fluid Dynamics Research* 41.5 (Sept. 2009), p. 051401. DOI: 10.1088/0169-5983/41/5/051401. URL: https://dx.doi.org/10.1088/0169-5983/41/5/051401.

[194] D. T. Loan et al. "Equation of state of neutron star matter, and the nuclear symmetry energy". In: *Physical Review C* 83.6 (June 2011). ISSN: 1089-490X. DOI: 10.1103/physrevc.83.065809. URL: http://dx.doi.org/10.1103/PhysRevC.83.065809.

[195] Z. P. Li and D. Vretenar. *Model for collective motion*. 2022. arXiv: 2203.07608 [nucl-th]. URL: https://arxiv.org/abs/2203.07608.

[196] D. G. Truhlar. "Potential Energy Surfaces". In: *Encyclopedia of Physical Science and Technology (Third Edition)*. Ed. by Robert A. Meyers. Third Edition. New York: Academic Press, 2003, pp. 9–17. ISBN: 978-0-12-227410-7. DOI: https://doi.org/10.1016/B0-12-227410-5/00606-2. URL: https://www.sciencedirect.com/science/article/pii/B0122274105006062.

[197] L. Shvedov, J. Blocki, and J. Wilczynski. "Potential Energy Surface in Nucleus-Nucleus Collisions Corrected for Exact Nuclear Masses". In: *Acta Physica Polonica. Series B* B34.3 (Mar. 2003), p. 1815–1824. ISSN: 0587-4254.

[198] C. Peng and Z. Q. Feng. "Potential energy surface and formation of superheavy nuclei with the Skyrme energy-density functional". In: *Communications in Theoretical Physics* 74.5 (May 2022), p. 055302. ISSN: 1572-9494. DOI: 10.1088/1572-9494/ac6491. URL: http://dx.doi.org/10.1088/1572-9494/ac6491.

[199] E.M Kozulin et al. "Investigation of the reaction 64Ni + 238U being an option of synthesizing element 120". In: *Physics Letters B* 686 (Mar. 2010), 227–232. DOI: 10.1016/j.physletb.2010.02.041.

[200] K. L. G. Heyde. *The Nuclear Shell Model*. Springer-Verlag, 1994.

[201] B. Remi et al. *Fission of ^{180}Hg and ^{264}Fm: a comparative study*. 2024. arXiv: 2409.02818 [nucl-th]. URL: https://arxiv.org/abs/2409.02818.

[202] A. Beekman, L. Rademaker, and J. van Wezel. "An introduction to spontaneous symmetry breaking". In: *SciPost Physics Lecture Notes* (Dec. 2019). ISSN: 2590-1990. DOI: 10.21468/scipostphyslectnotes.11. URL: http://dx.doi.org/10.21468/SciPostPhysLectNotes.11.

[203] M. Urban and M. Oertel. "Collective modes in the superfluid inner crust of neutron stars". In: *International Journal of Modern Physics E* 24.09 (Sept. 2015), p. 1541006. ISSN: 1793-6608. DOI: 10.1142/s0218301315410062. URL: http://dx.doi.org/10.1142/S0218301315410062.

[204] V. Tomar. *Spectral Techniques in Inorganic Chemistry*. PowerPoint slides. URL: https://chemistry.du.ac.in/wp-content/uploads/2023/01/Nuclear-Quadrupole-Resonance-NQR-spectroscopy.pdf.

[205] M. Baranger and M. Véneroni. "An adiabatic time-dependent Hartree-Fock theory of collective motion in finite systems". In: *Annals of Physics* 114.1 (1978), pp. 123–200. ISSN: 0003-4916. DOI: https://doi.org/10.1016/0003-4916(78)90265-8. URL: https://www.sciencedirect.com/science/article/pii/0003491678902658.

[206] F. Villars. "Adiabatic time-dependent Hartree-Fock theory in nuclear physics". In: *Nuclear Physics A* 285.2 (1977), pp. 269–296. ISSN: 0375-9474. DOI: https://doi.org/10.1016/0375-9474(77)90253-6. URL: https://www.sciencedirect.com/science/article/pii/0375947477902536.

[207] K. Goeke, P. G. Reinhard, and D. J. Rowe. "A study of collective paths in the time-dependent hartree-fock approach to large amplitude collective nuclear motion". In: *Nuclear Physics A* 359.2 (1981), pp. 408–430. ISSN: 0375-9474. DOI: https://doi.org/10.1016/0375-9474(81)90246-3. URL: https://www.sciencedirect.com/science/article/pii/0375947481902463.

[208] A. Baran et al. "Quadrupole collective inertia in nuclear fission: Cranking approximation". In: *Phys. Rev. C* 84 (5 Nov. 2011), p. 054321. DOI: 10.1103/PhysRevC.84.054321. URL: https://link.aps.org/doi/10.1103/PhysRevC.84.054321.

[209] D. R. Inglis. "Nuclear Moments of Inertia due to Nucleon Motion in a Rotating Well". In: *Phys. Rev.* 103 (6 Sept. 1956), pp. 1786–1795. DOI: 10.1103/PhysRev.103.1786. URL: https://link.aps.org/doi/10.1103/PhysRev.103.1786.

[210] D. J. Thouless and J. G. Valatin. "Time-dependent Hartree-Fock equations and rotational states of nuclei". In: *Nuclear Physics* 31 (1962), pp. 211–230. ISSN: 0029-5582. DOI: https://doi.org/10.1016/0029-5582(62)90741-1. URL: https://www.sciencedirect.com/science/article/pii/0029558262907411.

[211] A. S. Umar and V. E. Oberacker. "Density-constrained time-dependent Hartree-Fock calculation of 16O + 208Pb fusion cross-sections". In: *The European Physical Journal A* 39.2 (Jan. 2009), 243–247. ISSN: 1434-601X. DOI: 10.1140/epja/i2008-10712-5. URL: http://dx.doi.org/10.1140/epja/i2008-10712-5.

[212] P. G. Reinhard, F. Grümmer, and K. Goeke. "Collective mass parameters and linear response techniques in three-dimensional grids". In: *Z Physik A* 317 (1984), pp. 339–346. DOI: 10.1007/BF01438367.

[213] B. Link. "Dynamics of Quantum Vorticity in a Random Potential". In: *Physical Review Letters* 102.13 (Apr. 2009). ISSN: 1079-7114. DOI: 10.1103/physrevlett.102.131101. URL: http://dx.doi.org/10.1103/PhysRevLett.102.131101.

[214] P. Klausner et al. "Microscopic calculation of the pinning energy of a vortex in the inner crust of a neutron star". In: *Physical Review C* 108.3 (Sept. 2023). ISSN: 2469-9993. DOI: 10.1103/physrevc.108.035808. URL: http://dx.doi.org/10.1103/PhysRevC.108.035808.

[215] P. Avogadro et al. "Vortex–nucleus interaction in the inner crust of neutron stars". In: *Nuclear Physics A* 811.3–4 (Oct. 2008), 378–412. ISSN: 0375-9474. DOI: 10.1016/j.nuclphysa.2008.07.010. URL: http://dx.doi.org/10.1016/j.nuclphysa.2008.07.010.

[216] R. Epstein and G. Baym. "Vortex pinning in neutron stars". In: *The Astrophysical Journal* 328 (Apr. 1988), pp. 680–690. DOI: 10.1086/166325.

[217] P. Donati and P. M. Pizzochero. "Fully consistent semi-classical treatment of vortex–nucleus interaction in rotating neutron stars". In: *Nuclear Physics A* 742.3 (2004), pp. 363–379. ISSN: 0375-9474. DOI: https://doi.org/10.1016/j.nuclphysa.2004.07.002. URL: https://www.sciencedirect.com/science/article/pii/S0375947404008085.

[218] B. Link and Y. Levin. "Vortex Pinning in Neutron Stars, Slipstick Dynamics, and the Origin of Spin Glitches". In: *The Astrophysical Journal* 941.2 (Dec. 2022), p. 148. DOI: 10.3847/1538-4357/ac9b29. URL: https://doi.org/10.3847/1538-4357/ac9b29.

[219] D. Pęcak et al. "Properties of a quantum vortex in neutron matter at finite temperatures". In: *Physical Review C* 104.5 (Nov. 2021). ISSN: 2469-9993. DOI: 10.1103/physrevc.104.055801. URL: http://dx.doi.org/10.1103/PhysRevC.104.055801.

[220] P. Virtanen et al. "SciPy 1.0: Fundamental Algorithms for Scientific Computing in Python". In: *Nature Methods* 17 (2020), pp. 261–272. DOI: 10.1038/s41592-019-0686-2.

[221] L. P. Gaffney et al. “Studies of pear-shaped nuclei using accelerated radioactive beams”. English. In: *Nature* 497.7448 (2013), pp. 199–204. ISSN: 0028-0836. DOI: 10.1038/nature12073.

[222] P. MohanMurthy, U. Silwal, and J. A. Winger. “A survey of nuclear quadrupole deformation in order to estimate the nuclear MQM and its relative contribution to the atomic EDM”. In: *Interactions* 245 (2024), p. 64. DOI: 10.1007/s10751-024-01880-7.

[223] P. A. Butler. “Octupole collectivity in nuclei”. In: *Journal of Physics G: Nuclear and Particle Physics* 43.7 (June 2016), p. 073002. DOI: 10.1088/0954-3899/43/7/073002. URL: https://doi.org/10.1088/0954-3899/43/7/073002.

[224] P. A. Butler. “Pear-shaped atomic nuclei”. In: *Proceedings of the Royal Society A: Mathematical, Physical and Engineering Sciences* 476.2239 (2020), p. 20200202. DOI: 10.1098/rspa.2020.0202. URL: https://royalsocietypublishing.org/doi/abs/10.1098/rspa.2020.0202.

[225] K. Arita. “Nuclear shell structures in terms of classical periodic orbits”. In: *Physica Scripta* 91 (June 2016), p. 063002. DOI: 10.1088/0031-8949/91/6/063002.

[226] A. Zdanowicz et al. “Dynamical scheme for computing the mass parameter of a system in a medium: reproducibility packs”. In: (July 2025). DOI: 10.5281/zenodo.15808859. URL: https://doi.org/10.5281/zenodo.15808859.